

**The Search for Higgs Boson Production in Association  
with a Top-Quark Pair in  $pp$  Collisions at  $\sqrt{s} = 8$  TeV in  
the Lepton Plus Jets Final State**

John Garland Wood  
Charlottesville, VA

B.S., The University of California, Berkeley, 2008

A Dissertation presented to the Graduate Faculty  
of the University of Virginia in Candidacy for the Degree of  
Doctor of Philosophy

Department of Physics

University of Virginia  
May, 2015

## Abstract

The most important goal of the Large Hadron Collider (LHC) is to elucidate the mechanism of electroweak symmetry breaking. The Standard Model (SM) Higgs boson is thought to be a prime candidate for this. The newly discovered boson announced on July 4th, 2012, with a mass of  $\sim 125$  GeV/c $^2$ , has so far been shown to be consistent with a SM Higgs. However, the final confirmation of this new particle as the SM Higgs depends on subsequent measurements of all of its properties. The observation of this new particle in association with top-quark pairs would allow the couplings of this particle to top and bottom quarks to be directly measured.  $t\bar{t}H$  with Higgs decaying to  $b\bar{b}$  is an excellent channel to explore due to the dominant branching ratio of Higgs to  $b\bar{b}$  and the kinematic handle the  $t\bar{t}$  system offers on the event. However, it presents a plethora of difficult challenges due to a low signal to background ratio and uncertainties on kinematically similar SM backgrounds. This work discusses the search for Higgs boson production in association with a top-quark pair in  $pp$  collisions at  $\sqrt{s} = 8$  TeV, collected by the Compact Muon Solenoid (CMS) experiment at the LHC. The search has been performed and published in two stages. The first analysis used the first 5.1 fb $^{-1}$ , and was followed up by the second analysis with the full 2012 dataset, using a total integrated luminosity of 19.5 fb $^{-1}$ .

We approve the dissertation of John Garland Wood.

Date of Signature

---

Supervisor: Prof. Christopher Neu

---

Committee Member: Prof. Hank Thacker

---

Committee Member: Prof. Edward Murphy

---

Committee Member: Prof. Bradley Cox

---

PhD Committee Chair: Prof. Craig Group

# Contents

<b>Contents</b>	<b>iv</b>
<b>List of Figures</b>	<b>viii</b>
<b>List of Tables</b>	<b>xx</b>
<b>Acknowledgements</b>	<b>xxiii</b>
<b>1 Introduction</b>	<b>1</b>
<b>2 Theoretical Background</b>	<b>4</b>
2.1 An Overview of Quantum Field Theory . . . . .	4
2.2 Abelian Gauge Theories of Particle Interactions . . . . .	7
2.3 Non-Abelian Gauge Theories of Particle Interactions . . . . .	9
2.4 The Higgs Mechanism in an Abelian Theory . . . . .	12
2.5 The Higgs Mechanism in a non-Abelian Theory . . . . .	14
2.6 Glashow Weinberg Salam Theory . . . . .	16
2.7 The Standard Model of Particle Physics . . . . .	22
2.8 Higgs Production in $pp$ Collisions at the LHC . . . . .	24
2.9 $t\bar{t}H$ Production in $pp$ Collisions at the LHC . . . . .	26
2.10 Background Processes to $t\bar{t}H$ . . . . .	27
2.11 Potential BSM Effects on $t\bar{t}H$ production . . . . .	30
<b>3 The Large Hadron Collider</b>	<b>32</b>
3.1 The LHC Accelerator Complex . . . . .	34
3.2 LHC Magnets . . . . .	42
3.3 LHC RF Technology . . . . .	49
3.4 The LHC Cryogen System . . . . .	51
3.5 The LHC Vacuum System . . . . .	52

<b>4 The Compact Muon Solenoid</b>	<b>54</b>
4.1 The Tracker . . . . .	56
4.1.1 The Silicon Pixel Detector . . . . .	58
4.1.2 The Silicon Strip Detector . . . . .	60
4.2 The Electromagnetic Calorimeter . . . . .	63
4.2.1 Vacuum Photo-Triodes . . . . .	67
4.2.2 Test Rig at UVa . . . . .	68
4.2.3 Results of UVa Tests . . . . .	69
4.3 The Hadronic Calorimeter . . . . .	72
4.4 Muon Chambers . . . . .	77
4.5 Data Collection Overview . . . . .	81
<b>5 Particle Reconstruction at CMS</b>	<b>85</b>
5.1 Iterative Tracking . . . . .	85
5.2 Calorimeter Clustering . . . . .	86
5.3 Calorimeter Energy Calibration . . . . .	87
5.4 Linking . . . . .	89
5.5 Physics Object Reconstruction . . . . .	90
5.5.1 Muon Reconstruction . . . . .	90
5.5.2 Electron Reconstruction . . . . .	91
5.5.3 Charged Hadron Reconstruction . . . . .	92
5.5.4 Photon and Neutral Hadron Reconstruction . . . . .	92
5.5.5 Jet Reconstruction . . . . .	93
5.5.6 Missing Transverse Energy Reconstruction . . . . .	95
<b>6 Analysis I: The first <math>5.08 \text{ fb}^{-1}</math> of 8 TeV data</b>	<b>97</b>
6.1 Data and Simulated Samples . . . . .	99
6.1.1 Data Samples . . . . .	100
6.1.2 Signal Samples . . . . .	101
6.1.3 Background Samples . . . . .	101
6.1.4 MC pileup reweighting . . . . .	102
6.1.5 Additional Pileup Corrections . . . . .	103
6.2 Event Selection . . . . .	105
6.2.1 Event cleaning . . . . .	105
6.2.2 Trigger . . . . .	106
6.2.3 Muon Selection . . . . .	107

6.2.4	Electron Selection . . . . .	107
6.2.5	Lepton selection and trigger efficiencies . . . . .	108
6.2.6	Jet selection . . . . .	109
6.2.7	<i>b</i> -tagging selection . . . . .	111
6.2.8	Lepton + Jets Selection . . . . .	113
6.3	Multivariate Analysis . . . . .	114
6.3.1	Artificial Neural Network Overview . . . . .	117
6.3.2	MVA Input Variables, Data to Monte Carlo Comparisons . . . . .	121
6.3.3	MVA Output, Data to Monte Carlo Comparisons . . . . .	138
6.4	Systematic Uncertainties . . . . .	140
6.5	Statistical Methods . . . . .	146
6.6	Results and Conclusions . . . . .	149
<b>7</b>	<b>Analysis II: The Complete 19.5 fb<sup>-1</sup> of 8 TeV data</b>	<b>151</b>
7.1	Data and Simulated Samples . . . . .	151
7.1.1	Data Samples . . . . .	152
7.1.2	Signal Samples . . . . .	152
7.1.3	Background Samples . . . . .	152
7.1.4	MC pileup reweighting . . . . .	155
7.1.5	Top <i>p</i> <sub>T</sub> Reweighting . . . . .	155
7.2	Event Selection . . . . .	156
7.2.1	<i>b</i> -tag discriminant reweighting . . . . .	157
7.2.2	Lepton + Jets Selection . . . . .	158
7.3	Multivariate Analysis . . . . .	160
7.3.1	Boosted Decision Tree Overview . . . . .	160
7.3.2	MVA Input Variables, Data to Monte Carlo Comparisons . . . . .	162
7.3.3	MVA Output, Data to Monte Carlo Comparisons . . . . .	176
7.4	Systematic Uncertainties . . . . .	176
7.5	Statistical Methods . . . . .	184
7.6	Results and Conclusions . . . . .	186
<b>8</b>	<b>Analysis Improvements</b>	<b>188</b>
8.1	aMC@NLO, MadSpin, and Pythia8 Monte Carlo . . . . .	188
8.2	Analysis Techniques Under Development . . . . .	190
<b>9</b>	<b>Conclusions and Summary</b>	<b>194</b>

<b>Bibliography</b>	<b>197</b>
<b>List of Acronyms</b>	<b>210</b>

# List of Figures

1.1	The CMS experiment has observed a new boson at $m \sim 125 \text{ GeV}/c^2$ . . . . .	2
1.2	A Feynman diagram of the $t\bar{t}H$ process, with Higgs $\rightarrow b\bar{b}$ , and the $t\bar{t}$ -system decaying semi-leptonically . . . . .	3
2.1	Leading and Next to Leading Order Feynman diagrams for the coulomb scattering process . . . . .	6
2.2	The global average of $\alpha_s$ , the QCD coupling constant [1]. . . . .	7
2.3	A visual representation of the Higgs potential [2] . . . . .	12
2.4	Experimental milestones of the Standard Model . . . . .	23
2.5	Higgs production cross-sections at the LHC, for 7-14 TeV $pp$ collisions . . . . .	24
2.6	Feynman diagrams for the three largest Higgs production modes at the LHC . .	25
2.7	Feynman diagram for $t\bar{t}H$ production . . . . .	26
2.8	Feynman diagrams for the semileptonic $t\bar{t}H$ process and its irreducible background, $t\bar{t} + b\bar{b}$ . . . . .	27
2.9	Feynman diagrams for the $t\bar{t}W$ and $t\bar{t}Z$ background processes . . . . .	28
2.10	Feynman diagrams for the single $t$ s,t, and $tW$ background processes . . . . .	28
2.11	Feynman diagrams for the $W, Z$ plus jets, and diBoson ( $WW, WZ, ZZ$ ) production.	29
2.12	Measurements of $t\bar{t}H$ backgrounds at CMS [3] . . . . .	29
2.13	The cancellation of the divergent Higgs mass from a loop of top-quarks is cancelled by a loop of supersymmetric top-quarks, stop-quarks [4], . . . . .	31
3.1	Aerial view of the LHC complex, spanning the French-Swiss border [5] . . . . .	32
3.2	Integrated Luminosity delivered to the CMS experiment from 2010-12 [6] . . . .	34
3.3	The LHC accelerator complex, taking protons from a bottle of Hydrogen at the Linac2, all the way to the LHC ring [7] . . . . .	35
3.4	Features of the Linac2, the first stage of acceleration in the LHC injection chain	36
3.5	Features of the PS booster, the second stage of the LHC injection chain . . . .	37
3.6	Features of the PS, the third stage of the LHC injection chain . . . . .	40

3.7	Features of the SPS, the fourth and final stage of the LHC injection chain . . . . .	41
3.8	The LHC ring is divided into eight octants [8] . . . . .	43
3.9	The single turn injection scheme. A septum magnet makes the initial alignment. The kicker magnet times the injection and makes the final alignment. Bumper magnets align the LHC beam with the injected beam [9] . . . . .	44
3.10	Layout of Interaction Region 8, where one proton beam is injected into the LHC ring. A transfer line from the SPS bring a proton in from the right. In green, a septum magnet aligns the beam horizontally with the LHC. In blue, a kicker magnet makes the final vertical alignment into the LHC, and is timed to fill one of the 400 MHz buckets of the RF capture system [8] . . . . .	44
3.11	The initial filling of 6 batches of protons from the PSB to the PS, leaves 12 empty buckets in the PS bunch structure. The rise time of the SPS magnet creates an additional gap in the SPS bunch structure. Additional gaps emerge due to the rise time of the LHC injection and dumping kicker magnets [8] . . . . .	45
3.12	Features of the dipole magnets used in the LHC . . . . .	46
3.13	Features of the dipole magnets used in the LHC . . . . .	47
3.14	Features of the 400 MHz superconducting RF system used in the LHC . . . . .	48
3.15	A klystron uses a weak RF signal coupled to a resonance cavity to bunch an electron beam, which in turn creates an amplified RF signal as it passes through a second resonance cavity tuned to the same frequency [10]. . . . .	49
3.16	One of sixteen 300 kW, 400 MHz klystrons that power the superconducting RF cavities that accelerate the proton beam [11]. . . . .	50
3.17	Layout of the five cryogenic islands, which are home to the eight facilities that provide liquid helium to the LHC [12] . . . . .	51
3.18	Features of the 4.5 K refrigeration system [13] . . . . .	52
3.19	Cross section schematic of the cryogenic distribution system in the LHC tunnel [8]	52
3.20	Beam screen for the LHC, with slits to allow for easy pumping of residual gas molecules in the beam-pipe [14]. . . . .	53
4.1	A cutaway diagram of the CMS detector. Two humans are present at the bottom of the image to provide scale [15]. . . . .	54
4.2	A slice of the CMS detector showing how various particles interact and deposit energy. The trajectory of charged particles is measured in the tracker; electrons and photons deposit most of their energy in the ECAL; charged and neutral hadrons deposit most of their energy in the HCAL; the muon chambers measures the trajectory of muons or long-lived charged particles . . . . .	55

4.3 A side view of the tracker. The pixel detector is the innermost sub-system, with three concentric rings of detectors in the barrel, and two in the endcap. The tracker inner barrel (TIB) is a silicon strip detector, with four concentric rings. The tracker inner disks (TID) are three layers deep. The tracker outer barrel (TOB) is six concentric rings and the tracker end caps (TEC) are nine layers deep.	57
4.4 A head-on view of the beam-line and barrel components of the tracker . . . . .	57
4.5 The three barrel and two disk layers of the silicon pixel tracker provide coverage of $ \eta  < 2.5$ . . . . .	58
4.6 The readout electronics chain for the pixel detector . . . . .	59
4.7 In 2012 $pp$ collisions at $\sqrt{s} = 8$ TeV, the pixel detector performed with a resolution of $11.8 \mu\text{m}$ . The above is a plot of the residual difference between a pixel and the results of a fit to a particle track. . . . .	60
4.8 A silicon strip module, with two $500 \mu\text{m}$ thick sensors. . . . .	61
4.9 Schematic of the readout sequence of the silicon strip detector. . . . .	62
4.10 Measurements of the performance of the silicon strip track using $pp$ collisions from 2011 at $\sqrt{s} = 7$ TeV . . . . .	62
4.11 Layout of the ECAL sub-detector . . . . .	63
4.12 Typical Lead Tungstate crystal, with APD attached to the rear face in the left frame, and a VPT attached in the right frame. . . . .	63
4.13 A simulation of the evolution of a electromagnetic shower being initiated by an electron entering the center of the front face. . . . .	64
4.14 A module of 500 crystals (25 crystals wide by 20 crystal tall). . . . .	65
4.15 Schematic of the On-Detector Readout for the ECAL . . . . .	66
4.16 A section of the ECAL end-cap, a Dee. Two Dees form a disk with an inner bore for the beam-line to pass through. 5x5 modules, or supercrystals, are mounted in preparation for installation at CMS . . . . .	67
4.17 Vacuum Photo-Triode devices used in the ECAL end-caps (EE) . . . . .	67
4.18 Features of the UVa VPT test stand . . . . .	70
4.19 3 runs of 5 VPTs, exposed to blue LED light, and fit to a sum of two exponentials.	71
4.20 3 runs of 5 VPTs, exposed to orange LED light, and fit to a sum of two exponentials. . . . .	72
4.21 Longitudinal cross-section of the HCAL with the four sub-systems labeled . . . . .	73

4.22 Closeup of the HCAL barrel section. The center section of each of the 18 wedges are labeled, optical cables lay across the joint of the center and staggered edge sections of each wedge. The blue lines show the approximate azimuthal division of the wedge. . . . .	74
4.23 Over 1 million Russian shells of military artillery were re-processed in the construction of the HCAL . . . . .	75
4.24 Optical readout chain of the HCAL scintillator tiles . . . . .	75
4.25 HCAL endcap, 18 azimuthal divisions of alternating layers of brass and plastic scintillator. . . . .	76
4.26 Longitudinal cross-section of the HCAL forward calorimetry, the HF . . . . .	76
4.27 Longitudinal cross-section of one of the 5 wheels of the muon system. Drift tubes are placed in 4 concentric layers, with 2 being placed inside the return yoke of the magnet, and 12 azimuthal divisions. . . . .	78
4.28 A cross-section view of a drift cell. The anode wire is held at 3600 V, creating a potential difference with the walls. Electric field lines are shown in blue. . . . .	79
4.29 RPC layout for the barrel and endcaps . . . . .	79
4.30 Exploded diagram of an RPC . . . . .	80
4.31 Cross-section of one quarter of the muon endcap system, with the 4 disks of CSC systems shown in red . . . . .	80
4.32 A CSC station with 7 layers, making 6 gas chambers. Cathode strips are shown in yellow, perpendicular to the vertical anode wires in orange. . . . .	81
4.33 A block diagram of the L1 trigger . . . . .	82
4.34 A schematic of the $e/\gamma$ trigger algorithm . . . . .	82
4.35 Layout of the CMS DAQ . . . . .	83
 5.1 Results of the uncertainty on the ECAL intercalibration coefficients for the barrel (left) and endcaps (right) . . . . .	88
5.2 Instantaneous luminosity response to the crystals as measured by the laser and LED system. Additional crystal calibration constants are derived to normalize the crystal response over the range of collected data . . . . .	89
5.3 Results of using a $\chi^2$ minimization procedure to estimate the neutral hadron energy contribution in the HCAL using simulated events . . . . .	90
5.4 Muon validation plots for the particle-flow reconstruction . . . . .	91
5.5 Electron validation plots for the particle-flow reconstruction . . . . .	92
5.6 The anti- $k_t$ jet clustering algorithm with distance parameter $R=1.0$ . . . . .	93

5.7	Commissioning of the particle-flow algorithm on jets, involved comparing the energy measured from charged hadron tracks, to energy measured in calorimeter clusters linked to the tracks . . . . .	94
5.8	A $b$ -meson will travel a distance $L_{xy}$ before decaying and creating a secondary vertex. The impact parameter, $d_0$ measures the longitudinal displacement of the two vertices . . . . .	95
6.1	This figure shows the breakdown of jet-to-parton assignments for the two jets with the minimum $\Delta R$ separation in the event for events with greater or equal 4 $b$ -tagged jets. . . . .	98
6.2	Comparison of number of reconstructed vertices for data (black) and the $t\bar{t}$ MC sample before (blue) and after (red) pileup reweighting. After pileup reweighting, the MC matches the data well. . . . .	103
6.3	$H_T$ distribution for 8 TeV lepton plus jet events with $\geq 4$ jets and $\geq 2$ tags shown for different amounts of pileup. The left-hand plot shows low pileup, the middle plot shows medium pileup, and the right-hand plot shows high pileup. . . . .	104
6.4	$H_T$ distribution for 8 TeV lepton plus jet events with $\geq 4$ jets and $\geq 2$ tags. The left-hand plot shows the distribution before correction. The right-hand plot shows the distribution after correction. Note that the ratio in the right-hand plot is flatter than the left-hand plot. . . . .	105
6.5	Muon and electron ID, isolation selection and trigger efficiency scale factors in bins of $p_T$ and $\eta$ . . . . .	109
6.6	Number of jets (left) and number of $b$ -tagged jets (right) in data and simulation for events with $\geq 4$ jets + $\geq 2$ $b$ -tags in the lepton+jets channel at 8 TeV. The background is normalized to the SM expectation; the uncertainty band (shown as a hatched band in the stack plot and a green band in the ratio plot) includes statistical and systematic uncertainties that affect both the rate and shape of the background distributions. The $t\bar{t}H$ signal ( $m_H = 125 \text{ GeV}/c^2$ ) is normalized to $30 \times$ SM expectation. . . . .	114
6.7	A simple example of a MLP type ANN, with one layer of input neurons that make connections to a hidden layer, which is connected to the output layer . . . . .	117
6.8	The CFMlpANN architecture used in this analysis features two hidden layers, and 10 input variables for each jet/tag category (11 variables for the $\geq 6$ jets, $\geq 4$ $b$ -tags category) . . . . .	118
6.9	Comparisons of the testing and training samples used to optimize the CFMlpANN weights for each jet/tag category . . . . .	120

6.10 Lepton + jets data/MC comparison for the $\geq 6$ jets + 2 tag category. The uncertainty band includes statistical and systematic uncertainties that affect both the rate and shape of the background distributions. . . . .	125
6.11 Lepton + jets data/MC comparison for the $\geq 6$ jets + 2 tag category. The uncertainty band includes statistical and systematic uncertainties that affect both the rate and shape of the background distributions. . . . .	126
6.12 Lepton + jets data/MC comparison for the 4 jets + 3 tag category. The uncertainty band includes statistical and systematic uncertainties that affect both the rate and shape of the background distributions. . . . .	127
6.13 Lepton + jets data/MC comparison for the 4 jets + 3 tag category. The uncertainty band includes statistical and systematic uncertainties that affect both the rate and shape of the background distributions. . . . .	128
6.14 Distributions of the five ANN input variables with rankings 1 through 5, in terms of separation, for the 5 jets + 3 b-tags category of the lepton+jets channel at 8 TeV. Definitions of the variables are given in the text. The background is normalized to the SM expectation; the uncertainty band (shown as a hatched band in the stack plot and a green band in the ratio plot) includes statistical and systematic uncertainties that affect both the rate and shape of the background distributions. The $t\bar{t}H$ signal ( $m_H = 125 \text{ GeV}/c^2$ ) is normalized to the total background yield, for easier comparison of the shapes. . . . .	129
6.15 Distributions of the five ANN input variables with rankings 6 through 10, in terms of separation, for the 5 jets + 3 b-tags category of the lepton+jets channel at 8 TeV. Definitions of the variables are given in the text. The background is normalized to the SM expectation; the uncertainty band (shown as a hatched band in the stack plot and a green band in the ratio plot) includes statistical and systematic uncertainties that affect both the rate and shape of the background distributions. The $t\bar{t}H$ signal ( $m_H = 125 \text{ GeV}/c^2$ ) is normalized to the total background yield, for easier comparison of the shapes. . . . .	130
6.16 Lepton + jets data/MC comparison for the $\geq 6$ jets + 3 tag category. The uncertainty band includes statistical and systematic uncertainties that affect both the rate and shape of the background distributions. . . . .	131
6.17 Lepton + jets data/MC comparison for the $\geq 6$ jets + 3 tag category. The uncertainty band includes statistical and systematic uncertainties that affect both the rate and shape of the background distributions. . . . .	132

6.18 Lepton + jets data/MC comparison for the 4 jets + 4 tag category. The uncertainty band includes statistical and systematic uncertainties that affect both the rate and shape of the background distributions. . . . .	133
6.19 Lepton + jets data/MC comparison for the 4 jets + 4 tag category. The uncertainty band includes statistical and systematic uncertainties that affect both the rate and shape of the background distributions. . . . .	134
6.20 Lepton + jets data/MC comparison for the 5 jets + 4 tag category. The uncertainty band includes statistical and systematic uncertainties that affect both the rate and shape of the background distributions. . . . .	135
6.21 Lepton + jets data/MC comparison for the 5 jets + 4 tag category. The uncertainty band includes statistical and systematic uncertainties that affect both the rate and shape of the background distributions. . . . .	136
6.22 Lepton + jets data/MC comparison for the $\geq 6$ jets + 4 tag category. The uncertainty band includes statistical and systematic uncertainties that affect both the rate and shape of the background distributions. . . . .	137
6.23 Lepton + jets data/MC comparison for the $\geq 6$ jets + 4 tag category. The uncertainty band includes statistical and systematic uncertainties that affect both the rate and shape of the background distributions. . . . .	138
6.24 The distributions of the CFMlpANN output for lepton+jets events at 8 TeV in the various analysis categories. Background-like events have a low CFMlpANN output value. Signal-like events have a high CFMlpANN output value. The background is normalized to the SM expectation; the uncertainty (shown as a hatched band in the stack plot and a green band in the ratio plot) includes statistical and systematic uncertainties that affect both the rate and shape of the background distributions. The $t\bar{t}H$ signal ( $m_H = 125 \text{ GeV}/c^2$ ) is normalized to $30 \times \text{SM}$ expectation. . . . .	139
6.25 Comparison of the MVA discriminator for JES shift upwards (red) and downwards (blue) relative to the nominal (black) shape for the $t\bar{t}H(120)$ signal (left) and the main background sample $t\bar{t} +$ light flavor (right). The plots shown are from the $\geq 6$ jet $\geq 4$ tag category in the lepton+jets channel. All plots are normalized to unit area. . . . .	141

6.26 Comparison of the MVA discriminator for $b$ -tag scale factor shift upwards (red) and downwards (blue) relative to the nominal (black) shape for the $t\bar{t}H(120)$ signal (left) and the main background sample $t\bar{t}$ + light flavor (right). The plots are from the $\geq 6$ jets + $\geq 4$ tags category in the lepton+jets channel. All plots are normalized to unit area. . . . .	142
6.27 Comparison of the MVA discriminator for additional PU correction systematic upwards (red) and downwards (blue) relative to the nominal (black) shape for the $t\bar{t}H(120)$ signal (left) and the main background sample $t\bar{t}$ + light flavor (right). The plots are from the $\geq 6$ jets + $\geq 4$ tags category in the lepton+jets channel. All plots are normalized to unit area. . . . .	143
6.28 The rate and shape variations for selected categories due to the $Q^2$ uncertainty. . .	145
6.29 A dedicated CFMlpANN trained to isolate $t\bar{t} + b\bar{b}$ from $t\bar{t} + jets$ . The left plot shows is for the case of nominal $t\bar{t} + b\bar{b}$ cross-section, the right plot shows the case for x2 $t\bar{t} + b\bar{b}$ cross-section. The left-most region of both plots is the most sensitive to the $t\bar{t} + b\bar{b}$ normalization, and shows no significant improvement in data to MC agreement, justifying the reasoning that an uncertainty larger than 50% is needed.	146
6.30 The expected and observed 95% CL upper limits on the signal strength parameter $\mu = \sigma/\sigma_{SM}$ for the lepton+jets channel using the 2012 dataset. These limits were extracted using the asymptotic method. . . . .	150
7.1 Comparison of number of reconstructed vertices for data (black) and the sum of all background MC samples before (red) and after (blue) pileup reweighting. After pileup reweighting, the MC matches the data well. . . . .	155
7.2 The scale factors from top differential cross section group, the fitting as well as the $\pm 1\sigma$ variations. . . . .	156
7.3 Leading jet $p_T$ distribution for 8 TeV lepton plus jet events with $\geq 4$ jets and $\geq 2$ tags. The left-hand plot shows the distribution before top $p_T$ reweighting. The right-hand plot shows the distribution after top $p_T$ reweighting. Note that the ratio in the right-hand plot is flatter than the left-hand plot. . . . .	157
7.4 Comparison of yields for the different categories (top), number of jets (bottom left), and number of tagged jets (bottom right) in data and Monte Carlo for events with one lepton $\mu$ or $e$ , $\geq 4$ jets and $\geq 2$ tags. . . . .	159
7.5 Example of a decision tree, which chooses a set of variables to cut on, in order to produce a region of events with high signal purity . . . . .	161
7.6 Comparisons of the testing and training samples used to optimize the BDT weights for each jet/tag category . . . . .	163

7.7 Data/MC comparisons for events with one lepton and $\geq 6$ jets + 2b- tags. The uncertainty band includes statistical and systematic uncertainties that affect both the rate and shape of the background distributions. . . . .	166
7.8 Data/MC comparisons for events with one lepton and 4 jets + 3 b-tags. The uncertainty band includes statistical and systematic uncertainties that affect both the rate and shape of the background distributions. . . . .	167
7.9 Data/MC comparisons for events with one lepton and 5 jets + 3 b-tags. The uncertainty band includes statistical and systematic uncertainties that affect both the rate and shape of the background distributions. . . . .	168
7.10 Data/MC comparisons for events with one lepton and $\geq 6$ jets + 3 b-tags. The uncertainty band includes statistical and systematic uncertainties that affect both the rate and shape of the background distributions. . . . .	169
7.11 Data/MC comparisons for events with one lepton and $\geq 6$ jets + 3 b-tags. The uncertainty band includes statistical and systematic uncertainties that affect both the rate and shape of the background distributions. . . . .	170
7.12 Data/MC comparisons for events with one lepton and 4 jets + 4 b-tags. The uncertainty band includes statistical and systematic uncertainties that affect both the rate and shape of the background distributions. . . . .	171
7.13 Data/MC comparisons for events with one lepton and 5 jets + $\geq 4$ b-tags. The uncertainty band includes statistical and systematic uncertainties that affect both the rate and shape of the background distributions. . . . .	172
7.14 Data/MC comparisons for events with one lepton and 5 jets + $\geq 4$ b-tags. The uncertainty band includes statistical and systematic uncertainties that affect both the rate and shape of the background distributions. . . . .	173
7.15 Data/MC comparisons for events with one lepton and $\geq 6$ jets + $\geq 4$ b-tags. The uncertainty band includes statistical and systematic uncertainties that affect both the rate and shape of the background distributions. . . . .	174
7.16 Data/MC comparisons for events with one lepton and $\geq 6$ jets + $\geq 4$ b-tags. The uncertainty band includes statistical and systematic uncertainties that affect both the rate and shape of the background distributions. . . . .	175

7.17 Final BDT output for lepton + jet events. Background-like events have a low BDT output value. Signal-like events have a high BDT output value. The uncertainty band includes statistical and systematic uncertainties that affect both the rate and shape of the background distributions. The top, middle and, bottom rows are events with 4, 5, and $\geq 6$ jets, respectively, while the left, middle, and right-hand columns are events with 2, 3, and $\geq 4$ b-tags, respectively. The $t\bar{t}H$ signal ( $m_H = 125$ GeV) is normalized to $30 \times$ SM expectation. . . . .	177
7.18 Comparison of the MVA discriminator for JES shift upwards (red) and downwards (blue) relative to the nominal (black) shape for the $t\bar{t}H(125)$ signal (left) and the main background sample $t\bar{t} + b\bar{b}$ (right). The plots are from the $\geq 6$ jet $\geq 4$ tag category in the lepton+jets channel. All plots are normalized to unit area. . . . .	178
7.19 Comparison of the MVA discriminator when shifting the light flavor contamination in the heavy flavor scale factor determination shift upwards (red) and downwards (blue) relative to the nominal (black) shape for the $t\bar{t}H(125)$ signal (top row) and $t\bar{t} + b\bar{b}$ and $t\bar{t} + \text{LF}$ background samples (middle row and bottom row respectively). The plots are from the LJ $\geq 6$ jet $\geq 4$ category. All plots are normalized to unit area. . . . .	179
7.20 Comparison of the MVA discriminator when shifting the heavy flavor contamination in the light flavor scale factor determination shift upwards (red) and downwards (blue) relative to the nominal (black) shape for the $t\bar{t}H(125)$ signal (top row) and $t\bar{t} + b\bar{b}$ and $t\bar{t} + \text{LF}$ background samples (middle row and bottom row respectively). The plots are from the LJ $\geq 6$ jet $\geq 4$ category. All plots are normalized to unit area. . . . .	179
7.21 Comparison of the MVA discriminator when shifting to account for the statistical uncertainty on the heavy flavor scale factor extraction. Two classes of distortion in the scale factor are considered: linear distortions (labeled “Stat. Error 1”) and nonlinear distortions (labeled “Stat. Error 2”). Both shift upwards (red) and downwards (blue) relative to the nominal (black) shape for the $t\bar{t}H(125)$ signal (top row) and $t\bar{t} + b\bar{b}$ and $t\bar{t} + \text{LF}$ background samples (middle row and bottom row respectively) are shown. The plots are from the $\geq 6$ jet $\geq 4$ category. All plots are normalized to unit area. . . . .	180

7.22 Comparison of the MVA discriminator when shifting to account for the statistical uncertainty on the light flavor scale factor extraction. Two classes of distortion in the scale factor are considered: linear distortions (labeled “Stat. Error 1”) and nonlinear distortions (labeled “Stat. Error 2”). Both shift upwards (red) and downwards (blue) relative to the nominal (black) shape for the $t\bar{t}H(125)$ signal (top row) and $t\bar{t} + b\bar{b}$ and $t\bar{t} + \text{LF}$ background samples (middle row and bottom row respectively) are shown. The plots are from the $\geq 6$ jet $\geq 4$ category. All plots are normalized to unit area. . . . .	180
7.23 Comparison of the MVA discriminator when shifting to account for the uncertainty on the charm jets scale factor extraction. Two classes of distortion in the scale factor are considered: linear distortions (labeled “Error 1”) and nonlinear distortions (labeled “Error 2”). Both shift upwards (red) and downwards (blue) relative to the nominal (black) shape for the $t\bar{t}H(125)$ signal (top row) and $t\bar{t} + c\bar{c}$ and $t\bar{t} + \text{LF}$ background samples (middle row and bottom row respectively) are shown. The plots are from the $\geq 6$ jet $\geq 4$ category. All plots are normalized to unit area. . . . .	181
7.24 Comparison of the MVA discriminator for shifts in top quark $p_T$ reweighting upwards (red) and downwards (blue) relative to the nominal (black) shape for the $t\bar{t} + \text{LF}$ background (left) and the $t\bar{t} + b\bar{b}$ (right). The plots are from the $\geq 6$ jets $+ \geq 4$ tags category in the lepton+jets channel. All plots are normalized to unit area. . . . .	182
7.25 Comparison of the MVA discriminator when shifting the $Q^2$ scale up and down by its uncertainties. Shown are the shift upwards (red) and downwards (blue) relative to the nominal (black) shape for the $t\bar{t} + b\bar{b}$ (top row) $t\bar{t} + b$ (middle row) and $t\bar{t} + \text{LF}$ (bottom) background samples. The plots are from the LJ $\geq 6$ jet $\geq 4$ category. All plots are normalized to unit area. . . . .	183
7.26 The expected and observed 95% CL upper limits on the signal strength parameter $\mu = \sigma/\sigma_{SM}$ for the lepton+jets channel using the 2012 dataset. These limits were extracted using the asymptotic method. . . . .	186
8.1 The number of reconstructed jets passing selection (left) and that have additionally been $b$ -tagged (right) for $t\bar{t}H$ , $t\bar{t} + \text{jets}$ , and $t\bar{t} + b\bar{b}$ samples generated with the aMC@NLO and Pythia 8 framework . . . . .	190
8.2 The invariant mass of the $W$ boson in the $t\bar{t}$ decay for the case of the MC truth (red), correctly associated reconstructed jets (blue), and incorrectly associated reconstructed jets (green) . . . . .	191

8.3	The cosine of the angle between the momentum three-vectors for the $b$ -quarks from the top decays (left), the lepton and the up-type $W$ boson daughter (center), and the lepton and the down-type $W$ boson daughter (right) . . . . .	191
8.4	The difference in the $\phi$ coordinate between the momentum three-vectors for the $b$ -quarks from the top decays (left), the lepton and the up-type $W$ boson daughter (center), and the lepton and the down-type $W$ boson daughter (right) . . . . .	192
8.5	Jet times lepton charge, for the $b$ -jet associated with the same top as the lepton. Green shows incorrectly associated reconstructed jets, blue shows correctly associated jets, and red is the MC truth . . . . .	193

# List of Tables

2.1	The quantum numbers Isospin and Hypercharge are assigned for each of the $SU(2)$ and $U(1)$ symmetries respectively . . . . .	20
4.1	Fit Results for VPT Conditioning Studies at U.Va. and Brunel, Blue Reference LED . . . . .	71
4.2	Fit Results for VPT Conditioning Studies at U.Va., Orange LED . . . . .	72
6.1	The datasets analyzed for this analysis. . . . .	101
6.2	List of signal MC datasets and cross sections used to determine the SM expectation. . . . .	101
6.3	List of background MC datasets and cross sections used for normalization. . . . .	102
6.4	List of lepton+jets triggers . . . . .	106
6.5	Tight and loose muon definition . . . . .	108
6.6	Tight and loose muon definition . . . . .	108
6.7	Jet definition . . . . .	110
6.8	Jet Energy Resolution (JER) scale factors . . . . .	111
6.9	Expected event yields in $5 \text{ fb}^{-1}$ for signal and backgrounds in the $\mu+\text{jets}$ channel. . . . .	115
6.10	Expected event yields in $5 \text{ fb}^{-1}$ for signal and backgrounds in the $e+\text{jets}$ channel. . . . .	115
6.11	Expected event yields in $5 \text{ fb}^{-1}$ for signal and backgrounds in the $\mu+\text{jets}$ channel. . . . .	116
6.12	The ANN inputs for the nine jet-tag categories in the $8 \text{ TeV } t\bar{t}H$ analysis in the lepton+jets and dilepton channels. The choice of inputs is optimized for each category. Definitions of the variables are given in the text. The best input variable for each jet-tag category is denoted by $\star$ . . . . .	122
6.13	Summary of the systematic uncertainties considered on the inputs to the limit calculation. Except where noted, each row in this table will be treated as a single, independent nuisance parameter. . . . .	140
6.14	Relative yield change due to JES shift up/down for the $\geq 6$ jets + $\geq 4$ tags category in the lepton+jets channel. . . . .	141

6.15 Relative yield change due to $b$ -tag scale factor shift up/down for the $\geq 6$ jets + $\geq 4$ tags category in the lepton+jets channel. . . . .	142
6.16 Cross section uncertainties used for the limit settings. Each column in the table is an independent source of uncertainty, except for the last column which represents uncertainties uncorrelated with any others. Uncertainties in the same column for two different processes (different rows) are completely correlated. . . . .	144
6.17 Expected and observed upper limits for SM Higgs for lepton + jets channel using the first $5.1 \text{ fb}^{-1}$ of the 2012 dataset. These limits were extracted using the asymptotic method. . . . .	149
7.1 The datasets analyzed for this analysis. . . . .	152
7.2 List of signal MC datasets and cross sections used to determine the SM expectation.	153
7.3 List of background MC datasets and cross sections used for normalization. . . . .	154
7.4 Observed data event yields, expected event yields in $19.5 \text{ fb}^{-1}$ for signal and backgrounds in the lepton+jets channel. . . . .	159
7.5 Event variables used in dilepton and lepton+jets BDT training and their descriptions. . . . .	164
7.6 BDT input variable assignments for the lepton+jets categories. . . . .	165
7.7 List of variables used as inputs in each of the ttbb/ttH BDTs. See table 7.5 for definitions. . . . .	165
7.8 Relative yield change due to JES shift up/down for the $\geq 3$ tag category in the dilepton channel and the $\geq 6$ jets + $\geq 4$ tags category in the lepton+jets channel. . . . .	176
7.9 This table summarizes the rate effect of the six independent nuisance parameters that characterize the $b$ -tag uncertainties. (Note: The $b$ -tag rate uncertainties associated with JES variations are already included with the JES rate uncertainties in Table 6.14. The impact of statistical uncertainties is in the heavy-flavor and light-flavor scale factor extraction is incorporated using two separate nuisance parameters, as described above. The uncertainty labeled “Stat. Err. 1” represents statistical uncertainties resulting a linear distortion of the CSV scale factor, while the one labeled “Stat. Err. 2” corresponds to nonlinear distortions. . . . .	181
7.10 Relative yield change due to varying the top quark $p_T$ reweighting. The “up” variation corresponds to apply twice as much correction to the top quark $p_T$ distribution as the nominal, while the “down” correction corresponds to applying no correction to the default MC top quark $p_T$ distribution. . . . .	182

7.11	Cross section uncertainties used for the limit settings. Each column in the table is an independent source of uncertainty, except for the last column which represents uncertainties uncorrelated with any others. Uncertainties in the same column for two different processes (different rows) are completely correlated. . . . .	183
7.12	This table summarizes the rate effect of shifting $Q^2$ scale uncertainty for Madgraph. Note that the shifts are made independently for the following topologies: $t\bar{t} + 0p$ , $t\bar{t} + 1p$ , $t\bar{t} + 2p$ , $t\bar{t} + c\bar{c}$ , $t\bar{t} + b$ , and $t\bar{t} + b\bar{b}$ . . . . .	183
7.13	Summary for the of the systematic uncertainties considered on the inputs to the limit calculation. Except where noted, each row in this table will be treated as a single, independent nuisance parameter. . . . .	184
7.14	Specific effect of systematics on predicted background yields for events with $\geq 6$ jets and $\geq 4$ b-tags. Here we only consider the sum of the largest backgrounds, $t\bar{t} + lf$ , $t\bar{t} + b$ , $t\bar{t} + b\bar{b}$ , and $t\bar{t} + c\bar{c}$ . These three backgrounds account for 94% of all background events. The signal is 3.5% of the yield of the three main backgrounds. The signal fraction is directly comparable to the variations of the background in the table. The table shows that the signal is much smaller than many of the background variations. . . . .	185
7.15	Expected and observed upper limits for SM Higgs for lepton + jets channel using the 2012 dataset. These limits were extracted using the asymptotic method. . . .	186

# Acknowledgements

First and foremost, the analysis described in this dissertation would be impossible without the thousands of individuals that have contributed to the design, construction, and commissioning of the Large Hadron Collider (LHC) and Compact Muon Solenoid (CMS) experiment. The countless years of passion and dedication that have been poured into these machines have resulted in the most sophisticated tools ever available to mankind to explore the frontiers of high energy physics. I am extremely grateful for the opportunity to participate in this collaboration and to contribute to the understanding of physics at the TeV energy scale.

I would like to thank Mike Arenton, Dave Cockerill and Alexander Ledovskoy for their tutelage and mentorship in regards to my studies with the UVa Vacuum Photo-Triode (VPT) rig. This project has been a critical to improving my understanding of electronics, firmware, and signal analysis, and has been both a challenging and exciting experience. I would also like to thank Thomas Anderson, Brian Franchise, Joseph Goodell, Al Tobias, and Evan Wolfe for all of their help in maintaining the 4 T magnet and ensuring the VPT rig has survived long enough to collect and analyze the data on these devices. I woud also like to thank Professors Brad Cox and Bob Hirosky of the CMS research group here at UVa for always challenging me to improve the VPT rig and analysis, while still providing me with all of the tools and input I needed to succeed.

The  $t\bar{t}H$  analysis group at CMS has been provided an incredibly supportive environment to learn about particle physics and data analysis. I would like to thank Professor Kevin Lannon of the University of Notre Dame (ND) and Professors Richard Hughes and Brian Winer of the Ohio State University (OSU) for pushing the group as hard as possible while still maintaining a high level of quality for the work and studies presented each week. Additional thanks go out to the post-doctoral and graduate students at these Universities: Darren Puigh and Geoff Smith of ND and Jason Slaunwhite, Andrew Brinkerhoff, Wuming Luo, and Anna Woodard of OSU, without whom, this analysis would not have been published twice, nor would I be reflecting so fondly on a period of times that involved an intense set of deadlines and a lot of late nights.

To my fellow graduate students and good friends here at UVa: Thomas Anderson, Tanwa

Apornthip, Alexandre Arakelyan, Sana Deshmukh, Ryan Duve, Adam Fallon, Brian Francis, Joe Johnson, Manolis Kargiantoulakis, Micah Shiable, Julie Spencer, Niranjan Sridhar, Evan Wolfe, and too many more to list, you know who you are, thank you for so many wonderfully hazy nights that have helped me from going insane in graduate school. To my friends abroad: Supaksh Gupta, Kat Hunter, Ryan Karlsgodt, Kevin Karlsgodt, Ginny Morris, Mark Nicholson, Matt Pierce, Mikey Sheffield, Tyler Vickers, and the many others who also know who you are, thank you for continuing to be amazing friends throughout all these years apart.

I would like to give special thanks to Dr. Sarah Boutle, who has been an amazing mentor and friend. I owe so much of my understanding of particle physics, the LHC, and CMS to the countless conversations and coffee breaks we shared. I have been incredibly lucky to also have a role model of someone who has balanced a successful career as a scientist and still manages to maintain a caring, well-grounded personality with a great sense of humor, even during the most daunting and stressful of situations.

These acknowledgements would be incomplete without mention of Professor Chris Neu, who hooked me on studying particle physics at CMS during our first conversation together. Since then, I have had the privilege of being his student for the past six years. It has been an incredibly rewarding experience. Under his guidance, I have travelled around the world, analyzed and unblinded a historically significant dataset in the field of particle physics, and participated in one of the largest scientific collaborations in the history of mankind. I cannot thank him enough for everything I have learned, and for all of the amazing scientific opportunities he has provided.

I would like to acknowledge all of the love and support given to me by my family. Aunt Carolyn and cousin Gaylon, thank you for all of the Thanksgiving feasts, and for making me feel at home on the East Coast. Little sister, Carrie, thank you for always reminding me to keep an open heart and mind in all matters in life. Mom and Dad, thank for you encouraging me to follow my dreams and giving me every opportunity to do the things I love.

To the love of my life, Whitney Wegman, you have been the most incredible source of inspiration and happiness for me throughout the three and a half years we have been together at this point. I cannot have done this without all of your love and support.

<sup>1</sup> **Chapter 1**

<sup>2</sup> **Introduction**

<sup>3</sup> On July 4th, 2012, the Compact Muon Solenoid (CMS) and A Toroidal LHC Apparatus (ATLAS)  
<sup>4</sup> experiments announced the discovery of a new boson of mass  $\sim 125$  GeV [18][19]. The particle  
<sup>5</sup> has been shown to be increasingly consistent with the description of the boson predicted by  
<sup>6</sup> the Higgs mechanism of the SM, as measurements on its mass, width, and quantum numbers  
<sup>7</sup> are completed. Figure 1.1 shows a consistent mass peak between the  $H \rightarrow ZZ$  and  $H \rightarrow \gamma\gamma$   
<sup>8</sup> channels at the CMS experiment. However, there are several properties of this new boson, which  
<sup>9</sup> remain to be tested.

<sup>10</sup> The Yukawa coupling of the Higgs boson to the top-quark in the SM is the largest coupling  
<sup>11</sup> among the fundamental particles and is well predicted - thus offering an excellent test of the  
<sup>12</sup> nature of the coupling of the Higgs to fermions, as well as a potential probe into physics Beyond  
<sup>13</sup> the Standard Model (BSM) that would alter this value from the SM prediction. The production  
<sup>14</sup> of the Higgs boson in association with top-quark pairs is the best production mode at the LHC  
<sup>15</sup> that offers direct access to the top-Higgs coupling. The dominant production mode of Higgs  
<sup>16</sup> at the LHC, gluon-gluon fusion, involves a triangle loop of strongly-coupled fermions, which  
<sup>17</sup> includes all of the other quarks, as well as the potential for BSM particles, and thus does involve  
<sup>18</sup> a pure top-Higgs coupling.

<sup>19</sup>  $t\bar{t}H$  production also has the ability to constrain some extensions of the SM that would not  
<sup>20</sup> modify the Higgs branching fractions enough to be seen within current experimental precision.  
<sup>21</sup> Such models include Little Higgs models, models with extra dimensions, top-color models, and  
<sup>22</sup> composite Higgs models that introduce a vector-like top partner, a  $t'$ , that can decay to  $tH$ ,  
<sup>23</sup>  $bW$ , or  $tZ$  states. Both  $t't'$  and  $t't$  production would produce a  $t\bar{t}H$  final state, or one that is  
<sup>24</sup> indistinguishable from it ( $tHbW$ ). Upper limits on  $t\bar{t}H$  production would also provide limits  
<sup>25</sup> on the previously described models, which would be complementary to existing direct searches  
<sup>26</sup> for  $t'$  particles, which attempt to reconstruct the  $t'$  resonance.

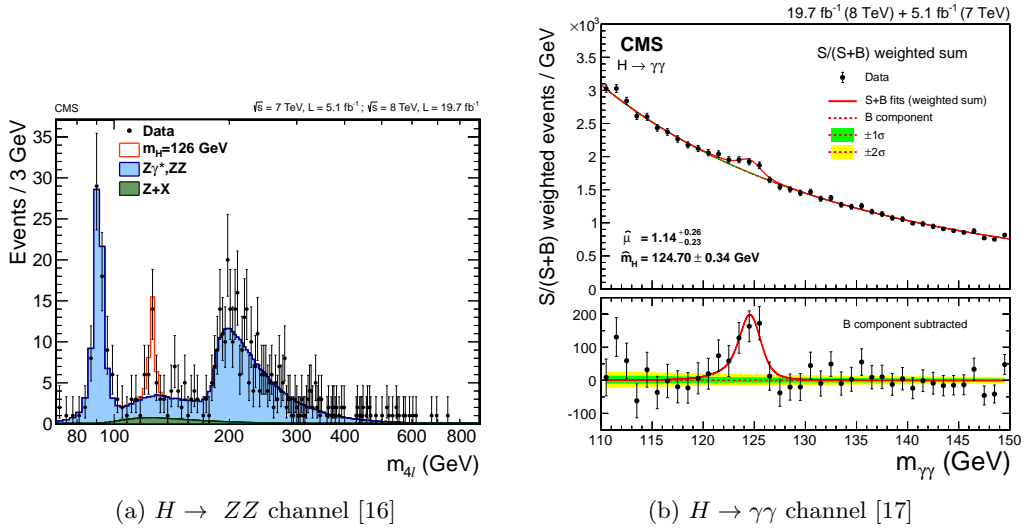


Figure 1.1: The CMS experiment has observed a new boson at  $m \sim 125 \text{ GeV}/c^2$

27        The  $t\bar{t}H$  channel has a rich set of possible final states. Each top-quark will decay to a  $b$ -quark  
 28        and a  $W$  boson. The  $W$  boson will subsequently decay to two quarks, or a lepton and a neutrino.  
 29        These decays are classified as either hadronic, semi-leptonic, or di-leptonic for zero, one, or both  
 30        top-quarks decaying leptוניתally respectively. The Higgs may decay to  $b$ -quark,  $W$ ,  $Z$ ,  $\tau$ ,  
 31        or  $\gamma$  pairs. In fact, this is one of the only production modes at the LHC which has access to  
 32        every Higgs decay mode, as other production mechanisms are swamped by large backgrounds  
 33        preventing measurements of all Higgs decay types.

34        The search is performed with the CMS experiment, a modern, general purpose particle  
 35        detector capable of reconstructing and identifying hadronic jets, photons, electrons, muons,  
 36        and tau leptons. The hermetic design, and its high precision and efficiency in reconstructing  
 37        and tracking every particle in a  $pp$  collision, also makes it suitable for reconstructing missing  
 38        transverse energy from the calculated momentum imbalance of all of the measured particles in  
 39        the event. This missing transverse energy is often the signature of a neutrino, which is the  
 40        only SM particle capable of escaping detection. The detector uses a 3.8 T axial magnetic field,  
 41        produced by the solenoid it is named after, to bend charged particles as they travel through  
 42        the detector. The measured curvature of their tracks allows the momentum of the particles to  
 43        be calculated with to a high precision. Tracks are formed and particles are reconstructed by a  
 44        combination of sub-detector systems which work together to form the final final reconstructed  
 45        image of each particle in the collision.

46        This thesis will focus on a semi-leptonic decay of the top-quarks, with the Higgs decaying to  
 47        a  $b$ -quark pair. Figure 1.2 is Feynman diagram of the  $t\bar{t}H$  process. The largest background to  
 48        this process is top-quark pair production with extra jets originating from Initial State Radiation  
 49        (ISR) or Final State Radiation (FSR) radiation,  $t\bar{t} + jets$ . The irreducible background is formed

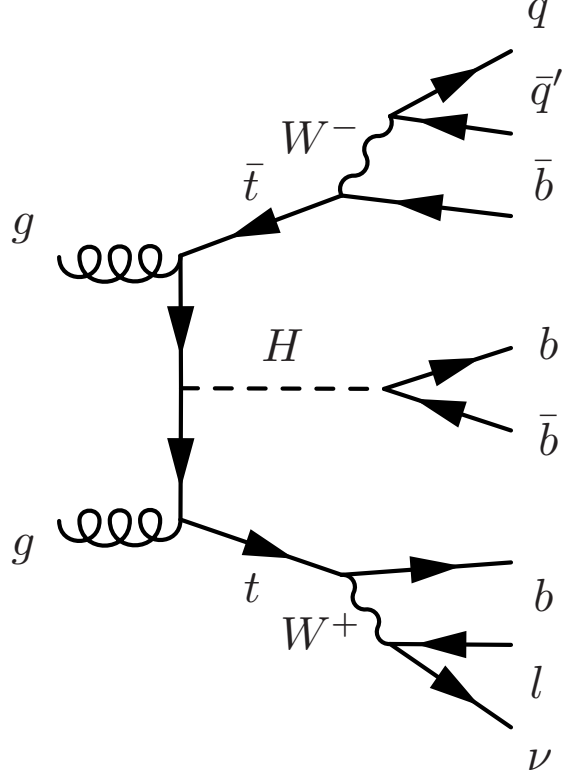


Figure 1.2: A Feynman diagram of the  $t\bar{t}H$  process, with Higgs $\rightarrow b\bar{b}$ , and the  $t\bar{t}$ -system decaying semi-leptonically

50 by top-quark pairs, where a gluon is radiated and decays to  $b$ -quark pairs,  $t\bar{t} + b\bar{b}$ . In addition  
 51 to the large backgrounds, the high jet multiplicity in the  $t\bar{t}H$  final state gives rise to a combina-  
 52 torics problem in associating each jet with its role in the  $t\bar{t}H$  system. This inevitably leads to  
 53 misidentifying which jets are the decay product of the Higgs, and thus additionally smears out  
 54 the resolution on the mass of the Higgs. Due to the similarity of the  $t\bar{t} + b\bar{b}$  background and the  
 55 combinatorics issue, no single variable is suitable for signal extraction. A Multi-Variate Analysis  
 56 (MVA) technique is used in an attempt to isolate the  $t\bar{t}H$  signal from the  $t\bar{t} + jets$  background.  
 57 The MVA provides a one-dimensional discriminant based on several input variables related to  
 58 the kinematics of the event. This discriminant is then used to perform signal extraction and set  
 59 upper-limits on  $t\bar{t}H$  production. The results of two searches will be presented. The first result  
 60 used the first  $5.1 \text{ fb}^{-1}$  of the 2012 dataset, with center of mass energy of 8 TeV, and was pub-  
 61 lished in the Journal of High Energy Physics (JHEP), May 2013. The second result was update  
 62 with the full  $19.4 \text{ fb}^{-1}$  8 TeV dataset, and was published in JHEP, Spetember 2014.

## <sup>63</sup> Chapter 2

# <sup>64</sup> Theoretical Background

<sup>65</sup> The Standard Model (SM) of particle physics represents the sum of knowledge about the funda-  
<sup>66</sup> mental particles and their interactions with each other. It is a Quantum Field Theory (QFT) that  
<sup>67</sup> represents the interactions of each of the fundamental forces through the symmetry of a mathe-  
<sup>68</sup> matical object known as a Lie group. It is the theory that dictates the rate that the  $t\bar{t}H$  process  
<sup>69</sup> is produced, as well as the kinematics of every particle involved. As such, its predictions are  
<sup>70</sup> critical for modeling the characteristic signature of the  $t\bar{t}H$  signal in the CMS detector, as well  
<sup>71</sup> as the background processes, like  $t\bar{t} + b\bar{b}$  which leave a kinematically similar final state signature.

### <sup>72</sup> 2.1 An Overview of Quantum Field Theory

<sup>73</sup> Quantum Field Theory (QFT) was developed out of the need for a relativistic description of  
<sup>74</sup> quantum mechanics. Since the Einstein relation  $E = mc^2$  allows for the creation of particle-  
<sup>75</sup> antiparticle pairs, the single-particle description used in non-relativistic quantum mechanics,  
<sup>76</sup> fails describe this phenomenon [20]. This additionally fails when considering that Heisenberg's  
<sup>77</sup> uncertainty relation,  $\Delta E \cdot \Delta t = \hbar$ , allows for an arbitrary number of intermediate, virtual  
<sup>78</sup> particles to be created. By quantizing a field representing a certain type of particle, multi-particle  
<sup>79</sup> states are naturally described as discrete excitations of that field.

<sup>80</sup> Lorentz invariance, and the need to preserve causality, also define a fundamental relationship  
<sup>81</sup> between matter and antimatter. The propagation of a particle across a space-like interval is  
<sup>82</sup> treated equivalently to the an anti-particle propagating in the opposite direction [20]. This is  
<sup>83</sup> done so that the net probability amplitude for the particles to have an effect on a measurement  
<sup>84</sup> occurring across a space-like interval cancel each other, thus preserving causality. This cancel-  
<sup>85</sup> lation requirement additionally implies that the particle and anti-particle have the same mass,  
<sup>86</sup> with opposite quantum numbers such as spin or electric charge.

<sup>87</sup> The Lorentz transformations for a scalar field are different than for a field with internal de-  
 grees of freedom, such as spin. A rotation on a vector field, will affect both its location, as well  
 as it's orientation [20]. This means the Lorentz invariant equation of motion describing a scalar  
 field will have a different form than equations of motion for a field with spin. The most relevant  
 equations describe the particles of SM, which contain spins of 0, 1/2, and 1. They are described  
 by the Klein-Gordon, Dirac, and Proca equations respectively.

93

Klein-Gordon equation, for scalar (spin 0) fields

$$(\partial^2 + m^2)\phi = 0 \quad (2.1)$$

Dirac equation, for spinor (spin 1/2) fields

$$(i\gamma^\mu \partial_\mu - m)\psi = 0 \quad (2.2)$$

Proca equation, for vector (spin 1) fields

$$\partial_\mu(\partial^\mu A^\nu - \partial^\nu A^\mu) + m^2 A^\nu = 0 \quad (2.3)$$

<sup>94</sup> With these equations, one can build a theory of free particles. The Lagrangian formulation is  
 the most appropriate since all expressions are explicitly Lorentz invariant [20]. The Lagrangians  
 for the Klein-Gordon, Dirac, and Proca equations are given as:

97

Klein-Gordon Lagrangian, for real and complex scalar fields

$$\begin{aligned} \mathcal{L} &= \partial_\mu \partial^\mu \phi^2 - \frac{1}{2} m^2 \phi^2 \\ \mathcal{L} &= (\partial_\mu \phi)^*(\partial^\mu \phi) - m^2 (\phi)^*(\phi) \end{aligned} \quad (2.4)$$

Dirac Lagrangian, for spinor fields

$$\mathcal{L} = i\bar{\psi}\gamma^\mu \partial_\mu \psi - m\bar{\psi}\psi \quad (2.5)$$

Proca Lagrangian, for vector fields

$$\mathcal{L} = -\frac{1}{4} F_{\mu\nu} F^{\mu\nu} + m^2 A^\nu A_\nu \quad (2.6)$$

<sup>98</sup> where  $F_{\mu\nu}$ , is the field strength tensor, defined as  $F_{\mu\nu} = \partial_\mu A_\nu - \partial_\nu A_\mu$

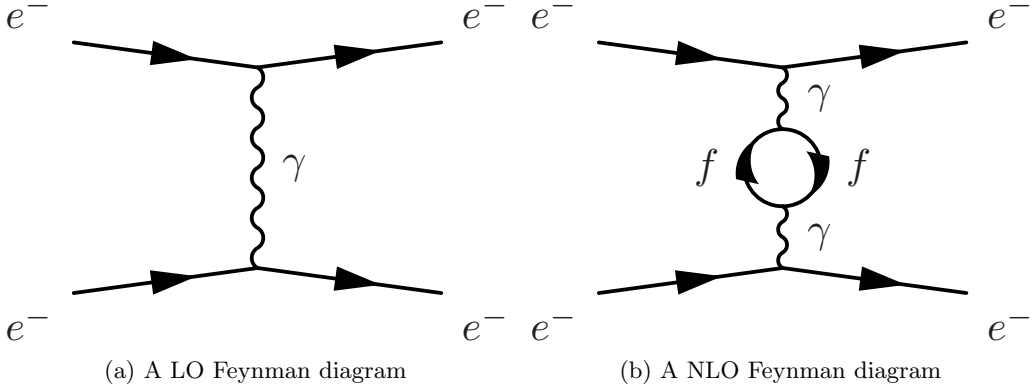


Figure 2.1: Leading and Next to Leading Order Feynman diagrams for the coulomb scattering process

99        Interactions are generated by coupling multiple fields together in a single term, such as  
 100       $ieA_\mu\bar{\psi}\psi$  and treating it as a perturbation to the free field theory. This implies every interaction  
 101      between particles is carried out by a virtual mediating particle. When two electrons scatter off  
 102      one another, they are really exchanging a virtual photon, the mediator of the electromagnetic  
 103      force. The  $W^\pm$  and  $Z$  bosons mediate the weak force, while the *gluons* mediate the strong force.

$$\mathcal{L} = \mathcal{L}_{Free} + \mathcal{L}_{Interacting} \quad (2.7)$$

104        In order to calculate the probability and dynamics of two particles interacting with one  
 105      another, an integral, constrained by energy and momentum conservation, over the phase space  
 106      of outgoing particles and the scattering amplitude,  $\mathcal{M}$ , is evaluated. The scattering amplitude is  
 107      calculated by using the propagator (Green's function of the free particle theory) for the incoming,  
 108      mediating, and outgoing particles, with an appropriate weighting function, or vertex factor,  
 109      for each point the particles interact in the scattering process, and then integrating over the  
 110      momentum of the mediating particle. Richard Feynman developed a set of rules for the writing  
 111      down the propagators and vertex factors directly from the Lagrangian, and easily computing the  
 112      scattering amplitude. He also introduced an elegant pictographic notation useful for visualizing  
 113      particle interactions, known as Feynman diagrams.

114        With these tools, one can calculate the probability amplitudes of a given process occurring  
 115      to Leading Order (LO) without any difficulties. However, when calculations in Next to Leading  
 116      Order (NLO) are performed, and loop diagrams of virtual particles are considered, the probability  
 117      amplitudes associated with a given process diverge to infinity. This occurs when one integrates  
 118      over all of the possible momentum allowed by intermediate, loops of virtual particles, which due  
 119      to Heisenberg's uncertainty principle, are allowed to take on any value of momentum. Figure  
 120      2.1 shows an example of a LO and NLO process.

121        The systematic removal of divergences from a theory is called renormalization. The di-

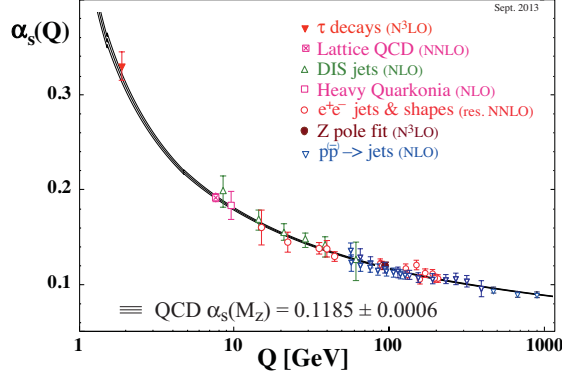


Figure 2.2: The global average of  $\alpha_s$ , the QCD coupling constant [1].

vergences are absorbed into the definitions of the free parameters of the theory, making the parameters a function of the energy scale the process occurs at, instead of a constant. This allows for the calculations of fundamental processes to completed, as long as the energy scale of the interaction is known. A modern interpretation of renormalization was provided by Kenneth Wilson [21] [22]. Instead of seeing the effects of high momentum calculations after moving to NLO in perturbation theory, one uses an effective Lagrangian, computed by integrating out shells of momentum beginning at the energy cutoff of the theory, where the NLO effects begin to dominate. The dimensions of integration are then rescaled and the result of evaluating the integral over the momentum shell is absorbed into the definition of free parameters. The processes is iterated until the energy scale of the interaction is reached. The functional dependence of the parameters is then directly present in the resulting effective Lagrangian, instead of appearing suddenly when accounting for the one-loop contributions at NLO. Regardless of how strange this procedure seem, the running of the coupling constant as a function of interaction energy has been validated experimentally time and time and again, as shown in Figure 2.2 [1].

## 2.2 Abelian Gauge Theories of Particle Interactions

In 1930, Herman Weyl introduced the idea that the interactions between fields can be generated by requiring them to be invariant under gauge transformations of a local symmetry [23]. For electromagnetism, the local symmetry is that of the Lie group,  $U(1)$ . It is an abelian group, which has the property that the generators of the group symmetry commutes with themselves. The  $U(1)$  symmetry is invariant under phase rotations. By requiring local gauge invariance, the Lagrangian must be unchanged under the

$$\psi(x) \rightarrow e^{i\alpha(x)}\psi(x). \quad (2.8)$$

<sup>143</sup> Consider the Lagrangian for a free spin 1/2 particle:

$$\mathcal{L} = \bar{\psi}(i\gamma^\mu \partial_\mu - m)\psi \quad (2.9)$$

<sup>144</sup> The first term in the Lagrangian, involving the derivative, acts on  $\alpha(x)$ , creating a new term in  
<sup>145</sup> the Lagrangian, breaking its invariance under the local phase transformation.

$$\mathcal{L} \rightarrow \mathcal{L} - (\partial_\mu \alpha) \bar{\psi} \gamma^\mu \psi \quad (2.10)$$

<sup>146</sup> Thus, a new term must be added to the original Lagrangian to cancel out the term arising from  
<sup>147</sup> the local phase transformation. This is achieved by defining the covariant derivative:

$$D_\mu = \partial_\mu + ieA_\mu \quad (2.11)$$

<sup>148</sup> where  $A_\mu$  is a new vector field that transforms as follows:

$$A_\mu(x) \rightarrow A_\mu(x) - \frac{1}{e}\partial_\mu \alpha(x) \quad (2.12)$$

<sup>149</sup> The covariant derivative thus transforms like

$$\begin{aligned} D_\mu \psi(x) &\rightarrow [\partial_\mu + ie(A_\mu - \frac{1}{e}\partial_\mu \alpha)] e^{i\alpha(x)} D_\mu \psi(x) \\ &= e^{i\alpha(x)} [\partial_\mu + ie(A_\mu - \frac{1}{e}\partial_\mu \alpha + \frac{1}{e}\partial_\mu \alpha)] D_\mu \psi(x) \\ &= e^{i\alpha(x)} (\partial_\mu + ieA_\mu) \psi(x) \\ &= e^{i\alpha(x)} D_\mu \psi(x) \end{aligned} \quad (2.13)$$

<sup>150</sup> This covariant derivative transforms in the same way that  $\psi(x)$  does, and the new locally gauge  
<sup>151</sup> invariant Lagrangian becomes

$$\begin{aligned} \mathcal{L} &= \bar{\psi}(i\gamma^\mu D_\mu - m)\psi - \frac{1}{4}F^{\mu\nu}F_{\mu\nu} \\ &= i\bar{\psi}\gamma^\mu \partial_\mu \psi - \bar{\psi}\gamma^\mu \psi A_{\mu u} - m\bar{\psi}\psi - \frac{1}{4}F^{\mu\nu}F_{\mu\nu} \end{aligned} \quad (2.14)$$

<sup>152</sup> where

$$F^{\mu\nu} = (\partial^\mu A^\nu - \partial^\nu A^\mu) \quad (2.15)$$

<sup>153</sup> and  $\frac{1}{4}F^{\mu\nu}F_{\mu\nu}$  is the kinetic energy term of the Proca equation for the new vector field.

<sup>154</sup> This new Lagrangian is identical to the QED Lagrangian, except it was derived beginning  
<sup>155</sup> with a free Dirac theory and requiring the field to be locally gauge invariant under  $U(1)$  trans-  
<sup>156</sup> formations. This necessitated the introduction of a new vector field,  $A_\mu$ , as well as an interaction

<sup>157</sup> term with it. This implies that the electromagnetic force can be represented by the requirement  
<sup>158</sup> of local  $U(1)$  symmetry on a free Dirac particle.

<sup>159</sup> It should be noted, that if the photon had mass, an additional term from the Proca equation  
<sup>160</sup> would have to be added to the Lagrangian,  $m^2 A_\mu A^\mu$ . This term complicates the picture since  
<sup>161</sup> it is not invariant under local phase transformations, and cannot be compensated for through a  
<sup>162</sup> different choice of  $A_\mu$ . This implies that the bosons of a gauge theory must be massless in order  
<sup>163</sup> to preserve local gauge invariance.

### <sup>164</sup> 2.3 Non-Abelian Gauge Theories of Particle Interactions

<sup>165</sup> In 1954, Yang and Mills worked to extend this idea to symmetries of different gauge groups [24].  
<sup>166</sup> Their most important accomplishment was developing this procedure for non-abelian groups.  
<sup>167</sup> These are groups, where the transformation does not involve a simple variable  $\alpha(x)$ , but rather an  
<sup>168</sup> entire matrix of dimension  $n > 2$ . These matrices do not commute with each other, and their work  
<sup>169</sup> developed the procedure for applying local gauge invariance described above to the more complex,  
<sup>170</sup> higher dimensional symmetries, such as  $SU(2)$  and  $SU(3)$ . Consider the case of  $SU(2)$  symmetry.  
<sup>171</sup> The theory is appropriate for describing the dynamics of two fermion fields, represented as a  
<sup>172</sup> doublet:

$$\psi = \begin{pmatrix} \psi_1(x) \\ \psi_2(x) \end{pmatrix} \quad (2.16)$$

<sup>173</sup> this will transform under the  $SU(2)$  transformation as a two-component spinor:

$$\psi \rightarrow \exp\left(i\alpha^i \frac{\sigma_i}{2}\right) \psi \quad (2.17)$$

<sup>174</sup> where  $\sigma^i$  are the Pauli matrices:

$$\sigma^1 = \begin{pmatrix} 0 & 1 \\ 1 & 0 \end{pmatrix}, \sigma^2 = \begin{pmatrix} 0 & -i \\ i & 0 \end{pmatrix}, \sigma^3 = \begin{pmatrix} 1 & 0 \\ 0 & -1 \end{pmatrix} \quad (2.18)$$

<sup>175</sup> and have the commutation relation defined by:

$$\left[ \frac{\sigma^i}{2}, \frac{\sigma^j}{2} \right] = i\epsilon^{ijk} \frac{\sigma^k}{2} \quad (2.19)$$

<sup>176</sup> Similar to the case of the  $U(1)$  Abelian symmetry, in order to form a Lagrangian that is  
<sup>177</sup> locally gauge invariant, three vector fields,  $A_\mu^i$ ,  $i = 1, 2, 3$ , are introduced, and coupled to  $\psi$   
<sup>178</sup> through the covariant derivative:

$$D_\mu = (\partial_\mu - igA_\mu^i \frac{\sigma^i}{2}) \quad (2.20)$$

<sup>179</sup> to ensure that the derivative covaries with the transformation, the fields,  $A_\mu^i$  will transform like:

$$A_\mu^i \frac{\sigma^i}{2} \rightarrow A_\mu^i \frac{\sigma^i}{2} + \frac{1}{g}(\partial_\mu \alpha^i) \frac{\sigma^i}{2} + i \left[ \frac{\alpha^i \sigma^i}{2}, A_\mu^i \frac{\sigma^i}{2} \right] \quad (2.21)$$

<sup>180</sup> The third term, which was absent from the abelian form of the transformation, is necessary to  
<sup>181</sup> account for the non-commutation of the Pauli matrices. This non-commutation also changes the  
<sup>182</sup> form of the field strength tensor,  $F_{\mu\nu}^i$ :

$$F_{\mu\nu}^i = \partial_\mu A_\nu^i - \partial_\nu A_\mu^i + g\epsilon^{ijk} A_\mu^j A_\nu^k \quad (2.22)$$

<sup>183</sup> The entire  $SU(2)$  invariant Lagrangian can then be written as:

$$\begin{aligned} \mathcal{L}_{Yang-Mills} &= -\frac{1}{4}F_{\mu\nu}^i F^{i\mu\nu} + \bar{\psi}(i\gamma^\mu D_\mu)\psi \\ &= -\frac{1}{4}F_{\mu\nu}^i F^{i\mu\nu} + \bar{\psi}(i\gamma^\mu \partial_\mu - igA_\mu^i \frac{\sigma^i}{2})\psi \end{aligned} \quad (2.23)$$

<sup>184</sup> This procedure generalizes to any continuous group of symmetries. The basic steps involve  
<sup>185</sup> identifying the generators of the transformation:

$$\psi(x) \rightarrow e^{i\alpha^a t^a} \psi \quad (2.24)$$

<sup>186</sup> where  $t^a$  are a set of matrices with the commutation relationship:

$$[t^a, t^b] = if^{abc}t^c \quad (2.25)$$

<sup>187</sup> where  $f^{abc}$  is the structure constant for the group. The covariant derivative is then defined as:

$$D_\mu = \partial_\mu - igA_\mu^a t^a \quad (2.26)$$

<sup>188</sup> where the fields,  $A_\mu^a$ , transform like:

$$A_\mu^a \rightarrow A_\mu^a + \frac{1}{g}\partial_\mu \alpha^a + f^{abc}A_\mu^b \alpha^c \quad (2.27)$$

<sup>189</sup> the field strength tensor is then formed as:

$$F_{\mu\nu}^a = \partial_\mu A_\nu^a - \partial_\nu A_\mu^a + f^{abc}A_\mu^b A_\nu^c \quad (2.28)$$

<sup>190</sup> and finally, the locally, gauge invariant Lagrangian will have the form:

$$\begin{aligned}\mathcal{L}_{\text{General, non-Abelian}} &= -\frac{1}{4}F_{\mu\nu}^a F^{a\mu\nu} + \bar{\psi}(i\gamma^\mu D_\mu)\psi \\ &= -\frac{1}{4}F_{\mu\nu}^a F^{a\mu\nu} + \bar{\psi}(i\gamma^\mu \partial_\mu - igA_\mu^a t^a)\psi\end{aligned}\quad (2.29)$$

In 1964, Murray Gell-Mann and Zweig independently developed a model of hadron interactions, that described the spectrum of baryons and mesons in terms of combinations of fundamental particles, which Gell-Mann named quarks [25] [26] [27]. In their model, three quarks:  $u, d, s$  formed an  $SU(3)$  flavor symmetry. However, this did not explain the appearance of only two and three quark combinations, the mesons and baryons. It also could not explain the spin statistics of the baryons. The  $\Delta^{++}$ ,  $\Delta^-$ , and  $\Omega^-$ , particles all have  $uuu$ ,  $ddd$ ,  $sss$  quark combinations, respectively, with their spins aligned. That is to say, these baryons seem to violate the Pauli-exclusion principle since all three quarks seem to occupy the same quantum state simultaneously.

In 1964, O.W. Greenberg solved this problem by proposing that quarks also have an additional quantum number, *color*, that come in three types: red, green, blue [28]. The requirement that all stable hadrons be color neutral: either possessing equal amounts of all three colors in  $qqq$  combinations, or a  $q\bar{q}$  pair sharing the same color, also explained the observation of only 2 and 3 quark combinations in experiments. These three colors form an  $SU(3)$  symmetry, and is the gauge symmetry describing the interactions of quarks and leptons. This theory is known as Quantum Chromodynamics (QCD). Its derivation follows from the procedure outlined above.

This group has eight generators, known as the Gell-Mann matrices, and are defined as:

$$\begin{aligned}t^1 &= \frac{1}{2} \begin{pmatrix} 0 & 1 & 0 \\ 1 & 0 & 0 \\ 0 & 0 & 0 \end{pmatrix}, \quad t^2 = \frac{1}{2} \begin{pmatrix} 0 & -i & 0 \\ i & 0 & 0 \\ 0 & 0 & 0 \end{pmatrix}, \quad t^3 = \frac{1}{2} \begin{pmatrix} 1 & 0 & 0 \\ 0 & -1 & 0 \\ 0 & 0 & 0 \end{pmatrix} \\ t^4 &= \frac{1}{2} \begin{pmatrix} 0 & 0 & 1 \\ 0 & 0 & 0 \\ 1 & 0 & 0 \end{pmatrix}, \quad t^5 = \frac{1}{2} \begin{pmatrix} 0 & 0 & -i \\ 0 & 0 & 0 \\ i & 0 & 0 \end{pmatrix} \\ , t^6 &= \frac{1}{2} \begin{pmatrix} 0 & 0 & 0 \\ 0 & 0 & 1 \\ 0 & 1 & 0 \end{pmatrix}, \quad t^7 = \frac{1}{2} \begin{pmatrix} 0 & 0 & 0 \\ 0 & 0 & -i \\ 0 & -i & 0 \end{pmatrix}, \quad t^8 = \frac{1}{2\sqrt{3}} \begin{pmatrix} 1 & 0 & 0 \\ 0 & 1 & 0 \\ 0 & 0 & -2 \end{pmatrix}\end{aligned}\quad (2.30)$$

and a Lagrangian defined as:

$$\begin{aligned}\mathcal{L}_{QCD} &= -\frac{1}{4}G_{\mu\nu}^a G^{a\mu\nu} + \bar{\psi}(i\gamma^\mu D_\mu)\\ &= -\frac{1}{4}G_{\mu\nu}^a G^{a\mu\nu} + \bar{\psi}(i\gamma^\mu \partial_\mu - igA_\mu^a t^a)\end{aligned}\quad (2.31)$$

where  $t^a$  are the Gell-Mann matrices defined in equation 2.30 and the fields  $A_\mu^a$  are the eight mediators of the QCD force, the *gluons*.

Like all non-abelian gauge theories, it is asymptotically free. Thus, the strength of the coupling constant,  $\alpha_s$ , decreases as the momentum-transfer,  $Q$  in interaction increases. This allows the use of perturbation theory for high-momentum calculations, therefore allowing calculations

<sup>214</sup> of hadronic-processes for experimental evaluation.

<sup>215</sup> The idea of local gauge invariance was successful in describing the dynamics of QED and  
<sup>216</sup> QCD, which only contain massless gauge bosons. Theorists had long postulated that the weak  
<sup>217</sup> force was so weak because it was being facilitated by massive bosons, but adding a mass term  
<sup>218</sup> for a boson breaks the local gauge invariance. So, a tool was needed to reconcile the concept of  
<sup>219</sup> local gauge invariance, which works so well for the other forces, with the prospect of the weak  
<sup>220</sup> force being facilitated by massive gauge bosons.

## <sup>221</sup> 2.4 The Higgs Mechanism in an Abelian Theory

<sup>222</sup> In 1964 Peter Higgs introduced the idea that the gauge bosons can acquire their mass through  
<sup>223</sup> the breaking of an underlying symmetry [29]. In other words, the natural symmetry of the  
<sup>224</sup> Lagrangian describing a particular interaction could be different than the symmetry we observe  
<sup>225</sup> in nature. Consider an abelian example of complex scalar field theory, coupled to itself and to  
<sup>226</sup> an electromagnetic field [20].

$$\mathcal{L} = -\frac{1}{4}(F_{\mu\nu})^2 + |D_\mu\phi|^2 - V(\phi) \quad (2.32)$$

<sup>227</sup> where  $D_\mu = \partial_\mu + ieA_\mu$ , is the familiar covariant derivative, and the Lagrangian is invariant under  
<sup>228</sup> the  $U(1)$  transformation as described earlier. The potential term,  $V(\phi)$  has the form

$$V(\phi) = -\mu^2\phi^*\phi + \frac{\lambda}{2}(\phi^*\phi)^2 \quad (2.33)$$

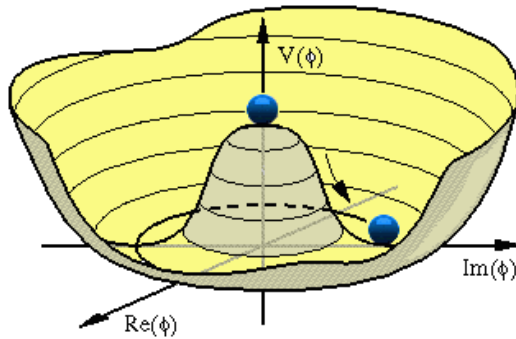


Figure 2.3: A visual representation of the Higgs potential [2]

<sup>229</sup> if  $\mu^2 > 0$  the shape of the potential no longer has a minimum at  $\langle\phi\rangle = 0$ . Figure 2.3 shows a plot  
<sup>230</sup> of the potential energy of  $\phi$  in terms of each of its components. The new minimum potential  
<sup>231</sup> energy occurs at:

$$\langle \phi \rangle = \phi_0 = \left( \frac{\mu^2}{\lambda} \right)^{1/2} \quad (2.34)$$

and while the field has a ground state at the zero potential point it is in an unstable equilibrium. Any quantum fluctuation about this point will take the field into the lower energy configuration with a ground state about the new minimum. When the Lagrangian is expanded about 2.34, the field,  $\phi$  is rewritten as:

$$\phi(x) = \phi_0 + \frac{1}{\sqrt{2}}(\phi_1(x) + i\phi_2(x)) \quad (2.35)$$

the potential term,  $V(x)$ , then becomes:

$$V(x) = -\frac{1}{2\lambda}\mu^4 + \frac{1}{2} \cdot 2\mu^2\phi_1^2 + \mathcal{O}(\phi_1^3) \quad (2.36)$$

where we can notice that  $\phi_1$  has acquired a mass term with,  $m = \sqrt{2}\mu$ , while the scalar field  $\phi_2$  remains massless, and is known as the Goldstone boson. The covariant derivative is also transformed as:

$$|D_\mu \phi|^2 = \frac{1}{2}(\partial_\mu \phi_1)^2 + \frac{1}{2}(\partial_\mu \phi_2)^2 + \sqrt{2}e\phi_0 \cdot A_\mu \partial^\mu \phi_2 + e^2\phi_0^2 A_\mu A^\mu + \dots \quad (2.37)$$

where cubic and quartic terms of  $A_\mu$ ,  $\phi_1$ , and  $\phi_2$  have been dropped. The important term is the last one, which can be interpreted as a mass term of the vector field,  $A_\mu$

$$\Delta\mathcal{L}_M = \frac{1}{2}m_A A_\mu A^\mu = e^2\phi_0^2 A_\mu A^\mu \quad (2.38)$$

where  $m_A = 2e^2\phi_0^2$ , has arisen from consequences of a non-zero vacuum expectation value of the  $\phi$  field. The remaining, massless Goldstone boson,  $\phi_2$  is not a physical particle, but rather a consequence of the choice of gauge. This is illustrated when we can use the  $U(1)$  gauge symmetry to rotate the field  $\phi(x)$  such that the field disappears.

$$\begin{aligned} \phi &\rightarrow \phi' = e^{i\alpha}(\phi_1 + \phi_2) \\ &= (\cos \alpha + i \sin \alpha)(\phi_1 + \phi_2) \\ &= (\phi_1 \cos \alpha - \phi_2 \sin \alpha) + i(\phi_1 \sin \alpha + \phi_2 \cos \alpha) \\ &= (\phi_1 - \phi_2 \tan \alpha) + i(\phi_1 \tan \alpha + \phi_2) \end{aligned} \quad (2.39)$$

Choosing  $\alpha = -\tan \phi_2/\phi_1$  will make  $\phi'$  a real quantity and eliminate its imaginary component,  $\phi'_2$ . The Lagrangian can then be rewritten in terms of the rotated field  $\phi'$  and see that massless boson is indeed removed from the theory.

$$\begin{aligned}\mathcal{L} = & \frac{1}{2}(\partial_\mu\phi'_1)(\partial^\mu\phi'_1) - \frac{1}{2} \cdot 2\mu^2\phi'_1\phi'_1 \\ & - \frac{1}{4}(F^{\mu\nu}F_{\mu\nu}) + \frac{1}{2} \cdot e^2\phi_0^2A_\mu A^\nu \\ & + \phi_0e^2\phi'_1A_\mu A^\mu + \frac{1}{2}e^2\phi'^2A_\mu A^\mu + \mathcal{O}(\phi'^3)\dots\end{aligned}\quad (2.40)$$

249 The degree of freedom that  $\phi_2$  represents, is absorbed as a longitudinal polarization of the  
250  $A_{mu}$  field, a forbidden for massless gauge bosons, but necessary for massive bosons.

251 For this case of an abelian symmetry  $U(1)$ , it was shown that if a complex scalar field, which  
252 interacts with itself and another vector field, can gains a non-zero vacuum expectation value.  
253 The Lagrangian can be expanded about this new minimum, generating a mass term for the  
254 vector field. One of the degrees of freedom of the original complex scalar field is then absorbed  
255 as a longitudinal polarization state of the massive vector field.

## 256 2.5 The Higgs Mechanism in a non-Abelian Theory

257 Before describing the electroweak gauge theory of  $SU(2) \otimes U(1)$ , it will be helpful to see the  
258 effects of the Higgs mechanism for the non-Abelian group,  $SU(2)$  by itself. Consider an an  
259 example of an  $SU(2)$  gauge field coupled to a scalar field that transforms like a real-valued  
260 vector under  $SU(2)$  transformations [20]. The field  $\phi$  will have the form:

$$\phi = \begin{pmatrix} \phi_1 \\ \phi_2 \\ \phi_3 \end{pmatrix} \quad (2.41)$$

261 where the components,  $\phi_i$  are real-valued fields. The  $SU(2)$  transformation for this scalar field  
262 will also look like:

$$\phi \rightarrow e^{i\alpha^i T^i} \phi \quad (2.42)$$

263 where the matrices,  $T^i$  are defined as:

$$iT^1 = \begin{pmatrix} 0 & 0 & 0 \\ 0 & 0 & 1 \\ 0 & -1 & 0 \end{pmatrix}, \quad T^2 = \begin{pmatrix} 0 & 0 & -1 \\ 0 & 0 & 0 \\ 1 & 0 & 0 \end{pmatrix}, \quad T^3 = \begin{pmatrix} 0 & 1 & 0 \\ -1 & 0 & 0 \\ 0 & 0 & 0 \end{pmatrix} \quad (2.43)$$

264 The Lagrangian for this field will feature a Higgs potential term along with the previously  
265 mentioned  $SU(2)$  gauge fields,  $A_\mu^a$  coupled to the scalar field,  $\phi$ , and is given by:

$$\mathcal{L} = -\frac{1}{4}F_{\mu\nu}^a F^{a\mu\nu} + |D_\mu\phi|^2 + \mu^2\phi^*\phi - \frac{\lambda}{4}(\phi^*\phi)^2 \quad (2.44)$$

266 where  $F_{\mu\nu}^a$ , the field strength tensor is defined as:

$$F_{\mu\nu}^a = (\partial_\mu A_\nu^a - \partial_\nu A_\mu^a) + g\epsilon^{abc} A_\mu^b A_\nu^c \quad (2.45)$$

<sup>267</sup> and the covariant derivative is defined as:

$$D_\mu = (\partial_\mu + igA_\mu^a T^a)\phi \quad (2.46)$$

<sup>268</sup> Similarly to the Abelian case, the Higgs potential will induce a spontaneous symmetry breaking,  
<sup>269</sup> and one of the components of the field  $\phi$  will gain a vacuum expectation value. After this  
<sup>270</sup> breaking and expanding around the ground state potential, the field  $\phi$  will have the form:

$$\phi = \frac{1}{\sqrt{2}} \begin{pmatrix} 0 \\ 0 \\ v+h \end{pmatrix} \quad (2.47)$$

<sup>271</sup> There has been no loss in generality in assuming this form since, similarly to the abelian case,  
<sup>272</sup> we can use the gauge symmetry of  $SU(2)$  to rotate the field into this configuration. Goldstone's  
<sup>273</sup> theorem tells us that we should expect two massive gauge bosons corresponding to the  $T^1$ , and  
<sup>274</sup>  $T^2$  generators, while the  $T^3$  generator will correspond to a massless gauge boson, since  $\phi$  is still  
<sup>275</sup> invariant under  $T^3$  transformations.

<sup>276</sup> As in the Abelian case, the mass terms for the gauge bosons are generated from the covariant  
<sup>277</sup> derivative term,  $|D_\mu\phi|^2$

$$\begin{aligned} D_\mu\phi &= \frac{1}{\sqrt{2}} \left( \partial_\mu + gA_\mu^1 \begin{pmatrix} 0 & 0 & 0 \\ 0 & 0 & 1 \\ 0 & -1 & 0 \end{pmatrix} + gA_\mu^2 \begin{pmatrix} 0 & 0 & -1 \\ 0 & 0 & 0 \\ 1 & 0 & 0 \end{pmatrix} + gA_\mu^3 \begin{pmatrix} 0 & 1 & 0 \\ -1 & 0 & 0 \\ 0 & 0 & 0 \end{pmatrix} \right) \begin{pmatrix} 0 \\ 0 \\ v+h \end{pmatrix} \\ &= \frac{1}{\sqrt{2}} \begin{pmatrix} 0 \\ 0 \\ \partial_\mu \end{pmatrix} + \frac{gA_\mu^1}{\sqrt{2}} \begin{pmatrix} 0 \\ v+h \\ 0 \end{pmatrix} - \frac{gA_\mu^2}{\sqrt{2}} \begin{pmatrix} v+h \\ 0 \\ 0 \end{pmatrix} \\ &= \frac{1}{\sqrt{2}} \begin{pmatrix} g(v+h)A_\mu^1 \\ g(v+h)A_\mu^2 \\ \partial_\mu h \end{pmatrix} \end{aligned} \quad (2.48)$$

<sup>278</sup> Therefore

$$|D_\mu \phi|^2 = \frac{1}{2} \partial_\mu h \partial^\mu h + \frac{g^2 v^2}{2} ((A_\mu^1)^2 + (A_\mu^2)^2) + \frac{g^2}{2} (h^2 + 2hv) ((A_\mu^1)^2 + (A_\mu^2)^2) \quad (2.49)$$

279 This theory produces two massive bosons,  $A_\mu^1$  and  $A_\mu^2$ , both with mass,  $m_A = gv$ . These  
 280 fields have  $h$ , and  $h^2$  couplings to the Higgs boson. The third gauge field,  $A_\mu^3$ , remains massless  
 281 and is not coupled to the Higgs field. This model is beginning to resemble a description of  
 282 electroweak physics, however, a third massive boson is necessary, as is a new gauge symmetry  
 283 in order to generate it. That is the subject of the next section.

## 284 2.6 Glashow Weinberg Salam Theory

285 Glashow, Weinberg, and Salam published their theory unifying electromagnetic and weak forces  
 286 in the 1960s [30] [31] [32]. It begins with the requirement of a  $SU(2)_L \otimes U(1)$  symmetry  
 287 and incorporates the Higgs mechanism to give mass to the gauge bosons of the weak force. As  
 288 described earlier, the  $U(1)$  symmetry requires introducing a vector field, which will be labeled  $B_\mu$ ,  
 289 and an interaction term, which is absorbed into the covariant derivative,  $D_\mu$ . The transformation  
 290 will also be parameterized with a with a quantum number,  $Y$ , known as hypercharge. The  
 291  $SU(2)$  symmetry requires the introduction of three new vector fields, which will be labeled  
 292  $W_\mu^i, i = 1, 2, 3$ . The quantum number associated with this gauge group is known as isospin, and  
 293 is determined by the  $T^3$  operator, acting on an  $SU(2)$  doublet on the third generator of the  
 294 group. The  $SU(2) \otimes U(1)$  transformation,  $U(x)$ , will then be give by:

$$U(x) = e^{i\alpha^a(x)\tau^a} e^{iY\alpha(x)} \quad (2.50)$$

295 where  $\tau^a = \sigma^a/2$ , the Pauli matrices, 2.18. These gauge fields will be coupled, via the covariant  
 296 derivative, to a doublet of complex scalar fields  $\phi$ , with hypercharge  $Y = +1/2$ . A Higgs potential  
 297 will be added to generate the spontaneous symmetry breaking that will give mass to three of  
 298 the gauge fields, and leave one massless. In order to preserve the  $SU(2)_L \otimes U(1)$  symmetry, the  
 299 new covariant derivative will take the form:

$$D_\mu = (\partial_\mu - igW_\mu^a \tau^a - \frac{i}{2}g'B_\mu) \quad (2.51)$$

300 The subscript L on  $SU(2)_L$  refers to the experimental results that the weak force violates  
 301 parity maximally, by only interacting with the left-handed chiral component of a field. Right  
 302 versus left chirality is determined by whether the spin of a particle is aligned or anti-aligned  
 303 with its direction of motion, and in general a particle is represented by a linear combination

of its right and left handed components. This idea was first proposed by Chen Ning Yang and Tsung-Dao Lee, in the 1950s. Their ideas were validated by the experimental discovery of parity violation in 1957, through the beta decays of Cobalt 60 atoms by C.S Wu. That same year, Yang and Lee were awarded the nobel prize for their insight [33]. In this model, then, the left-handed components of the particles participate in the weak interaction and are formed into doublets, while the right handed components are singlets, and will only interact with the electromagnetic field,  $B_\mu$ . The quantum numbers of the doublet will be given by  $+1/2$  for the upper component of the  $SU(2)$  doublet, and  $-1/2$  for the lower component. The fermion content of this theory is then given by:

$$\begin{pmatrix} \nu_L \\ e_L \end{pmatrix}, e_R \quad \begin{pmatrix} u_L \\ d_L \end{pmatrix}, u_R, d_R \quad (2.52)$$

where the right handed neutrino,  $\nu_R$  has been omitted, since it has zero charge, and isospin, and therefore does not participate in any of the interactions of this theory. The complete Lagrangian is given by a sum of free particle terms for massless bosons, fermions, and Higgs scalar fields; the Higgs potential; and a Yukawa coupling term between the fermions and the Higgs, which generates their masses.

$$\mathcal{L}_{GWS} = \mathcal{L}_{BosonKE} + \mathcal{L}_{Higgs} + \mathcal{L}_{FermionKE} + \mathcal{L}_{Yukawa} \quad (2.53)$$

The Higgs potential will have the form:

$$\mathcal{L}_{Higgs} = (D_\mu \phi)^\dagger (D^\mu \phi) + \mu^2 \phi^\dagger \phi - \lambda (\phi^\dagger \phi)^2 \quad (2.54)$$

The Higgs potential will break the symmetry of the Lagrangian when one of the four degrees of freedom in the complex scalar doublet,  $\phi$ , spontaneously acquires a vacuum expectation value. In this case, it will generate three massive gauge bosons, one massless gauge boson, and a massive scalar field. After gaining a vacuum expectation value, and expanding about this value, the scalar fields will have the form:

$$\langle \phi \rangle = \frac{1}{\sqrt{2}} \begin{pmatrix} 0 \\ v + h \end{pmatrix} \quad (2.55)$$

where no loss of generality has occurred since we are always able to rotate into this form through the appropriate gauge transformations, similar to what was described in the Abelian case. It should also be noted that this form is not invariant to any of the individual generators  $t^a$ , however  $\phi$  will be invariant to a combination of  $T^3 + Y$  generators. Per Goldstone's theorem, we should

expect this linear combination of fields to be the massless vector boson after symmetry breaking. The massless eigenstate will be the electromagnetic field,  $A_\mu \sim A_\mu^3 + B_\mu$ . The electric charge quantum number,  $Q$ , is then defined as

$$Q = T^3 + Y \quad (2.56)$$

<sup>323</sup> As before, the generation of the masses for the gauge bosons are generated by the interaction  
<sup>324</sup> of their fields with the Higgs field via the covariant derivative.

$$\begin{aligned} D_\mu \phi &= \frac{1}{\sqrt{2}} \left( \partial_\mu - \frac{ig}{2} A_\mu^1 \begin{pmatrix} 0 & 1 \\ 1 & 0 \end{pmatrix} - \frac{ig}{2} A_\mu^2 \begin{pmatrix} 0 & -i \\ i & 0 \end{pmatrix} - \frac{ig}{2} A_\mu^3 \begin{pmatrix} 1 & 0 \\ 0 & -1 \end{pmatrix} \right) \begin{pmatrix} 0 \\ v+h \end{pmatrix} \\ &= \frac{1}{\sqrt{2}} \left( \partial_\mu + i(\frac{1}{2}(v+h)(gA_\mu^3 - g'B_\mu)) \right) \end{aligned} \quad (2.57)$$

<sup>325</sup> Taking the dot product of this with its hermitian conjugate gives the  $|D_\mu \phi|^2$  term:

$$\begin{aligned} |D_\mu \phi|^2 &= \frac{1}{2} \partial_\mu h \partial^\mu h + \frac{1}{2} \frac{g^2 v^2}{4} ((A_\mu^1)^2 + (A_\mu^2)^2) + \frac{v^2}{4} (gA_\mu^3 - g'B_\mu)^2 \\ &\quad + \frac{1}{2} g^2 4(h^2 + 2vh)((A_\mu^1)^2 + (A_\mu^2)^2) + \frac{1}{2} \frac{1}{4} (h^2 + 2vh)(gA_\mu^3 - g'B_\mu) \end{aligned} \quad (2.58)$$

<sup>326</sup> From equation 2.58 we can identify three massive and one massless gauge bosons, corresponding  
<sup>327</sup> to the charged and neutral weak currents, and the electromagnetic current.

$$\begin{aligned} W_\mu^\pm &= \frac{1}{\sqrt{2}} (A_\mu^1 \mp iA_\mu^2) && \text{with mass } m_W = g \frac{v}{2}; \\ Z_\mu^0 &= \frac{1}{\sqrt{g^2 + g'^2}} (gW_\mu^3 - g'B_\mu) && \text{with mass } m_Z = \frac{v}{2} \sqrt{g^2 + g'^2}; \\ A_\mu &= \frac{1}{\sqrt{g^2 + g'^2}} (gW_\mu^3 + g'B_\mu) && \text{with mass } m_A = 0; \end{aligned} \quad (2.59)$$

<sup>328</sup> where the last field,  $A_\mu$  is absent from the covariant derivative term, but already identified as  
<sup>329</sup> the massless gauge boson of the theory due to it's gauge invariance under a  $T^3 + Y$  rotation.  
<sup>330</sup> Using these definitions the covariant derivative has the following form:

$$\begin{aligned} D_\mu &= \partial_\mu - \frac{ig}{\sqrt{2}} (W^+ T^+ + W^- T^-) \\ &\quad - \frac{i}{\sqrt{g^2 + g'^2}} Z_\mu^0 (gT^3 - g'Y) - \frac{gg'}{\sqrt{g^2 + g'^2}} A_\mu (T^3 + Y) \end{aligned} \quad (2.60)$$

<sup>331</sup> where  $T^\pm = \frac{1}{2}(\sigma^1 \pm \sigma^2)$ . From this form, we can identify the fundamental electric charge,  $e$ , as

$$e = \frac{gg'}{\sqrt{g^2 + g'^2}} \quad (2.61)$$

332 The similarity in the forms between  $Z_\mu^0$  and  $A_\mu$  suggest that their relationship can be ex-  
 333 pressed in a simpler form, as the rotation of underlying gauge fields  $A_\mu^3$  and  $B_\mu$  through the  
 334 weak mixing angle,  $\theta_W$

$$\begin{pmatrix} Z_\mu^0 \\ A_\mu \end{pmatrix} = \begin{pmatrix} \cos \theta_W & -\sin \theta_W \\ \sin \theta_W & \cos \theta_W \end{pmatrix} \begin{pmatrix} A_\mu^3 \\ B_\mu \end{pmatrix} \quad (2.62)$$

335 where  $\tan \theta_W = \frac{g'}{g}$ . Expanding 2.62, we have the definitions of the  $Z_\mu^0$  and  $A_\mu$  fields in terms of  
 336  $\theta_W$

$$\begin{aligned} Z_\mu^0 &= A_\mu^3 \cos \theta_W - B_\mu \sin \theta_W \\ A_\mu &= A_\mu^3 \sin \theta_W + B_\mu \cos \theta_W \end{aligned} \quad (2.63)$$

337 The weak mixing angle,  $\theta_W$ , also provides a simple relationship between the  $W_\mu^\pm$  and  $Z_\mu^0$  fields:

$$m_W = m_Z \cos \theta_W \quad (2.64)$$

338 The covariant derivative,  $D_\mu$  is also rewritten in terms of the mass eigenstates of the gauge fields

$$D_\mu = (\partial_\mu - \frac{ig}{\sqrt{2}}(W_\mu^+ + W_\mu^- T^-) - \frac{ig}{\cos \theta_W} Z_\mu^0(T_3 - \sin^2 \theta_W Q) - ieA_\mu Q) \quad (2.65)$$

339 where  $g = e/\cos \theta_W$ . The square of the covariant derivative is then written as

$$\begin{aligned} |D_\mu|^2 &= \frac{1}{2}\partial_\mu h \partial^\mu h + \frac{1}{2}m_W^2 W_\mu^+ W^{\mu+} + \frac{1}{2}m_W^2 W_\mu^- W^{\mu-} + \frac{1}{2}m_Z^2 Z_\mu^0 Z^{\mu 0} \\ &+ \left(\frac{h^2}{v^2} + \frac{h}{v}\right)\left[\frac{1}{2}m_W^2(W_\mu^+ W^{\mu+} + W_\mu^- W^{\mu-}) + \frac{1}{2}m_Z^2 Z_\mu^0 Z^{\mu 0}\right] \end{aligned} \quad (2.66)$$

340

341

342 With the form of the covariant derivative in place, the fermionic kinematic term of the  
 343 Lagrangian can be described. As mentioned earlier, the masses of the fermions in the model  
 344 will be generated by the Yukawa interaction term with the Higgs, so this term only involves the  
 345 covariant derivatives acting on the left-handed doublet and right-handed singlet states of this  
 346 model.

347 The quantum number assignments for the leptons, which are chosen in order to reproduce the  
 348 known values of their electric charges, are shown in table 2.1. The values of these quantum  
 349 numbers enter into the covariant derivative via the  $Z_\mu^0$  term of equation 2.65. The fermionic

	$\nu_L$	$e_L$	$e_R$	$u_L$	$d_L$	$u_R$	$d_R$
Isospin	+1/2	-1/2	0	+1/2	-1/2	0	0
Hypercharge	-1/2	-1/2	-1	+1/6	1/3	2/3	-1/3
Electric Charge	0	-1	-1	2/3	-1/3	2/3	-1/3

Table 2.1: The quantum numbers Isospin and Hypercharge are assigned for each of the  $SU(2)$  and  $U(1)$  symmetries respectively

350 kinetic energy term of the Lagrangian is given by:

$$\begin{aligned} \mathcal{L}_{Fermion} = & \bar{E}_L(i\gamma^u D_\mu)E_L + \bar{e}_R(i\gamma^u D_\mu)e_R \\ & \bar{Q}_L(i\gamma^u D_\mu)Q_L + \bar{u}_R(i\gamma^u D_\mu)u_R + \bar{d}_R(i\gamma^u D_\mu)d_R \end{aligned} \quad (2.67)$$

351 Expanding the covariant term for the left-handed electron shows its explicit coupling to the  
352 gauge boson fields.

$$\begin{aligned} \mathcal{L}_{E_L} = & \begin{pmatrix} \bar{\nu}_L & \bar{e}_L \end{pmatrix} \left( (i\gamma^\mu(\partial_\mu - \frac{ig}{\sqrt{2}}(W_\mu^+ T^+ + W_\mu^- T^-) - \frac{ig}{\cos \theta_W} Z_\mu^0(T^3 - \sin^2 \theta_W Q) - ie A_\mu Q)) \right) \begin{pmatrix} \nu_L \\ e_L \end{pmatrix} \\ = & \bar{\nu}_L i\gamma^\mu \partial_\mu \nu_L + \bar{e}_L i\gamma^\mu \partial_\mu e_L + \frac{ig}{\sqrt{2}} W_\mu^+ \bar{\nu}_L \gamma^\mu e + \frac{ig}{\sqrt{2}} W_\mu^- \bar{e}_L \gamma^\mu \nu_L \\ & + \frac{ig}{\cos \theta_W} \bar{\nu}_L (1/2) \gamma^\mu \nu_L + \frac{ig}{\cos \theta_W} \bar{e}_L \gamma^\mu (-1/2 + \sin^2 \theta_W (+1)) e_L + (ie) \bar{e}_L \gamma^\mu A_\mu (-1) \end{aligned} \quad (2.68)$$

353 All of the terms will be combined with the final, spontaneously broken GWS Lagrangian at the  
354 end of this section.

355 The final term to discuss in the theory, before combining all of the results, is the Yukawa  
356 interaction term between the fermion fields and the Higgs. For the electron, this term takes the  
357 form:

$$\begin{aligned} \mathcal{L}_{Yukawa} = & -\lambda_e \bar{e}_L \cdot \phi e_R - \lambda_e E_L \cdot \phi \bar{e}_R \\ = & -\frac{\lambda_e}{\sqrt{2}} (v + h) (\bar{e}_L e_R + e_L \bar{e}_R) \\ = & -\frac{\lambda_e v}{\sqrt{2}} (\bar{e}_L e_R + e_L \bar{e}_R) + -\frac{\lambda_e}{\sqrt{2}} (\bar{e}_L e_R + e_L \bar{e}_R) h \end{aligned} \quad (2.69)$$

358 where the mass of the electron is identified as  $m_e = \frac{\lambda_e v}{\sqrt{2}}$ . In order to generate the masses of  
359 the particles, each fermion has its own unique  $\lambda$  value. So while the Higgs mechanism is able  
360 to generate the masses in a way that preserves the underlying  $SU(2) \otimes U(1)$  symmetry, it does  
361 not explain the hierarchy of masses since each  $\lambda$  value is unique to each lepton. The second  
362 term in last equation of 2.69 is the coupling of the Higgs particle,  $h$ , to the fermions. The  
363 coupling is proportional to the mass of the particle. The largest of these is to the top quark,  
364 with  $m_t = 73.21 \pm 0.51 \pm 0.71 GeV$ .

The Yukawa coupling for the quarks is necessarily modified when additional quarks besides the  $u$  and  $d$  are added to the theory. This is because there can be additional coupling terms that mix generations. This occurs when the mass eigenstate of the quarks is not the same as the interaction eigenstate. The modification requires the expansion of the  $u_L$  and  $d_L$  components into a vector of left handed quarks. If we let

$$u_L^i = (u_L, c_L, t_L), \quad d_L^i = (d_L, s_L, b_L) \quad (2.70)$$

represent the up and down-type quarks in the original weak interaction basis, then the vectors,  $u_L^i$  and  $d_L^i$ , can be defined as the diagonalized basis for the Higgs coupling. They are related through a unitary transformation.

$$u_L^i = U_u^{ij} u_L^{j'}, \quad d_L^i = U_d^{ij} d_L^{j'} \quad (2.71)$$

The interaction terms with the charged gauge boson currents must then be rewritten as

$$J_W^{\mu+} = \frac{1}{\sqrt{2}} \bar{u}_L^i \gamma^\mu d_L^i = \frac{1}{\sqrt{2}} \bar{u}_L^{i'} \gamma^\mu (U_u^\dagger U_d) d_L^{j'} = \frac{1}{\sqrt{2}} \bar{u}_L^{i'} \gamma^\mu V_{ij} d_L^{j'} \quad (2.72)$$

where  $V_{ij}$  is the 3x3 Cabibbo-Kobayashi-Maskawa (CKM) matrix describing the mixing among six quarks [34] [35]. It is an extension of the Glashow-Iliopoulos-Maiani mechanism, which was a 2x2 matrix that predicted the existence of a fourth quark, the charm quark. The GIM mechanism was an attempt to suppress flavor-changing-neutral currents, which occur at LO in a three-quark model, but not in a four-quark model. The CKM matrix, however, was motivated by an attempt to explain  $CP$  violation in the weak interaction. At the time of its publication, the bottom and top quarks were not predicted. After these were discovered, they were awarded the nobel prize in physics in 2008.

At this point, all the pieces are ready to write down the GWS Lagrangian, after the Higgs mechanism has spontaneously broken the  $SU(2) \otimes U(1)$  symmetry.

$$\begin{aligned} \mathcal{L}_{Unbroken} = & -\frac{1}{4} A_{\mu\nu}^a A^{\mu\nu a} - \frac{1}{4} F_{\mu\nu} F^{\mu\nu} \\ & + |D_\mu \phi|^2 + \mu^2 (\phi^\dagger \phi) - \lambda (\phi^\dagger \phi)^2 \\ & + \bar{E}_L (i\gamma^\mu D_\mu) E_L + \text{similar terms for } e_R, U_L, u_R, d_R \\ & - \lambda_e \bar{E}_L \cdot \phi e_R + h.c. + \text{similar terms for } e_R, U_L, u_R, d_R \end{aligned} \quad (2.73)$$

$$\begin{aligned}
\mathcal{L}_{GWS} = & -\frac{1}{4}(Z_{\mu\nu}^0)^2 - \frac{1}{2}(W_{\mu\nu}^+ W_{\mu\nu}^-) - \frac{1}{4}(F_{\mu\nu})^2 \\
& + ig \cos \theta_W ((W_\mu^- W_\nu^+ - W_\nu^- W_\mu^+) \partial^\mu Z^{0\nu} + W_{\mu\nu}^+ W^{-\mu} Z^{0\nu} + W_{\mu\nu}^- W^{+\mu} Z^{0\nu}) \\
& + ie ((W_\mu^- W_\nu^+ - W_\nu^- W_\mu^+) \partial^\mu A^\nu + W_{\mu\nu}^+ W^{-\mu} A^\nu - W_{\mu\nu}^- W^{+\mu} A^\nu) \\
& + g^2 \cos^2 \theta_W (W_\mu^+ W_\nu^- Z^{0\mu} Z^{0\nu} - W_\mu^+ W^{-\mu} Z_\nu^0 Z^{0\nu}) \\
& + g^2 (W_\mu^+ W_\mu^- A^\mu A^\nu - W_\mu^+ W^{-\mu} A_\nu A^\nu) \\
& + ge \cos \theta_W (W_\mu^+ W_\nu^- (Z^{0\mu} A_\nu + Z^{0\nu} A^\mu) - 2W_\mu^+ W^{-\mu} A^\nu) \\
& + \frac{1}{2}g^2 (W_\mu^+ W_\nu^-) (W^{+\mu} W^{-\nu} - W^{+\nu} W^{-\mu}) \\
& + \frac{1}{2}\partial_\mu h \partial^\nu h - v^2 \lambda h^2 + \frac{1}{2}m_W^2 W_\mu^+ W^{+\mu} + \frac{1}{2}m_W^2 W_\mu^- W^{-\mu} + \frac{1}{2}m_Z^2 Z_\mu^0 Z^{0\mu} \\
& + \left(\frac{h^2}{v^2} + \frac{h}{v}\right) \left(\frac{1}{2}m_W^2 (W_\mu^+ W^{+\mu} + W_\mu^- W^{-\mu}) + \frac{1}{2}m_Z^2 Z_\mu^0 Z^{0\mu}\right) - \lambda v h^3 - \frac{1}{4}\lambda h^4 \\
& + \bar{E}_L (i\gamma^\mu \partial_\mu) E_L + e_R^- (i\gamma^\mu \partial_\mu) e_R + \bar{Q}_L (i\gamma^\mu \partial_\mu) Q_L + u_R^- (i\gamma^\mu \partial_\mu) u_R + \bar{d}_R (i\gamma^\mu \partial_\mu) d_R \\
& + g (W_\mu^+ J_W^{\mu+} + W_\mu^- J_W^{\mu-} + Z_\mu^0 J_Z^\mu) + e A_\mu J_{EM}^\mu \\
& - \frac{\lambda_e v}{\sqrt{2}} (\bar{e}_L e_R + \bar{e}_R e_L) - \frac{\lambda_e h}{\sqrt{2}} (\bar{e}_L e_R + \bar{e}_R e_L) \\
& - \frac{\lambda_u v}{\sqrt{2}} (\bar{u}_L u_R + \bar{u}_R u_L) - \frac{\lambda_u h}{\sqrt{2}} (\bar{u}_L u_R + \bar{u}_R u_L) \\
& - \frac{\lambda_d v}{\sqrt{2}} (\bar{d}_L d_R + \bar{d}_R d_L) - \frac{\lambda_d h}{\sqrt{2}} (\bar{d}_L d_R + \bar{d}_R d_L)
\end{aligned} \tag{2.74}$$

where the currents of the electroweak interaction,  $J_W^{\mu+}$ ,  $J_W^{\mu-}$ ,  $J_Z^\mu$ ,  $J_A^\mu$  are defined as:

$$\begin{aligned}
J_W^{\mu+} &= \frac{1}{\sqrt{2}} (\bar{\nu}_L \gamma^\mu e_L + \bar{u}_L^i \gamma^\mu V_{ij} d_L^j) \\
J_W^{\mu-} &= \frac{1}{\sqrt{2}} (\bar{e}_L \gamma^\mu \nu_L + \bar{d}_L^i \gamma^\mu V_{ij} u_L^j) \\
J_Z^\mu &= \frac{1}{\cos \theta_W} (\bar{\nu}_L \gamma^\mu (+1/2) \nu_L + \bar{e}_L \gamma^\mu (-1/2 + \sin^2 \theta_W) e_L + \bar{e}_R \gamma^\mu \sin^2 \theta_W e_R \\
&\quad + \bar{u}_L \gamma^\mu (1/2 - 2/3 \sin^2 \theta_W) u_L + \bar{u}_R \gamma^\mu (-2/3 \sin^2 \theta_W) u_R \\
&\quad + \bar{d}_L \gamma^{mu} (-1/2 + 1/3 \sin^2 \theta_W) d_L + \bar{d}_R \gamma^\mu (1/3 \sin^2 \theta_W) d_R) \\
J_{EM}^\mu &= e_{L,R}^- \gamma^\mu (-1) e_{L,R} + u_{L,R}^- \gamma^\mu (2/3) u_{L,R} + d_{L,R}^- \gamma^\mu (-2/3) d_{L,R}
\end{aligned} \tag{2.75}$$

## 384 2.7 The Standard Model of Particle Physics

The Standard Model of particle physics, extends the GWS model by incorporating the QCD interaction between the quarks and gluons. The symmetry of this theory is that of:

$$SU(3)_C \otimes SU(2)_L \otimes U(1)_Y \tag{2.76}$$

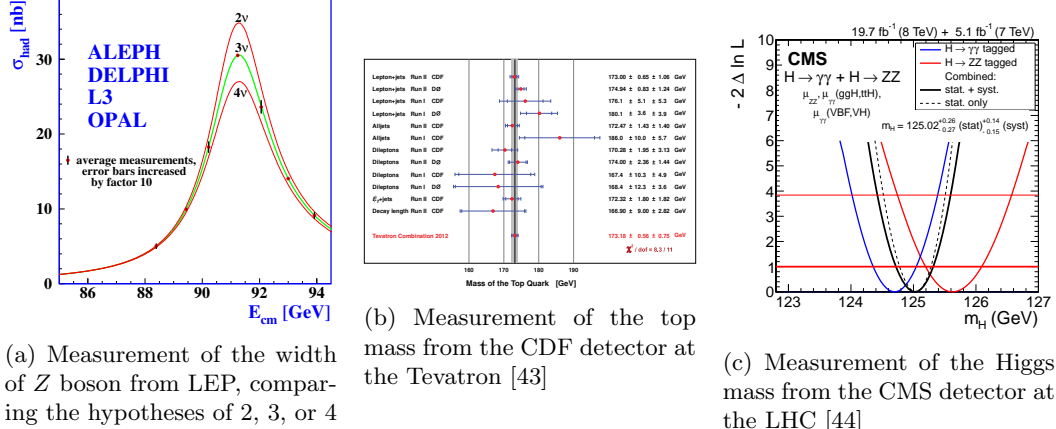


Figure 2.4: Experimental milestones of the Standard Model

385 The Lagrangian of the model is given by

$$\mathcal{L}_{SM} = \mathcal{L}_{GWS} - \frac{1}{4} G_{\mu\nu}^a G^{a\mu\nu} + g_S C_\mu^a J_{QCD}^{a\mu} \quad (2.77)$$

386 where the current for the QCD interaction,  $J_{QCD}^{a\mu}$  is defined as:

$$J_{QCD}^a = \bar{u}^i \gamma^\mu t^a u^i + \bar{d}^i \gamma^\mu t^a d^i \quad (2.78)$$

387 where  $t^a$  are the Gell-Mann matrices defined in equation 2.30. The field strength tensor for the  
388 eight gluon fields,  $G_{\mu\nu}^a$ , is defined as

$$G_{\mu\nu}^a = (\partial_\mu C_\nu^a - \partial_\nu C_\mu^a) - g_S f^{abc} C_\mu^b C_\nu^c \quad (2.79)$$

389 The experimental evidence in favor of the SM is compelling. It has not only been able  
390 to describe existing phenomenon to great precision, but has also predicted the existence of  
391 new forms of matter and interactions among fundamental particles. The UA1 [36] [37] and  
392 UA2 [38] [39] experiments at CERN, under the leadership of Carlo Rubbia, discovered the  
393  $W$  and  $Z$  bosons in 1983. The experiments observed a handful of events, in  $p\bar{b}$  collisions, at  
394  $\sqrt{s} = 540$  GeV, and were able to measure the masses to be  $M_W \sim 80$  GeV and  $M_Z \sim 95$  GeV.

395 In the following years, from 1989-2000, the Large electron-positron (LEP) collider at CERN  
396 conducted precision measurements of the Standard Model [40] [41]. Along with high-precision  
397 measurements on the  $W, Z$  masses:

$$m_Z = 91.1875 \pm 0.0021 \text{ GeV} \quad (2.80)$$

$$m_W = 80.376 \pm 0.0033 \text{ GeV}$$

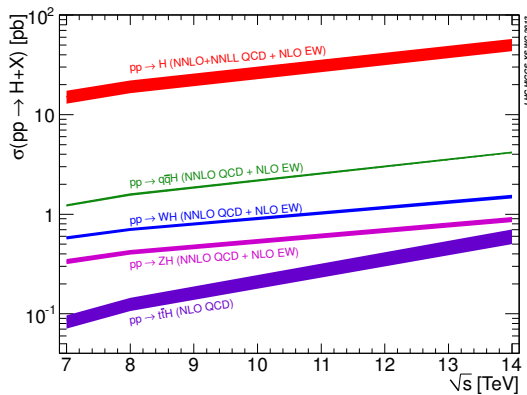
398 the experiment was also able to put stringent limits on the existence of more than three families of

399 leptons and quarks by measuring the width of the  $Z$  boson. Figure 2.4(a) shows the comparison  
400 of two, three, and four family hypotheses to data.

401 Another milestone for the Standard Model occurred in 1995 when the CDF [45] and D0 ex-  
402 periments [46] at the Tevatron announced the observation of the top quark, with  $m_t \sim 176$  GeV,  
403 in  $p\bar{p}$  collisions at  $\sqrt{s} = 1.8$  TeV. Figure 2.4(b) shows a plot from 2012, the latest top quark  
404 mass measurements from CDF, which reports a  $m_t = 173.18 \pm 0.56 \pm 0.75$  GeV. It was the  
405 last quark predicted by the CKM matrix to be observed, and earned Makoto Kobayashi and  
406 Toshihide Maskawa the nobel prize in 2008 for their work extending the quark sector to three  
407 families and parameterizing their electroweak mixing.

408 Yet another milestone was reached in 2012, when the CMS and ATLAS detectors at CERN  
409 announced the observation of a new boson, with characteristics strikingly similar to the elusive  
410 Higgs boson of the SM. Figure 2.4(??) shows the latest measurement results on the mass from  
411 the  $H \rightarrow \gamma\gamma$  and  $H \rightarrow ZZ$  channels, with a  $m_H = 125.02 \pm 0.27 \pm 0.15$ . One of the most  
412 important remaining goals is to measure the couplings of this new boson to all of the other  
413 particles in the Standard Model. Of particular interest is the coupling to the top-quark, since it  
414 offers the largest value of the Higgs Yukawa coupling to measure. This offers a test of the nature  
415 of the coupling, as well as a probe into deviations from its value.

## 416 2.8 Higgs Production in $pp$ Collisions at the LHC



746 Figure 2.5: Higgs production cross-sections at the LHC, for 7–14 TeV  $pp$  collisions

747 The rest of the thesis will describe the search for Higgs boson production in proton-proton  
748 collisions at the LHC, so it will be useful to understand the production mechanisms for the Higgs  
749 in this scenario. At the LHC collision energies 7 – 14 TeV, there are four dominant production  
750 mechanisms that produce Higgs events: gluon-gluon fusion (ggf), vector-boson fusion (vbf),  
751 associated production with vector bosons (VH), and associated production with top-quark pairs  
752 (tth). Figure 2.5 shows the relative cross sections for each of these mechanisms.

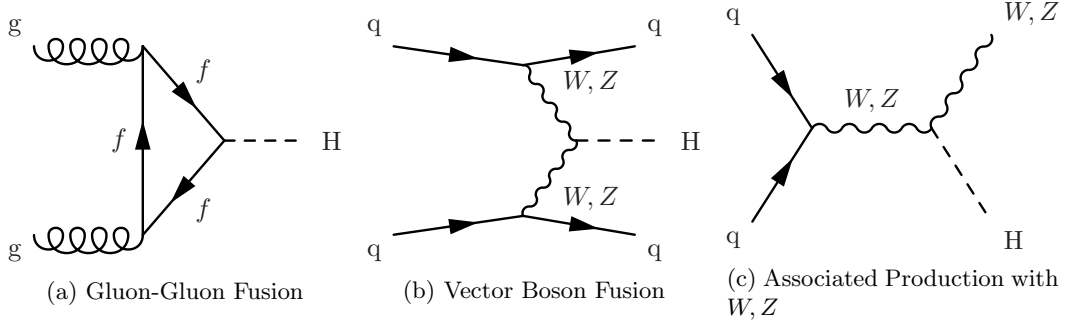


Figure 2.6: Feynman diagrams for the three largest Higgs production modes at the LHC

Gluon-gluon fusion, which proceeds via a heavy quark loop [47], is the dominant production mechanism at the LHC. The QCD radiative corrections to the total cross section have been computed at the next-to-leading order (NLO) and at the next-to-next-to-leading order (NNLO accuracy). The cross section for Higgs production at  $m_H = 125$  GeV and  $\sqrt{s} = 8$  TeV, the cross section is given as:

$$\sigma_{ggF} = 19.27 \pm \text{QCD Scale Unc.}^{+7.2\%}_{-7.8\%} \pm \text{PDF} + \alpha_S \text{ Unc.}^{+7.4\%}_{-6.9\%} \text{ pb}^{-1} \quad (2.81)$$

423 Figure 2.6(a) shows a Feynman diagram for this process. The triangle loop contains all strongly  
424 coupled fermions, which is dominated by the top-quark since the Yukawa coupling to the Higgs  
425 is the largest.

Vector boson fusion proceeds through the fusion of  $W^+W^-$  or  $Z^0Z^0$  gauge bosons [47]. The characteristic signature of the production mode is the associated production of two quarks, typically at a low angle relative to the proton beam. This process has been calculated to NNLO for QCD and NLO for Electroweak corrections [47]. The cross section at  $m_H = 125$  GeV and  $\sqrt{s} = 8$  TeV is given as:

$$\sigma_{VBF} = 1.653 \pm \text{EW Unc.}^{+4.5\%}_{-4.5\%} \pm \text{QCD Scale Unc.}^{+0.2\%}_{-0.2\%} \pm \text{PDF} + \alpha_S \text{ Unc.}^{+2.6\%}_{-2.8\%} \text{ pb}^{-1} \quad (2.82)$$

426 Figure 2.6(b) shows a Feynman diagram for VBF production. The large coupling to the  $W, Z$   
427 bosons helps to make this the sub-dominant production mechanism at the LHC. However, the  
428 gluon content of the proton at TeV energies is much larger than that of the valence quarks, thus  
429 the relative suppression.

The third largest production mechanism for Higgs bosons at the LHC is through associated production with a  $W$  or  $Z$  boson [47]. It has been calculated to NNLO for QCD and NLO for Electroweak corrections. This process is also sometimes referred to as, Higgstrahlung, since it resemble the bremsstrahlung process of an electron radiating a photon. The higher order

electroweak corrections are similar to that of the Drell-Yan, so much of the technology to compute the cross-section can be borrowed from existing EW calculations. The cross section for  $m_H = 125 \text{ GeV}$  and  $\sqrt{s} = 8 \text{ TeV}$  is:

$$\begin{aligned}\sigma_{WH} &= 0.7046 \pm \text{QCD Scale Unc.}^{+1.0\%}_{-1.0\%} \pm \text{PDF}+\alpha_S \text{ Unc.}^{+2.3\%}_{-2.3\%} \text{ pb}^{-1} \\ \sigma_{ZH} &= 0.4153 \pm \text{QCD Scale Unc.}^{+3.1\%}_{-3.1\%} \pm \text{PDF}+\alpha_S \text{ Unc.}^{+2.5\%}_{-2.5\%} \text{ pb}^{-1}\end{aligned}\quad (2.83)$$

430 Figure 2.6(c) shows the Feynman diagram for VH production. This channel is most useful for  
431 identifying hadronic decays of the Higgs, since the associated gauge boson can decay to leptons,  
432 giving a strong kinematic handle over backgrounds that would normally overwhelm a similar  
433 search in the ggF channel.

## 434 2.9 $t\bar{t}H$ Production in $pp$ Collisions at the LHC

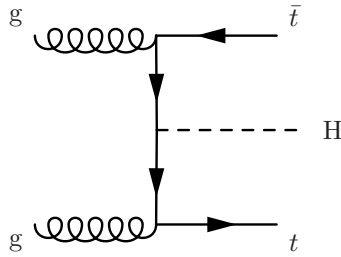


Figure 2.7: Feynman diagram for  $t\bar{t}H$  production

435 The  $t\bar{t}H$  production mode is the fourth largest production mode at the LHC [47]. This pro-  
436 duction mode has been calculated to NLO in QCD [48] [49] and has been studied recently with the  
437 state of the art NLO tools using the aMC@NLO [50] and POWHEG (PYTHIA+HERWIG) [51]  
438 frameworks. Studies have also been performed interfacing NLO QCD studies [52] with the  
439 Sherpa parton shower framework [53]. Additional studies on the effects of spin correlations with  
440 the aMC@NLO and Madspin framework have also been performed [54].

It has been found that the addition of NLO effects increases the cross-section relative to LO by  $\sim 20\%$ . The largest theoretical uncertainty comes from the variation of the renormalization and factorization scale, the QCD coupling  $\alpha_S$ , and the PDF uncertainty. The renormalization and factorization scales are set to  $\mu_R = \mu_F = (1/2)(m_T + m_T + m_H)$  and are varied by a factor of 2 to determine the cross-section's dependence on these parameters. Three different PDF sets, MSTW2008, CTEQ6.6, and NNPDF2.0 were used with the appropriate corresponding values of  $\alpha_S$  to determine the combined effect of varying PDF+ $\alpha_S$ . The cross section for  $m_H = 125 \text{ GeV}$

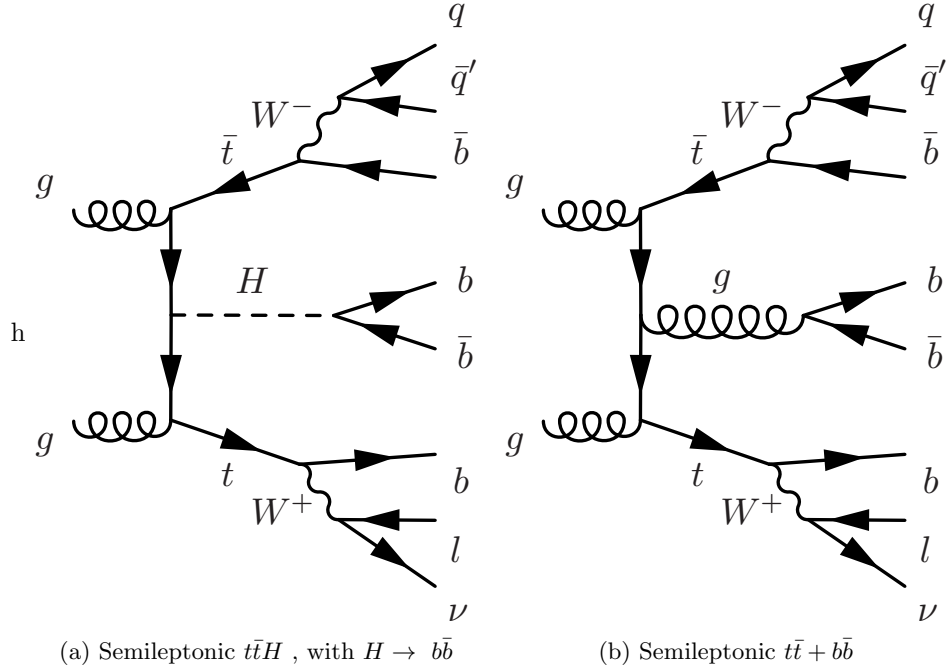


Figure 2.8: Feynman diagrams for the semileptonic  $t\bar{t}H$  process and its irreducible background,  $t\bar{t} + b\bar{b}$

and  $\sqrt{s} = 8$  TeV is given by:

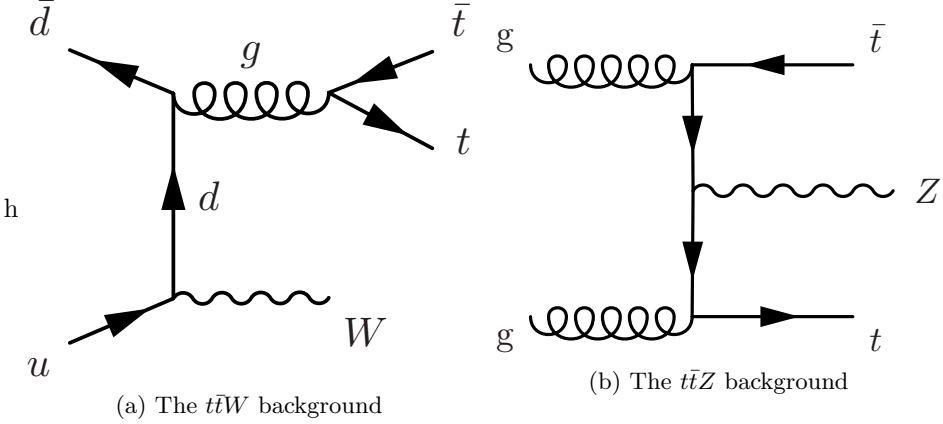
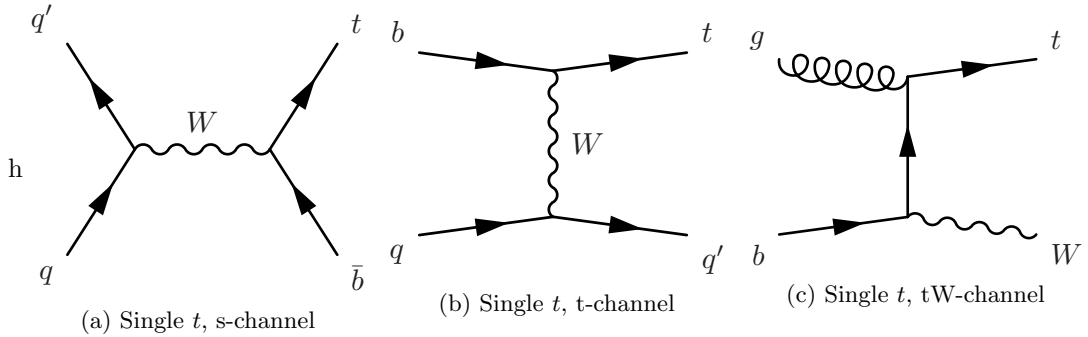
$$\sigma_{ttH} = 0.1293 \pm \text{QCD Scale Unc.}^{+3.8\%}_{-9.3\%} \pm \text{PDF} + \alpha_S \text{ Unc.}^{+8.1\%}_{-8.1\%} \text{ pb}^{-1} \quad (2.84)$$

441 A search for the Higgs in this production mode is additionally challenging due to this large  
442  $\sim 10\%$  error on the theoretical cross-section. Figure 2.7 shows a Feynman diagram for this  
443 process before the branching of the top-quarks or Higgs to final states.

444 When asking for the Higgs to decay to b-quark pairs, yet another complication arises when  
445 trying to identify which b-quarks came from a top decay or from a Higgs decay. For example, in  
446 the semileptonic decay of top quarks, there will be four b-quarks, and two light-flavor quarks in  
447 the final state. This means there are 15 (six choose four) possibilities to associate quarks to the  
448 top system. Although this is potentially constrained by b-tagging, and kinematic requirements  
449 (such as forming the top or  $W$  masses), the number of remaining possibilities smears out the  
450 resolution on peaking variables such as the invariant mass of b-quark pairs.

## 451 2.10 Background Processes to $t\bar{t}H$

452 The dominant background for  $t\bar{t}H$  production of top-quark pairs with additional ISR/FSR jets,  
453  $t\bar{t} + jets$ . The irreducible component of this background is comes when the extra radiation  
454 produces a final state with two additional b-quarks,  $t\bar{t} + b\bar{b}$ . Figure 2.8 compares the Feynman

Figure 2.9: Feynman diagrams for the  $t\bar{t}W$  and  $t\bar{t}Z$  background processesFigure 2.10: Feynman diagrams for the single  $t$  s,t, and  $tW$  background processes

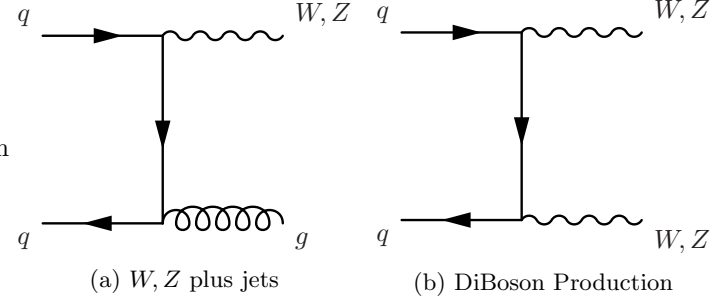
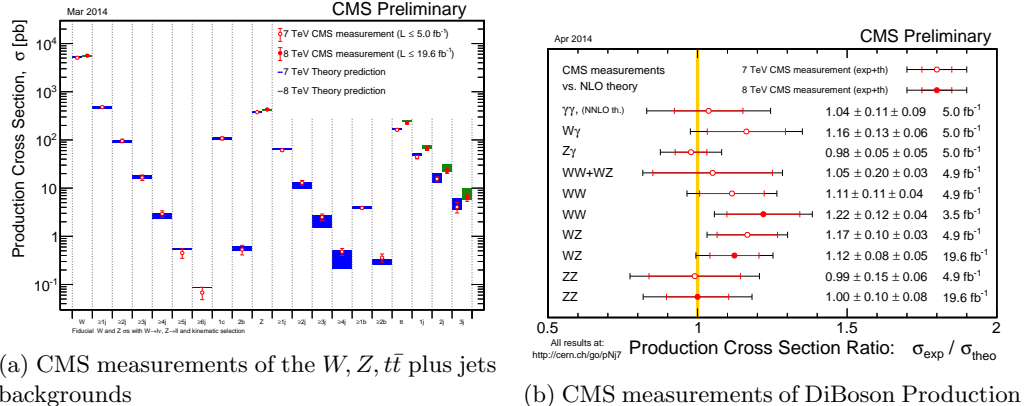
455 diagrams for the semileptonic decays of  $t\bar{t}H$  and  $t\bar{t} + b\bar{b}$ .

456 Additional difficulties come from the theoretical uncertainty on the  $t\bar{t} + b\bar{b}$  background [47].

457 The process has been calculated to NLO QCD in Sherpa [53] and OpenLoops [55] [56] [57]. It  
458 has been found that depending on selection cuts, and use of NLO PDF inputs, the difference  
459 between LO and NLO calculations on the cross section can be anywhere from 0.99% to 1.96%.

460 The light flavor component of the  $t\bar{t} + jets$  background also enters in the selection when any  
461 of the jets from the  $t\bar{t}$  system or extra radiation are misidentified as  $b$ -jets. The cross-section for  
462 the  $t\bar{t} + jets$  process is  $\sim 245 \text{ pb}^{-1}$ . This is a factor of 1800, so even if a  $b$ -tagging algorithm  
463 performs with a 1% mis-identification rate of light-jets, there will still be a large contribution  
464 from this process that will leave a very similar signature in the detector as  $t\bar{t}H$ .

465 The next largest background is the production of vector bosons in association with top-  
466 quark pairs,  $t\bar{t}W$  and  $t\bar{t}Z$ . Figure 2.9 shows Feynman diagrams from these two processes. They  
467 have cross-sections of  $\sigma_{ttW} = 0.249 \text{ pb}^{-1}$  and  $\sigma_{ttZ} = 0.208 \text{ pb}^{-1}$ , which are only a factor of  $\sim 2$   
468 greater than the  $t\bar{t}H$  process. These processes can enter the semileptonic  $t\bar{t}H$  selection by a  
469 semileptonic  $t\bar{t}$  decay, while the vector bosons decay to quarks, or through a hadronic  $t\bar{t}$  decay,  
470 while the vector bosons decay to quarks, and in the case of  $t\bar{t}Z$ , of the leptons is not identified  
471 in the reconstruction.

Figure 2.11: Feynman diagrams for the  $W, Z$  plus jets, and diBoson ( $WW, WZ, ZZ$ ) production.Figure 2.12: Measurements of  $t\bar{t}H$  backgrounds at CMS [3]

Single top production is also an important background to consider in a search for  $t\bar{t}H$  production. Figure 2.10 shows Feynman diagrams for this process. It does not have as large of a contribution as the other backgrounds, since it requires additional radiation in order to have a similar final state jet multiplicity as  $t\bar{t}H$ . However, since a top-quark is still involved in the process, the final state kinematics of its decay products will be very similar. Single  $t$  production has a cross section of  $\sigma_t = 71.3 \text{ pb}^{-1}$ , while Single  $\bar{t}$  production has a cross section of  $\sigma_{\bar{t}} = 43.6 \text{ pb}^{-1}$ , due to charge asymmetry of the valence quarks of the proton

The last backgrounds to consider are the electroweak production of  $W$  and  $Z$  bosons in association with jets, as well as  $WW$ ,  $WZ$ , and  $ZZ$  pairs in association with jets. Figure ?? shows the Feynman diagrams for these processes, where the  $V$ , stands in for either  $W$  or  $Z$  bosons. For a semileptonic selection of  $t\bar{t}H$  events,  $Z$  plus jets events enter from a misidentification of one of the leptons from the  $Z$  boson decay. Extra FSR/ISR radiation is also to leave a similar signature in the signal region of a  $t\bar{t}H$  search, so it mainly contributes to control regions of the data.

All of these backgrounds have been measured at CMS. With the exception of a small degree of tension in the  $WW$  cross-section measurement, all backgrounds are in good agreement with Standard Model predictions. Figure 2.12(a) shows the results of CMS measurements on  $V+jets$  and  $t\bar{t} + jets$  backgrounds. Figure 2.12(b) shows the same, but for diBoson production.

## 490 2.11 Potential BSM Effects on $t\bar{t}H$ production

491 The phenomenological motivation for the existence of physics beyond the Standard Model come  
 492 from the observation of phenomenon or states of matter not described by the theory. Observations  
 493 of the cosmic microwave background from the Plank telescope have estimated that only  
 494  $\sim 5\%$  of the observable universe is composed of ordinary matter [58]. The remaining composition  
 495 is divided between Dark Matter ( $\sim 27\%$ , and  $\sim 68\%$  respectively). Evidence for Dark Matter  
 496 also comes from discrepancies between the observed rotational velocities of galaxies, and the  
 497 observed mass distributions, suggesting the presence of additional form of matter which does  
 498 not interact electromagnetically [59].

499 Additionally, in 1998, the Super-Kamiokande experiment proved that neutrinos oscillated  
 500 between flavors, implying indirectly that they also have mass [60]. This is something not de-  
 501 scribed in the Standard Model of physics. Due to their neutral charge, these particles are  
 502 extremely difficult to detect, so experiments have only been able to measure differences in the  
 503 mass squared between the three mass eigenstates. In 2005, the KamLAND experiment reported  
 504  $|\Delta m_{12}^2 = 0.000079 eV^2|$  [61]. In 2006, the MINOS experiment reported  $|\Delta m_{23} = 0.0027 eV^2|$  [62].

505 One of the largest theoretical problems with the Standard Model, comes the mechanism which  
 506 made it all possible- the Higgs. In equation 2.73 there are terms that couple the Higgs boson to  
 507 itself,  $-\lambda vh^3$ , and  $-\frac{1}{4}\lambda h^4$ . When computing NLO effects, these terms lead to a divergence in  
 508 the Higgs mass, when considering the effect of a loop of fermions on the Higgs propagator. The  
 509 corrections are of the form  $\Delta m_H = -\frac{\lambda_f^2}{8\pi^2} \Lambda_{UV}$ . Where  $\Lambda_{UV}$  is the high energy cut off for the  
 510 theory, which in the limit of a perfect theory, should extend to infinity. This is known as the  
 511 hierarchy problem.

512 Beyond the Standard Model physics is a term that describes extensions of the Standard  
 513 Model in order to describe the observed phenomenon. For the neutrino oscillations, a solution  
 514 similar to CKM matrix has been proposed, the PontecorvoMakiNakagawaSakata (PMNS) ma-  
 515 trix. This proposes that the mass eigenstates of the neutrino are linear combinations of the weak  
 516 eigenstates, allowing for the mixing of flavors. Current experiments now seek to measure the  
 517 free parameters of this matrix.

518 Both the dark matter and hierarchy problems suffer in the fact that there is no clear model,  
 519 such as the PMNS matrix, to provide a theoretical solution. Out of the plethora of theories that  
 520 attempt to solve these problems, supersymmetry (SUSY) is the most popular in the theoretical  
 521 and experimental community. It suggests that there is a broken symmetry between fermions  
 522 and bosons, and introduces a partner to each Standard Model particle with a spin quantum  
 523 number less 1/2 [63]. For the hierarch problem, this provides a set of particles to cancel out the

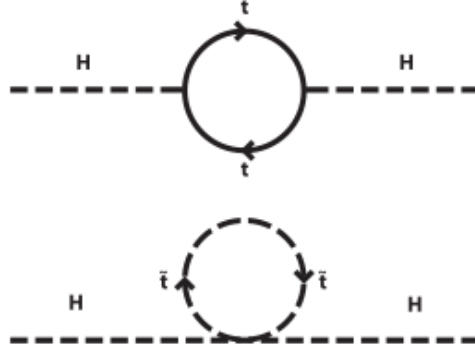


Figure 2.13: The cancellation of the divergent Higgs mass from a loop of top-quarks is cancelled by a loop of supersymmetric top-quarks, stop-quarks [4],

524     divergences in the NLO corrections to the Higgs mass. Figure 2.13 shows the Feynman diagrams  
 525     for a supersymmetric top-quark, or stop quark, that would cancel the divergent contribution  
 526     from the Standard Model top quark. Depending on the specific form of the SUSY model, the  
 527     stop quarks can potentially couple directly or indirectly to the top-quark, producing them at a  
 528     higher rate during  $pp$  collisions. This would effect the number of observed events making it into  
 529     the  $t\bar{t}H$  selection.

530       A number of extensions to the SM also involve introducing new top-like particles into the  
 531     theory. Vector-like quarks would be spin 1/2 particles that transform as triplets under the  $SU(3)$   
 532     color group and whose left and right-handed components have the same color and electroweak  
 533     quantum numbers [64]. These objects are common to several different types of models. Little  
 534     Higgs models [65] [66] [67], models with extra dimensions [68] [69], top-color models [70], and  
 535     composite Higgs models [71], include a vector-like top partner,  $t'$  that decays to a top-quark and  
 536     either a Higgs,  $W$ , or  $Z$  particle. Both  $t't'$  pair production and  $t't$  production would yield the  $t\bar{t}H$   
 537     final state, or at least one indistinguishable detector signature.  $t\bar{t}H$  search can provide indirect  
 538     limits on these models, by observing an excess or lack thereof of  $t\bar{t}H$  events, without having to  
 539     directly construct a  $t'$  resonance.

540 **Chapter 3**

541 **The Large Hadron Collider**



Figure 3.1: Aerial view of the LHC complex, spanning the French-Swiss border [5]

542 The Large Hadron Collider (LHC), is a superconducting, proton-proton, accelerator and  
543 collider operated by the European Center for Nuclear Research (CERN) laboratory in Geneva,  
544 Switzerland [8]. Figure 3.1 shows an aerial view of the LHC complex, with the main laboratory  
545 campus being labeled as CERN, with four of the detector experiments being labeled as ALICE,  
546 ATLAS, CMS, and LHCb. Three smaller experiments, not pictured, also use the LHC ring, and  
547 are TOTEM, LHCf, and MOeDAL. It was designed to elucidate the mechanism of electroweak  
548 symmetry breaking and explore TeV scale of particle physics. As such, it is required to produce  
549 a large number of high center-of-mass energy events. The high center-of-mass energy allows the  
550 creation of heavy particles, while a large luminosity allows for the creation of rare processes.  
551 The number of events produced at a collider is a product of the luminosity of the collider and

552 the total cross-section for the objects being collided.

$$N_{events} = L\sigma_{event} \quad (3.1)$$

553 The cross-section,  $\sigma_{event}$ , can be estimated from the theory of the Standard Model as described  
 554 in section 2.1 and validated by measurement at detectors, such as CMS, as shown in section 2.10.  
 555 The luminosity is a control of the experiment, and for Gaussian distributed beams, is given by  
 556 the equation:

$$L = \frac{N_b^2 n_b f_{rev} \gamma_r}{4\pi \epsilon_n \beta^*} F \quad (3.2)$$

557 The parameters of this equation and their value for the LHC is as follows:

- 558 •  $N_b$  - Number of particles per bunch, squared since there are two beams. The mechanism  
 559 of achieving such high energies is based in Radio-Frequency (RF) cavity technology, which  
 560 clusters the protons together into packets, which are all accelerated and collided together.  
 561 For the LHC,  $N_b = 1.15 \times 10^{11}$ .
  - 562 •  $n_b$  - Number of bunches per beam. The maximum design for the LHC allows for  $n_b = 2808$   
 563 bunches, however in practice, lower number of bunches have been run with in order to  
 564 create more time between bunch crossings.
  - 565 •  $f_{rev}$  - Revolution frequency of the protons in the LHC ring. This is determined by ring  
 566 circumference, and for the LHC,  $f_{rev} = 11.2$  kHz.
  - 567 •  $\gamma_r$  - This is the relativistic gamma-factor, determined by the speed, and thus the center of  
 568 mass energy of the collisions.
  - 569 •  $\epsilon_n$  - This is the normalized transverse emittance of the beam, which describes the RMS  
 570 spread of the beam in its transverse plane. For the LHC  $\epsilon_n = 3.75 \mu\text{m}$ .
  - 571 •  $\beta^*$  - Is the minimum of the  $\beta$  function, which is defined as the square of the transverse  
 572 beam-size divided by  $\epsilon_n$ . It is minimized at interaction regions, where the beams are being  
 573 squeezed into the smallest region possible, to maximize the probability of protons colliding  
 574 during each bunch crossing. For the LHC,  $\beta^* = 0.55$
  - 575 •  $F$  - This is the efficiency for having the two beams head-on, and is determined by the  
 576 crossing angle at which the two counter-rotating beams meet each other.
- 577 The LHC is designed to deliver a maximum luminosity of  $L = 10^{34} \text{ cm}^{-2}\text{s}^{-1}$  to the CMS and ATLAS  
 578 experiments, with a maximum center-of-mass energy of  $\sqrt{s} = 14 \text{ TeV}$ .

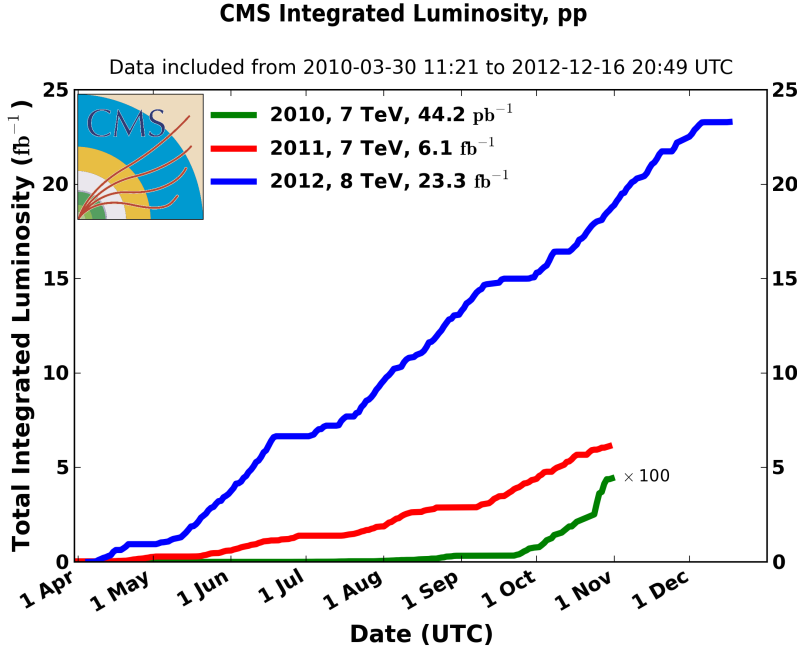


Figure 3.2: Integrated Luminosity delivered to the CMS experiment from 2010-12 [6]

579 In 2010-11, the LHC ran at center-of-mass energy,  $\sqrt{s} = 7 \text{ TeV}$  and delivered  $\sim 6 \text{ fb}^{-1}$  of  
 580 data to the CMS experiment. In 2012, it ran at  $\sqrt{s} = 8 \text{ TeV}$  and collected  $\sim 23 \text{ fb}^{-1}$ . Figure 3.2  
 581 shows a diagram of the luminosity collected as a function of time for each year running.

582 The next sections will describe the LHC accelerator complex, the chain of events leading  
 583 up to collisions of protons at the LHC, and the associated technologies that allow for the con-  
 584 trol and operation of the high-energy, high-luminosity beams that allow the CMS and ATLAS  
 585 experiments to search for heavy particles and rare-processes.

### 586 3.1 The LHC Accelerator Complex

587 The main LHC ring is a 26.7 km tunnel, that is 45 m to 170 m underneath the surface of the  
 588 earth, with 1.4% slope towards Lake Leman. It extends across the French-Swiss border, into  
 589 the French countryside. The tunnel was originally constructed between 1984 and 1989 for the  
 590 Large Electron Positron (LEP) experiment that is famous for its precision measurements of  
 591 several Standard Model parameters [8]. The choice to build the ring underground was driven by  
 592 real estate costs, but the underground setting also provides natural radiation shielding from the  
 593 beam-line and greatly reduces the impact of cosmic radiation on the detectors.

594 The LHC also utilizes the existing accelerator complex from the LEP experiment, which is  
 595 shown in figure 3.3. The complex is composed a series of increasingly powerful accelerators that  
 596 gradually increase the energy of the protons.

597 Protons are initially accelerated by the Linac2 linear accelerator up to 50 MeV [78] [79]. A

## The LHC injection complex

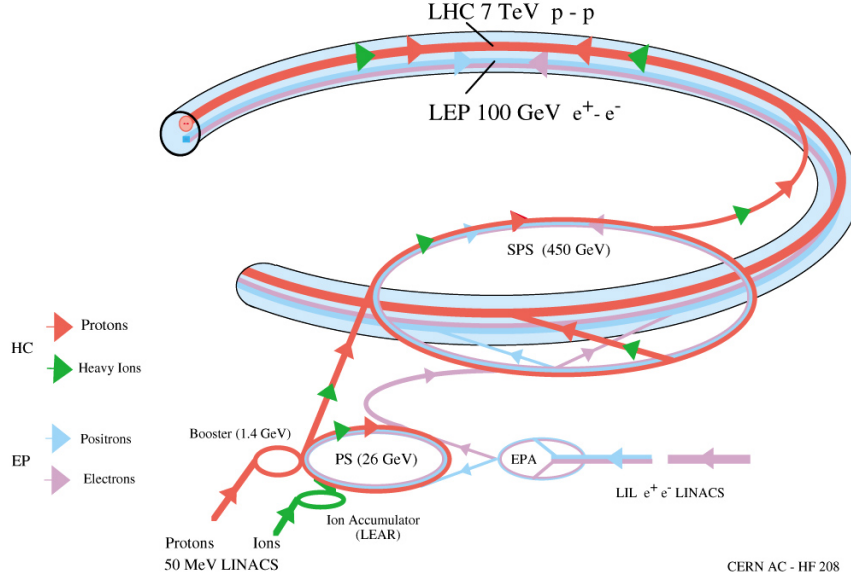


Figure 3.3: The LHC accelerator complex, taking protons from a bottle of Hydrogen at the Linac2, all the way to the LHC ring [7]

598 bottle of Hydrogen is attached to a duoplasmatron source. This device ionizes the Hydrogen,  
 599 and creates a 300 mA beam of protons, through a high-voltage anode, and a geometry designed  
 600 to focus and collimate the beam as it leaves the device. Figure 3.4(a) shows a schematic for  
 601 this device, showing the gas input on the left, and proton beam leaving to the right. Figure  
 602 3.4(b) shows the actual device used in the Linac2 at CERN. The proton beam then enters the  
 603 Radio-Frequency Quadrupole (RFQ) system, which accelerates and bunches the protons up to  
 604 750 keV. The RFQ is a waveguide with four flanges, which have been machined with a sinusoidal  
 605 modulation in the longitudinal direction, which creates an standing electric wave in this direction,  
 606 accelerating the protons. Figure 3.4(c) shows a schematic of this modulation, and figure 3.4(d) is  
 607 a close-up image of this modulation in an actual RFQ. The last stage of acceleration is provided  
 608 by three Alvarez tanks. Each Alvarez tank holds a series of electrically isolated cylinders, known  
 609 as drift tubes, coaxial with the main tank, with gaps in between them. An alternating electric  
 610 field is present in the gaps, and space between each drift tube and the walls of the tank. Protons  
 611 passing through the center of the drift tubes feel no electric field, but the gaps are located such  
 612 that, a proton will always see an accelerating field in the gap, and are thus receive a boost of  
 613 energy from each gap as it traverses the length of the three tanks. Figure 3.4(e) shows an image  
 614 of the inside of an Alvarez tank, and figure 3.4(f) shows the tanks at the Linac2 at CERN. The  
 615 final product is a 180 mA, 50 MeV proton beam, which is steered to the Proton Synchrotron  
 616 Booster for the next stage of acceleration.

617 The Proton Synchrotron Booster (PS booster) complex accelerates the protons up to 1.4

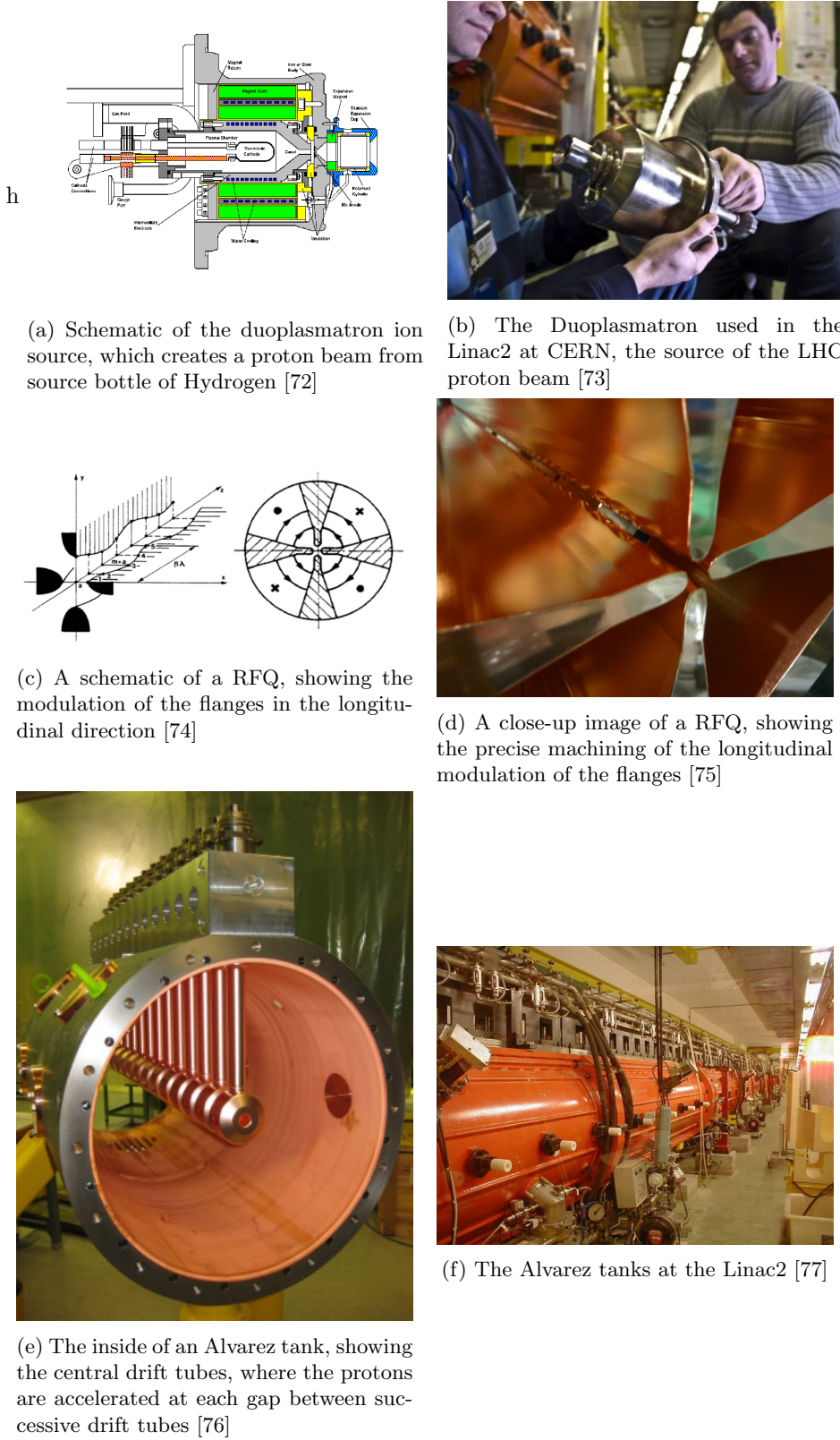


Figure 3.4: Features of the Linac2, the first stage of acceleration in the LHC injection chain

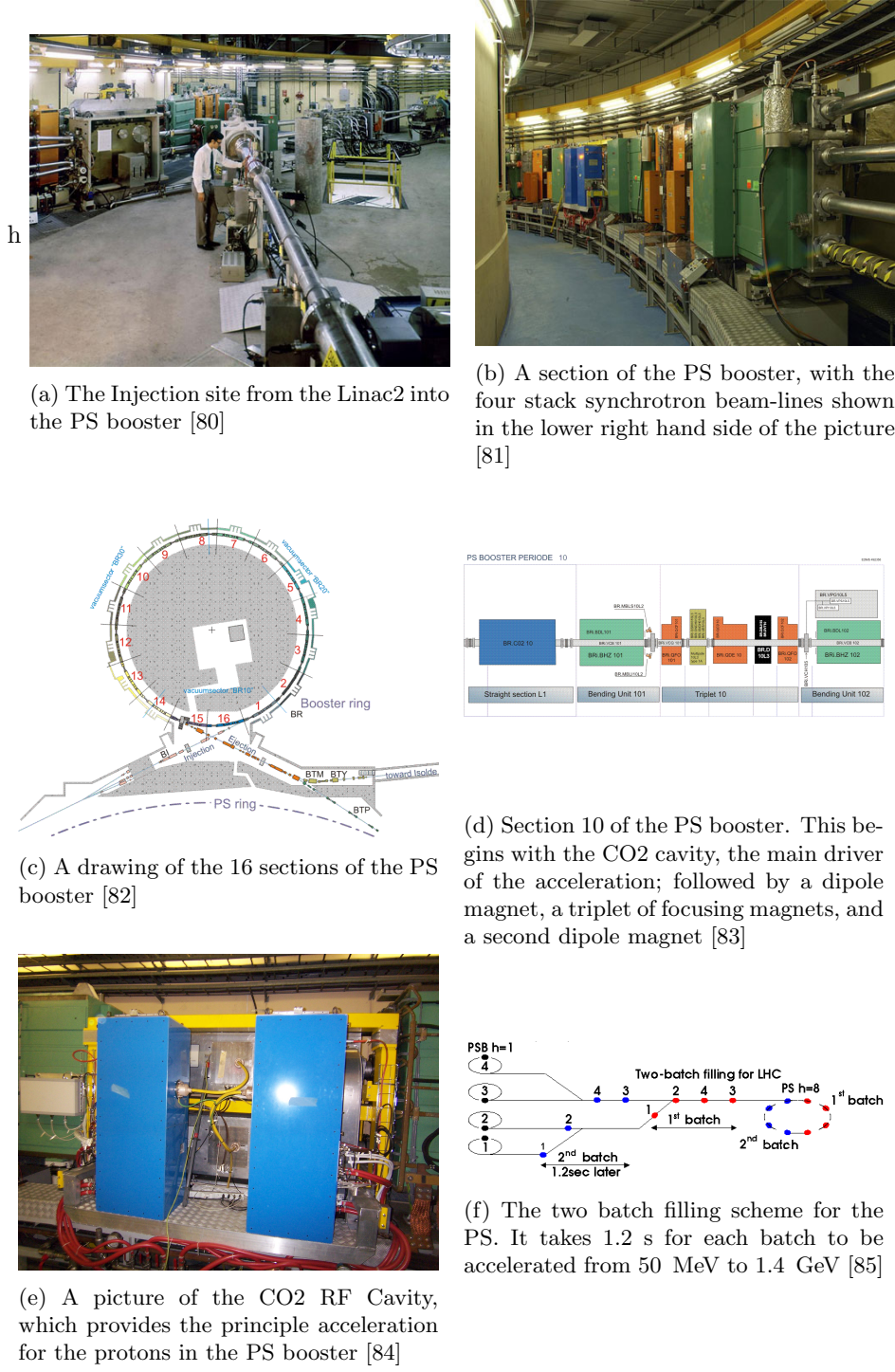


Figure 3.5: Features of the PS booster, the second stage of the LHC injection chain

618 GeV [78]. The complex takes the proton beam from the Linac2 and splits the beam into four  
 619 separate, synchrotrons, stacked on top of one another. Figure 3.5(a) shows the injection site of  
 620 the proton beam from the Linac2 into the PS booster. The right side of figure 3.5(b) shows the  
 621 four synchrotron beam pipes stacked vertically on top one another. The splitting of the beam is  
 622 done in order to reduce the effect of the space charge of the proton beam, which would increase  
 623 the transverse emmitance beyond a tolerable degree. The PS booster uses thirty-two 0.87 T  
 624 dipole magnets to bend the beams, and fourty-eight quadrupoles to focus the beam as it makes  
 625 its way around each of the 50 m diameter rings. Each magnet is composed of a vertical stack of  
 626 four magnets, one for each of the synchrotrons, and share a common yoke, allowing one power  
 627 supply to provide the current to all of them in series [86]. The booster is divided into 16 arcs, as  
 628 shown in figure 3.5(c). Each arc contains a bending dipole, 3 focusing quadrupoles, and a second  
 629 bending dipole, followed by a straight section containing beam diagnostic, injection and ejection  
 630 systems, and in three sections, the Radio-Frequency (RF) cavities, which is the mechanism of  
 631 accelerating the beam [87]. Figure 3.5(d) shows the layout of the tenth arc, which also contains  
 632 one of the RF cavities in the first section.

633 An RF cavity is a specially shaped, hollow conductor, that the beam passes through [88].  
 634 The shape of the cavity determines the resonant frequency and harmonics (integer multiples of  
 635 the fundamental frequency), of the standing electromagnetic fields that result when the cavity  
 636 is driven by an alternating voltage source. The idea is to choose a resonant frequency such  
 637 that the proton will always experience a positive electric field, and thus an acceleration, each  
 638 time it passes through the RF cavity. This means that the revolution frequency of the proton  
 639 must be equal to the fundamental frequency or harmonic of the RF cavity,  $f_{RF} = n \times f_{rev}$ , with  
 640  $n = 1, 2, 3, \dots$ . Eventually, the proton is accelerated up to an equilibrium speed and will enter  
 641 the cavity just as the standing electric field is alternating through it's zero point. If arrives too  
 642 early for this (moving too fast), then it will experience a negative electric force, a deceleration,  
 643 which will eventually bring it back to the equilibrium revolution frequency, where it experiences  
 644 zero net force. A diffuse beam of protons will be bunched into groups of protons through this  
 645 effect as well, as the faster protons in the beams are decelerated, and the slower ones accelerated,  
 646 until they all reach the same equilibrium revolution frequency. Driving the RF cavity with a  
 647 harmonic,  $n$ , of the proton's revolution speed will thus create  $n$  bunches of protons. Each one of  
 648 the potential  $n$  bunch positions is referred to as a bucket. In the case where a proton has to be  
 649 accelerated through a wide range of energies, the frequency of the cavity must also increase to  
 650 maintain synchronization with the proton revolution frequency.

651 Three types of RF cavities are used to accelerate the beam during each revolution. The first  
 652 of the three types of RF cavities is the CO2, with frequency range of 0.6 to 2.0 MHz and is used

653 to drive the  $h = 1$  harmonic of the synchrotron, and is pictured in figure 3.5(e). The second type  
 654 of cavity is the CO4 chamber, with a frequency range of 1.2 to 3.9 MHz, and drives the  $h = 2$   
 655 mode of the synchrotron. This second mode is capable of splitting the beam and creating two  
 656 separate bunch structures. However, for LHC running, only one bunch is used, and is driven  
 657 primarily by the  $h = 1$  mode. The  $h = 2$  mode is supplemental and is used to shape the beam. A  
 658 third type of RF cavity, CO16, has a frequency range of 5 to 16 MHz, and is used to control the  
 659 longitudinal shape of a bunch during acceleration. The beam leaves the PS booster and enters  
 660 the PS in a two-batch filling scheme, taking only 1.2 s to accelerate a second batch of protons  
 661 from 50 MeV to 1.4 GeV. This second batch enters just as the first batch has traveled to the  
 662 opposite side of the PS ring. A schematic of this process is shown in figure 3.5(f). To achieve  
 663 the 25 ns bunch spacing design of the LHC, only 6 bunches of proton beam need to be delivered  
 664 to PS. This is achieved by either using a 4+2 or 3+3 filling scheme, in terms of the number of  
 665 proton bunches delivered from the four possible synchrotrons.

666 The next stage is the Proton Synchrotron (PS), which will boost the protons up to 25  
 667 GeV [78]. The layout is shown in figure 3.6(a). The ring has a circumference of 628 m, and  
 668 uses 100 dipole magnets and 177 higher-order focusing magnets, to steer the beam around the  
 669 ring. Figure 3.6(b) shows a picture of one of the dipole magnets used at the PS. In addition  
 670 to providing acceleration up to 25 GeV, the PS forms the basis of the bunch structure that is  
 671 eventually used in the LHC. The  $h = 7$  harmonic is used to capture the 6 bunches of protons  
 672 delivered from the PS booster, leaving a gap in the place of a seventh bunch. The beam is then  
 673 split into three, by using three different RF cavities tuned to the  $h = 7, 14, 21$  modes of the PS.  
 674 Figure 3.6(c) shows a simulation of a proton bunch being divided into three over the course of  
 675 25 ms. The  $h = 21$  mode is then used to accelerate the protons to from 1.4 to 25 GeV using the  
 676 20 MHz RF cavity. Each bunch is then split twice, using the  $h = 21, 42, 84$  synchrotron modes,  
 677 to create 72 bunches, spaced 25 ns apart, with a 320 ns gap for the 12 unused buckets of the  
 678  $h = 84$  harmonic. This process is simulated in figure 3.6(d), over the course of 125 ms. The 320  
 679 ns gap is created to account for the rise time of the kicker magnet, which ejects the beam out of  
 680 the PS into the SPS. The entire splitting process is summarized in figure 3.6(e). For the case of  
 681 50 ns bunch spacing, the final stage of splitting is not performed, and the  $h = 21, 42$  modes are  
 682 used to split the beam. Finally, in order to fit the bunches into the 200 MHz RF acceleration  
 683 scheme of the SPS, the bunch length must be compressed from 11 ns to 4 ns. This is achieved  
 684 by rotating the beam in the energy vs time phase space by sequential increases in voltage to  
 685 the 40 MHz  $h = 84$  mode, followed by an increase to the 80 MHz  $h = 168$  mode. Figure 3.6(f)  
 686 shows the result of this rotation - a distortion free ellipse with a smaller 4 ns spread, but a larger  
 687 spread in the energy spectrum of the proton beam.

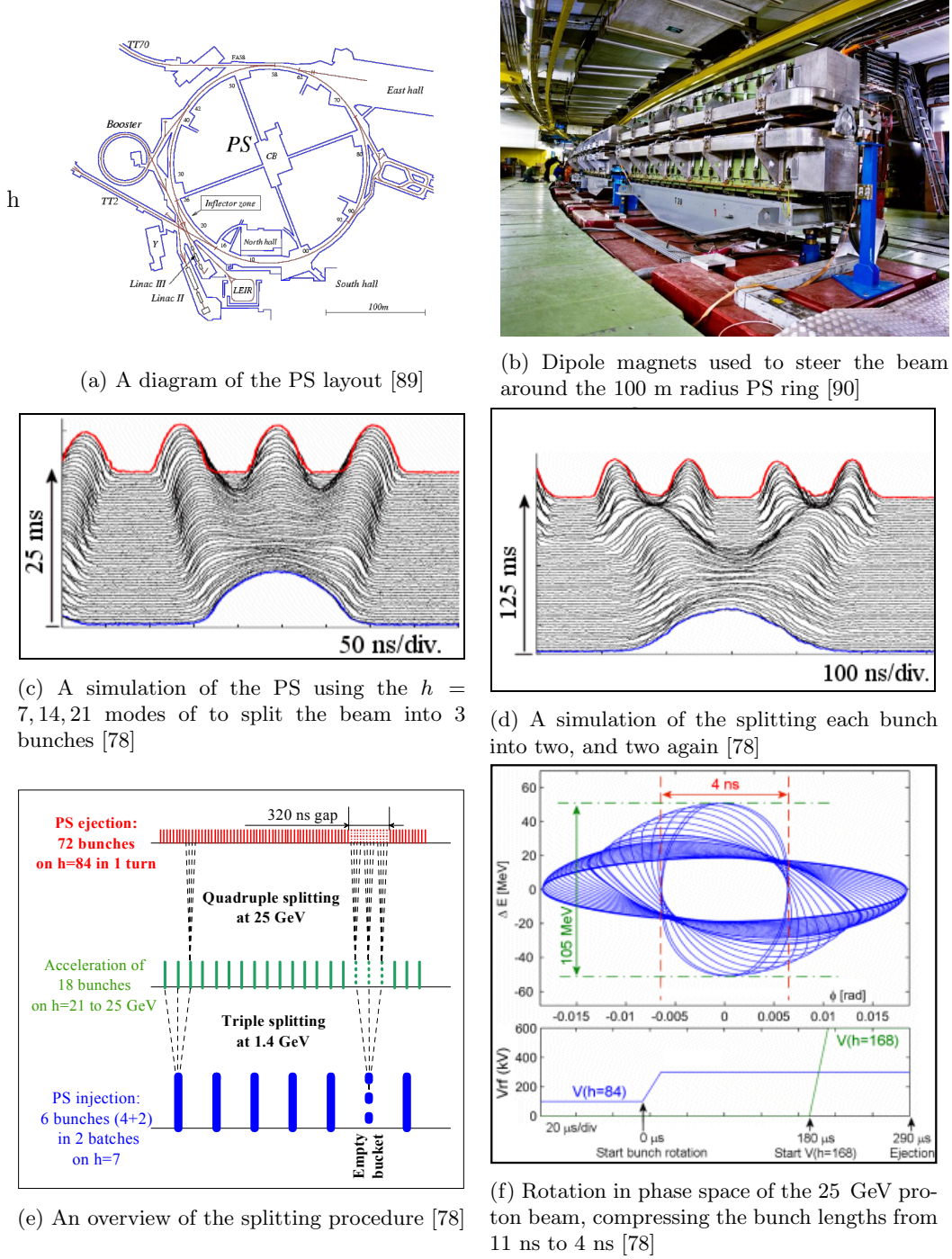


Figure 3.6: Features of the PS, the third stage of the LHC injection chain

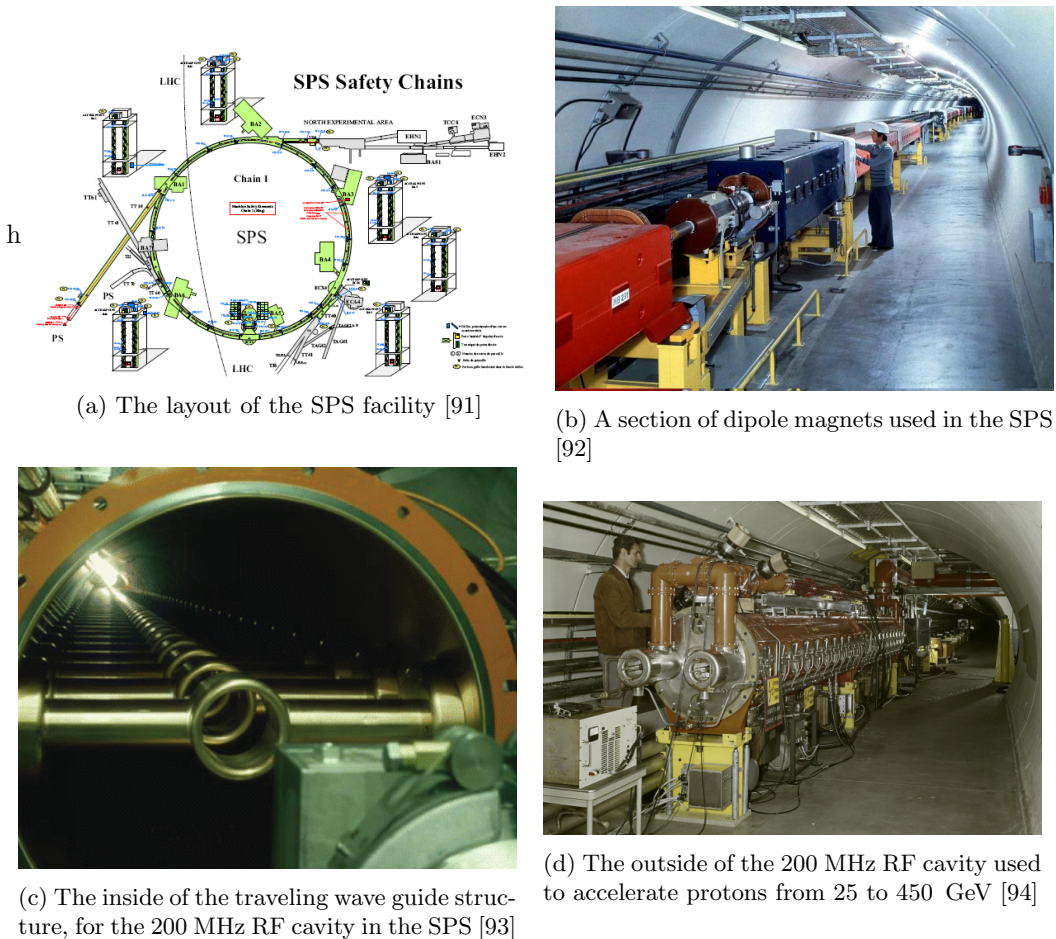


Figure 3.7: Features of the SPS, the fourth and final stage of the LHC injection chain

688 Next, the protons arrive at the Super Proton Synchrotron (SPS), where they will be acceler-  
 689 erated to 450 GeV. The SPS is the last stage of acceleration before the protons are injected  
 690 into the LHC. The layout is show in figure 3.7(a). It has a circumference of 7 km, and steers  
 691 the proton beam with 744 dipole magnets, with 573 higher-order focusing magnets [95]. Figure  
 692 3.7(b) shows one of the dipole magnets in the SPS tunnel. Like all the other synchrotrons in  
 693 the injection chain, the acceleration is provided by RF cavities. A 200 MHz system of RF cavi-  
 694 ties capture and fill the SPS by using 2-4 batches of 72 bunch proton beams from the PS [78].  
 695 Although the relative change in frequency is small, the large degree of acceleration necessitates  
 696 the use of a tunable RF cavity. The 200 MHz system has 2 sections of 4 traveling wave cavities  
 697 in series, and another 2 sections of 5 cavities in series. Figure 3.7(c) shows the inside of this  
 698 structure, which uses drift tubes to accelerate protons in the gaps between tubes, with horizon-  
 699 tally mounted bars, spaced 374 mm [96] apart, determining the periodicity of the resonant RF  
 700 field that builds up inside. The outside of the structure is shown in figure 3.7(d). An additional  
 701 800 MHz system is used to control the transverse emmitance. It is also used to stabilize the  
 702 beam-line and prevent coupled-bunch instabilities [78].

703 Finally, protons are injected into the LHC ring in one clockwise, and another counter-  
 704 clockwise rotating beams. In order to work in the limited space of the existing LEP tunnel,  
 705 the two beams are contained within a single mechanical and cryostat structure, with a dual-bore  
 706 design for each of the beams. Here, each proton beam is accelerated to their final energy of 7  
 707 TeV, moving at 99.9999991% the speed of light, before they meet head on, producing 14 TeV  
 708 center-of-mass collisions.

709 The LHC ring itself is divided into eight octants, with eight straight sections that are located  
 710 in front and behind each of the eight collision points, where the beams are made to cross and  
 711 collide, as shown in figure 3.8. These crossings are known as interaction regions (IRs). Four  
 712 of these points are currently being used by experiments. TOTEM has detectors on either side  
 713 of the CMS experiment at one interaction region, known as point 5 (P5). LHCf has detectors  
 714 on either side of ATLAS at point 1 (P1). MOeDAL has detectors near LHCb at point 8 (P8)  
 715 and the ALICE detector is located at point 2 (P2). The following sections will cover the RF,  
 716 magnet, cryogen, and vacuum technologies used in the LHC ring.

## 717 3.2 LHC Magnets

718 Several types of magnets are used in order to properly circulate and focus the proton beam as  
 719 it makes its way around the 26.7 km long tunnel. A complete list of all types, can be found in  
 720 the technical design report [97], as well as through CERN's outreach web resources [98]. This

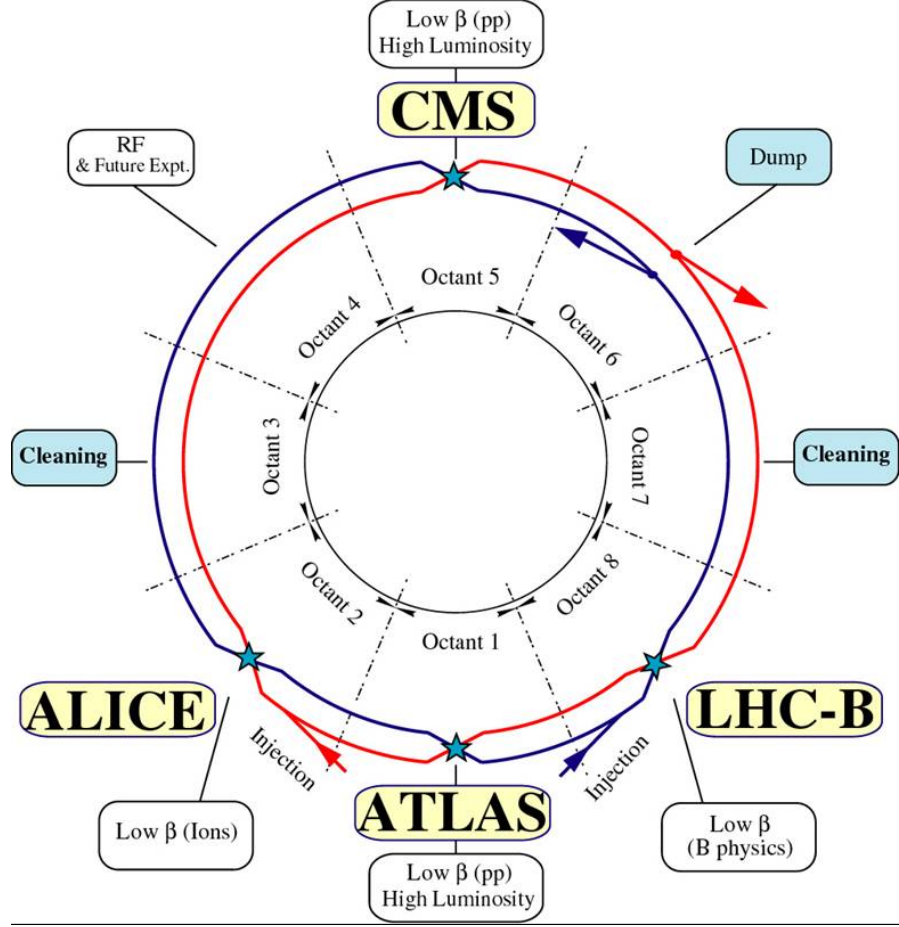


Figure 3.8: The LHC ring is divided into eight octants [8]

721 section will give an overview of the a few of the critical subsystems: the septum and kicker  
 722 magnets used for injection from the SPS, the dipole magnets used for bending the beam around  
 723 the circumference of the ring, and the higher-order-pole magnets that are used for focusing the  
 724 beam.

725 The injection and extraction of proton beams from one synchrotron to another involves  
 726 three types of magnets, septums, kickers, and bumpers. Septum magnets contain a partition,  
 727 or a septum, that provides a boundary between a high magnetic field region and a near-zero  
 728 magnetic field region and are operated in DC or a slow-pulsed mode [99]. In case of injecting  
 729 a beam of protons into a synchrotron, the target beam-pipe of the synchrotron passes through  
 730 the low-field region, so the trajectory is unaffected by the high-field region, which bends the  
 731 injection beam towards the synchrotron aligning it horizontally, with the target beam. The  
 732 kicker magnet, is a fast-pulsed magnet and provides the timing selection in order to make a final  
 733 bend vertical bend into the synchrotron orbit, and into the correct basket of the synchrotron  
 734 bunch train [9]. Finally, bumper magnets make small bends to the beam and align it with the  
 735 injection site. Figure 3.9 shows a schematic for this process, where a transfer line brings protons  
 736 to a septum, which bends the beam to a kicker, which makes the final corrections to match the

## Single-turn injection

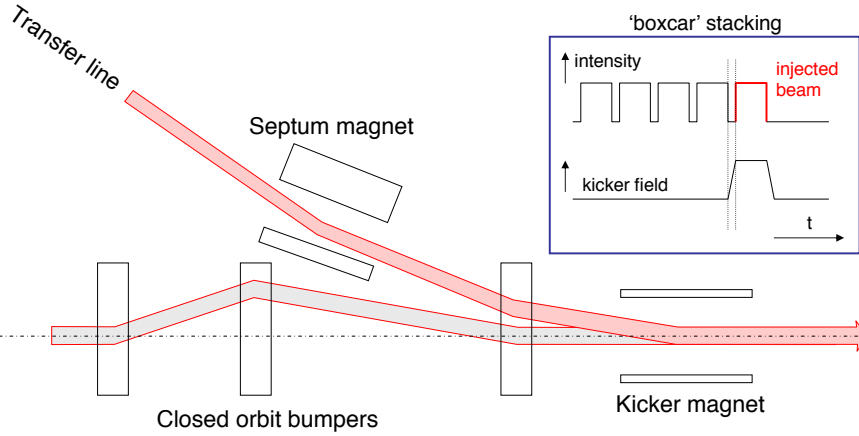


Figure 3.9: The single turn injection scheme. A septum magnet makes the initial alignment. The kicker magnet times the injection and makes the final alignment. Bumper magnets align the LHC beam with the injected beam [9]

737 synchrotron orbit. For extraction, the kicker magnet quickly displaces a portion of the beam,  
 738 which is steered away by the septum, while the original beam passes through its low-field region  
 739 unaffected.

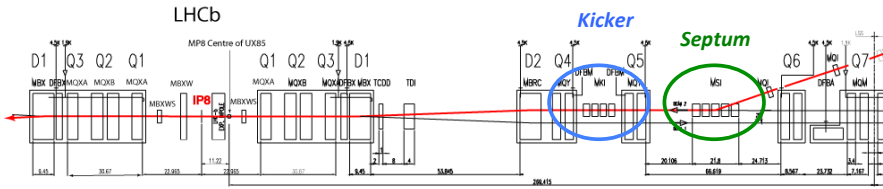


Figure 3.10: Layout of Interaction Region 8, where one proton beam is injected into the LHC ring. A transfer line from the SPS brings a proton in from the right. In green, a septum magnet aligns the beam horizontally with the LHC. In blue, a kicker magnet makes the final vertical alignment into the LHC, and is timed to fill one of the 400 MHz buckets of the RF capture system [8]

740 At the LHC, beam is injected at Interaction Regions (IR) 2 and 8 [8]. Two transfer lines bring  
 741 the beam extracted from the SPS to  $\sim 150$  m of the LHC ring. Five Labertson-type septum  
 742 magnets, of field strength  $\sim 1$  T, are used to deflect each of the transfer line beams 12 mrad  
 743 to align the transfer beam horizontally with the LHC orbit. Then, four  $\sim 0.12$  T MKI kicker  
 744 magnets quickly deflect the beam 0.85 mrad to close the orbit with the LHC ring. Figure 3.10  
 745 shows the layout of the injection point at IR 8. The green circle encloses the septum structure,  
 746 which provides the horizontal alignment, and the blue encloses the kicker structure, which makes  
 747 the final vertical alignment and synchronizes the injection of the beam into the LHC. The rise  
 748 time for the field provided by the kicker magnets in the LHC and SPS determine the final bunch  
 749 structure of the LHC. Figure 3.11 extends figure 3.6(e) showing how the rise times of the kickers  
 750 that inject, or eject beam create gaps in the bunch structure of the LHC. The initial filling of

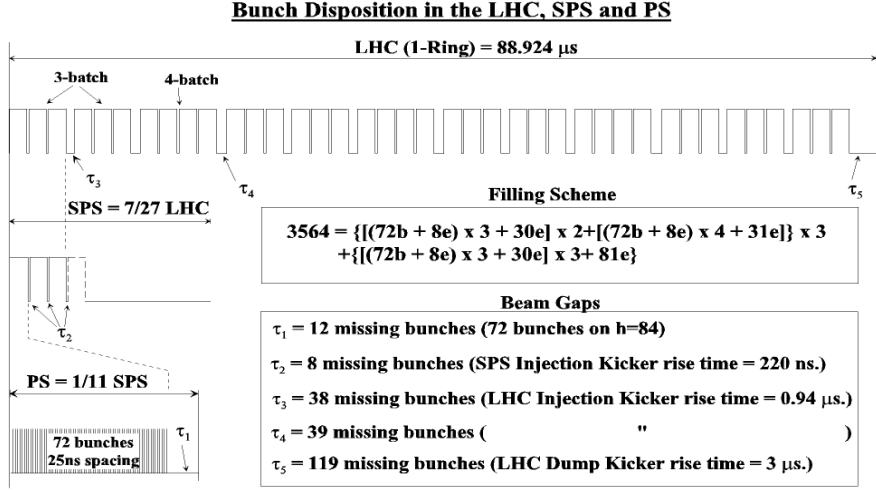


Figure 3.11: The initial filling of 6 batches of protons from the PSB to the PS, leaves 12 empty buckets in the PS bunch structure. The rise time of the SPS magnet creates an additional gap in the SPS bunch structure. Additional gaps emerge due to the rise time of the LHC injection and dumping kicker magnets [8]

751 the PS with 6 batches of protons from the PSB, leaves one initial bucket unused in the PS. After  
 752 the splitting of the beam into the 25 ns bunches, there 12 empty buckets at the of the PS bunch  
 753 train. The SPS is filled with three to four of these trains, leaving an additional 8 25 ns buckets  
 754 unfilled due to the 220 ns rise time of the SPS kicker magnet. These three to four trains are  
 755 then injected into the LHC, where there are 38 or 39 bunch gaps due to the LHC injector 0.94  
 756  $\mu$ s rise time. At the end of a full LHC orbit, 119 buckets are left empty to allow for the rise time  
 757 of the beam dumping kicker magnet, used to remove beam from the LHC.

758 Once the beam is injected, the curved path around the circumference of the LHC is main-  
 759 tained via 1232 superconducting dipole magnets. The superconducting material niobium-titanium,  
 760 NbTi, is cooled to 1.9 K in order to produce the 8.33 T field. Figure 3.12(a) shows a cross-section  
 761 view of one of the LHC dipoles. The dual-bore design of the beam-pipe is enclosed by an iron  
 762 yoke, that serves as the cold mass to maintain the superconducting temperature, and provides  
 763 a 195 mm gap between each beam. A close up picture of the non-magnetic collar and supercon-  
 764 ducting coils are shown in figure 3.12(b). A simulation of the magnet in figure 3.12(c) shows the  
 765 homogenous, vertical magnetic field produced in the center of the coil. Diagram 3.12(d) shows  
 766 an exaggerated view of the 2812 m radius curvature of each dipole. However, since each dipole  
 767 is only  $\sim 14$  m in length, this curvature is hardly noticeable, as shown in a photo of an actual  
 768 dipole magnet in a staging area at CERN, awaiting installation in figure ??(e).

769 Quadrupole, sextupole, octupole, and other multipole magnets are used to focus a single  
 770 beam, as well as squeeze the two beams together. There are 392 quadrupole magnets on the  
 771 LHC ring, each controlling the height and width of the beam. Figure 3.13(a) shows a schematic  
 772 of a dual-bore quadrupole magnet, and figure 3.13(b) shows an actual quadrupole in a staging

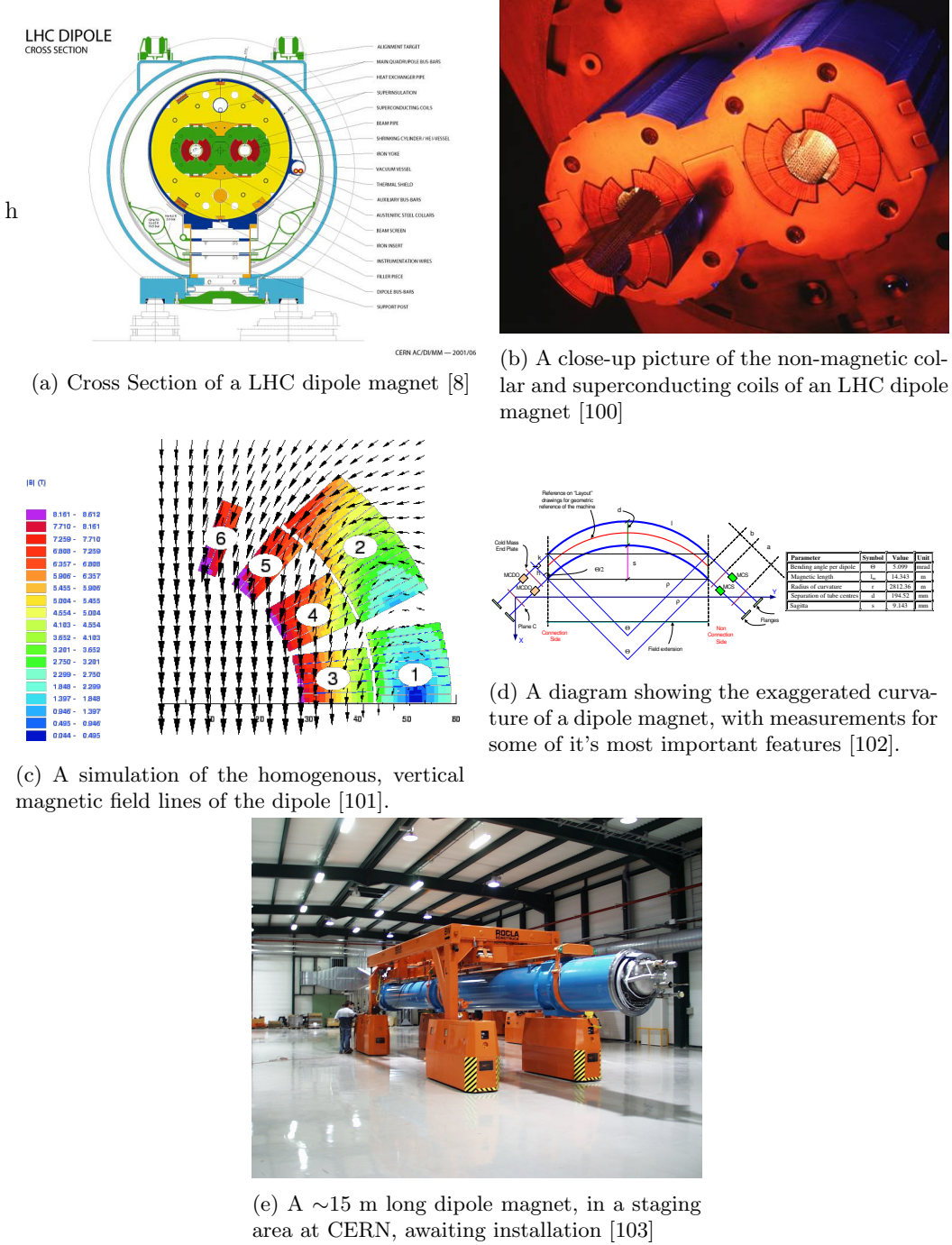


Figure 3.12: Features of the dipole magnets used in the LHC

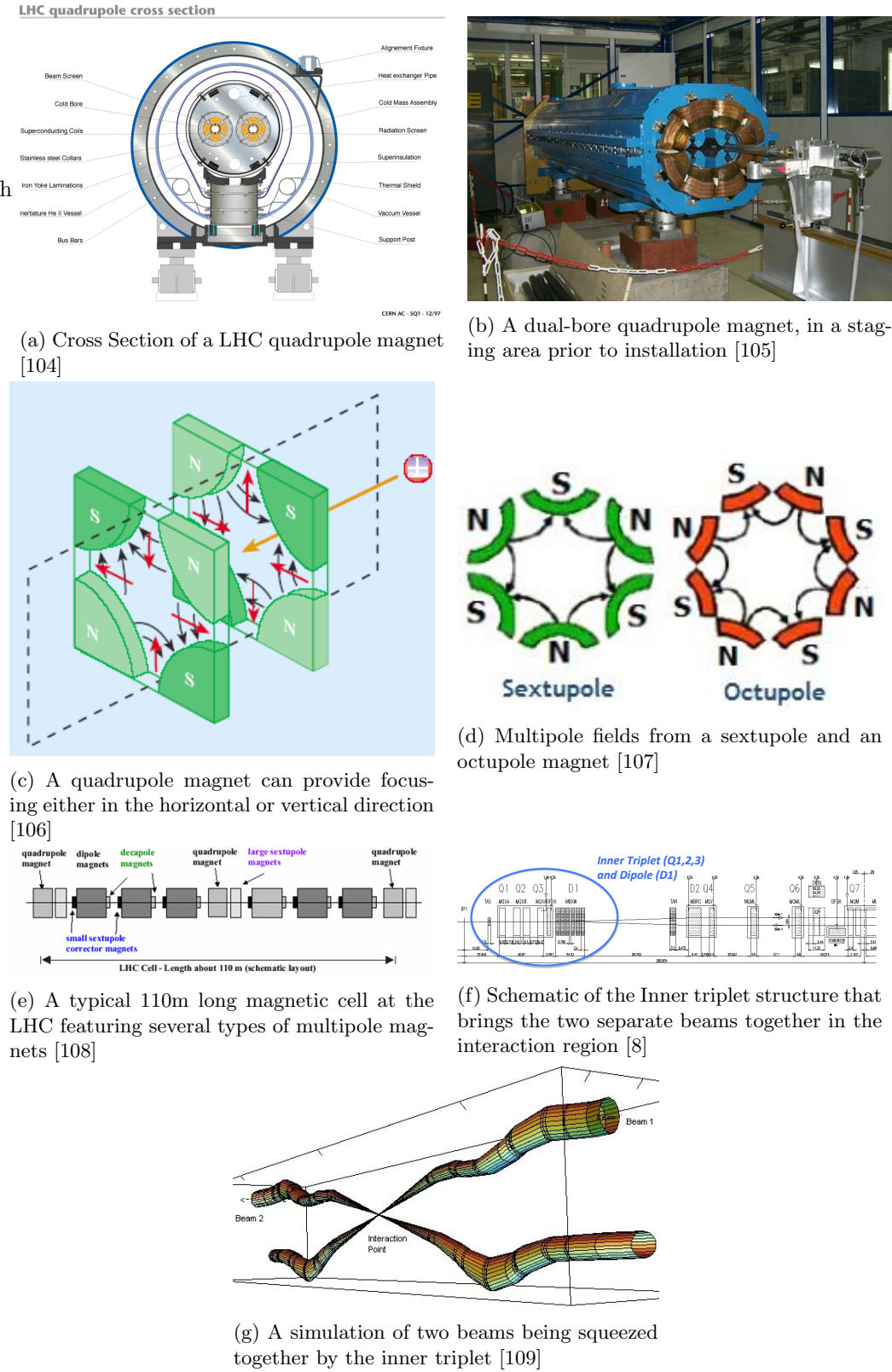


Figure 3.13: Features of the dipole magnets used in the LHC

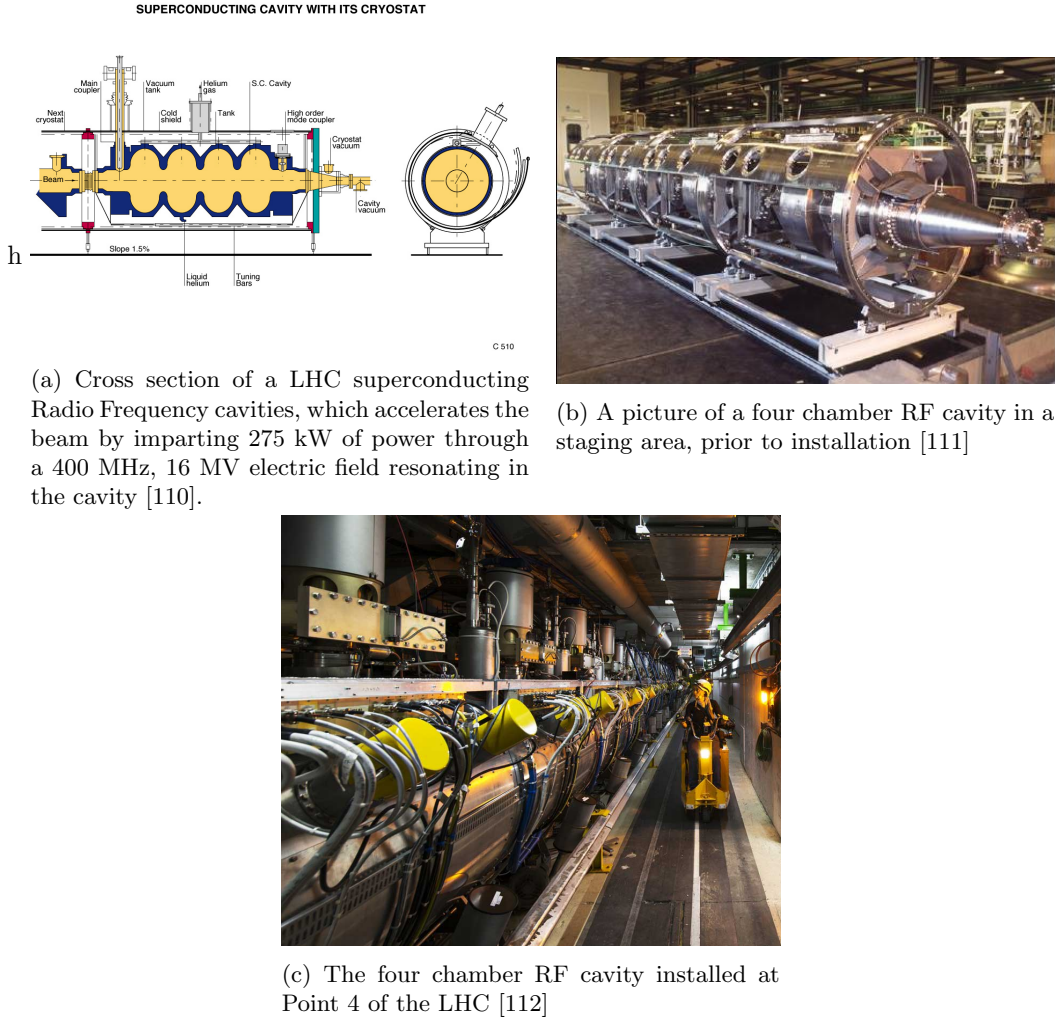


Figure 3.14: Features of the 400 MHz superconducting RF system used in the LHC

773 area before installation. Quadrupole magnets use four sets of coils to create a magnetic field that  
 774 either squeezes the beam horizontally or vertically, as shown in figure 3.13(c). Finer corrections  
 775 to the beam shape are made with the multipole magnets, since they are able to compress the  
 776 beam from more than two axes. Figure 3.13(d) shows the fields lines of a sextupole and octupole  
 777 magnet. A typical cell of magnets, 110 m long, in the LHC optimizes is shown in a diagram in  
 778 figure 3.13(e), where the dipole, quadrupole and higher order magnet work in series to confine  
 779 the protons to the LHC ring. Finally, a set of single bore magnets, known as an inner triplet,  
 780 bring the two beams together into an interaction region. Figure 3.13(f) shows the arrangement  
 781 of magnets that squeeze the beam together, while figure 3.13(g) shows a simulation of the beams  
 782 being brought together to collide in the interaction region.

### 783 3.3 LHC RF Technology

784 The LHC uses a 400 MHz superconducting RF cavity system to capture and accelerate the beam  
 785 from 450 GeV to 7 TeV [8]. Two independent system are used to provide 8 MV of RF voltage  
 786 at injection at 16 MV during equilibrium at 7 TeV and deliver 275 kW of power to each beam.  
 787 This is provided by 16 niobium sputtered cavities, housed in 4.5 K refrigeration units, known as  
 788 cryo-modules, at Point 4 of the LHC octant. The superconducting material covering the inside  
 789 of the cavity has near-zero resistivity, which dissipates much less power and has a much narrower  
 790 resonance width, or Q-factor, than a cavity made from normally conducting material. Figure  
 791 3.14(a) shows a schematic of a four cavity cryo-module. The beam pipe passes through the  
 792 center of each chamber and longitudinal (left to right in the diagram) electric fields accelerate  
 793 the protons each time they circulate the LHC ring. Figure 3.14(b) shows an actual four cavity  
 794 module in a staging area prior to installation. In this picture, the resonance cavities are concealed  
 795 underneath the cylindrical housing of the vacuum tank and cryostat. Figure 3.14(??) is a picture  
 796 of the module installed at Point 4. The thin cylindrical structures extending off the top is the  
 797 LHe intake valve and quench system. The thicker cylindrical structures are the waveguides that  
 798 couple the cavities to the source of the electric field, the klystrons.

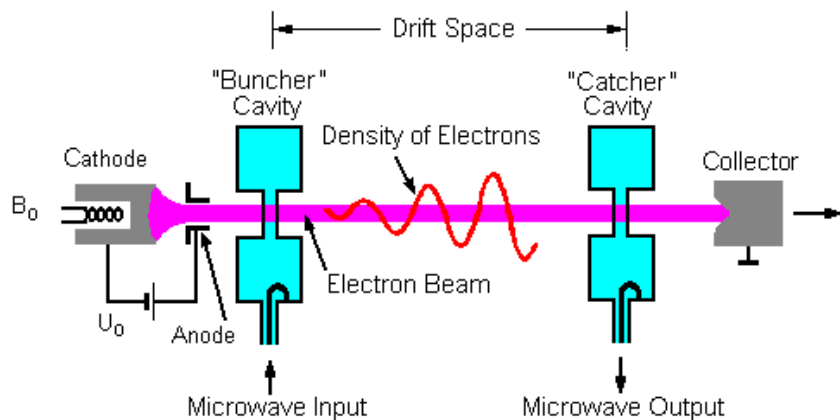


Figure 3.15: A klystron uses a weak RF signal coupled to a resonance cavity to bunch an electron beam, which in turn creates an amplified RF signal as it passes through a second resonance cavity tuned to the same frequency [10].

799 A Klystron is the source of RF power that builds up as a resonance in the cavities that  
 800 accelerate the protons. Figure 3.15 shows a diagram of the basic operating principle. The device  
 801 uses an anode to accelerate the thermionic emission of electrons off of a cathode material into  
 802 one or more bunching cavities tuned to the frequency the device is designed to produce. This  
 803 cavity is driven with a weak RF source, that groups electrons into bunches. Just as discussed for  
 804 protons earlier, when electrons arrive at the entrance of the cavity at just the right time, it will  
 805 experience the zero-point of the oscillation of the resonating electric field. If it arrives early or

late, it is accelerated or decelerated and thus bringing it closer to its neighbors, and increasing the density of the beam. After passing through multiple chambers, the tightly bunched electrons enter a catcher cavity tuned to the same resonance frequency. As the electrons pass through at this resonance frequency, standing electric waves are excited and quickly build up in the catcher cavity. The electron beam is thus used to amplify the original RF signal in the catcher cavity, which is then transported via waveguide to power the RF cavity used to accelerate the proton beam-line.

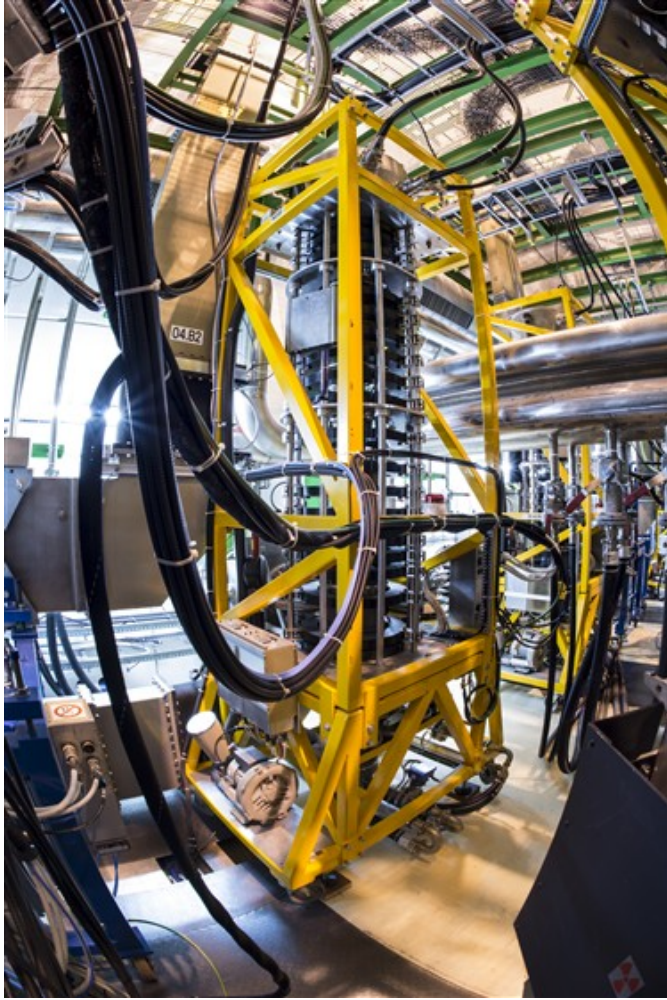


Figure 3.16: One of sixteen 300 kW, 400 MHz klystrons that power the superconducting RF cavities that accelerate the proton beam [11].

At the LHC, 16 400 MHz, 300 kW klystrons, work together to provide 4800 kW of power to the superconducting RF cavities [8]. They are also located at Point 4, in the UX45 service cavern adjacent to the RF cavities, about 6 m below the beam-line. An average of 22 m of waveguide is used to transport the power generated by the klystrons to the RF cavities. Figure 3.16 shows a klystron installed at the LHC, and like most modern klystrons, it also utilizes a multi-bunching chamber design.

## 819 3.4 The LHC Cryogen System

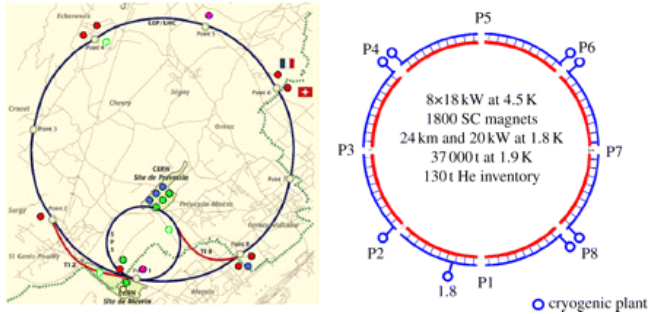


Figure 3.17: Layout of the five cryogenic islands, which are home to the eight facilities that provide liquid helium to the LHC [12]

820 The LHC is the largest cryogenic system in the world [113], as its operating temperature is  
 821 1.8 K, in order to produce the high-magnetic fields needed by the dipole magnets. Additionally,  
 822 the acceleration, mechanism, the RF cavities, are also superconducting, and must be cooled to  
 823 4.5 K. Over 120 tons of Helium are used as the cryogenic medium, since once it is cooled below  
 824 2.17 K, it becomes a superfluid, a phase of matter with a high thermal conductivity, making  
 825 it ideal for refrigeration. Cryogenic and auxiliary equipment are concentrated into 5 cryogenic  
 826 islands at Points 1,2,4,6, and 8 [8]. As shown in figure 3.17, Point 4,6, and 8 house two facilities  
 827 each, making a total of eight, one for each octant of the LHC arc.

828 At each cryogenic plant, He is cooled to 80 K by circulating it through refrigeration equip-  
 829 ment with liquid nitrogen in the heat exchangers[113]. Next, the He is brought to 4.5 K with  
 830 refrigerators recovered from the LEP experiment [114]. The He gas is first compressed and al-  
 831 lowed to expand, where it is cooled by losing energy through mechanical turbo-expanders that  
 832 run at up to 140,000 rpm on helium-gas bearings. Figure 3.18(a). The He is then liquified after  
 833 passing through a vacuum sealed box containing heat exchangers and more turbo-expanders [13].  
 834 The compressor for this system is pictured in figure 3.18(b). Finally, the liquified He is brought  
 835 to 1.8 K with a refrigeration unit that uses a cold compression train to decrease the saturation  
 836 pressure, and thus temperature as well.

837 In the LHC tunnel, a cryogenic distribution line runs parallel to the machine [114]. It consists  
 838 of eight 3.2 km long cryostats, that contain the equipment to supply and recover helium with  
 839 temperatures ranging from 4 K to 75 K. A total of 310 service modules, are used to control the  
 840 system and provide safety mechanisms against pressure buildup and magnet quenching. Figure  
 841 3.19 shows a cross section of the cryogen distribution system in the tunnel.



Figure 3.18: Features of the 4.5 K refrigeration system [13]

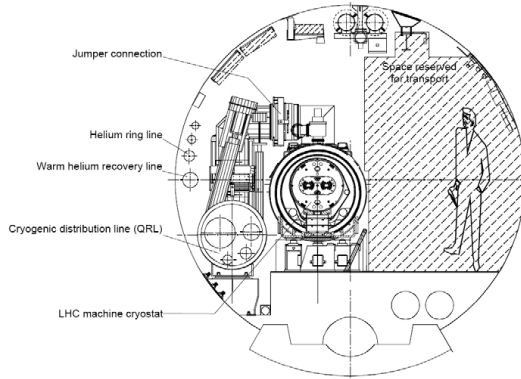


Figure 3.19: Cross section schematic of the cryogenic distribution system in the LHC tunnel [8]

### 3.5 The LHC Vacuum System

The LHC is also the largest operational vacuum system in the world and is capable of achieving pressures lower than outer space [115]. Three different types of vacuum systems are used: one for insulating the helium distribution lines, another for insulating the dipole magnets, and a final ultra-high vacuum system for the beam pipe [8].

The vacuum systems for insulating the helium distribution and dipoles involves some 104 km of piping and over 250,000 welding joints [115]. Pressure here is required to be kept at  $10^{-1}$  mbar, but at cryogenic temperatures, pressures tend to equalize at a much lower level, to  $10^{-6}$  mbar ( $\sim 10^{-9}$  atm) [8].

The most stringent requirements come on the vacuum of the beam-pipe. The beam must minimize the number of interactions it has with any particles outside of the interaction region. A pressure of  $10^{-10}$  to  $10^{-11}$  mbar are maintained in the 54 km of beam-pipe [115]. Weeks of



Figure 3.20: Beam screen for the LHC, with slits to allow for easy pumping of residual gas molecules in the beam-pipe [14].

854 cryogenic pumping, eventually condenses gas trapped in the beam-pipe into a liquid that can be  
855 absorbed by the walls of the beam-pipe. The inside beam-pipe is also coated with a thin layer  
856 of a special substance developed at CERN, a titanium-zirconium-vanadium alloy, which absorbs  
857 residual particles when heated. 780 ion pumps are used to remove the noble gases and methane,  
858 which do not interact with the substance, which acts as its own distributed pumping system.  
859 Room-temperature sections of the beam-pipe are also heated to 300<sup>deg</sup> to be baked-out from the  
860 outside. This is done to periodically remove any material which may have settled and become  
861 trapped. Additionally, the beam-pipe is designed with a racetrack shape, which optimizes the  
862 available aperture while leaving space for the cooling tubes, as shown in figure 3.20. Slits also  
863 allow for gas molecules to be easily pumped out from inside its volume.

864 **Chapter 4**

865 **The Compact Muon Solenoid**

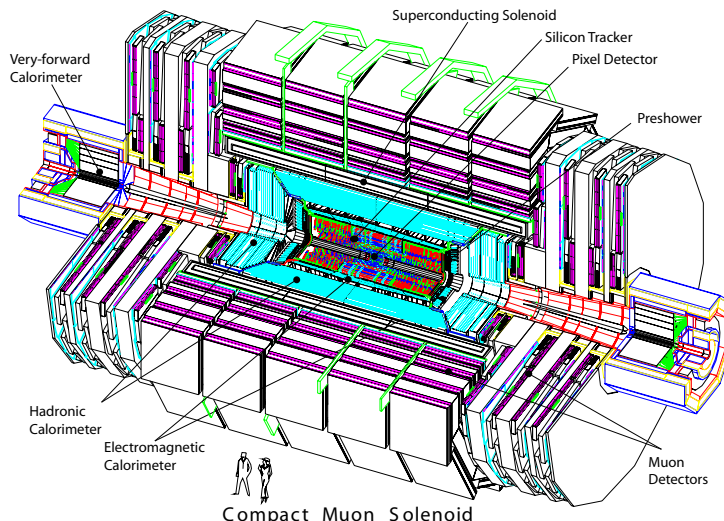


Figure 4.1: A cutaway diagram of the CMS detector. Two humans are present at the bottom of the image to provide scale [15].

866 The Compact Muon Solenoid (CMS) experiment is a general-purpose particle detector ca-  
867 pable of performing a wide range of physics measurements at the TeV energy scale. It provides  
868 hermetic,  $4\pi$ , coverage surrounding the interaction region on Point 5 of the LHC octant, and  
869 is capable of identifying and reconstructing charged and neutral hadrons, photons, electrons,  
870 and muons directly. Tau leptons, are measured indirectly through a careful reconstruction of  
871 its decay products. The hermetic coverage allows the detection of neutrinos by measuring a  
872 momentum imbalance in a given collision. The detector is assembled in five sections and weights  
873 over 14,000 tons. The "Compact" part of the experiment's name comes from its relatively small  
874 volume for a modern particle detector, with length of 28.7 m and a diameter of 15.0 m. Ironically,  
875 this is as tall as most 4-5 story buildings and weights as much as  $\sim$ 7000 cars. Figure 4.1 shows  
876 a cutaway drawing of the CMS detector. Unless otherwise stated, all technical information on

877 the CMS detector is taken from [15].

878 A right-handed coordinate system is used to measure particle positions within the detector.  
 879 The origin is centered at the nominal interaction point with the  $\hat{x}$  direction pointed towards the  
 880 center of the LHC ring, the  $\hat{y}$  direction towards the sky, and the  $\hat{z}$  direction pointed counter-  
 881 clockwise along the LHC ring towards Point 2 and the ALICE experiment. In the much more  
 882 natural polar coordinates,  $\hat{r}$ , points radially outward from the interaction point, the azimuthal  
 883 angle  $\hat{\phi}$  is measured as the angle relative to the  $\hat{x}$  axis, and the polar angle,  $\hat{\theta}$ , is measured as  
 884 the angle relative to the  $\hat{z}$  axis. An important Lorentz invariant position variable is the rapidity,  
 885  $y$ , and its approximation in terms of the polar angle, the pseudorapidity,  $\eta$ :

$$\begin{aligned} y &= \frac{1}{2} \ln \left( \frac{E + p_z c}{E - p_z c} \right) \\ \eta &= -\ln \left( \tan \frac{\theta}{2} \right) \end{aligned} \quad (4.1)$$

886 The psuedorapidity is useful since it is an approximately Lorentz invariant version of polar angle,  
 887 which allows for a more intuitive understanding of the distribution of particles when boosting  
 888 into different measurement reference frames. The component of the momentum transverse to  
 889 the beam-line,  $p_T$  is the most common form of measuring the momentum, and is defined as  
 890  $p_T = |p| \cos \phi$ .

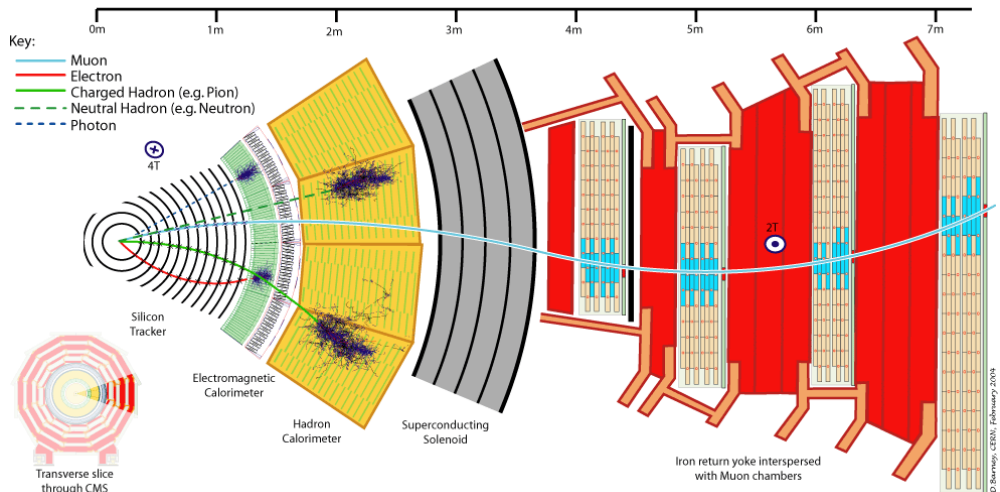


Figure 4.2: A slice of the CMS detector showing how various particles interact and deposit energy. The trajectory of charged particles is measured in the tracker; electrons and photons deposit most of their energy in the ECAL; charged and neutral hadrons deposit most of their energy in the HCAL; the muon chambers measures the trajectory of muons or long-lived charged particles

891 CMS is composed of a system of sub-detectors, each specialized in measuring a certain type or  
 892 characteristic of a particle. They are arranged approximately as concentric cylinders of increasing  
 893 radius, wrapped around the interaction region of the  $pp$  collisions and an analogy is often made

between the layers of sub-detectors being similar to the layers of an onion. The closest sub-detector to the interaction region is the tracker system. It is an all silicon pixel and strip detector, with a high precision position resolution, which is used to identify the trajectory of charged particles close to the primary vertex of a collision. The Electromagnetic Calorimeter (ECAL) is the next layer, and is used to absorb energy of electromagnetically interacting particles. It uses lead-tungstate ( $\text{PbWO}_4$ ) crystals which act as both the absorbing and scintillating medium for energy deposited by charged particles and photons as they pass through this sub-detector. The Hadronic Calorimeter (HCAL) uses brass and steel tiles to absorb energy and induce hadronic interactions, while a plastic scintillator material layered between the absorber tiles samples the energy of hadrons. The tracker, ECAL, and HCAL systems are all contained in the bore of the 3.8 T solenoid from the CMS namesake. This device bends the trajectory of charged particles as they traverse the detector, and the curvature of this bend is used to obtain information on the charge and momentum of the measured particle. The muon system sits outside of the solenoid structure, and uses three types of detection systems: drift tubes (DTs), resistive strip chambers (RPCs) and cathode strip chambers (CSCs), which provide excellent timing and position resolution. The return yoke structure of the magnet also provides the mechanical support for the muon chambers. Figure 4.2 shows a slice of the CMS experiment showing how various particles interact and traverse the different sub-detector regions, as described above.

At center-of-mass energy of  $\sqrt{s} = 14 \text{ TeV}$ , the expected event rate is approximately  $10^9$  events/second. This is too much information to store and analyze, and is mainly dominated by Standard Model QCD multi-jet production, a background for searches for new particles or physics. An online event selection, or trigger, must be used to reduce this rate to a manageable 100 events/second. This is achieved through a combination of hardware, firmware, and software that provides a rough reconstruction of events in near real-time, and makes a decision about whether it meets a minimum set of criteria to be used in an analysis.

## 919 4.1 The Tracker

920 The innermost sub-detector is an all silicon pixel and strip tracker designed to provide precise  
 921 and efficient measurement of the trajectories of charged particles and reconstruction secondary  
 922 vertices necessary for identification of  $b$ -jets and  $\tau$  leptons.

923 At peak LHC design luminosity of  $10^{34} \text{ cm}^{-2} \text{ s}^{-1}$ , and bunch spacing of 25 ns, there will be  
 924  $\sim 1000$  particles from 20 overlapping  $pp$  collisions for each bunch crossing. This corresponds to a  
 925 hit rate density of  $1 \text{ MHz/mm}^2$  at a radius of 4 cm,  $60 \text{ kHz/mm}^2$  at 22 cm, and  $3 \text{ kHz/mm}^2$  at  
 926 115 cm from the beam line. This large particle flux will also cause intense radiation damage to

detector components. These conditions necessitate the use radiation-hard silicon, with a high-granularity to create a low occupancy for each detector element, which are read out by fast electronics. Additional mitigation of the effects of radiation damage is taken by cooling and operating the entire detector to  $-10^\circ$  C in order to maintain a signal to noise ratio of 10:1 for the sensors. After 10 years of running, it is anticipated that this will need to decrease to  $-27^\circ$  in order to compensate for the accumulated damage.

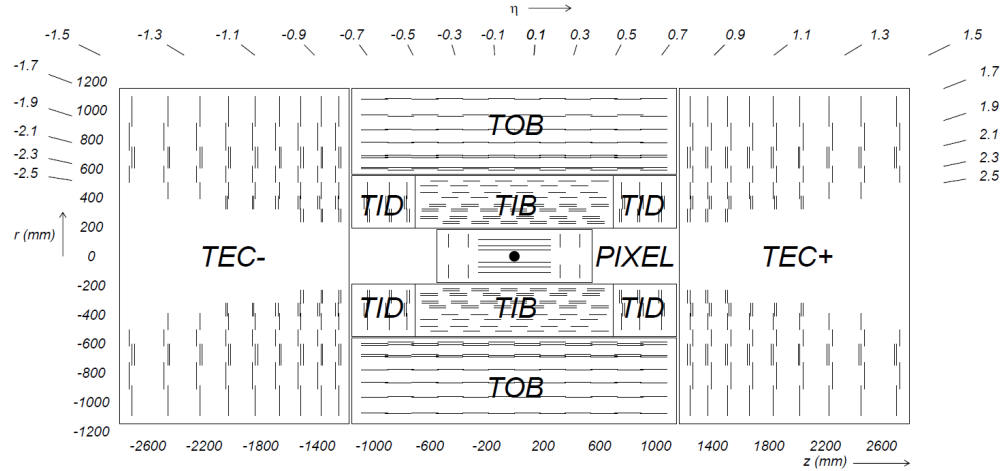


Figure 4.3: A side view of the tracker. The pixel detector is the innermost sub-system, with three concentric rings of detectors in the barrel, and two in the endcap. The tracker inner barrel (TIB) is a silicon strip detector, with four concentric rings. The tracker inner disks (TID) are three layers deep. The tracker outer barrel (TOB) is six concentric rings and the tracker end caps (TEC) are nine layers deep.

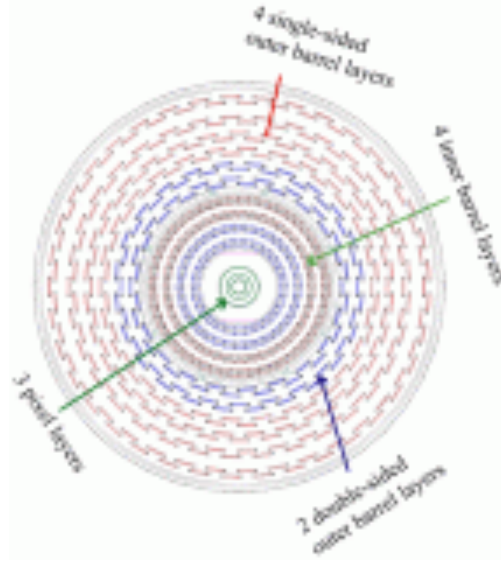


Figure 4.4: A head-on view of the beam-line and barrel components of the tracker.

The tracker has a cylindrical shape that surrounds the interaction region, with a length of 5.8 m and a diameter of 2.5 m. The large particle flux close to the beam-line requires the use of a pixel detector sub-system in the innermost region, from radius 4.4 cm to 10.2 cm from the

beam-line. The particle flux drops off sufficiently at larger radii to use silicon strip detectors, arranged into four different sub-systems: the tracker inner barrel (TIB), tracker inner disks (TID), tracker outer barrel (TOB) and tracker end caps (TEC), which extend to a radius of 1.2 m from the beam-line. Figure 4.3 shows a side view of the tracker layout and figure 4.4 shows a view down the beam-line of the barrel sections. The tracker has a total acceptance of  $|\eta| < 2.5$ .

There are competing factors for the radial length of the tracker. More layers allow for more samples of a particle's trajectory, giving a higher spatial precision, but more material means photons and hadrons are more likely to decay, and create a shower of particles that would better measured through the absorption of energy via calorimeters. The depth of the tracker varies from 0.4 to 1.8 radiation lengths, resulting in small degradation of the ECAL performance, since approximately half the photons will be converted to  $e^+e^-$  pairs.

#### 4.1.1 The Silicon Pixel Detector

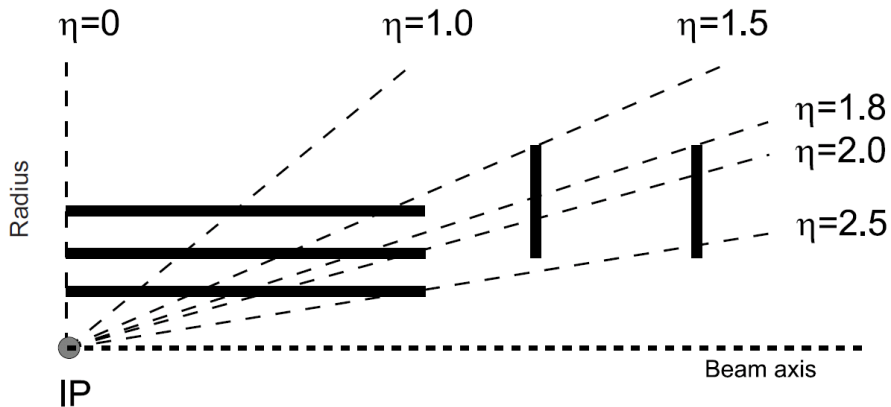


Figure 4.5: The three barrel and two disk layers of the silicon pixel tracker provide coverage of  $|\eta| < 2.5$

The pixel detector consists of 66 million  $100 \times 150 \mu\text{m}$  pixels, arranged in three concentric cylindrical layers of radius of 4.4, 7.3, and 10.2 cm from the beam line and two disc layers on either side of the barrel detectors. Figure 4.5 shows the eta coverage of the detector out to  $|\eta| < 2.5$ .

The sensor technology uses a  $n$ -on- $n$  concept, where a high-dose  $n$ -implant is introduced onto a  $n$ -substrate with large resistance. A  $p - n$  junction is made by the placement of a  $p$ -type semiconductor on the back side of the substrate. When a charged particle passes through the face of the substrate, between the  $p - n$  junction, it liberates electrons from the silicon atoms, creating electron-hole pairs. The  $p$ -side has a voltage bias of 150 V in the barrel, and 300 V in the disks, that sweeps the pair apart, creating a current. Pixels are isolated from one another using a moderated  $p$ -spray in the barrel region, and open  $p$ -stops in the disks in order to create

an additional  $p-n$  structure that acts like a diode to limit current flow between pixels. The 3.7 T magnetic field of the CMS solenoid also induces a Lorentz drift of the current in the  $\hat{\phi}$  direction. This results in the current produced in one pixel being shared among multiple neighboring pixels. The charge collected by each of the multiple pixels are read-out, using an interpolation between pixels, resulting in a  $15\text{-}20 \mu\text{m}$  spatial resolution on the trajectory of the charged particle - much smaller than the size of an individual pixel. In order to induce this effect in the disks (where the pixels are orientated perpendicular to the barrel), the pixels are angled  $20^\circ$  in the  $\hat{y}$  direction.

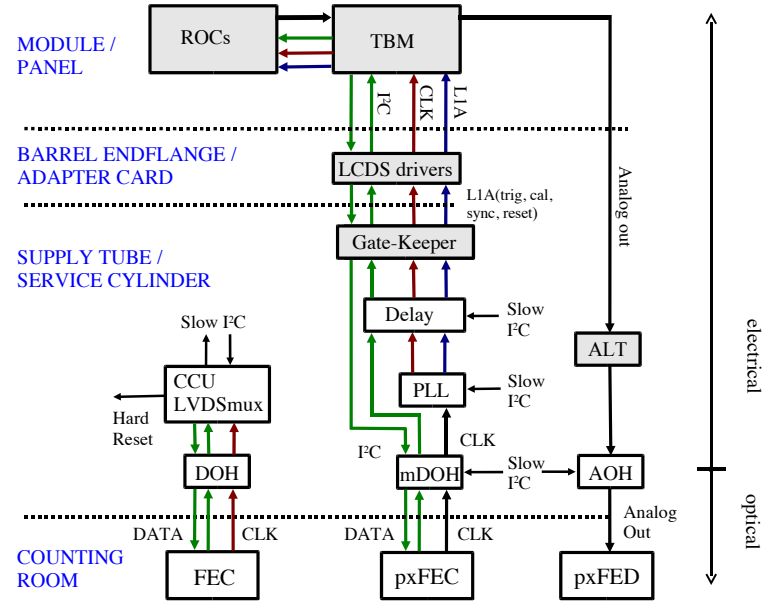


Figure 4.6: The readout electronics chain for the pixel detector

The current created by the charged particle is collected by a readout chip (ROC) that is soldered with a bump bond type connection to the pixel. The ROC is a custom ASIC chip, that processes the signals for a grid of  $52 \times 80$  pixels. It provides amplification, buffering, and zero suppression (threshold) of the charge from each pixel. Depending on the layer, 8-16 ROCs in the barrel, and 21-24 ROCs in the disks are connected and read-out by a single token bit manager (TBM) chip. This chip communicates information from the sensors to the trigger system, which is used to determine whether a given event is stored as data for analysis later. The pixel front end controller (pxFEC) interfaces with the ROC and TBM and provides central clocking and communicates to the CMS data acquisition system. The pixel front end digitizer (pxFED) converts the analog signals from the ROC and TBMs. A total of 40 pxFED (32 in the barrel and 8 in the disks) modules are used to read-out the entire pixel detector, and figure 4.6 shows a schematic of the pixel read-out chain.

The resolution of the pixel detector was measured in 2012 with  $\sqrt{s} = 8 \text{ TeV}$  pp collision. The

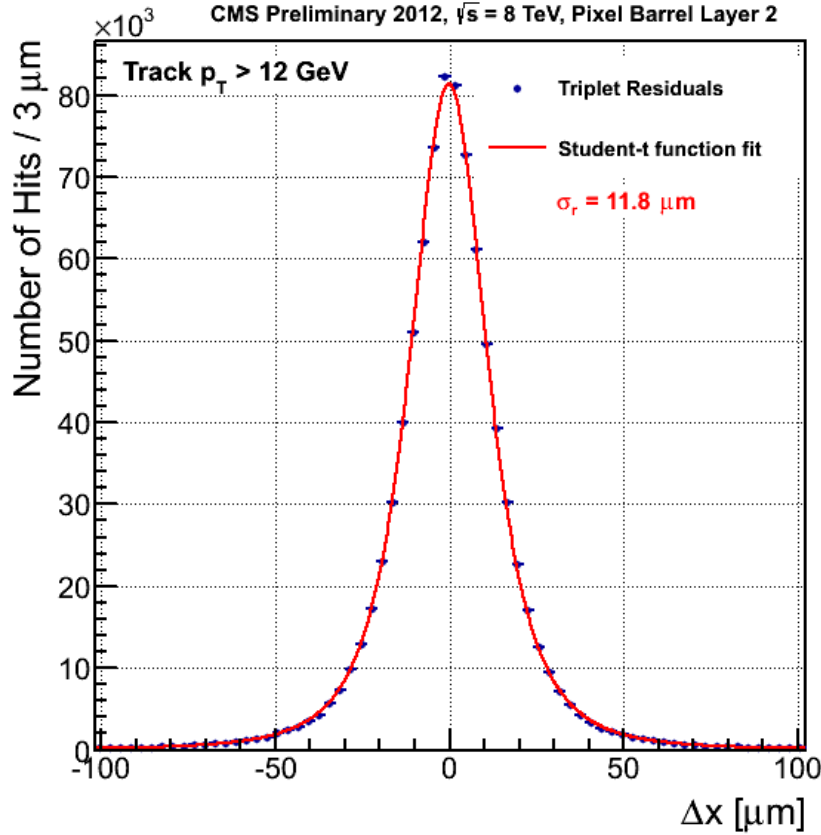


Figure 4.7: In 2012  $pp$  collisions at  $\sqrt{s} = 8$  TeV, the pixel detector performed with a resolution of  $11.8 \mu\text{m}$ . The above is a plot of the residual difference between a pixel and the results of a fit to a particle track.

979 residual distance between the hit position recorded by a pixel, and an interpolated track that  
 980 uses that hit is plotted and fit with a student-t function in figure 4.7. For tracks with  $p_T > 12$   
 981 GeV, the pixel detector was found to have a spatial resolution of  $11.8 \mu\text{m}$ .

#### 982 4.1.2 The Silicon Strip Detector

983 As shown in figure 4.3, the silicon strip tracking system has four components: the tracker inner  
 984 barrel (TIB), tracker inner disks (TID), tracker outer barrel (TOB) and tracker end caps (TEC).  
 985 A total of 15,148 detector modules are distributed among these systems, each with either one  
 986  $320 \mu\text{m}$  thick sensor, or two  $500 \mu\text{m}$  thick sensors, making 24,244 sensors with an active area of  
 987  $198 \text{ m}^2$  of silicon. A module with two sensors is shown in figure 4.8. Each sensor has either 512  
 988 or 768 strips since they are read out by two multiplexed 128-channel front end chips, making it  
 989 possible to only read out sensors in groups of 256. Each strip has a pitch that varies between 80  
 990 and  $200 \mu\text{m}$  and lengths that vary between 10 and 25 cm. All in all, 9.3 million strips are used  
 991 in the silicon tracker.

992 The TIB and TID provide radial coverage from 20 to 55 cm. The TIB has four barrel layers,

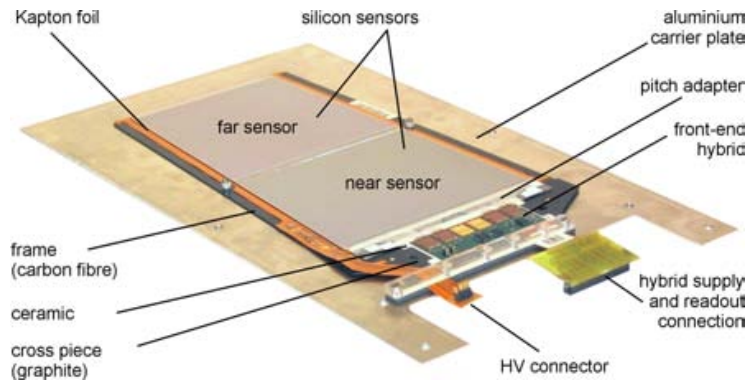


Figure 4.8: A silicon strip module, with two  $500 \mu\text{m}$  thick sensors.

with  $80 \mu\text{m}$  pitch strips on the first two layers, and  $120 \mu\text{m}$  strips on the outer two, giving a single point resolution of  $23$  and  $35 \mu\text{m}$  respectively. The strip pitch varies between  $100$  and  $141 \mu\text{m}$  in the three discs of the TID. The TOB surrounds the TIB/TID and is composed of six barrel layers that extend the tracker radius to  $116 \text{ cm}$ . It is composed of  $500 \mu\text{m}$  thick strip sensors, with pitches of  $183 \mu\text{m}$  in the first four layers and  $122 \mu\text{m}$  in the outer two layers. It provides  $6$  measurement points of the particle trajectory with a single point resolution of  $53$  ( $35 \mu\text{m}$ ) in the first four (last two) layers. Each TEC is made of  $9$  discs, each with  $7$  rings of strip detectors. The inner four rings of each disk use the single,  $320 \mu\text{m}$  thick strip modules, while the outer three rings use the double,  $520 \mu\text{m}$  thick strip modules. The average pitch varies between  $97$  to  $184 \mu\text{m}$  in each of the rings. In the first two layers of the TIB, the first two rings of the TID, the first two layers of the TOB, and rings  $1$ ,  $2$ , and  $5$  in each disk of the TEC contain modules mounted back-to-back, with an angle of  $100 \text{ mrad}$  between them to provide a two-dimensional measurement of a particle's trajectory.

Each of the strips is a single sided  $p$ -on- $n$  type silicon sensor manufactured on  $6$  inch wafers, with a base material of  $n$  doped silicon. The front side of the wafer is implanted with a  $p^+$  type semiconductor. A uniform  $n^+$  implantation on the back forms the ohmic contact to  $500 \text{ V}$ . This forms a  $pn$  junction and when a charged particle passes through the face of the wafer, atoms in the junction are ionized and the  $500 \text{ V}$  potential difference creates a current out of the resulting electron/hole pairs. This current is collected and processed through the read-out system.

A custom integrated circuit, the APV25, is used to amplify, shape, and buffer the signals produced from the silicon strips. It has  $128$  read-out channels, and samples the detector signals at the  $40 \text{ MHz}$ , suitable for the  $25 \text{ ns}$  collisions. It is able to store data for up to  $4 \mu\text{s}$  to account

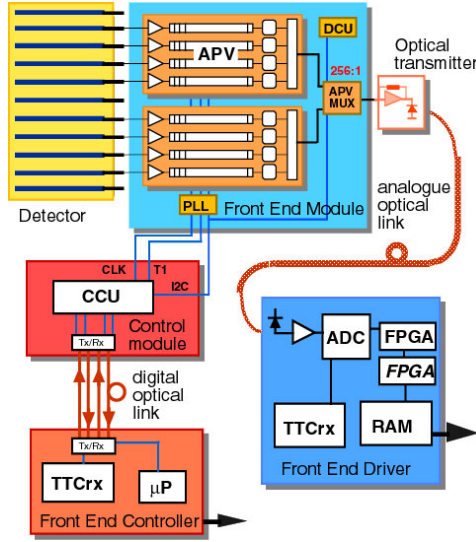


Figure 4.9: Schematic of the readout sequence of the silicon strip detector.

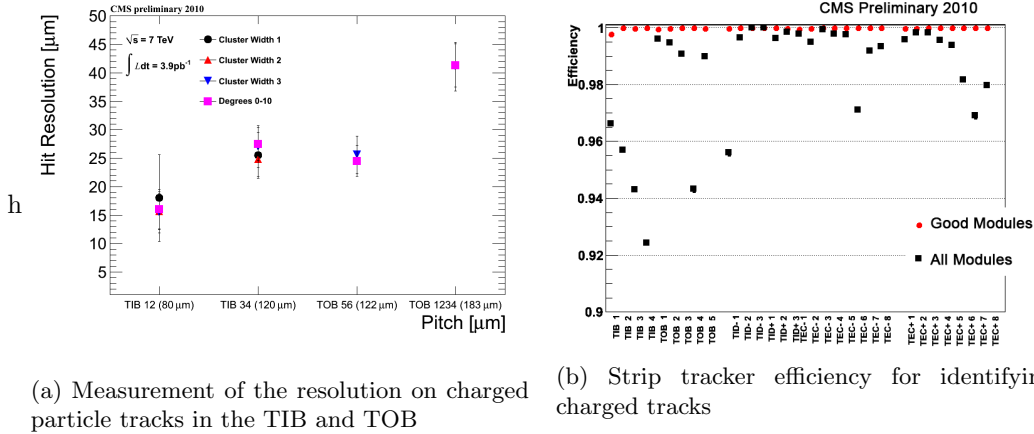


Figure 4.10: Measurements of the performance of the silicon strip track using  $pp$  collisions from 2011 at  $\sqrt{s} = 7 \text{ TeV}$

for trigger latency. Two APV25 chips are linked with fiber optics to the Front End Driver (FED) system. Each FED receives data from 94 optical fibers, and digitizes them in parallel. The Front End Controller (FEC) transmits clock, trigger, and control data to the APV25s. The entire readout chain is shown in figure 4.9.

In 2011, the strip efficiency and resolution were measured from data in center-of-mass energy,  $\sqrt{s} = 7 \text{ TeV}$   $pp$  collisions. Figure 4.10(a) shows the resolution varying between  $15\text{--}40 \mu\text{m}$  for the TIB and TOB detectors. Figure 4.10(b) shows the efficiency for reconstructing tracks with the strip tracker, which is well above 99% when only considering operational modules.

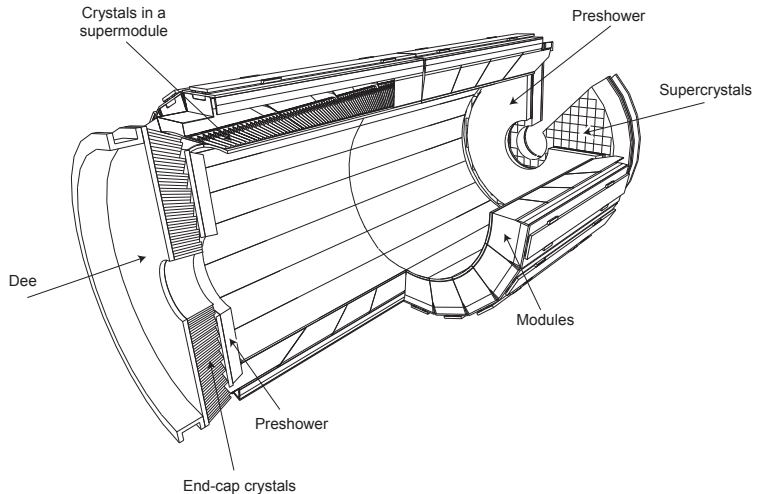


Figure 4.11: Layout of the ECAL sub-detector

## 1023 4.2 The Electromagnetic Calorimeter

1024 The Electromagnetic Calorimeter (ECAL) surrounds the inner tracker with 61,200 high density  
 1025 lead tungstate ( $\text{PbWO}_4$ ) crystals in the central barrel section, and 7,324 crystals in each of  
 1026 the two endcaps. The crystals have a fast response, provide fine granularity, and are radiation  
 1027 resistant, making them ideal for the LHC environment and the physics goal of observing the  
 1028 Standard Model Higgs boson decay to two high energy photons. The primary background for  
 1029 this process comes from neutral pions decaying to two photons, which is especially difficult when  
 1030 the photons are close together and can potentially be reconstructed as a single high-energy  
 1031 photon. This occurs most frequently in the endcaps, so an additional detector, the preshower,  
 1032 provides additional spatial resolution with silicon microstrip detectors, similar to those in the  
 1033 tracker. Figure 4.11 shows the layout of the ECAL.

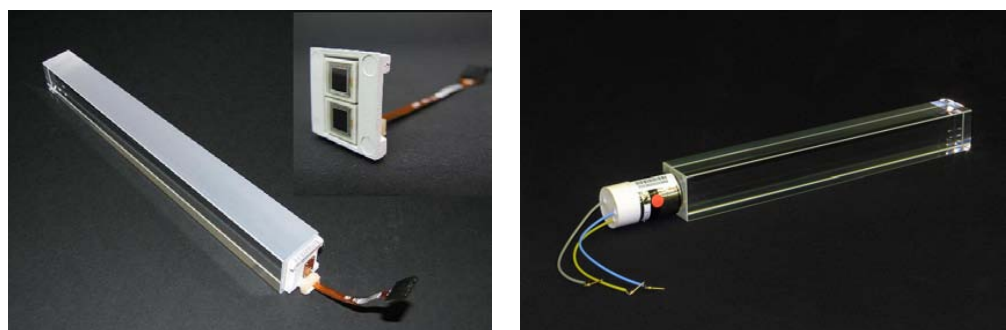


Figure 4.12: Typical Lead Tungstate crystal, with APD attached to the rear face in the left frame, and a VPT attached in the right frame.

1034 Lead tungstate is an ideal material for electromagnetic calorimetry. Figure 4.12 shows a  
 1035 typical crystal, with photomultipliers attached to the rear faces, which will be discussed later.

1036 The material has a high density,  $8.28 \text{ g/cm}^3$ , giving it a large electromagnetic cross-section,  
 1037 making it much more likely for a particle traversing the crystal to interact with one of the atoms  
 1038 in its structure. When a particle interacts with the crystal, it does so by depositing energy into  
 1039 its atoms, which excite the electrons that are bound to it. The atoms then relax by emitting  
 1040 photons, in a process known as scintillation and the  $\text{PbWO}_4$  crystals release 80% of their light  
 1041 in the 25 ns LHC bunch crossing time. This light is collected by photomultipliers attached to  
 1042 the rear face of the crystal and converted into an electrical signal. Read-out electronics amplify,  
 1043 digitize, and buffer the signal until it can be stored as data or discarded.

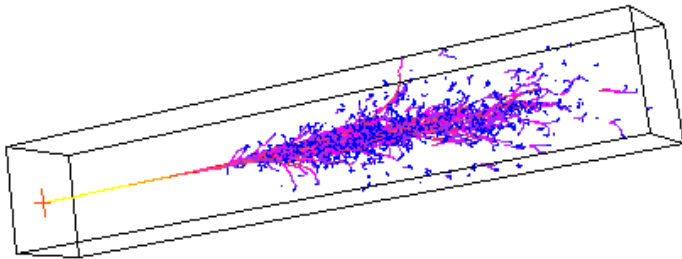


Figure 4.13: A simulation of the evolution of a electromagnetic shower being initiated by an electron entering the center of the front face.

1044 As a charged particle or photon begins to deposit energy, it begins a decay chain into many  
 1045 lower energy photons and electrons, known as an electromagnetic shower. Electrons, being  
 1046 bent by the CMS magnetic field, and multiple scattering off of the  $\text{PbWO}_4$  crystals, create  
 1047 bremsstrahlung photon radiation. Since the intensity of bremsstrahlung is inversely proportional  
 1048 to the mass of the particle squared, particles heavier than electrons such as muons and hadrons  
 1049 do not leave a large signature in the ECAL. Photons convert to  $e^+e^-$  pairs, which in turn create  
 1050 additional bremsstrahlung. The crystals have a short radiation length,  $X_0=0.89\text{cm}$ , which is  
 1051 the distance it takes an electron to deposit  $1/e$  of its energy through bremsstrahlung, and  $7/9$   
 1052 of the mean free path of a high energy photon before it converts to an  $e^+e^-$  pair. A corollary  
 1053 of the crystal's short radiation length is its small Moliere radius,  $2.2\text{cm}$ , which is the radius of  
 1054 a cylinder that encloses 90% of the electromagnetic shower's energy deposition. A typical  
 1055 crystal has a front face that is  $22\times 22 \text{ mm}^2$ , a rear face of  $26\times 26 \text{ mm}^2$ , and a length of  $230 \text{ mm}$ ,  
 1056 or  $25.8 X_0$  radiation lengths. This means that a relatively small grid of crystals can be used to  
 1057 fully collect the energy deposited by a high energy electron or photon. As previously mentioned,  
 1058 heavier charged particles will not bremsstrahlung as much as electrons, and will travel through  
 1059 the entire ECAL, depositing only a moderate fraction of their energy in the crystals. Figure 4.13  
 1060 shows a simulation of an electromagnetic shower produced by an electron entering the front face  
 1061 of a crystal.

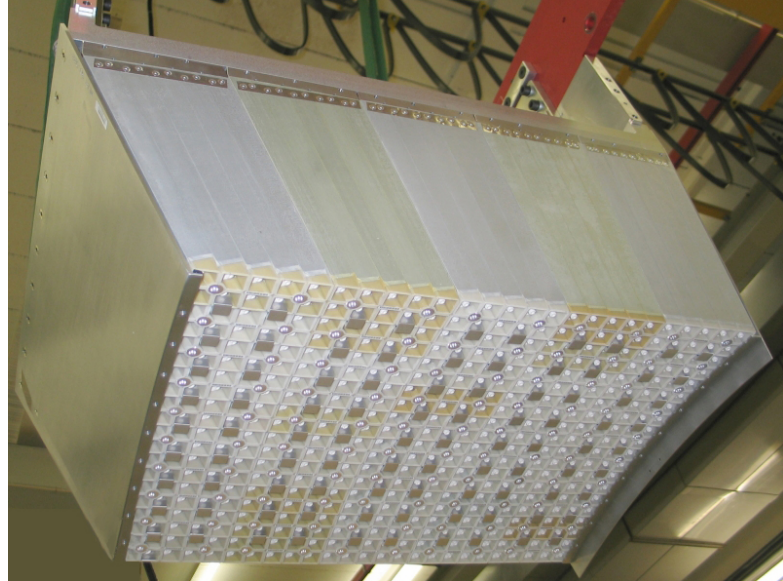


Figure 4.14: A module of 500 crystals (25 crystals wide by 20 crystal tall).

1062        The barrel of ECAL (EB) covers a psuedorapidity range of  $|\eta| < 1.479$  with 61,200 crystals at  
 1063        a radius 1.29 m from the beam-line. The crystals are positioned in a quasi-projective geometry,  
 1064        such that their axes make a  $3^\circ$  angle with respect to the vector pointing to the nominal interaction  
 1065        point. This ensures that particles will not pass through the cracks and spaces between crystals,  
 1066        and are forced to interact with a portion of the ECAL. Crystals are assembled in groups of  
 1067        400 or 500 into modules, as shown in figure 4.14 . Four of these modules are assembled into a  
 1068        supermodule contain 1700 crystals, and 36 supermodules make up the barrel region.

1069        The crystals in the EB are read out by Avalanche Photo-Diode (APD) photomultipliers,  
 1070        shown in the left frame of figure 4.12. The APDs were manufactured by Hamamatsu and are a  
 1071        bulk *n*-type silicon material, with a *p*-type implanted on its surface to form a *pn*-junction. The  
 1072        operation principle is similar to that of tracker. When scintillation light from the lead tungstate  
 1073        crystals enters the face of the APD, it creates electron-hole pairs in the intrinsic region between  
 1074        the *p* implantation and the *n* bulk material. The APD is biased with 45 V, which creates a  
 1075        current from the electron-hole pairs and is the signal that a particle has created scintillation in  
 1076        the crystal. The APD provides a gain of 50 and has a quantum efficiency of 75%. Both the  
 1077        APDs and the PbWO<sub>4</sub> exhibit a strong temperature dependence, so the entire system is kept at  
 1078        18° C with a water-based cooling system distributed throughout the barrel and end-caps.

1079        The ECAL readout electronics are designed to read-out a  $5 \times 5$  array of crystals, known as a  
 1080        trigger tower, in the EB, and a single supercrystal in the EE. Each trigger or tower or supercrystal  
 1081        consists of 5 Very Front End (VFE) boards, each connected to 5 APDs (VPTs), one Front End  
 1082        (FE) board, two (EB) or six (EE) Gigabit Optical Hybrids (GOHs), one Low Voltage Regulator  
 1083        (LVR) and a motherboard. Once triggered, the APD (or VPT in the EE) is sampled 10 times, at

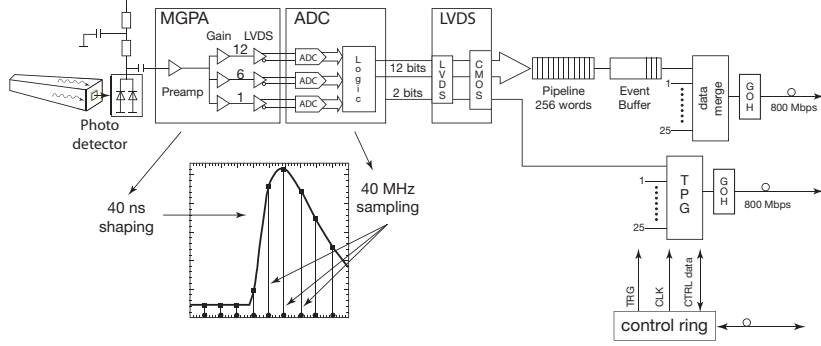


Figure 4.15: Schematic of the On-Detector Readout for the ECAL

a 40 MHz sampling rate, and amplified by a multi-gain amplifier (MGPA), with nominal gains of 1, 6, and 12 contained on the VFE. These digitized samples are sent to the FE, where they are buffered until receiving a Level-1 trigger, where they are sent to the off-detector electronics Data Concentrator Card (DCC) via the GOHs. Figure 4.15 shows a schematic of the on-detector read-out.

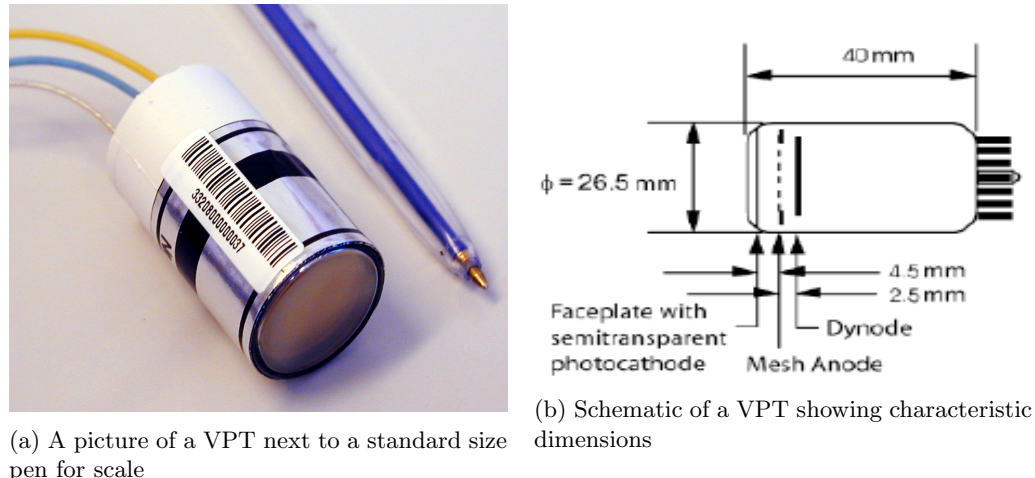
In the barrel, the  $5 \times 5$  trigger towers are divided in the 5 strips in the  $\hat{\phi}$  direction. The energy deposits in these strips is summed by the FE cards and define the transverse energy of the tower. In the endcaps, supercrystals are divided into groups of five contiguous crystals of variable shape, known as psuedo-strips. The energy of these strips is performed by the FE, and the off-detector electronics use these to compute the transverse energy deposition.

The preshower detector sits in front of the ECAL end-caps and provides coverage from  $1.653 < |\eta| < 2.6$ . It is a two-layer sampling calorimeter. Lead radiators initiate electromagnetic showers from electrons and photons, and silicon strips are placed behind them to measure trajectories and deposited energy of passing particles. The total thickness is 20cm, which corresponds to a 2 radiation lengths in the first layer, and another radiation length in the second layer. 95% of photons are converted to  $e^+e^-$  pairs after the first layer. Each silicon sensor is composed of 31 strips, with thickness of 320  $\mu m$  and are 1.9 mm in pitch. A front-end ASIC performs pre-amplification, shaping, voltage sampling, and communicates information to the trigger system to determine if data is stored or discarded. The structure is formed into Dees, and two Dees form a disk with a hole for the beam-line to pass through.

Behind the preshower is the ECAL end-cap (EE). It covers the pseudorapidity range of  $1.479 < |\eta| < 3.0$ , and sits a longitudinal distance of 315.4 cm from the nominal interaction point. Crystals are grouped into  $5 \times 5$  modules known as supercrystals (SCs). Like the preshower, each endcap is divided into two sections, Dees, which form a disk with an inner bore for the beam line to pass through, as shown in figure 4.16. Each Dee holds 3,662 crystals, which are divided



Figure 4.16: A section of the ECAL end-cap, a Dee. Two Dees form a disk with an inner bore for the beam-line to pass through. 5x5 modules, or supercrystals, are mounted in preparation for installation at CMS



(a) A picture of a VPT next to a standard size pen for scale

(b) Schematic of a VPT showing characteristic dimensions

Figure 4.17: Vacuum Photo-Triode devices used in the ECAL end-caps (EE)

1109 into 138 supercrystals, and 18 special partial-supercrystals for the inner and outer sections of  
 1110 the Dee.

### 1111 4.2.1 Vacuum Photo-Triodes

1112 The photomultiplier used to readout the lead tungstate crystals in the EE is the Vacuum Photo-  
 1113 Triode (VPT), shown in the right frame of figure 4.17(a). Each device is 26.5mm in diameter  
 1114 and 40mm in length as shown in figure 4.17(b). It is a gain stage device. Photons from the  
 1115 lead tungstate scintillation light enter the front face of the VPT and liberate electrons from the  
 1116 grounded bi-alkali photocathode (SbKCs) via the photoelectron effect. The cathode material  
 1117 has a quantum efficiency of  $\sim 20 - 25\%$ . The photo-electrons are accelerated towards the mesh

1118 anode grid, which is held at 800 V. Approximately half the photo-electrons pass through the  
 1119 mesh and encounter a dynode plate held at 600 V. Electrons either collide with the dynode,  
 1120 liberating secondary electrons from the collision, or are turned around by the 200 V difference  
 1121 between anode and dynode. Electrons are thus constantly accelerated towards the anode, and  
 1122 create secondary electrons as they collide with the anode. The process repeats with the secondary  
 1123 electrons, creating an avalanche of charge near the anode. As these charges eventually recombine  
 1124 with the anode over the course of a few nanoseconds, the voltage of anode drops, signaling the  
 1125 device has detected a photon from the PbWO<sub>4</sub> crystals.

1126 The performance of the VPT is degraded over time by two effects associated with exposure to  
 1127 the scintillation light from the crystals. The first is loss of the vacuum inside the tube. Molecules  
 1128 from the air become ionized by the large voltages and the positive ions are accelerated towards  
 1129 the photo-cathode, which is damaged through the resulting collision. The second effect is the  
 1130 gradual depletion of photo-electrons from the bi-alkali cathode material. The result is a decrease  
 1131 in the current, and thus signal, produced by the anode. Both of these effects can be effectively  
 1132 modeled as the sum of two falling exponential functions. The University of Virginia has studied  
 1133 the performance of VPTs with respect to their light exposure rates over the course of several  
 1134 years in order to characterize the device's response and long-term behavior.

#### 1135 4.2.2 Test Rig at UVa

1136 The University of Virginia (UVa) has continuously monitored four production VPTs operated  
 1137 at 800 V anode and 600 V dynode, in a 3.8 T field, at 15° to the tube axis, with photocath-  
 1138 ode currents of approximately 10 nA. This was done to simulate light exposure from the lead  
 1139 tungstate crystals in the forward regions of the ECAL end-caps, as well as provide an accelerated  
 1140 simulation of photocurrents that would be experienced in the larger eta regions. As described  
 1141 above, the light exposure is theorized to be the most significant cause of the loss of response  
 1142 in the VPT, known as burn-in. The amount of light that the device has been exposed to is  
 1143 measured in terms of the total number amount of charge liberated from the cathode, measured  
 1144 from the cathode current draw, and is known as the integrated charge. By operating at such  
 1145 high photocurrents, UVa is able to probe this burn-in effect in an attempt to understand the  
 1146 long term behavior of the VPT response to light.

1147 The University of Virginia is well suited to test these devices, since it operates a 3.8 T  
 1148 solenoid magnet, with a sufficiently large inner bore to accommodate a rig containing five (5)  
 1149 VPTs, LEDs, LED driving hardware, and amplifying equipment. The magnet itself was built  
 1150 by Oxford instruments and has an inner bore diameter of 0.4 m and an outer bore diameter of  
 1151 1.5 m. The inner bore is 0.13 m in height from the ground, and the magnet has a length of 1.5m

1152 along its z-axis, which is perpendicular to the normal of the floor.

1153 The VPTs were supplied with high voltage (800 V anode, 600 V cathode) from a CAEN  
1154 High Voltage supply. This manufacturer also provides high voltage supplies for the VPTs used  
1155 in CMS. They are preferable due to their stability, programmable user interface, and capacity  
1156 to drive multiple VPTs simultaneously. A voltage separation between anode and cathode much  
1157 larger than this is not recommended due to its potential do damage the device.

1158 The VPTs were pulsed with blue and orange LEDs at rates of 10 kHz, and 20 kHz, to capture  
1159 the same features (frequency and rate) that light from the lead tungstate crystals would produce  
1160 while collisions were occurring in the detector. The driving circuits are the same as those used in  
1161 the LED system in the end-caps at point 5 (the location of CMS at CERN), with the exception  
1162 that the current limiting resistors are larger. They are Dallas Semiconductor DS1040Z-D70  
1163 Programmable One-Shot Pulse Generators. The TTL signals from the FPGA serve as a trigger  
1164 for a Dallas Semiconductor pulse generator chip on the board that generates a 30 nSec pulse, so  
1165 there is no overlap in pulses generated by the VPT. The pulsing was also run in an on/off cycle  
1166 of 16 hrs on, 8 hrs off to be consistent with the LHC beam fill cycle.

1167 The LED pulsing and data acquisition was automated via a PXI unit manufactured by Na-  
1168 tional Instruments, which contains a FPGA card, a digital oscilloscope, and computer running  
1169 Windows XP. The FPGA card was programmed with LabVIEW software which controlled LED  
1170 pulse rate, low voltage power, and measurements of VPT signals. The data acquisition was  
1171 triggered by means of a PIN diode placed next to the VPT. This served the dual purpose of in-  
1172 dependent data triggering and also provided the means to correct fluctuations in the illumination  
1173 provided by the LEDs.

1174 The current from the VPTs anode and cathode are ultimately routed to the PXI Crates  
1175 switches, and then on to the crates DMM or oscilloscope via a preliminary amplification stage.  
1176 The VPTs anode is connected directly to a Stephenson amplifier, which connects to a high-  
1177 frequency switch. The PIN diode signal passes unmodified to that same high-frequency switch.  
1178 The cathode signal cables connect to a distribution box near the PXI Crate. The distribution  
1179 box then routes their signals to the terminal block on a low-frequency switch. All of these signals  
1180 leave the rig over BNC cables before terminating at or adjacent to the PXI Crate. Figure 4.18  
1181 highlights different components of the test stand at UVa.

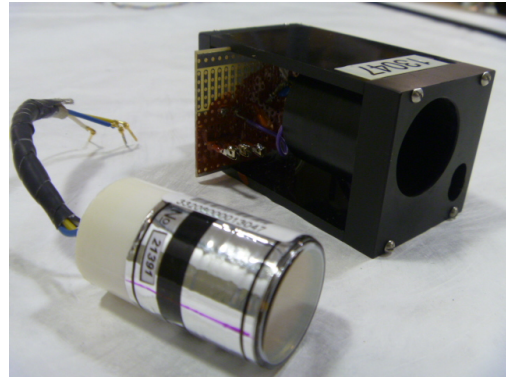
### 1182 4.2.3 Results of UVa Tests

1183 The University of Virginia rig ran three sets of 5 VPTs for approximately 30 wks each in a  
1184 3.8 T magnetic field under high light conditions from blue and orange frequencies to simulate  
1185 a large light yield found in large eta regions of the end-cap. The large photocurrents allowed

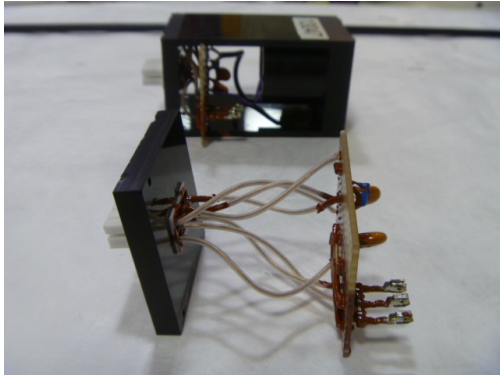


h

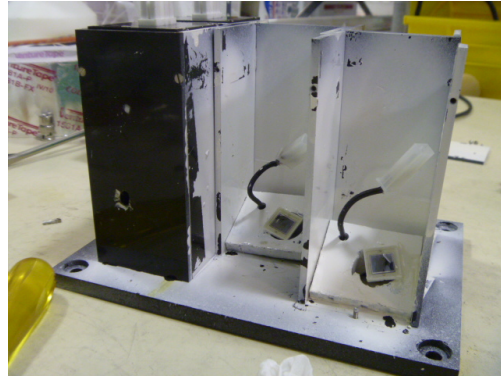
(a) The 3.8 T superconducting solenoid magnet used at UVa to study VPT performance



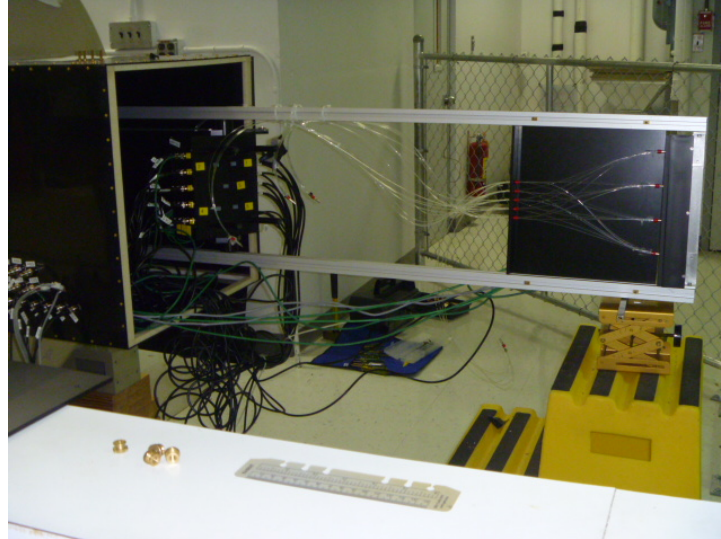
(b) A VPT before being installed in the rig and the housing that provides mechanical support and high voltage connections



(c) The housing for the VPT also provides simple HV filtering to provide stable power to the device



(d) The structure which holds 5 vpts in their housing. A PIN diode is used to measure the LED light and make corrections for fluctuations in brightness



(e) The VPT rig in maintenance position outside of the bore of magnet (during operation the rail is inserted into the bore such that the vpt housing is at the center). Fiber optics feed from the left into the VPT and amplifier housing.

Figure 4.18: Features of the UVa VPT test stand

the collection of an integrated charge of  $\sim 48$  mC for the largest gain VPT, and  $\sim 16$  mC for the other three. All VPTs were characterized by an initial steep decline followed by a plateau region, which was fit with a double exponential function of the form

$$f(x) = A + B \exp(Cx) + D \exp(Ex) \quad (4.2)$$

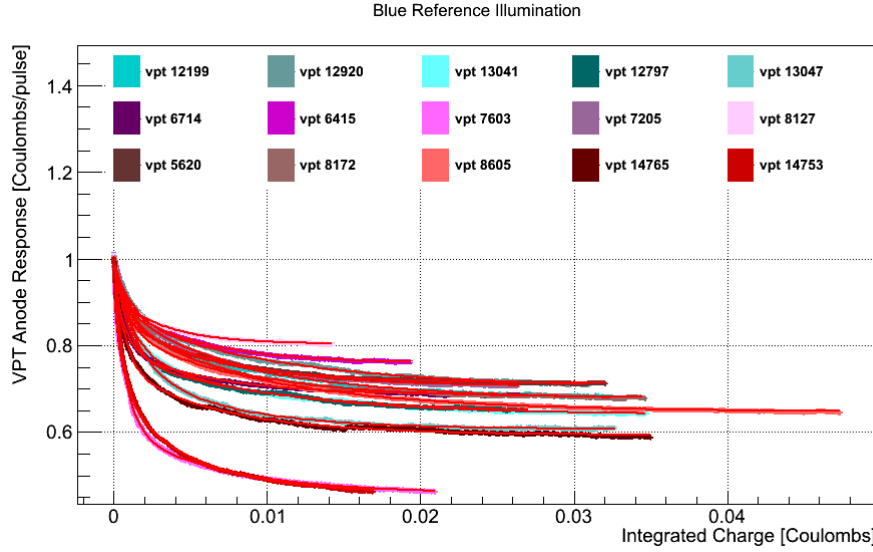


Figure 4.19: 3 runs of 5 VPTs, exposed to blue LED light, and fit to a sum of two exponentials.

Table 4.1: Fit Results for VPT Conditioning Studies at U.Va. and Brunel, Blue Reference LED

RIE Number	% Drop	$\chi^2/NDF$	Pedestal	Fast exp Amplitude	Fast exp $\tau$	Slow exp Amplitude	Slow exp $\tau$
12199	30.1	1.20e+00	1.51e-09	3.42e-10	-8.84e-04	3.85e-10	-1.00e-02
12920	27.0	7.27e-01	1.72e-09	3.16e-10	-1.16e-03	4.03e-10	-1.05e-02
13041	33.5	8.46e-01	1.09e-09	3.43e-10	-1.20e-03	2.46e-10	-9.31e-03
12797	33.6	1.07e+00	6.39e-10	2.18e-10	-9.72e-04	1.31e-10	-9.87e-03
13047	38.1	1.06e+00	5.48e-10	1.98e-10	-1.40e-03	1.49e-10	-6.19e-03
6714	29.3	8.37e-01	1.55e-09	4.10e-10	-6.66e-04	2.48e-10	-6.11e-03
6415	23.6	1.28e-01	1.19e-09	1.54e-10	-6.55e-04	2.20e-10	-5.16e-03
7603	50.3	3.25e+00	1.44e-09	1.02e-09	-8.22e-04	4.87e-10	-6.72e-03
7205	29.4	4.53e-01	1.41e-09	2.14e-10	-5.68e-04	3.94e-10	-5.96e-03
8127	19.6	1.97e-01	1.71e-09	1.82e-10	-3.12e-04	2.35e-10	-3.30e-03
5620	27.4	4.57e+00	1.68e-09	2.85e-10	-5.20e-04	3.68e-10	-6.19e-03
8172	30.3	8.75e+00	8.32e-10	1.52e-10	-1.06e-03	2.27e-10	-6.87e-03
8605	32.1	6.94e+00	1.36e-09	3.33e-10	-8.97e-04	3.94e-10	-1.03e-02
14765	38.9	2.78e+01	3.47e-10	1.37e-10	-7.46e-04	9.24e-11	-6.77e-03
14753	52.9	2.53e+01	1.19e-09	7.45e-10	-5.86e-04	6.10e-10	-4.77e-03
Average	31.0	4.62e+00	1.17e-09	2.94e-10	-1.09e-03	1.66e-10	-3.07e-01

where A is a pedestal parameter, B is the amplitude of the fastest dropping exponential, C is the time constant of the fast dropping exponential, D is the amplitude of the slow dropping exponential, and E is the time constant of the fast exponential. The summary of the fit parameters for blue LED light is shown in table 4.1 and the summary of fit parameters for the orange LED light is shown in table 4.2. Plots of the VPT anode response versus integrated charge, and

the associated fit for each of the devices is shown in figure 4.19 for blue LED exposure and in figure 4.20 for orange LED exposure. Based on these findings, it can be concluded that the VPT "burn-in" eventually reaches a plateau at about  $\sim 70\%$  for blue LED exposure and  $\sim 50\%$  for orange LED exposure.

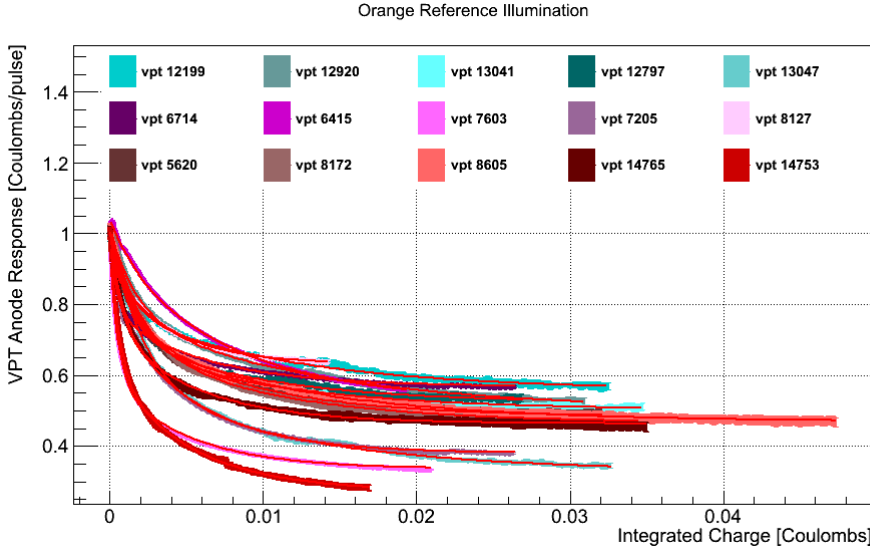


Figure 4.20: 3 runs of 5 VPTs, exposed to orange LED light, and fit to a sum of two exponentials.

Table 4.2: Fit Results for VPT Conditioning Studies at U.Va., Orange LED

RIE Number	% Drop	$\chi^2/NDF$	Pedestal	Fast exp Amplitude	Fast exp $\tau$	Slow exp Amplitude	Slow exp $\tau$
12199	41.9	6.23e-01	4.23e-10	1.79e-10	-1.10e-03	1.76e-10	-1.10e-02
12920	45.3	1.84e-01	6.73e-10	3.24e-10	-1.67e-03	3.72e-10	-1.26e-02
13041	48.3	7.42e-01	2.75e-10	1.81e-10	-1.63e-03	1.04e-10	-1.02e-02
12797	46.4	5.05e-01	2.05e-10	1.14e-10	-1.23e-03	7.87e-11	-8.77e-03
13047	63.0	1.09e+00	1.34e-10	1.73e-10	-2.18e-03	1.07e-10	-1.16e-02
6714	43.4	1.43e+01	7.73e-10	3.29e-10	-4.49e-04	2.84e-10	-6.11e-03
6415	46.5	2.34e+01	4.41e-10	8.75e-11	-1.80e-03	3.47e-10	-7.95e-03
7603	64.8	3.20e+01	3.01e-10	3.42e-10	-5.42e-04	2.24e-10	-5.04e-03
7205	63.2	6.52e+01	1.94e-10	1.29e-10	-4.49e-04	2.16e-10	-5.13e-03
8127	39.4	2.24e+01	7.09e-10	1.54e-10	-2.08e-04	3.10e-10	-3.75e-03
5620	50.3	2.30e-01	4.07e-10	2.13e-10	-1.16e-03	2.37e-10	-7.79e-03
8172	51.7	1.56e-01	4.01e-10	2.73e-10	-1.91e-03	2.08e-10	-9.48e-03
8605	49.6	1.83e-01	2.39e-10	1.46e-10	-1.45e-03	1.33e-10	-1.12e-02
14765	53.3	3.08e-01	2.07e-10	1.27e-10	-8.55e-04	1.17e-10	-5.66e-03
14753	72.2	2.22e-01	1.94e-10	2.76e-10	-6.01e-04	2.47e-10	-5.06e-03
Average	52.0	1.08e+01	3.72e-10	2.03e-10	-1.15e-03	2.11e-10	-8.10e-03

### 4.3 The Hadronic Calorimeter

The Hadronic Calorimeter (HCAL) is divided into four sub-systems: the barrel (HB), the endcap (HE), the outer calorimeter (HO), and the forward calorimeter (HF). It is especially important for measuring hadronic jets and neutrinos by measuring an imbalance in energy trans-

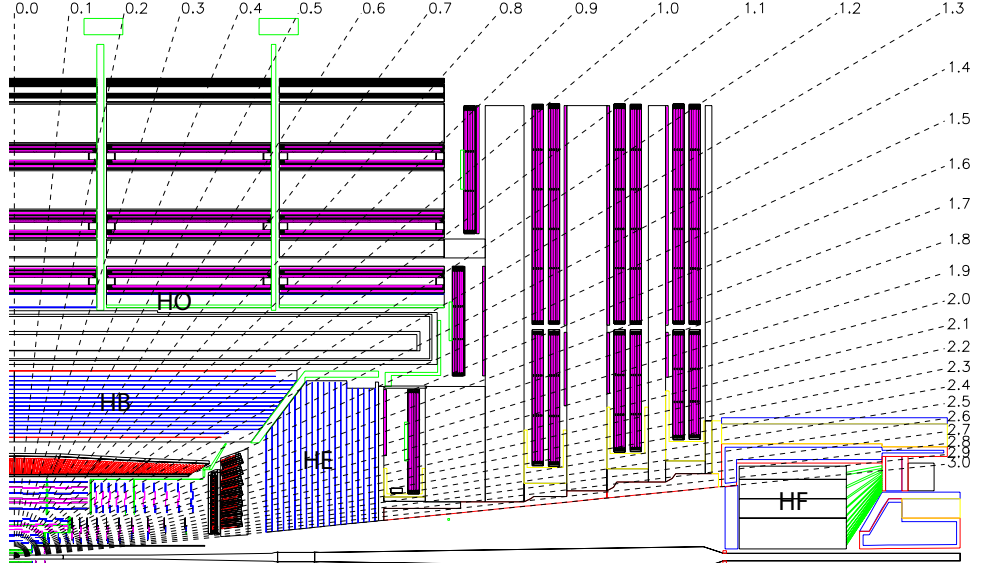


Figure 4.21: Longitudinal cross-section of the HCAL with the four sub-systems labeled

verse to the beam-line. It provides coverage from  $|\eta| < 3$  from the HB, HE, and HO, and the HF extends the coverage out to  $|\eta| < 5.2$ . A diagram of the longitudinal cross section is shown in figure 4.21.

The barrel section of the HCAL, the HB, is divided into two sections longitudinally, each with 18 identical azimuthal wedges wrapped around the beam-line. Each wedge has four azimuthal sections, with the center two sections aligned and each edge piece angled and staggered in a configuration that creates no projective dead material for the full radial extent of the HCAL. Figure 4.22 shows a closeup photograph of four wedges, where optical fibers are laid out across the seam that joins the staggered edge layers to the two aligned center layers, and blue lines highlight the four azimuthal divisions for a single wedge.

The HB is a sampling calorimeter, with each azimuthal section composed of 14 alternating layers of brass absorber plates, and layers plastic scintillator tiles, with steel plates on the top and bottom layers for structural support. Each quarter-barrel section of scintillator has 16  $\eta$  divisions, giving a segmentation of  $(\Delta\eta, \Delta\phi) = (0.087, 0.087)$ . The brass absorber plates are C26000/Cartridge Brass. The material was chosen since the absorber material could not be distorted or bend under the stress of its own weight for at least 15 years of experimental running. Much of the material was purchased, but over a million Russian WW2 brass shell casings, designed to withstand the stresses of travel aboard 1940s Navy vessels, were melted down and processed into absorber tiles. Figure 4.24 shows members of the Russian Navy posing with some of the shells.

When a hadron passes through a wedge, the brass and steel plates absorb energy and ini-



Figure 4.22: Closeup of the HCAL barrel section. The center section of each of the 18 wedges are labeled, optical cables lay across the joint of the center and staggered edge sections of each wedge. The blue lines show the approximate azimuthal division of the wedge.

tiates the decay of the hadron into a number of lighter particles. These particles pass through the scintillator layer, which absorb energy from the interactions or collisions with the passing particles. The electrons of the scintillator become excited and relax by emitting a number of photons in the blue-violet range of the visible spectrum proportional to the amount of energy absorbed by the scintillator. These photons are absorbed by wavelength shifting fibers (WSFs), which re-emit the light in the green part of the visible spectrum. The WSFs are spliced into four clear fiber optical cables. These fibers transport the light from each of the layers to an optical decoding unit (ODU), which arranges the fibers into readout towers. A hybrid photodiode (HPD) converts this light into electric signals and is digitized by an ADC contained on the front-end electronics. The HPD is a photo-cathode, which converts light to electrons via the photoelectric effect, that sits above a silicon diode that amplifies the signal of the cathode. The HPD provides a gain of 2000 to the light signals received from the scintillator trays. The on-detector electronics communicate to the HCAL trigger/readout (HTR) boards, which communicate with the trigger system to decide whether to store the event as data or discard it.

The brass absorbing material has a nuclear interaction length, or the length necessary to reduce the number of charged particles in a hadron shower by  $1/e$ , of 16.42 cm, and a radiation length of 1.49 cm. This means that the HB will be able to contain a large part of most hadron showers produced at LHC energies, but a portion will still pass through the entire radial distance. The outer barrel layer, HO is designed to measure the remnants of the hadron shower. It sits



Figure 4.23: Over 1 million Russian shells of military artillery were re-processed in the construction of the HCAL

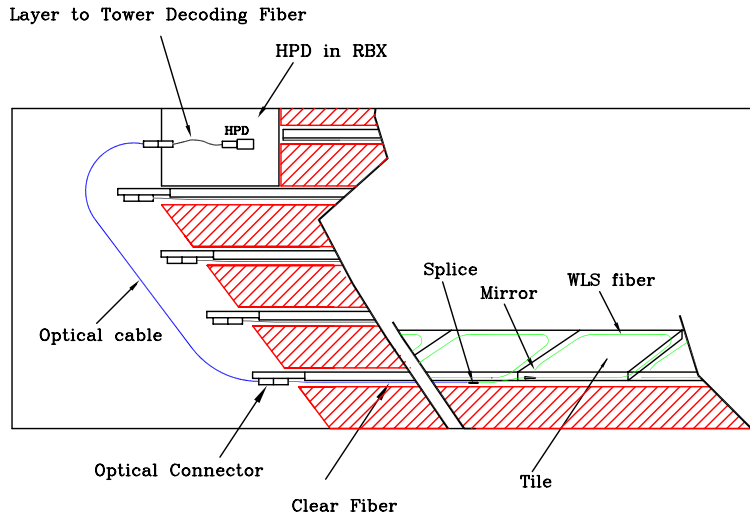


Figure 4.24: Optical readout chain of the HCAL scintillator tiles

1242 outside of the solenoid magnet, using it as an absorber layer  $1.4/\sin \theta$  interaction lengths. It  
 1243 consists of 5 sections along the z-axis, which form rings around the beam-line. Each ring is a layer  
 1244 of scintillator tiles at radial distance of 4.07m, except for the center ring. Since it corresponds  
 1245 to the  $\eta = 0$  ring, there is a minimum amount of absorber material in front of it. The central  
 1246 ring is thus two layers of scintillator at radial distances 3.82 and 4.07 m, which sit on either side  
 1247 of a 19.5cm thick piece of iron absorber.

1248 The endcap system, the HE, provide a substantial portion of the total  $\eta$  coverage, from  
 1249  $1.3 < |\eta| < 3.0$ , and contains  $\sim 1/3$  of the final state particles in a collision. Like the HB, it is  
 1250 a sampling calorimeter with alternating layers of brass and plastic. The demand for radiation  
 1251 hardness, and the need for a non-magnetic material, lead to the same choice of C26000 cartridge

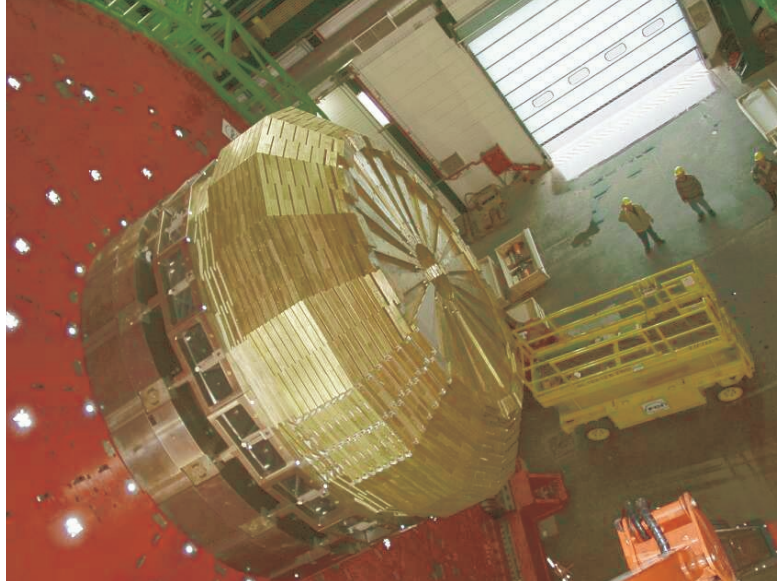


Figure 4.25: HCAL endcap, 18 azimuthal divisions of alternating layers of brass and plastic scintillator.

1252 brass found in the HB. It is also divided into 18 azimuthal wedges, and 16  $\eta$  divisions, giving  
1253 it the same  $(\Delta\eta, \Delta\phi) = (0.087, 0.087)$  segmentation. Figure 4.25 shows an image of a partially  
1254 assembled endcap before being installed.

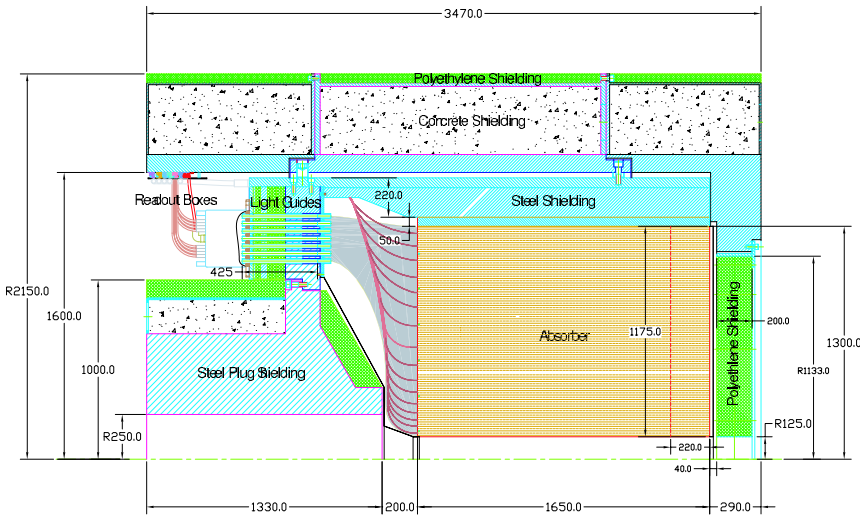


Figure 4.26: Longitudinal cross-section of the HCAL forward calorimetry, the HF

1255 The forward calorimetry, HF, extends the HCAL coverage from  $3.0 < |\eta| < 5.0$ , and neces-  
1256 sarily must sit in the region of the detector with the largest particle fluxes and thus radiation  
1257 exposure. The HF is a cylindrical steel structure with an inner bore 12.5 cm from the beam line,  
1258 and a outer radius of 130.0 cm. It sits 11.2 m away from the nominal interaction point in the

1259  $\hat{z}$  direction. Like the HE, it has 18 azimuthal divisions on either side of the interaction point.  
 1260 Relativistic particles that move through the steel generate Cherenkov light, which is collected  
 1261 by radiation hard quartz fibers, which transport the light to HPDs which are readout in the  
 1262 manner as described above. Since the detection mechanism is Cherenkov light, this sub-system  
 1263 is primarily sensitive to the electromagnetic component of the hadronic shower. Figure 4.26  
 1264 shows a cross-sectional view of the HF detector.

## 1265 4.4 Muon Chambers

1266 In  $pp$  collisions, muons are only created through electroweak or exotic physics processes, making  
 1267 the detection of this particle an invaluable tool for reducing the large hadronic backgrounds  
 1268 produced at the LHC. The muon chambers, positioned furthest from the beam-line, sit behind  
 1269 the ECAL and HCAL detectors, which absorb almost all of the hadronic activity from a collision.  
 1270 They operate in a relatively low flux environment, allowing for robust measurement of their  
 1271 kinematics, making it an excellent trigger system. One of the most important discovery channels  
 1272 for the Higgs boson, involved the decay of the Higgs into two  $Z$  bosons, which decay to two pairs  
 1273 of muons. Only 25 events were needed for a statistically significant observation in that channel,  
 1274 since the backgrounds had been reduced to only 5 expected events and the muons had provided  
 1275 high resolution on the invariant mass of the Higgs.

1276 The muon chambers are composed of three types of gaseous detector technology: drift tubes  
 1277 (DTs), cathode strip chambers (CSCs), and resistive plate chambers (RPCs). In the muon barrel  
 1278 system (MB), where the magnetic field is uniform DTs provide  $\eta$  coverage, for  $|\eta| < 1.4$ , and  
 1279 are supplemented by a system of RPCs that provide an independent trigger source and faster  
 1280 timing resolution. In the muon endcap system (ME), where the magnetic field would degrade  
 1281 the performance of DTs, a system of CSCs and RPCs provide  $\eta$  coverage from  $1.4 < |\eta| < 2.4$ .

1282 The DTs are located in the MB system, which is divided into 5 longitudinal, cylindrical  
 1283 sections around the beam-line, known as wheels. In each wheel there are 4 concentric layers of  
 1284 drift tube stations, one on either side of the magnet return yoke, and two interspersed inside of  
 1285 it. Each wheel is divided into 12 azimuthal sections, making 48 stations in the barrel, as shown  
 1286 in figure 4.27. Each station on the first three (fourth) layers contain 3(2) superlayers, where  
 1287 each superlayer is made of a stack of 4 layers of rectangular drift cells, which are staggered  
 1288 by half a cell each. Two of the superlayers are oriented such that they are parallel to the  
 1289 beam, measuring the muon in the  $r - \phi$  plane. The first three layers contain a third superlayer,  
 1290 orientated perpendicular to the beam, measuring a  $z$  component of the muon trajectory. Each  
 1291 drift cell is a hollow  $13 \times 42$  mm tube, with a relatively thick 1.5mm wall to provide isolation

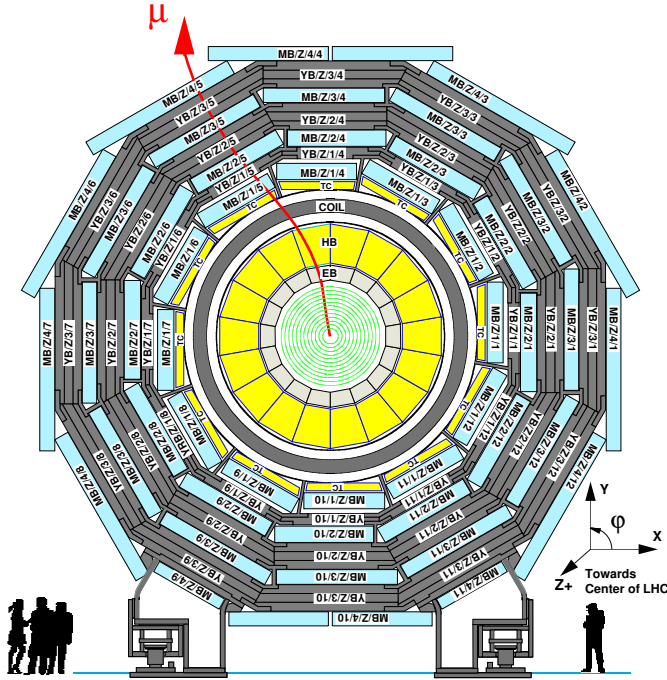


Figure 4.27: Longitudinal cross-section of one of the 5 wheels of the muon system. Drift tubes are placed in 4 concentric layers, with 2 being placed inside the return yoke of the magnet, and 12 azimuthal divisions.

1292 between adjacent cells. Each cell is filled with a mixture of 85% argon + 15% CO<sub>2</sub> gas mixture,  
 1293 and contains an anode wire that is held at 3600 V that runs down the axis of the cell. The  
 1294 walls of the cell are held at 1800 V or -1200 V depending on the wall. When a muon passes  
 1295 through the chamber, it's charge ionizes molecules of the CO<sub>2</sub> gas, causing the electrons to drift  
 1296 towards the anode wire, and the CO<sub>2</sub> ions drift towards the wall. As the electrons approach the  
 1297 anode, they are accelerated and liberate secondary electrons from other CO<sub>2</sub> molecules, creating  
 1298 an avalanche of electrons near the wire, resulting in a drop in voltage as they are collected. The  
 1299 voltage drop is read out by front end electronics as a signal that a muon has passed through  
 1300 the chamber. The Argon gas quenches the avalanche reaction, and the maximum drift time  
 1301 for electrons in the gas is 380 ns. This long time scale necessitates the use of an additional,  
 1302 fast-timing system, the RPCs. Figure 4.28 shows a cross-section view of a drift cell, including  
 1303 electric field lines produced by the potential difference between the anode wire and the walls of  
 1304 the drift cell.

1305 The resistive place chambers (RPCs) are the fast timing system chosen to supplement the  
 1306 DTs in the barrel, and the CSCs in the endcaps. In the barrel, they are adhered to the top and  
 1307 bottom of the first two layers of drift stations. In the outer two layers, they are only adhered  
 1308 to the bottom of each station. Figure 4.29(a) shows the layout of the barrel RPC system. The  
 1309 muon endcap system is composed of three disks on either side of the interaction point, and is

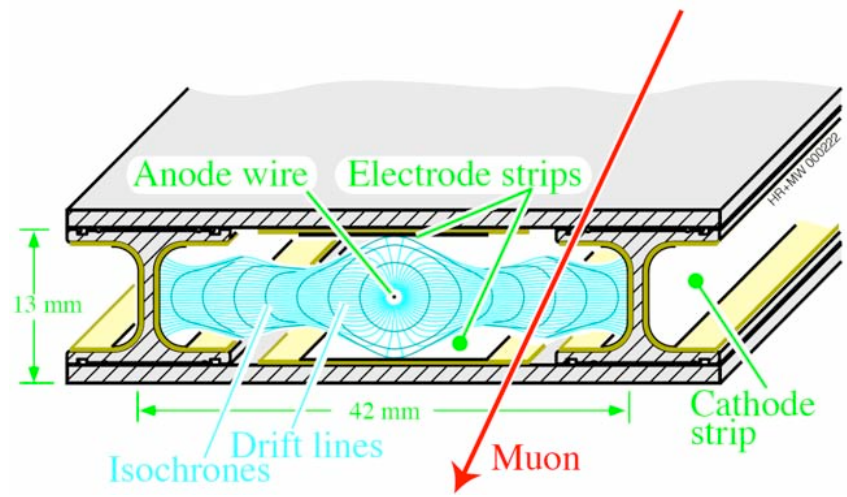
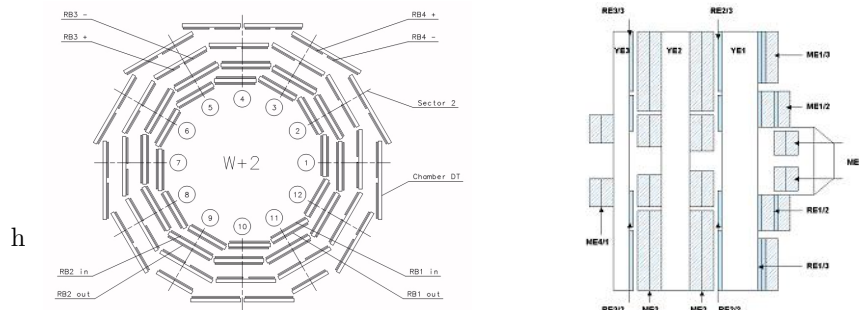


Figure 4.28: A cross-section view of a drift cell. The anode wire is held at 3600 V, creating a potential difference with the walls. Electric field lines are shown in blue.

1310 shown in figure 4.29(b). RPCs are mounted on the back of the CSC stations of the innermost  
 1311 and outermost disks, and on the front of the CSC for the middle disk. Each RPC consists  
 1312 of two plates of high resistance material, one held at a positive voltage, the anode, and the  
 1313 other held at a negative voltage, the cathode. The volume between the plates is filled with  
 1314 a gas similar to the drift tubes. When a muon passes between the plates, it ionizes the gas  
 1315 molecules, and the electrons are accelerated towards the positive plate, creating an avalanche of  
 1316 secondary electrons that combine with the positive plate creating a voltage drop that is read out  
 1317 as a signal. The timing resolution achieved from the RPCs is less than the 25 ns LHC bunch



(a) A longitudinal cross-section of the muon barrel RPC system. RPCs are attached to the top and bottom of the first two layers of drift stations, and to the bottom of the outer two layers

(b) Cross-section of muon endcap system. It is composed of three disks, with RPCs mounted on the back of CSC system on the first and last disks, and on the front of the CSC in the middle disk

Figure 4.29: RPC layout for the barrel and endcaps

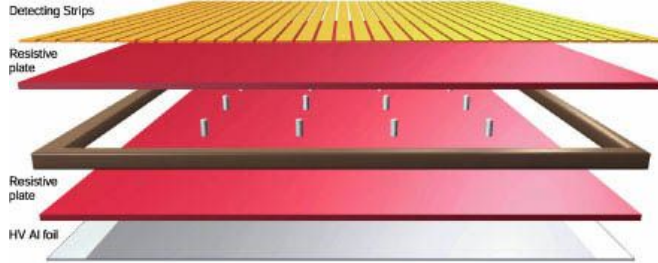


Figure 4.30: Exploded diagram of an RPC

1318 crossing, supplementing the spatial resolution provided by the DTs in the barrel, and the CSCs  
1319 in the endcap.

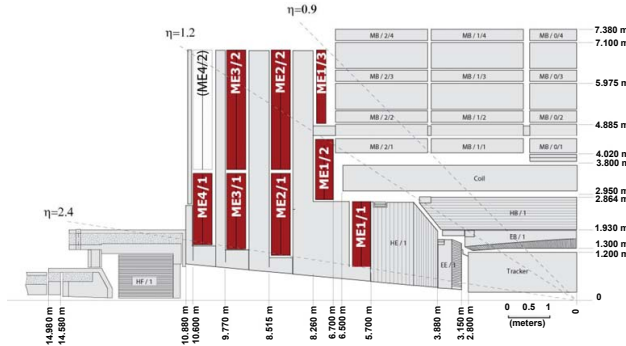


Figure 4.31: Cross-section of one quarter of the muon endcap system, with the 4 disks of CSC systems shown in red

1320 In addition to RPCs, the muon endcap (ME) system, uses cathode strip chambers (CSCs)  
1321 to provide additional spatial resolution on muons. Each endcap has 4 layers of CSCs, with a  
1322 trapezoidal shape, with 468 cathode strip chambers disturbed on each. Three groups of 72 are  
1323 located on the inner disk, a group of 36 and a group of 72 in the second and third disk, and  
1324 a group of 36 in the outer disk. Figure 4.32 shows the layout of a quarter section of the CSC  
1325 system in the ME. A CSC station consists of 6 layers of gas chambers, where each chamber is  
1326 an array of anode wires, held at a positive voltage, arranged perpendicular to cathode strips,  
1327 held at negative voltage. The volume of the chamber is filled with a gas that is 40% Argon,  
1328 50% CO<sub>2</sub>, and 10% CF<sub>4</sub>. When a muon passes through the volume, the gas is ionized, and now,  
1329 since the anode and cathode strips are perpendicular, when the electrons and gas ions combine  
1330 with the anode and cathode respectively, a 2-D measurement of the muon's position is recorded.  
1331 Figure 4.32 shows a diagram of a CSC chamber with 7 layers to create the 6 gas chambers.

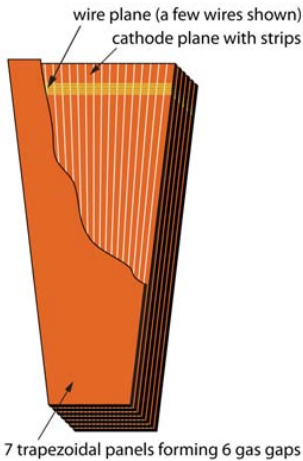


Figure 4.32: A CSC station with 7 layers, making 6 gas chambers. Cathode strips are shown in yellow, perpendicular to the vertical anode wires in orange.

## 1332 4.5 Data Collection Overview

1333 The LHC is designed to deliver protons at 40 MHz, corresponding to a bunch crossing every 25 ns.  
1334 The majority of the interactions will be glancing, low-energy collisions, which do little to reveal  
1335 new phenomenon, and would be impossible to store for analysis. A trigger system is designed to  
1336 select interesting events with a large potential of revealing new physics. The rate is reduced in  
1337 two steps through the Level-1 (L1) trigger, and the High-Level Trigger (HLT). The L1 trigger is  
1338 composed of programmable electronics and hardware that buffers the data and perform simple  
1339 calculations on tracks and calorimeter energy deposits to determine whether an event should be  
1340 kept for analysis. This reduces the event rate from 40 MHz to 10 kHz. The HLT is a computer  
1341 farm of  $\sim$ 1000 computer processors, that perform a more sophisticated reconstruction of the  
1342 tracks and energy deposits, as well as more complicated calculations between reconstructed  
1343 objects. This stage reduces the rate to a much more manageable 100 Hz.

1344 The L1 trigger is composed of local, regional, and global components. The process of deter-  
1345 mining whether to accept or reject the event begins by calculating Trigger Primitive Generators  
1346 (TPGs) based on calorimeter energy deposits, and tracks in the muon chambers. The entire  
1347 process has a latency time of  $3.2 \mu\text{s}$ , which corresponds to the length of the LHC abort gap.  
1348 Sufficiently large data buffers allow the storage of all the events processed during a bunch train,  
1349 meaning that CMS is capable of running with zero dead time due to detector readout latency.

1350 In the ECAL a trigger tower consists of a  $5 \times 5$  array of crystals. Front-end electronics on the  
1351 crystals receive ADC counts on the amplitudes of the photomultipliers, and uses information  
1352 encoded in the electronics to convert this sum to the transverse energy,  $E_T$  deposited in the  
1353 crystals. The EB TPG also encodes information about the distribution of energy, and thus the

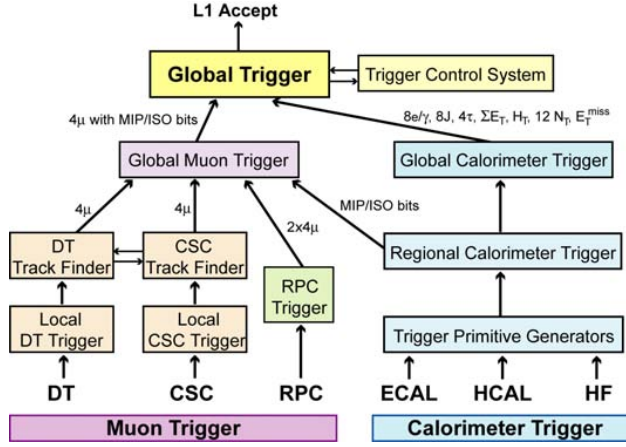
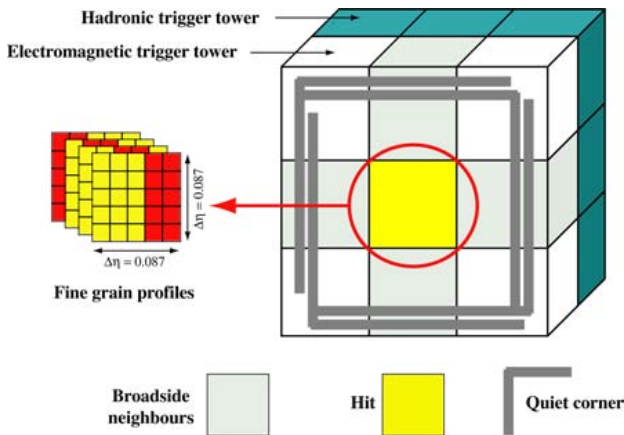


Figure 4.33: A block diagram of the L1 trigger

1354 shower shape in the  $5 \times 5$  array, which is used to veto anomalous signals. In the HCAL, a trigger  
1355 tower consists of one of the 16 azimuthal wedges, with segmentation  $(\Delta\eta, \Delta\phi) = (0.087, 0.087)$ ,  
1356 in the barrel and endcap. Similarly to the ECAL, front-end electronics digitize the signal from  
1357 the HCAL HPDs, and convert the ADC counts into sums of transverse energy. These calorimeter  
1358 TPGs are sent to a Regional Calorimeter Trigger (RCT) that is composed of a  $4 \times 4$  array of  
1359 trigger towers, with the exception of the HF, which is formed by a single trigger tower.

Figure 4.34: A schematic of the  $e/\gamma$  trigger algorithm

1360 The RCT determines electron and photon candidates from the calorimeter sums. The  $e/\gamma$   
1361 trigger searches for the highest energy trigger tower in the ECAL. Within that trigger tower,  
1362 it checks that the EM shower is contained in a  $2 \times 5$  array of crystals and that the ratio of  
1363 ECAL to HCAL energies is less than 5%. It is considered an isolated electron if all eight of  
1364 its nearest neighbors pass these requirements, and a corner of five neighbors has energy below  
1365 a threshold requirement. It is considered a non-isolated electron if only the second highest  $E_T$

1366 broadside neighbor trigger tower passes these criteria. Up to four isolated, and four non-isolated  
 1367  $e/\gamma$  candidates per RCT are passed to the Global Calorimeter Trigger (GCT).

1368 The GCT determines jets, total transverse energy, missing transverse energy, jet counts, and  
 1369  $H_T$  (scalar sum of transverse momentum), in addition to the highest rank isolated and non-  
 1370 isolated *egamma* candidates. Jets are found in a clustering algorithm that looks for large energy  
 1371 deposits in  $2 \times 12$  cells of  $\phi$  or  $\eta$  that span  $40^\circ$  and half the detector in each of coordinates. Up  
 1372 to four jets, and four tau jets from the HCAL and four jets from the HF are forwarded to the  
 1373 Global Trigger (GT).

1374 The non-calorimeter based triggers are based on measurements of the DTs, CSCs, and RPCs  
 1375 in the muon drift chambers. The barrel DTs look for hit patterns among neighboring tubes in  
 1376 successive layers, and fits a track segments in the  $\eta$  and  $\phi$  coordinates. The endcap CSCs provide  
 1377 3-dimensional track segments and are combined with the DTs to form tracks that are passed to  
 1378 the Global Muon Trigger (GMT). The RPCs provide an independent set of tracks and timing  
 1379 hits to the GMT. Each bunch crossing the GMTs receive up to four muon candidates in the  
 1380 barrel RPCs, four from the barrel DTs, four from the endcap RPCs, and four from the endcap  
 1381 CSCs. The GMT records the candidate's  $p_T$ , charge,  $\eta$ , and  $\phi$  position, as well as a quality code  
 1382 related to the fit of the track to the hit positions of the detector. The GMT sends then sends  
 1383 these muon candidates to the GT.

1384 The Global Trigger can execute up to 128 trigger algorithms in parallel to analyze the  $p_T$ ,  
 1385 charge,  $\eta$ , and  $\phi$  position, and associated quality codes for muons, electrons, photons, jets, and  
 1386 missing transverse energy. Most algorithms compare single object characteristics to thresholds  
 1387 to determine if they pass minimally interesting criteria. If any of the algorithms return a passing  
 1388 decision, the L1 trigger issues an accept statement that allows the data stored in buffers to be  
 1389 readout by the CMS Data Acquisition (DAQ) system.

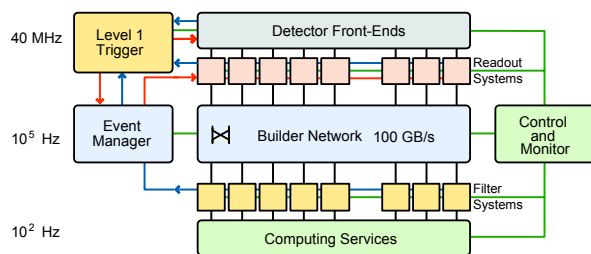


Figure 4.35: Layout of the CMS DAQ

The CMS DAQ collects information from 626 sub-detector Front End Drivers (FEDs), which extract the buffered information from the various front-end systems, upon the arrival of a L1 trigger accept. An event builder algorithm assembles the fragments from the various sub-systems into a single coherent event, and transmits the information to the HLT computing farms. Figure 4.35 shows a schematic of the DAQ system.

The HLT computer farm performs the final reduction of data rate, from 100kHz from the L1 to 100Hz. The computer farm performs basic consistency checks to ensure the quality of the data, then performs calculations based on topology of the HLT path. Typically, a more sophisticated reconstruction of an object takes place, and kinematic cuts are applied to the object or in relationship to other objects in the event. Each HLT path forms its own data set, thus creating single muon, single electron, electron+jets, etc. type datasets. The unpacked detector information read by the DAQ is composed of ADC counts for each readout channel, TPGs, and the L1 decision. This is known as the RAW dataset. Reconstructed physics objects are stored RECO data tier, and finally an analysis object data (AOD) tier is created containing only information about the reconstructed objects without having to store detector information. This last format requires the least amount of data per event for storage, and contains the reconstructed physics objects, such as electrons, muons, jets, etc. which are be used to search for new physics phenomenon.

1408 **Chapter 5**

1409 **Particle Reconstruction at CMS**

1410 Charged and neutral hadrons in the form of jets, missing transverse energy (MET), photons,  
1411 electrons, muons, and tau leptons are reconstructed at CMS using the particle flow event-  
1412 reconstruction algorithm [116]. The algorithm is based on a three step process of identifying  
1413 charged particle tracks using the muon chambers and silicon tracker, identifying clusters of en-  
1414 ergy in the ECAL and HCAL, and linking the tracks to the calorimeter clusters. The calorimeter  
1415 energy deposits were calibrated with test beam sources, data from cosmic rays and beam dumps,  
1416 and finally from collision data. The algorithm constructs muons by fitting the tracks formed  
1417 between the muon chambers, pixel and silicon trackers. Electrons have tracks from the pixel and  
1418 silicon tracker matched to the ECAL, with a minimum energy deposited in the HCAL. Jets are  
1419 formed from tracks, ECAL, and HCAL clusters falling with a conical angle. The identification of  
1420 one, three, or larger odd number of tracks, and the majority of the energy contained in a small  
1421 cone size, allows a jet to be tagged as a hadronically decaying tau lepton. Additional algorithms  
1422 are also used to identify a jet as coming from the decay of a b-quark, primarily by looking for  
1423 secondary vertices in the pixel and silicon tracker.

1424 **5.1 Iterative Tracking**

1425 Since approximately two-thirds of the energy of a jet is carried by charged hadrons, the tracker  
1426 is the cornerstone of the particle-flow algorithm [116]. The path of a charged particle in a  
1427 magnetic field follows a helical pattern, described by 5 parameters. The extraction of these  
1428 requires three 3-dimensional measurements of the particle, or two 3-dimensional measurements  
1429 and a constraint on the origin [117]. The pixel detector is ideal for this since each pixel provides  
1430 a 3-dimensional measurement of the particle's location. Track reconstruction is the process of  
1431 using hits in the pixel and silicon detector elements to estimate the momentum and trajectory of

1432 the charged particle responsible for the hit [117]. The tracking software at CMS is known as the  
1433 Combinatorial Track Finder (CTF), which is based on producing tracks over multiple iterations  
1434 of the reconstruction sequence, removing the tracks with the largest  $p_T$  closest to the interaction  
1435 region first, reducing the combinatorial complexity over each iteration.

1436 Each iteration begins by identifying a seed for the particle tracks, which is a minimum  
1437 combination of pixel or silicon tracker hits that is used as an initial estimate of the trajectory  
1438 of the particle [117]. Then, tracks are found by applying the Kalman filter [118]. This method  
1439 is based on applying a small Gaussian uncertainty to the location of the seed hits, fitting an  
1440 initial track to these hits, then looking for additional hits that fall within the error of the initial  
1441 estimate, deeper in the tracker. These hits are added to the fit with their own uncertainties,  
1442 and the fit is re-calculated, each time attempting to minimize the mean-square estimation of the  
1443 error. The 5 helical trajectory parameters are extracted, and tracks with poor fits are discarded.

1444 A total of six iterations is used, each with a different starting seed or kinematic requirement  
1445 on the  $p_T$  of the track, as well as the transverse and longitudinal distance from the reconstructed  
1446 vertex [118]. The first iteration is seeded by three hits in the pixel detector. The second, is  
1447 seeded by two hits in the pixel detector and a pixel vertex, which is formed when at least four  
1448 pixel tracks point back to a common origin. The third iteration is seeded once again by three  
1449 hits in the pixel detector, except with a looser minimum  $p_T$  cut. The fourth iteration uses seeds  
1450 from any three hits in the pixel detector or silicon tracker, with at least one hit coming from the  
1451 pixel detector. In the fifth iteration seeds are formed from the inner two rings of the TIB, TID,  
1452 and TEC. The final iteration begins with seeds from the first two rings of the TOB and the fifth  
1453 ring of the TEC.

## 1454 5.2 Calorimeter Clustering

1455 The clustering algorithm is used to detect the energy and direction of stable, neutral particles  
1456 such as photons and neutral hadrons [116]. It also separates the energy contributions from  
1457 the neutral and charged hadrons, and provides an additional energy measurement for charged  
1458 hadrons with very low or high  $p_T$  tracks, both cases that degrade the energy resolution. Finally,  
1459 the clustering algorithm properly accounts for bremsstrahlung energy losses from electrons. The  
1460 algorithm is performed independently for the ECAL barrel, ECAL endcaps, HCAL barrel, and  
1461 HCAL endcaps. In the HF, no clustering algorithms are used, as each cell is used as its own  
1462 cluster in an event.

1463 The clustering algorithm begins by identifying "cluster seeds", which are the highest  $p_T$  cells  
1464 above a defined energy threshold [116]. Then, "topological clusters" are formed by grouping

1465 adjacent cells together with energy above 80 MeV in the ECAL barrel, 300 MeV in the ECAL  
 1466 endcaps, and 800 MeV in the HCAL. As a new cell is added, the total cluster energy and  
 1467 position is updated until no new cells are able to be added. Each cluster seed thus gives rise  
 1468 to a "particle-flow cluster". Each of these clusters is used as a candidate to be associated with  
 1469 tracks during the third stage of the algorithm, the linking step.

### 1470 5.3 Calorimeter Energy Calibration

1471 One of the most critical steps in reconstructing particles is the calorimeter energy calibration,  
 1472 which is the conversion of calorimeter scintillator light and photodetector current to the energy  
 1473 deposited in the calorimeter by the particle traversing it. This is done by exposing the crystals  
 1474 to particles of a known energy, using large samples of cosmic ray muons, by measuring minimum-  
 1475 bias events assuming a  $\phi$  symmetry, the of  $\pi^0$  and  $\eta^0$  meson resonances decaying into photons,  
 1476 and  $W$  and  $Z$  bosons into electrons.

1477 Before installation at P5, the ECAL and HCAL were pre-calibrated using test beam. In  
 1478 2006, the ECAL was exposed to an electron beam with energies between 15 and 250 GeV [119]  
 1479 at CERN. Additionally, intercalibrations between crystals were performed with 90 and 120 GeV  
 1480 beams. Also at CERN in 2006, the HCAL was calibrated, prior to installation using a beam of  
 1481 50 GeV pions [120].

1482 Once both calorimeters were installed, the detectors were calibrated with cosmic ray muon  
 1483 events in 2007 with the CMS magnet de-energized during the CRUZET (Cosmic RUn at ZZero  
 1484 Tesla) data taking campaign, and again with the CMS field on in 2008 during the CRAFT  
 1485 (Cosmic Run At Four Tesla) campaign. Shortly after the CRAFT campaign, the LHC delivered  
 1486 450 GeV proton beams to collimator targets upstream of the CMS detector, creating accelerator  
 1487 muons that are additionally used to calibrate the detector response. The ECAL encap energy  
 1488 resolution was improved from 7.6% to 6.3%, and in the barrel, the intercalibrations from the test  
 1489 beam were validated at a 2% level of agreement [121]. The HCAL energy calibration resulted in  
 1490 5% energy resolution in the HB, 10% in the HE, 12% in the HF, and 5% in the HE[122].

1491 After an initial set of data collection three independent calibration methods are combined to  
 1492 determine the absolute energy scale and intercalibration coefficients for the crystals [?]. The first  
 1493 method uses a large amount of data collected from minimum-bias trigger events, events which  
 1494 are dominated by glancing collisions and QCD jet production. The processes that contribute  
 1495 to these events have final state particles symmetrically distributed in the  $\phi$  coordinate. By  
 1496 grouping the crystals into rings of  $\eta$ , and the response of each crystal can be determined and  
 1497 modified such that it matches the average crystal response in that  $\eta$  ring, with the uncertainty on

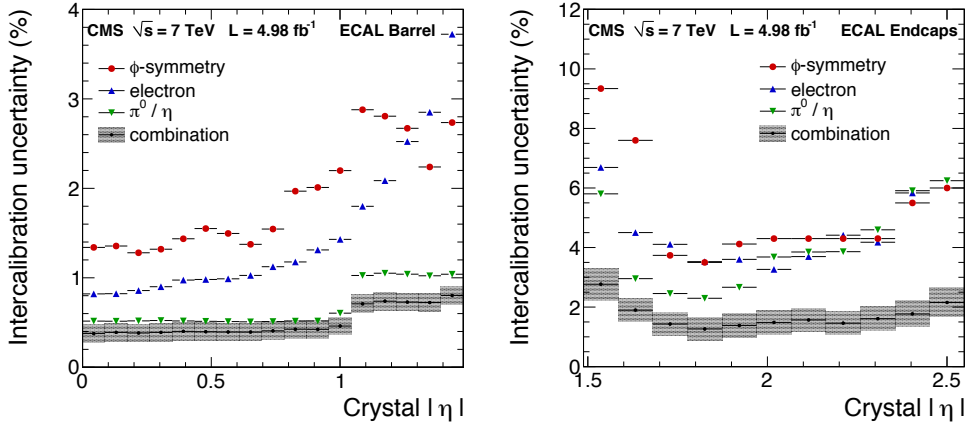


Figure 5.1: Results of the uncertainty on the ECAL intercalibration coefficients for the barrel (left) and endcaps (right)

1498 the average representing the uncertainty on the intercalibration coefficient. The second method  
 1499 involves reconstructing the resonances of the  $\pi^0$  and  $\eta^0$  mesons decaying to two photons and  
 1500 relying on the high-precision measurements from other experiment to determine the exact mass  
 1501 of the resonance. Events near the resonance of these two particles are once again divided into  
 1502 rings of  $\eta$ , and averaged over the  $\phi$  coordinate. Decays of the  $Z$  boson an electron pair is also  
 1503 used to determine the absolute scale (ADC counts/GeV) of the crystals, once again relying on  
 1504 the higher-precision measurements of previous experiments for the location of the mass peak.  
 1505 Finally, comparisons between the energy measured in the tracker and that measured in the  
 1506 ECAL are made from  $W$  and  $Z$  boson decays to a electrons. Figure 5.1 shows the results of  
 1507 combining all three methods, to determine the uncertainty of the intercalibration coefficients.

1508 The ECAL also has a strong dependence on the rate of instantaneous luminosity that the  
 1509 crystals are exposed to. It is therefore necessary to perform additional crystal calibrations as  
 1510 a function of time during a run of data collection. Blue and orange LED light, and blue laser  
 1511 light is fed through a network of optical fibers to each crystal. A known amount of light is  
 1512 injected and the crystal response is measured. Figure 5.2 shows a plot of the crystal response  
 1513 versus time. Rings of  $\eta$  are formed and crystals within the same  $\eta$  ring are used to calculated  
 1514 an average response, as is done in the intercalibration procedures described above.

1515 The performance of the HCAL calibration to the 50 GeV pion beam is validated by comparing  
 1516 energy measurements in the tracker to energy deposits in the HCAL [123]. Since neutral hadrons  
 1517 contribute approximately 10% of the energy contained in a jet, it is necessary to recalibrate the  
 1518 measured energy in the HCAL using simulated events where the true hadronic energy is known.  
 1519 The equation for the total calorimeter energy is given by:

$$E_{\text{calib}} = a + b(E, \eta)E_{\text{ECAL}} + c(E, \eta)E_{\text{HCAL}} \quad (5.1)$$

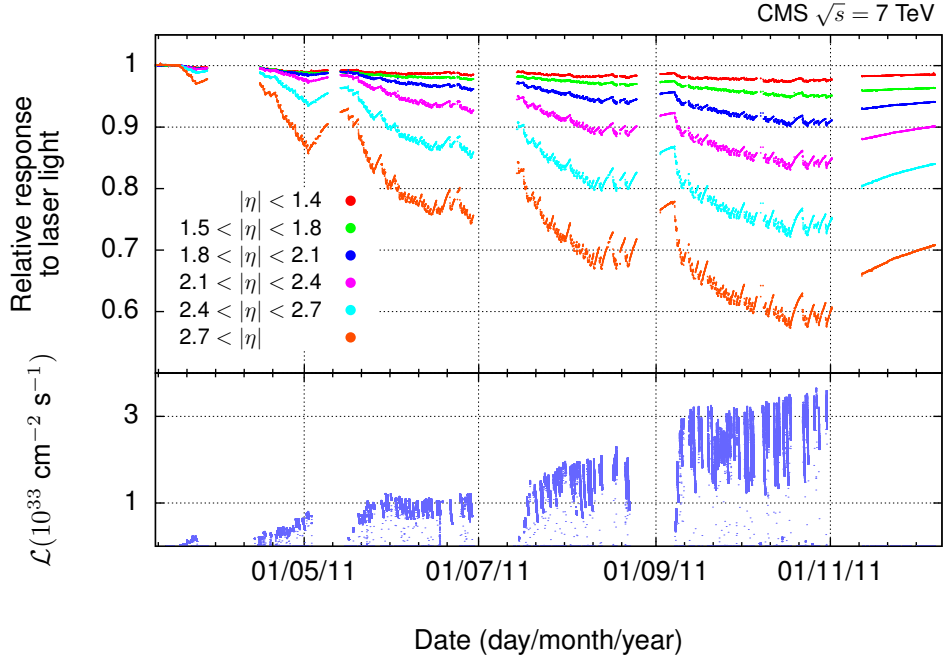


Figure 5.2: Instantaneous luminosity response to the crystals as measured by the laser and LED system. Additional crystal calibration constants are derived to normalize the crystal response over the range of collected data

1520 The coefficients, a, b, and c are determined through a  $\chi^2$  minimization procedure over each bin  
 1521 of energy, minimizing the difference between the reconstructed and true energies and solving for  
 1522 the parameters a, b, and c. Figure 5.3 shows the resulting HCAL energy resolution as a function  
 1523 of energy, and the values of the coefficients a, b, and c.

## 1524 5.4 Linking

1525 Once clusters are formed in the ECAL and HCAL barrels and endcaps, they are associated with  
 1526 nearby tracks in the pixel and silicon tracker in the phase of the particle-flow algorithm known  
 1527 as linking [116]. Single particles are formed out of the tracks and calorimeter clusters without  
 1528 double counting contributions from different detectors, forming "blocks" of linked elements. Due  
 1529 to the high granularity of each sub-detector, blocks of two-four elements are typical.

1530 The linking procedure between pixel and silicon strip tracks and the calorimeter deposits  
 1531 occurs in a three steps: extrapolating the track to the ECAL preshower (PS); then to the ECAL  
 1532 to a depth corresponding to the maximum longitudinal shower profile; and finally to the HCAL  
 1533 to a depth corresponding to one interaction length. A track is then linked to a cluster if it  
 1534 falls within the cluster boundaries. One HCAL cluster may be associated to many tracks, but  
 1535 each track can only be associated with a single cluster, determined as the track with the shortest

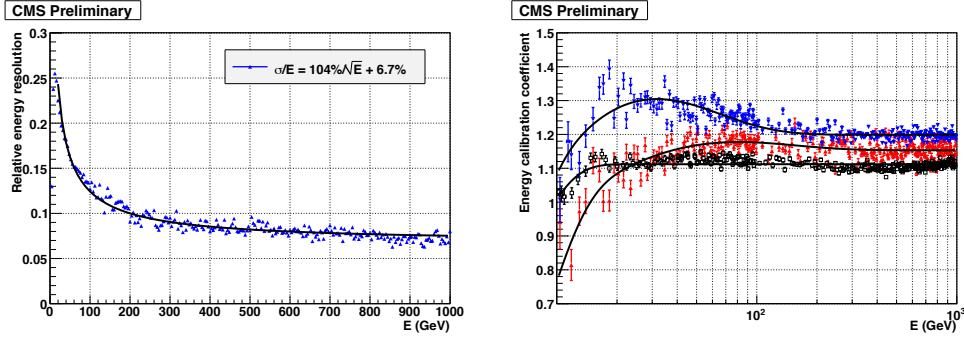


Figure 5.3: Results of using a  $\chi^2$  minimization procedure to estimate the neutral hadron energy contribution in the HCAL using simulated events

1536 distance. For the ECAL, one track may be associated with many energy clusters, since they may  
 1537 have originated from hadronic shower fluctuations, so links to tracks should be preserved to avoid  
 1538 double counting the hadron energy. In order to account for the bremsstrahlung energy losses of  
 1539 electrons, tangent lines to the tracks are linked to the ECAL. If this extrapolated, tangent track  
 1540 falls within the ECAL cluster boundaries, it becomes a candidate for a bremsstrahlung photon  
 1541 from an electron. Since the ECAL has a finer granularity than the HCAL, clusters of the ECAL  
 1542 are linked to HCAL clusters if an ECAL cluster falls within the boundary of the HCAL cluster.  
 1543 Finally, linking between the muon chambers and the inner tracker occurs via a  $\chi^2$  fit to a muon  
 1544 trajectory that would traverse the entire detector.

## 1545 5.5 Physics Object Reconstruction

1546 Once tracks have been formed from the muon chambers, pixel, and silicon tracker detectors  
 1547 and linked to clusters in the ECAL and HCAL, particles can be reconstructed. The process  
 1548 begins by reconstructing muons, then electrons and photons, finishing with charged and neutral  
 1549 hadrons. The charged and neutral hadrons are then clustered together to make jets, which  
 1550 can be tagged as  $\tau$  or  $b$ -jets. After each object is formed, the tracks and calorimeter energy  
 1551 depositions associated with it are removed from the collection of blocks that are used to form  
 1552 the particle-flow candidates, ensuring that no double counting of energy contributions is taking  
 1553 place.

### 1554 5.5.1 Muon Reconstruction

1555 The reconstruction of physics objects in the particle-flow algorithm begins by identifying muons  
 1556 [116]. The algorithm begins by identifying tracks in the pixel and silicon strip detectors that have  
 1557 been linked to tracks in the muon chambers, and fit with a muon trajectory with a minimum

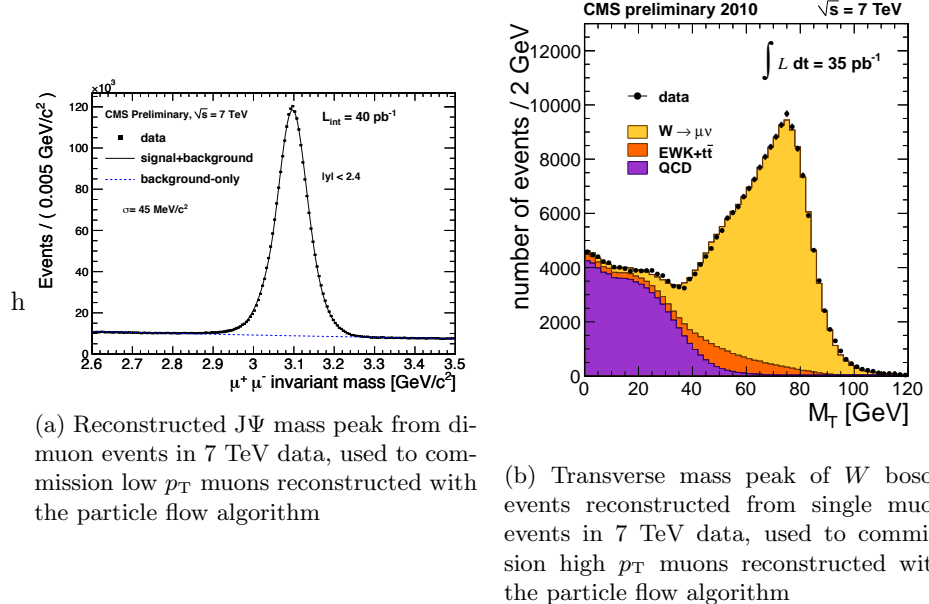


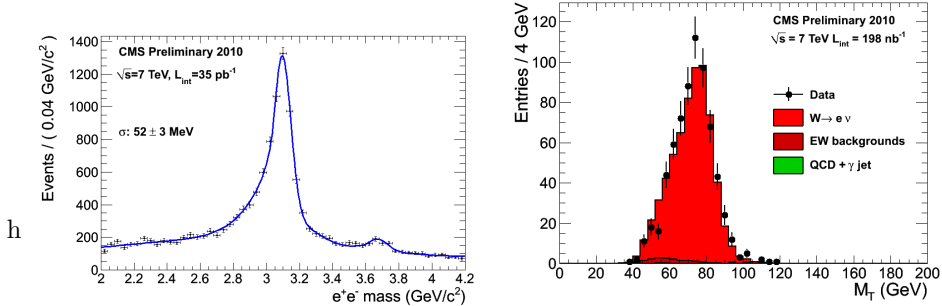
Figure 5.4: Muon validation plots for the particle-flow reconstruction

1558  $\chi^2$ . Additionally, it is required that muon track that is fit with both muon chambers, pixel,  
1559 and silicon tracker information is compatible within 3 sigma, to a track fit with the pixel and  
1560 silicon tracker information alone. When the "particle-flow" muon is removed from the collection  
1561 of candidate blocks, the muon tracks, and based on studies from the CRAFT data run, 3 (0.5)  
1562 GeV  $\pm 100\%$  is removed from the HCAL (ECAL) cells that the muon traverses.

1563 In 2010, 7 TeV data was collected [124] in order to commission the reconstruction of muons.  
1564 The  $J/\Psi$  resonance at 3.1 GeV provides a large number of low  $p_T$  di-muon pairs. Figure 5.4(a)  
1565 shows the reconstructed  $J/\Psi$  mass with  $40 \text{ pb}^{-1}$  of data. High  $p_T$  muons are commissioned by  
1566 reconstructing the  $W$  boson mass. Figure 5.4(b) shows the results the first  $35 \text{ pb}^{-1}$  of 7 TeV  
1567 data.)

### 1568 5.5.2 Electron Reconstruction

1569 The next stage in particle-reconstruction is the identification of electrons [116]. Electrons leaves  
1570 hits in the tracker and deposits most of its energy into the ECAL, with the clustering widest  
1571 in the  $\phi$  direction due to bremsstrahlung. Electron tracks tend to be shorter and lose energy  
1572 in the tracker due to bremsstrahlung, a highly non-linear process, that the Kalman fitter used in  
1573 the track identification phase is not optimized for. These tracks are re-fit using the Gaussian  
1574 Sum Filter (GSF) algorithm [125]. This algorithm accounts for the change in trajectory of the  
1575 electron due to bremsstrahlung, extending the linking to ECAL clusters in the  $\phi$  direction. Blocks  
1576 that have GSF tracks linked to ECAL clusters, including clusters identified as bremsstrahlung  
1577 photons, and additionally linked to a HCAL cluster with a much smaller energy deposition than



(a) Reconstructed  $J/\psi$  mass peak from di-electron events in 7 TeV data, used to commission low  $p_T$  electrons reconstructed with the particle flow algorithm

(b) Transverse mass peak of  $W$  boson events reconstructed from single electron events in 7 TeV data, used to commission high  $p_T$  electrons reconstructed with the particle flow algorithm

Figure 5.5: Electron validation plots for the particle-flow reconstruction

1578 in the ECAL are then identified as a "particle-flow electron".

1579 Similarly to the muons, the electron identification from the particle-flow algorithm was com-  
 1580 missioned using 7 TeV data collected in 2010. Low  $p_T$  electrons were commissioned from the  
 1581  $J/\psi$  mass peak, shown in figure 5.5(a) and high  $p_T$  electrons were commissioned from  $W$  boson  
 1582 decays, shown in figure 5.5(b).

### 1583 5.5.3 Charged Hadron Reconstruction

1584 Charged hadrons are reconstructed next in the particle flow algorithm [116]. Tracks linked to  
 1585 both ECAL and HCAL energy deposits give rise to "particle-flow charged hadrons" if calorimeter  
 1586 energy is compatible measured from the curvature of the tracks in the pixel and silicon detector.  
 1587 A fit is then performed between all of the tracks and the HCAL energy clusters to determine an  
 1588 optimally measured momentum. In the case where there is only one track, this fit reduces to a  
 1589 weighted average between the track and HCAL energy clusters.

### 1590 5.5.4 Photon and Neutral Hadron Reconstruction

1591 The next step in the algorithm is to identify ECAL and HCAL energy clusters that aren't linked  
 1592 to tracks or clusters that are linked to tracks, but have a much larger energy measurement . In  
 1593 the latter case, blocks are kept if the excess energy in the calorimeter clusters is larger than the  
 1594 energy resolution of the calorimeter. In both cases, if the total energy excess in the HCAL is  
 1595 larger than the energy measured in the ECAL, than a "particle-flow photon" is created using the  
 1596 energy in the ECAL and the remaining HCAL energy forms a "particle-flow neutral hadron",  
 1597 with calibrations performed in the manner described in section 5.3. In the case where the ECAL  
 1598 energy is larger than the HCAL energy, both cluster energies form a particle-flow photon. This is

1599 justified the observation that, in jets, the neutral component of the hadronic energy only deposits  
 1600 3% of the total jet energy in the ECAL, compared to 25% of the jet energy from photons.

### 1601 5.5.5 Jet Reconstruction

1602 After the formation of photons, charged and neutral hadrons, jets can be formed by clustering  
 1603 groups of these objects together based on their momentum weighted, spatial separation from  
 1604 one another. This clustering procedure is performed with the anti- $k_T$  algorithm [126]. The  
 1605 momentum weighted spatial separation function between two particles,  $i$  and  $j$ , is defined as:

$$d_{ij} = \min\left(\frac{1}{p_{iT}^2}, \frac{1}{p_{jT}^2}\right) \frac{\Delta_{ij}^2}{R^2} \quad (5.2)$$

1606 where  $\Delta_{ij}^2 = (y_i - y_j)^2 + (\phi_i - \phi_j)^2$  and  $y_{i,j}$  is the rapidity, and  $\phi$  is the azimuthal angle in the  
 1607 CMS detector.  $R$  is the distance parameter, which is a user-defined quantity for the algorithm.

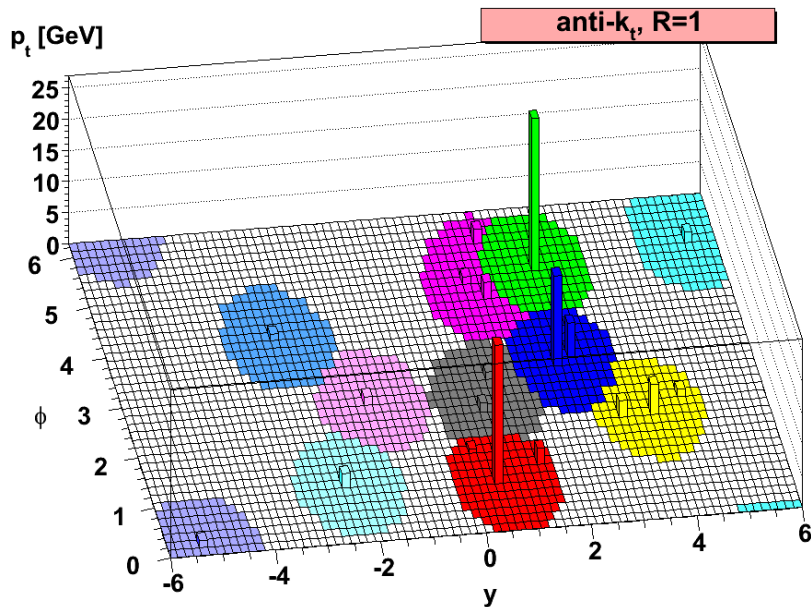


Figure 5.6: The anti- $k_T$  jet clustering algorithm with distance parameter  $R=1.0$

1608 The algorithm proceeds by looping over all of the particle-flow candidate objects that have  
 1609 been formed and calculates the quantity  $d_{ij}$ , and combines the two objects with smallest value,  
 1610 into a single object. The process is repeated until the smallest value,  $d_{ij}$  has a value  $d_{ij} > \frac{1}{p_{iT}^2}$  for  
 1611 all remaining pairs. The parameter,  $d_{ij}$ , will be larger for two small  $p_T$  objects, when compared  
 1612 to a pair of equally spatially separated high  $p_T$  objects. Thus, softer particles will cluster around  
 1613 harder objects before clustering amongst themselves. No hard particles are present, within the  
 1614 distance parameter, then the object will accumulate soft particles in a circle of radius  $R$ . The  
 1615 tendency is to produce circular jets, but in the case where a soft  $p_T$  cluster intersects with a hard

<sub>1616</sub>  $p_T$  cluster, objects the  $1/p_T^2$  weighting will tend to favor clustering around the harder  $p_T$  object.  
<sub>1617</sub> Figure 5.6 shows an example of the results of an anti-kt algorithm with distance parameter R  
<sub>1618</sub> = 1.0, in the azimuthal-rapidity coordinate system. An example of the preferential grouping  
<sub>1619</sub> around harder  $p_T$  objects can be seen at  $\phi = 5, y = 2$ .

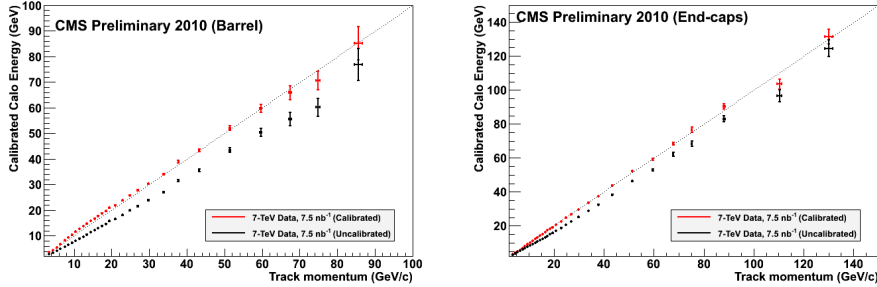


Figure 5.7: Commissioning of the particle-flow algorithm on jets, involved comparing the energy measured from charged hadron tracks, to energy measured in calorimeter clusters linked to the tracks

<sub>1620</sub> In 2010, the particle-flow algorithm for jet reconstruction was commissioned with 7 TeV data  
<sub>1621</sub> [127]. The calibration procedure involved selecting charged hadrons from tracks in the pixel and  
<sub>1622</sub> silicon strip detector, and comparing the energy measured there to the energy measured in the  
<sub>1623</sub> calorimeter. After calibration, the measurements between tracker and calorimeter agree within  
<sub>1624</sub> error bars up to 100 GeV, as shown in figure 5.7.

## <sub>1625</sub> Hadronic Tau Reconstruction

<sub>1626</sub> Tau leptons are unstable particles which decay via a weak interaction to lighter particles. If it  
<sub>1627</sub> decays hadronically via a  $W$  boson to two quarks, the tau lepton can be reconstructed analyzing  
<sub>1628</sub> the resulting jets that are clustered by the anti-kt algorithm. Tau jets are characterized by the  
<sub>1629</sub> number of charged hadrons produced in the decay. Since charge must be conserved, this results  
<sub>1630</sub> in one charged hadron being produced  $\sim 85\%$  of the time, known as a "one-pronged" decay, and  
<sub>1631</sub> three charged hadrons being produced  $\sim 15\%$  of the time, known as a "three-pronged" decay.  
<sub>1632</sub> Thus, a tau jet is identified as a jet with only 1 or 3 tracks associated with the calorimeter cluster.  
<sub>1633</sub> Additionally, the jets from hadronic tau decays tend to have their energy more collimated than  
<sub>1634</sub> jets produced from quarks or gluons. Jets are clustered twice, using two different distance-  
<sub>1635</sub> parameters. The ratio of energies of the smaller to the larger of the distance parameter jets is  
<sub>1636</sub> used to determine how collimated a jet is. If the ratio is within a given threshold, determined by  
<sub>1637</sub> the analyst in terms of the reconstruction efficiency and fake rate, the jet is tagged as a hadronic  
<sub>1638</sub> tau jet.

1639 **b-Tagging**

1640 Jet that originate from  $b$ -quarks have unique characteristics that allow them to be distinguished  
1641 from jets originating from other quarks or gluons. This identification process is known as  $b$ -tagging.  
1642 Several algorithms exist to identify  $b$ -jets, since there are many kinematic variables  
1643 that distinguish them from other jets. Due to the heavier nature of the  $b$ -quark,  $b$ -jets have  
1644 a larger transverse momentum compared to lighter-flavor quarks. Since it belongs to the third  
1645 quark generation, it is much more likely to find a non-prompt lepton embedded in the jet. Muons  
1646 are especially useful to tag  $b$ -jets since the information they leave in the tracker can be used to easily  
1647 identify if it came from prompt decay or not.

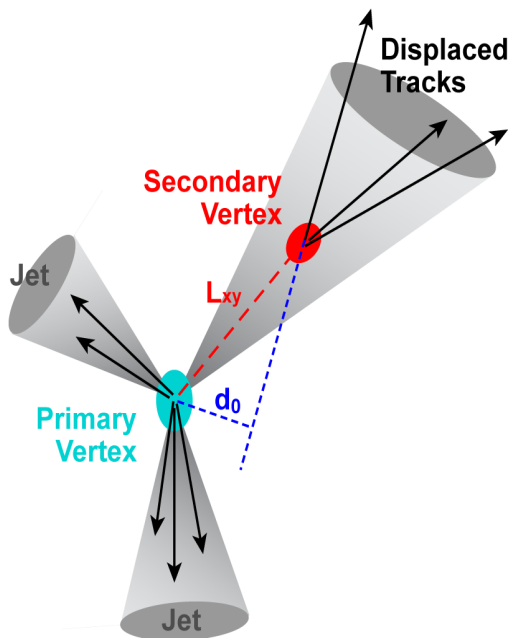


Figure 5.8: A  $b$ -meson will travel a distance  $L_{xy}$  before decaying and creating a secondary vertex. The impact parameter,  $d_0$  measures the longitudinal displacement of the two vertices

1648 The most important characteristic of the  $b$ -quark is its relatively long lifetime compared to  
1649 lighter-flavor quarks. The consequence is that a  $b$ -meson will travel a very small, but observable  
1650 distance within the tracker before it decays, forming a secondary vertex. The distance and  
1651 uncertainty measured on the distance between the primary and secondary vertex is then used as  
1652 discriminating variables to tag  $b$ -jets. Figure 5.8 shows a cartoon of a  $b$ -jet creating a secondary  
1653 vertex after traveling some distance from the primary vertex.

1654 **5.5.6 Missing Transverse Energy Reconstruction**

1655 CMS has a hermetic design to ensure that all particles produced in a collision would pass through  
1656 the detector. Only long-lived, neutral particles avoid detection, such as neutrinos in the standard

<sup>1657</sup> model. Many BSM theories, such as SUSY, are also characterized by stable, neutral particles.  
<sup>1658</sup> These particles can only be detected by measuring a momentum imbalance after measuring all  
<sup>1659</sup> of the particles in the event.

<sup>1660</sup> The missing transverse energy (MET),  $\cancel{E}_T$ , is the vector sum of all of particle-flow candidates  
<sup>1661</sup> reconstructed in the event. It is defined as

$$\cancel{E}_T = \left| - \sum_{i=1}^{nPF} \vec{p}_{Ti} \right| \quad (5.3)$$

<sup>1662</sup> where nPF is the number of particle-flow candidates in the event, and  $\vec{p}_{Ti}$  is the vector sum of  
<sup>1663</sup> their transverse momentum.

<sup>1664</sup> The particle-flow algorithm for reconstructing MET was commissioned in 2010 with 7 TeV data  
<sup>1665</sup> [127]. Minimum-bias collisions and QCD multi-jet production are processes that produce no real  
<sup>1666</sup> MET. Therefore, a sample of these events were collected, allowing for the algorithm to be tuned  
<sup>1667</sup> and calibrated.

1668 **Chapter 6**

1669 **Analysis I: The first 5.08 fb<sup>-1</sup> of  
1670 8 TeV data**

1671 The search for  $t\bar{t}H$  production begins by identifying  $pp$  collisions consistent with the production  
1672 of a top quark pair with additional  $b$  jets. Top quarks decay  $\sim 100\%$  of the time to a bottom  
1673 quark and a  $W$  boson, and the  $W$  boson can decay either into a charged lepton and a neutrino  
1674 or into a pair of quarks. Since there are two  $W$  bosons in the event, the decays of the  $W$   
1675 bosons determine the specific top pair signatures recorded in the detector. The decay of the two  
1676  $W$  bosons define the categorizations of  $t\bar{t}$ -like events as either all-hadronic, in the case of zero  
1677 charged leptons; semi-leptonic, in the case of one charged lepton; and di-leptonic in the case of  
1678 two charged leptons. the detector. This analysis describes the Lepton+Jets (LJ) channel, where  
1679 one of the  $W$  bosons has decayed to an electron or a muon and the corresponding neutrino,  
1680 while the other  $W$  boson decays into two quarks. To compensate for the low production rate,  
1681 the analysis is optimized to search for the Higgs boson decaying to a  $b$ -quark pair. The final  
1682 state is then  $l\nu qqbbbb$ , where  $l$  refers to either an electron or a muon. In the case of an ideal  
1683 reconstruction of the event, the LJ signal events contains six jets, four of which are  $b$ -tagged.  
1684 However, to accommodate jets lost to detector acceptance and merging between separate partons,  
1685 and the  $b$ -tagging efficiency, events with four or more jets and two or more  $b$ -tags are included  
1686 in the signal region.

1687 The largest background contribution is  $t\bar{t}$ +jets production. This process can be decomposed  
1688 in terms of the flavor of the extra jets produced in the event. For this analysis, the inclusive  
1689  $t\bar{t}\text{jets}$  process is broken into three sub-processes:  $t\bar{t}$ + light flavor jets where one or more of the  
1690 jets is mistagged,  $t\bar{t} + c\bar{c}$  and  $t\bar{t} + b\bar{b}$ . Smaller background contributions come from  $W$ +jets,  
1691  $Z$ +jets, single top quark, diboson, and  $t\bar{t} + W/Z$  production.

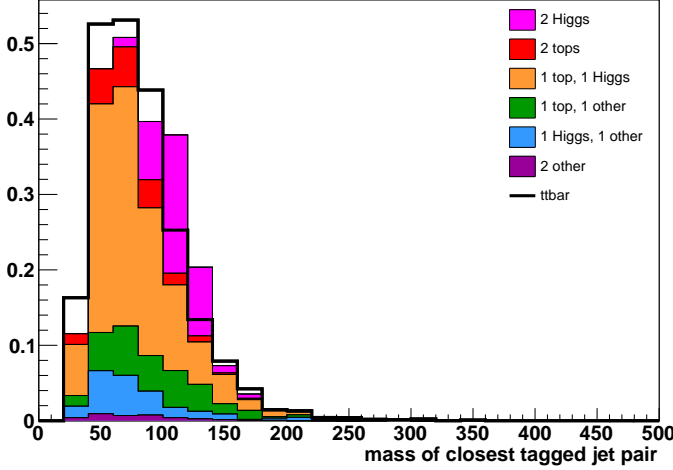


Figure 6.1: This figure shows the breakdown of jet-to-parton assignments for the two jets with the minimum  $\Delta R$  separation in the event for events with greater or equal 4  $b$ -tagged jets.

In other Higgs searches involving the decay to two  $b$ -quarks, the most powerful discriminating variable is the invariant mass of the  $b\bar{b}$  pair, which has a peak at the mass of the Higgs. However, for  $t\bar{t}H$  production, with a final state of four  $b$ -quarks, the combinatorics of selecting the quarks coming from the Higgs, instead of the  $t\bar{t}$  system, prevents the reconstruction of a clear resonant peak, as shown in figure 6.1. This results in an additional loss of mass resolution, or smearing, on the  $b\bar{b}$  invariant mass spectrum.

Although there is poor resolution on the Higgs boson resonance in the  $b$ -quark dijet mass spectrum, there are a number of kinematic variables that can be used to discriminate between the  $t\bar{t}$ +jets background and the  $t\bar{t}H$  signal. For example, the recoil of the Higgs off of the  $t\bar{t}$  system, the decay products of the top quarks from the  $t\bar{t}H$  signal will have, on average, a slightly larger component of momentum transverse to the beam-line. Additionally, the larger number of authentic  $b$ -jets in  $t\bar{t}H$  events can be exploited through the likelihood value returned by a  $b$ -tagging algorithm for all of the jets in the event. By themselves, none of these variables provide a large degree of discriminating power to separate the  $t\bar{t}H$  signal from the large, and kinematically similar background. Therefore, the discriminating power of several variables is combined using a multivariate analysis technique (MVA), which is used to set upper limits on  $t\bar{t}H$  production in the data set.

The following sections will describe the analysis that was carried out on the first  $5\text{ fb}^{-1}$  of data collected by the CMS detector. This includes definitions of the simulated samples used to estimate the expected backgrounds in data, the event selection used to isolate the  $t\bar{t}H$  signal, the application of MVA techniques, evaluation of systematic uncertainties, and upper limit setting on the production rate of  $t\bar{t}H$ .

## **6.1 Data and Simulated Samples**

*pp* collision data is collected by the CMS detector, as described in previous chapters. The signal and background signatures are estimated using Monte Carlo simulation techniques. The simulation involves the combination of the most current theoretical and empirical information about the interactions of the known particles. The simulation of an event is decomposed into a sequence of calculations and each signal and background process is calculated separately. Information about Monte Carlo event simulation techniques is taken from reference [128].

The first stage of event simulation for a given signal or background process is to calculate the probability that some set initial state particles with a certain momentum will create a final state of particles with a certain momentum. For example, in the case of the  $t\bar{t}H$  signal, this is the probability that two protons traveling towards each other along the z-axis (beam-line), each with a given energy and momentum, will produce a top quark pair and a Higgs boson, each with some momentum vector,  $\hat{p}_t$ ,  $\hat{p}_{\bar{t}}$ ,  $\hat{p}_H$ , which points into the hermetic CMS detector. As discussed in section 2.1, this probability is calculated by examining the Lagrangian of the theory describing the process and calculating its scattering amplitude, to some order in perturbation theory, using the Feynman rules derived from the Lagrangian. The scattering amplitude is a multi-dimensional probability function, which depends on the initial and final state momentum of the particles in the process. Thus, given some initial state momentum,  $p_i$ , it tells you the probability to produce a final state particle with momentum  $p_f$ . It is understandable that the scattering amplitude is often referred to as a matrix element, since given a vector of initial state particles with a certain momentum, the scattering amplitude would be a matrix, whose elements would give the probability of creating the vector of final state particles.

Since protons are composite objects, when they collide, it is their quarks or gluons which are actually interacting. The momentum distribution of each of the valence quarks, the gluons, and the sea quarks, which account for quantum fluctuations that temporarily create all other quark flavors inside the proton, is described by a Parton Distribution Function (PDF). The PDF describes what fraction of the proton's momentum is distributed among each of its constituents. Due to the large strength of the QCD interactions that bind the quarks together, the PDF cannot be calculated perturbatively from QCD. It has been measured empirically, and is composition of the results of several experiments over the past decades.

Event generator algorithms are computer programs that, given a Lagrangian of particle theory, will calculate the matrix element for a given process. Then, the generator is provided with values of the momentum of the initial state particles. For protons, this would be the beam energy of the LHC. To assign momentum values to the constituent quarks or gluons that actually participate in the interaction, random values are sampled from the probability distributions

1749 described by a PDF that is provided to the algorithm. Given a choice of momentum for the  
1750 input particles, a value and direction of the momentum for each of the final state particles is  
1751 sampled from the probability function provided by the calculated the matrix element (ME). The  
1752 process of randomly sampling a probability function, in order to conduct a calculation, is known  
1753 as a Monte Carlo sampling technique.

1754 In the case where final state particles are quarks or gluons, also known as partons, an ad-  
1755 ditional calculation is necessary to create the physical hadron states. First, the decay sequence  
1756 of each parton is calculated until the decay products reach a user defined value, known as the  
1757 hadronization scale. This decay sequence is referred to as the parton shower (PS), since each  
1758 parton creates a multitude, or a shower, of additional partons. Once the parton shower is cal-  
1759 culated, each of the colored partons are transformed into color-singlet primary hadrons, which  
1760 themselves decay, and form secondary hadrons. This process, known as hadronization, results in  
1761 a collimated spray of hadrons, each with a component of momentum along the original parton's  
1762 direction. These hadrons are clustered together and referred to as a hadron jet.

1763 Once the hadronization is completed, the next stage of the event generation is to simulate the  
1764 response of the CMS detector when this process occurs at the interaction point where the LHC  
1765 beams are made to collide. The Geant 4 detector simulation framework is used to create a model  
1766 of each and every detector element, electronic readout, and mechanical support structures that  
1767 make compose CMS. Geant 4 is also about to describe how energy is deposited into the different  
1768 types of material as a particle passes through each detector element, simulating the response  
1769 each element to presence of a particle in the detector. The digitization and signal acquisition of  
1770 the electronics that read-out the detector elements is also simulated.

1771 The final stage the generation of an event is the reconstruction of the simulated detector  
1772 signals into physics objects. This process is described in detail in the previous chapter. It  
1773 proceeds with simulated, instead of real detector signals.

1774 The entire event simulation, reconstruction, and subsequent analysis is implemented in a  
1775 software framework that is known as CMS Software (CMSSW).

### 1776 6.1.1 Data Samples

1777 The results presented here are based on the first  $5.08\text{ fb}^{-1}$  of the 2012 CMS dataset. Data-sets  
1778 are collected through HLT triggers and stored offline for analysis. Table 7.1 lists the datasets  
1779 used for this analysis, which is composed of two runs of data collection triggered on the presence  
1780 of one muon or electron in an event. The luminosities are quoted from a calculation performed  
1781 with minimum-bias events measured with the HF detector and have been determined to have a  
1782 2.2% uncertainty.

Dataset	Run Range	Integrated Luminosity
/SingleMu/Run2012A-PromptReco-v1/AOD	190645–193621	0.87 fb <sup>-1</sup>
/SingleMu/Run2012B-PromptReco-v1/AOD	193834–196531	4.21 fb <sup>-1</sup>
<b>Total SingleMu</b>	<b>190645–196531</b>	<b>5.08 fb<sup>-1</sup></b>
/SingleElectron/Run2012A-PromptReco-v1/AOD	190645–193621	0.87 pb <sup>-1</sup>
/SingleElectron/Run2012B-PromptReco-v1/AOD	193834–196531	4.21 pb <sup>-1</sup>
<b>Total SingleElectron</b>	<b>190645–196531</b>	<b>5.08 fb<sup>-1</sup></b>

Table 6.1: The datasets analyzed for this analysis.

### 1783 6.1.2 Signal Samples

1784 The  $t\bar{t}H$  signal is modeled using the Pythia Monte Carlo generator. Signal events were generated  
 1785 privately using the same conditions and configuration as the "Summer" MC campaign, which  
 1786 generated the background samples used in this analysis and is a central effort by a dedicated  
 1787 team of collaborators within the CMS experiment. The samples and associated cross sections  
 1788 used are listed in Table 7.2.

Mass	Dataset	Cross Sect.
110 GeV/c <sup>2</sup>	/TTH_HToAll_M_110_8TeV_FastSim_pythia6/lannon-TTH_HToAll_M_110_8TeV _FastSim_pythia6-dff75535147f54d9d70123289019ff88/USER	0.1887 pb
115 GeV/c <sup>2</sup>	/TTH_HToAll_M_115_8TeV_FastSim_pythia6/lannonTTH_HToAll_M_115_8TeV _FastSim_pythia6f8fb6149649333009ec8462da200312d/USER	0.1663 pb
120 GeV/c <sup>2</sup>	/TTH_HToAll_M_120_8TeV_FastSim_pythia6/puighTTH_HToAll_M_120_8TeV _FastSim_pythia695111b4e2be5b1aa536a508d15d97f92/USER	0.1470 pb
122.5 GeV/c <sup>2</sup>	/TTH_HToAll_M_122p5_8TeV_FastSim_pythia6/slaunwhj- TTH_HToAll_M_122p5_8TeV_FastSim_pythia61e2fdcc9a937df208692b27cb39e0444/USER	0.1383 pb
125 GeV/c <sup>2</sup>	/TTH_HToAll_M_125_8TeV_FastSim_pythia6/lwmingTTH_HToAll_M_125_8TeV _FastSim_pythia6191b19832235558f2b51f7486e9bfa14/USER	0.1302 pb
127.5 GeV/c <sup>2</sup>	/TTH_HToAll_M_127p5_8TeV_FastSim_pythia6_crabv2/jgwoodTTH_HToAll _M_127p5_8TeV_FastSim_pythia6_crabv28cc2ab68d00e069563cff89a5be0e271/USER	0.1227 pb
130 GeV/c <sup>2</sup>	/TTH_HToAll_M_130_8TeV_FastSim_pythia6/neuTTH_HToAll_M_130_8TeV _FastSim_pythia65052c957a6363e9b1d5c2be444ffc86d/USER	0.1157 pb
135 GeV/c <sup>2</sup>	/TTH_HToAll_M_135_8TeV_FastSim_pythia6/lwmingTTH_HToAll_M_135_8TeV _FastSim_pythia6c8734ad98f674743d713309ea4b6ad34/USER	0.1031 pb
140 GeV/c <sup>2</sup>	/TTH_HToAll_M_140_8TeV_FastSim_pythia6/lwmingTTH_HToAll_M_140_8TeV _FastSim_pythia6cf0b11a8bdd755ec1ec3d7a35c9a88be/USER	0.09207 pb

Table 6.2: List of signal MC datasets and cross sections used to determine the SM expectation.

### 1789 6.1.3 Background Samples

1790 In order to estimate the rate and kinematic behavior of the backgrounds, this analysis primarily  
 1791 uses Monte Carlo (MC) samples from the "Summer12" MC campaign. Most of the samples are  
 1792 generated either with the Madgraph tree-level matrix element generator matched to Pythia for  
 1793 the parton shower, or with the NLO generator Powheg combined with Pythia. These samples  
 1794 are reconstructed with the same CMSSW version as the data samples listed above. Table 7.3  
 1795 lists the background MC samples and associated cross sections.

Sample	Dataset	Cross Sect.
$t\bar{t}$ +jets	/TTJets_MassiveBinDECAY_TuneZ2star_8TeVmadgraph-tauola/Summer12PU_S6_START52_V9v1/AODSIM	225.197 pb
$t\bar{t} + W$	/TTWJets_8TeVmadgraph/Summer12PU_S7_START52_V9v1/AODSIM	0.249 pb
$t\bar{t} + Z$	/TTZJets_8TeVmadgraph_v2/Summer12PU_S7_START52_V9-v1/AODSIM	0.208 pb
$W$ +jets	/WJetsToLNu_TuneZ2Star_8TeVmadgraphtarball/Summer12-PU_S7_START52_V9v1/AODSIM	36257.2 pb
$Z/\gamma^*$ + jets $M_{\ell\ell} > 50 \text{ GeV}/c^2$	/DYJetsToLL_M50_TuneZ2Star_8TeVmadgraphtarball/Summer12-PU_S7_START52_V9v2/AODSIM	3503.17 pb
$10 \text{ GeV}/c^2 < M_{\ell\ell} < 50 \text{ GeV}/c^2$	/DYJetsToLL_M10To50filter_8TeVmadgraph/Summer12-PU_S7_START52_V9v1/AODSIM	860 pb
Single $t$ schannel	/T_schannel_TuneZ2star_8TeVpowhegtauola/Summer12-PU_S7_START52_V9v1/AODSIM	3.79 pb
$t$ channel	/T_tchannel_TuneZ2star_8TeVpowhegtauola/Summer12-PU_S7_START52_V9v1/AODSIM	56.4 pb
$tW$	/T_tWchannelDR_TuneZ2star_8TeVpowhegtauola/Summer12-PU_S7_START52_V9v1/AODSIM	11.1 pb
Single $\bar{t}$ schannel	/Tbar_schannel_TuneZ2star_8TeVpowhegtauola/Summer12-PU_S7_START52_V9v1/AODSIM	1.76 pb
$t$ channel	/Tbar_tchannel_TuneZ2star_8TeVpowhegtauola/Summer12-PU_S7_START52_V9v1/AODSIM	30.7 pb
$tW$	/Tbar_tWchannelDR_TuneZ2star_8TeVpowhegtauola/Summer12-PU_S7_START52_V9v1/AODSIM	11.1 pb
$WW$	/WW_TuneZ2star_8TeV_pythia6_tauola/Summer12-PU_S7_START52_V9v1/AODSIM	54.8 pb
$WZ$	/WZ_TuneZ2star_8TeV_pythia6_tauola/Summer12PU_S7_START52_V9-v1/AODSIM	32.3 pb
$ZZ$	/ZZ_TuneZ2star_8TeV_pythia6_tauola/Summer12PU_S7_START52_V9-v1/AODSIM	7.7 pb

Table 6.3: List of background MC datasets and cross sections used for normalization.

### 1796 6.1.4 MC pileup reweighting

1797 During 2012 data collection, the LHC provided increasingly large instantaneous luminosities to  
 1798 the CMS experiment. Consequently, the average number of overlapping events reconstructed in  
 1799 single detector readout window has also increased. When these overlapping events, known as  
 1800 pileup events, occur within the same bunch crossing, which is referred to as "in-time" pileup.  
 1801 Alternatively, "out-of-time" pileup, comes from energy deposits in the detector from previous  
 1802 bunch crossings and from very early arrivals of particles from the forthcoming bunch crossing.  
 1803 Pileup events can affect many aspects of the reconstruction of a more interesting event, such as  
 1804 the degradation of lepton isolation and jet energy resolution. The simulated samples used in  
 1805 the analysis must also have the same distribution of pileup events as what was measured in the  
 1806 data.

1807 During the generation of the simulated samples used in the analysis, the average amount of  
 1808 expected pileup was unknown. Events were thus simulated with a conservatively large estimate  
 1809 of the pileup distribution, so that if the measured data revealed a smaller average value, the  
 1810 simulation could be reweighted to match the data. For the simulation, number of interactions  
 1811 is a user defined value added to every generated event. For the data, the number of pileup

interactions for each unit of time depends on the instantaneous luminosity for each bunch pair and the total inelastic cross section,  $\sigma_{inelastic}$ , of the proton. The value of  $\sigma_{inelastic} = 69.4$  mb was found to describe the data well. To estimate the effect of the systematic uncertainty of this choice, the value was varied by  $\pm 7\%$ .

To gauge the accuracy of the calibration of the pileup distribution used in the simulated samples, a comparison of the number of reconstructed vertices between data and the simulated  $t\bar{t}$  MC sample is shown in figure 7.1. The unweighted MC distribution is shown in blue, the reweighted distribution in red, and the measured data in black points. After reweighting, there is a good level of agreement between the data and MC distributions.

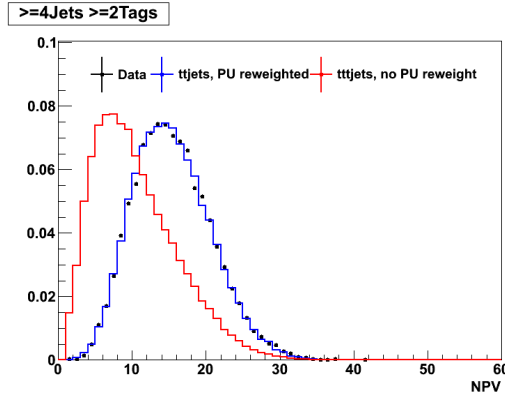


Figure 6.2: Comparison of number of reconstructed vertices for data (black) and the  $t\bar{t}$  MC sample before (blue) and after (red) pileup reweighting. After pileup reweighting, the MC matches the data well.

### 6.1.5 Additional Pileup Corrections

Studies comparing the Monte Carlo simulations to observed data revealed that the jet  $p_T$  spectra was not well modeled. Many sources of this discrepancy were investigated, but the clearest correlations arises when the 8 TeV data events are divided into three categories according to their amount of pileup:

- Low PU, number of primary vertices  $\leq 10$
- Medium PU, number of primary vertices from 11 to 15
- High PU, number of primary vertices  $\geq 16$

The modeling of jet  $p_T$  was worse for events with a larger number of pileup events overlapping in the detector. The same effect was present for the majority of the jets in the event, evidenced by the discrepancy in the  $H_T$  distribution, shown in figure 6.3, where  $H_T$  is defined as the scalar sum of the transverse momentum for reconstructed jets in the event:

$$H_T = \sum_i^{jets} p_T^i \quad (6.1)$$

The effect makes the data have a softer  $p_T$  spectrum than the simulations. The same effect was observed in 7 TeV data as well. It was present, even after employing several sophisticated reconstruction techniques designed to mitigate pileup effects. These techniques included the removal of charged hadrons in the particle-flow algorithm, not associated with the primary vertex and re-weighting the simulated samples to match the pileup distribution measured in the data.

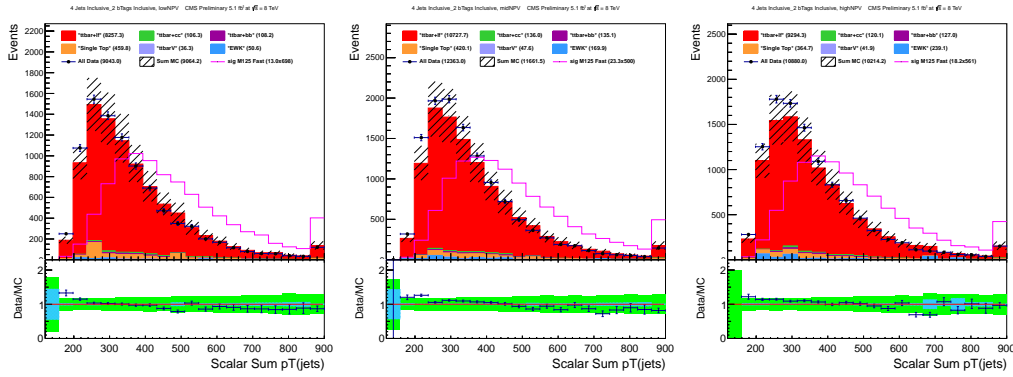


Figure 6.3:  $H_T$  distribution for 8 TeV lepton plus jet events with  $\geq 4$  jets and  $\geq 2$  tags shown for different amounts of pileup. The left-hand plot shows low pileup, the middle plot shows medium pileup, and the right-hand plot shows high pileup.

Although the exact underlying cause of the jet mis-modeling effect was not able to be identified, the magnitude of the effect seemed to be related to the number of pileup events. As such, an additional correction factor is needed to account for the remaining difference in pileup effects between data and Monte Carlo. The correction factor was calculated from data that was dominated by background events, with a single lepton,  $\geq 4$  jets, and  $\geq 2$  tags. The expected signal-to-background ratio in this sample is 0.002, which is low enough that the correction factor will not be biased by signal events. The correction factor is based on the  $H_T$  distribution for data and Monte Carlo for Low pileup (PU), Medium PU, and High PU events. The correction factor is the bin-by-bin ratio of the data and the Monte Carlo  $H_T$  distributions in each PU category. By preparing a separate correction factor for each PU category smaller adjustments were made to well-modeled Low PU events and larger adjustments to the poorly modeled High PU events.  $H_T$  shows the same mis-modeling as each of the jet  $p_T$ s and it effects all of the jet  $p_T$ s. This makes it a natural choice for a correction factor.

In order to evaluate the systematic shape uncertainty introduced by the correction factor, the uncorrected simulated distributions are used as  $-1\sigma$  systematic uncertainty and the  $+1\sigma$  uncertainty is determined by doubling the correction factor. The factor of two for the  $+1\sigma$

1855 variation is motivated by the desire to provide a large enough systematic uncertainty to cover  
 1856 any possible over-correction of the simulations. This is a reasonable choice because it creates a  
 1857 deviation that is the same size as the original observed difference between data and simulations.

1858 The correction factor and uncertainty improved the agreement between data and Monte  
 1859 Carlo. Figure 6.4 compares the  $H_T$  distributions before and after reweighting. The data-to-MC  
 1860 ratio plots are the clearest indicators of the improvement from the correction factor. Before the  
 1861 correction, the  $H_T$  ratio plot forms a line with a slope. After the correction the slope is gone.

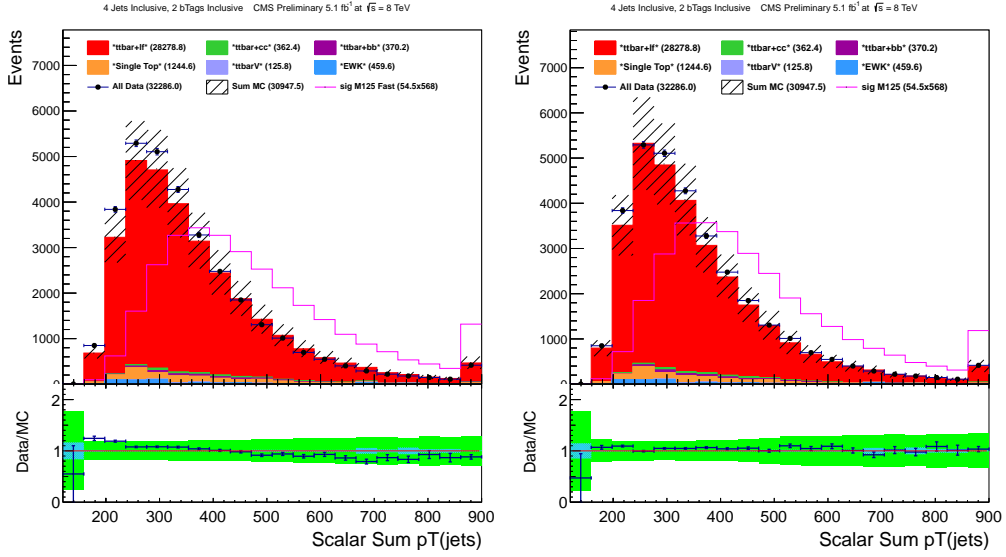


Figure 6.4:  $H_T$  distribution for 8 TeV lepton plus jet events with  $\geq 4\text{jets}$  and  $\geq 2\text{tags}$ . The left-hand plot shows the distribution before correction. The right-hand plot shows the distribution after correction. Note that the ratio in the right-hand plot is flatter than the left-hand plot.

## 1862 6.2 Event Selection

1863 This section defines the common physics objects and event selection requirements. Leptons are  
 1864 classified into two categories, tight and loose, defined for muons in section 6.2.3 and for electrons  
 1865 in 6.2.4. For this analysis, exactly one tight muon or exactly one tight electron is required and  
 1866 events with any additional loose leptons are rejected.

### 1867 6.2.1 Event cleaning

1868 For data and MC events, certain cuts are applied to remove events that are either non-physical  
 1869 or that come from non-collision events, such as instrumental noise or beam backgrounds. In the  
 1870 data, every event is required to pass the following filters:

- 1871 • CSC tight beam halo filter - Secondary particles are produced in showers which are ini-  
 1872 tiated by collisions of the beam with residual gas inside the LHC vacuum chamber or by

interactions of the particles with a large transverse emmitance with limiting apertures.

- HBHE noise filter with isolated noise rejection - this filters spurious signals from the HCAL barrel and endcap sub-detectors which are not associated with particles measured in a collision event.

- HCAL laser filter - ensures that data is not taken simultaneous with the laser calibration system

- ECAL dead cell trigger primitive (TP) filter - removes dead or noisy ECAL cells from being used in the reconstruction, these compose  $< 1\%$  of the total crystals in the ECAL

- Tracking failure - designed to catch events with too few tracks

- Noisy SCs in EE - new filter from the ECAL Detector Performance Group (PDG), and validated by the MET Physics Object Group (POG)

which are described in [129].

Additionally, beam scraping events are filtered based on the fraction of good tracks. At least 25% of tracks are required to be of high purity. Finally, every data event must contain at least one primary vertex (PV) that passes the following selection:

- The number of degrees of freedom used to find the PV must be larger than 4,
- The absolute value of the  $z$ -coordinate of the PV must be smaller than 24 cm,
- The absolute value of the  $\rho$ -coordinate of the PV must be smaller than 2 cm,
- The PV must not be identified as fake.

## 6.2.2 Trigger

Each data and MC event is required to pass one of the triggers in Table 6.4, which are a subset of the total number of SingleMu and SingleEle HLT triggers available. Muon+jet events must pass the SingleMu trigger, while electron+jet events must pass the SingleEle trigger.

Dataset	Trigger Name
SingleMu	HLT_IsoMu24_eta2p1_v*
SingleEle	HLT_Ele27_WP80_v*

Table 6.4: List of lepton+jets triggers

<sup>1896</sup> **6.2.3 Muon Selection**

<sup>1897</sup> In this analysis, muons are selected from the set of "particle-flow" muon" objects that have been  
<sup>1898</sup> reconstructed in the event. Muons are classified into two categories: tight and loose, according  
<sup>1899</sup> to the quality of their reconstruction. This is ensured by applying the selection cuts shown in  
<sup>1900</sup> Table 6.5. The cuts are defined as follows:

- <sup>1901</sup> •  $p_T$  - the component of the momentum transverse to the beam-line.
- <sup>1902</sup> • PFRelIso - this is the quantity known as relative isolation, computed by the particle flow  
<sup>1903</sup> algorithm. It is a ratio of the energy deposits remaining in the calorimeter and tracker,  
<sup>1904</sup> after the contribution from the muon has been removed, in a cone size  $\Delta R = 0.3$ , around  
<sup>1905</sup> the muon track.
- <sup>1906</sup> •  $|\eta|$  - the absolute value of the psuedorapidity of the muon
- <sup>1907</sup> • ID - This refers to whether the muon was reconstructed with a  $\chi^2$  fit to the tracks from  
<sup>1908</sup> the tracker only (tracker muon), the tracker and the muon chambers (global muon), or if  
<sup>1909</sup> the particle was reconstructed from the particle-flow algorithm (PFmuon)
- <sup>1910</sup> •  $N_{layers}(\text{tracker})$  - the number of layers in the tracker with hits used in the muon track  
<sup>1911</sup> reconstruction
- <sup>1912</sup> •  $X^2$  of track fit - the reduced  $\chi^2$  (raw  $\chi^2$ /Number of Degrees of Freedom in the fit), typically  
<sup>1913</sup> a value of 1 indicates the fit is describes the data well
- <sup>1914</sup> •  $N_{layers}(\text{pixel})$  - the number of layers in the inner pixel detector with hits used in the muon  
<sup>1915</sup> track reconstruction
- <sup>1916</sup> •  $N_{segments}(\mu)$  - the number of segments in the muon chambers used to the reconstruct the  
<sup>1917</sup> muon tracks
- <sup>1918</sup> •  $|d0(\text{BS})|$  - the absolute value of the transverse distance of the extrapolated muon track to  
<sup>1919</sup> the primary vertex, as calculated from the beam spot (BS)
- <sup>1920</sup> •  $|dZ(\text{BS})|$  - the absolute value of the longitudinal distance of the extrapolated muon track  
<sup>1921</sup> to the primary vertex

<sup>1922</sup> **6.2.4 Electron Selection**

<sup>1923</sup> Electrons are selected from the set of "particle-flow electron" objects reconstructed in the event.  
<sup>1924</sup> Similarly to muons, electrons are classified into two categories: tight and loose, according to the

Cuts	Tight $\mu$	Loose $\mu$
$p_T$	$>30$ GeV/c	$>10$ GeV/c
PFRelIso(0.4)	0.12	<0.2
$ \eta $	<2.1	<2.5
ID	Global Muon	Global Muon or Tracker Muon
ID	PFMuon	PFmuon
$N_{layers}$ (tracker)	>5	
$X^2$ of track fit	<10	
$N_{layers}$ (pixel)	>0	
$N_{segments}(\mu)$	>1	
$ d0(BS) $	<0.2 cm	
$ dZ(BS) $	<0.5 cm	

Table 6.5: Tight and loose muon definition

1925 quality of their reconstruction. The selection cuts are shown in the Table 6.6. The definitions  
 1926 are identical to the ones provided in section 6.2.3. Additional variables not described are:

- 1927 •  $E_T$  - the transverse energy of the electron, which due to its relatively light mass, is ap-  
 1928 proximately equal to its  $p_T$
- 1929 • ID - electron ID is passed on a multivariate analysis (MVA) technique, which provides a  
 1930 discriminant value to separate fake from real electrons, and is trained with events that are  
 1931 required to pass a HLT trigger (mvaTrigV0), or not (mvaNonTrigV0). The "passConver-  
 1932 sionVeto" ID ensures that the electron has not been reconstructed from a photon which  
 1933 has converted to an electron positron pair

Cuts	Tight $e$	Loose $e$
$E_T$	$>30$ GeV/c $^2$	$>15$ GeV/c $^2$
PFRelIso(0.3)	<0.1	<0.2
$ \eta $	<2.5	<2.5
ID	MVA ID("mvaTrigV0") >0.0	MVA ID("mvaNonTrigV0") >0.0
ID	passConversionVeto	passConversionVeto
$ d0(PV) $	<0.02 cm	
$ dZ(PV) $	<1 cm	

Table 6.6: Tight and loose muon definition

### 1934 6.2.5 Lepton selection and trigger efficiencies

1935 The cumulative reconstruction efficiency of id+isolation+trigger has been calculated from data,  
 1936 as a function of pT and eta, as shown in figure 6.5 for electrons and muons. In order to reproduce  
 1937 the same response in the simulations as found in data, an event-by-event scale factor  
 1938 is applied to correct for this difference in efficiency.

1939 The efficiency in data was measured by selected events with two tight muons, or two tight  
 1940 electrons with an invariant mass in a range between 70 and 130 GeV. This is centered on the  
 1941  $Z$  boson resonance, and ensures that the selected leptons are authentic. The two leptons are  
 1942 additionally required to have opposite charge, which is measured by the direction of the curvature

of their tracks in the magnetic field. A "tag" lepton is selected if has  $p_T > 30$  GeV, and passes the appropriate muon or electron trigger. The second lepton, the "probe" lepton, since selected as a pair coming from a  $Z$  boson, should be identical to the tag lepton, and thus should be identically reconstructed. The efficiency is then the ratio of the number events where both tag and probe leptons pass the  $p_T$  and trigger requirements over the number of events where only the tag lepton passes the  $p_T$  and trigger requirements. This study is repeated in bins of  $p_T$  and  $\eta$  to remove any kinematic dependence on lepton efficiency.

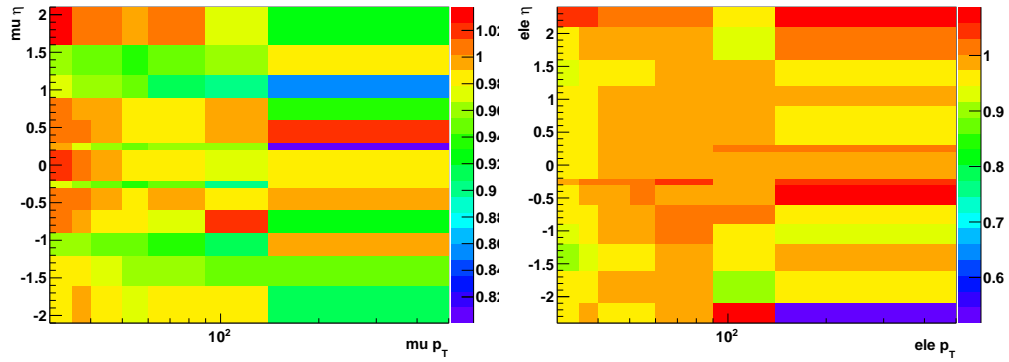


Figure 6.5: Muon and electron ID, isolation selection and trigger efficiency scale factors in bins of  $p_T$  and  $\eta$ .

The combined ID, isolation, and trigger scale factor uncertainty is evaluated by looking at the variation of the scale factor as a function of parameters besides  $p_T$  and  $\eta$ , such as pileup and  $b$ -tag scale factor reweighting. A flat uncertainty of 4% covers the variations that are observed, and is thus adopted as a conservative estimate of the uncertainty on the combined lepton reconstruction efficiency.

### 6.2.6 Jet selection

As described in the previous chapter, jets are reconstructed with the anti-KT clustering algorithm [126], with a distance parameter of 0.5, starting from the set of objects reconstructed by the particle flow algorithm [116]. Non-isolated leptons, not associated with the decay of a  $W$  boson, are allowed to be clustered into the jets. The selection cuts defining our jets can be found in Table 6.7. The cuts use the following variables to ensure the reconstruction of authentic hadronic jets:

- $p_T$  - component of the momentum transverse to the beam-line
- $\eta$  - the pseudorapidity of the reconstructed jet
- CEF - Charged Electromagnetic Fraction: the ratio of charged particles to the total number

1965 of particles in the jet

- 1966 • NHF - Neutral Hadron Fraction: the ratio of neutral particles to the total number of  
 1967 particles in the jet

- 1968 • NEF - Neutral Electromagnetic Fraction: the ratio of photons to the total number of  
 1969 particles in the jet

- 1970 • CHF - Charged Hadron Fraction: the ratio of charged hadrons to the total number of  
 1971 particles in the jet

- 1972 • NCH - Number of Charged Hadrons: raw charged hadron multiplicity

- 1973 •  $N_{\text{constituents}}$  - Number of constituents, which can be charged and neutral hadrons, as well  
 1974 as non-prompt photons and leptons.

Cuts	Jet
$p_T$	$>30\text{ GeV}/c$
$ \eta $	$<2.4$
CEF, NHF, NEF	$<0.99$
CHF, NCH	$>0$
$N_{\text{constituents}}$	$>1$

Table 6.7: Jet definition

1975 Additional correction factors are required such that the measured energy of the jet correctly  
 1976 reproduces the energy of the initial parton. This is done in four stages. The L1 Charged  
 1977 Hadron Subtraction (CHS) correction, is implemented in the particle-flow algorithm, and involves  
 1978 subtracting the energy contributions from charged hadrons that are not associated with the jet  
 1979 from the energy cluster. The next stage, L2 correction is a relative correction to make the  
 1980 measured jet response flat in  $\eta$ . The third stage, L3, is an absolute correction to the measured  
 1981  $p_T$  of a jet in order to match the simulated jet  $p_T$  created using generator level input and a similar  
 1982 jet clustering algorithm. The L2 and L3 corrections are calculated using Monte Carlo, and thus  
 1983 an fourth correction factor, the L2L3 residual correction is applied that fixes the discrepancies  
 1984 between Monte Carlo and data. The correction factors are described in reference [130], and are  
 1985 derived from 2011 7 TeV data, with a selection of dijet events near the  $Z$ -boson mass peak. A  
 1986 "tag-and-probe" procedure similar to the lepton scale factors is applied to jets to determine the  
 1987 kinematic dependence ( $p_T$  and  $\eta$ ) of the detector in both simulations and data. Additionally, a  
 1988 scale factor is needed to adjust for the difference in jet energy resolution as measured in data  
 1989 and predicted in simulation. Table 6.8 gives the scale factors, and uncertainties, as derived from  
 1990 dijet events [130] as a function of  $\eta$  only, since no significant  $p_T$  dependence was observed.

$ \eta $	Data/MC Ratio (factor +stat. +syst.- syst.)
0.00.5	$1.052 \pm 0.012 + 0.062 - 0.061$
0.51.1	$1.057 \pm 0.012 + 0.056 - 0.055$
1.11.7	$1.096 \pm 0.017 + 0.063 - 0.062$
1.72.3	$1.134 \pm 0.035 + 0.087 - 0.085$
2.35.0	$1.288 \pm 0.127 + 0.155 - 0.153$

Table 6.8: Jet Energy Resolution (JER) scale factors

### 1991 6.2.7 $b$ -tagging selection

1992 The algorithm used to perform  $b$ -tagging in this analysis is the combined secondary vertex (CSV)  
 1993 algorithm [131]. It relies on the superior ability of the inner tracker to reconstruct secondary  
 1994 vertices, which are the characteristic signature of  $b$ -quark decays. Tracks are selected if they  
 1995 meet the following requirements:

- 1996 • At least 8 hits in the pixel and silicon tracker, with at least 2 hits in the pixel detector
- 1997 • tracks must have  $p_T > 1$  GeV
- 1998 •  $\chi^2/\text{NDF}$  of the fitted track  $< 10$
- 1999 •  $|d_0|$  - transverse impact parameter  $< 2\text{mm}$ , since  $b$ -quarks will on average travel 0.45 mm  
 2000 in the detector before decaying

2001 Additionally, the following cuts are required:

- 2002 • The transverse distance between the primary and secondary vertices,  $L_T$ , is between 100  
 2003  $\mu\text{m}$  and 2.5 cm
- 2004 • The ratio of  $L_T$  and the uncertainty on its measurement,  $L_T/\sigma_{L_T} < 3$
- 2005 • The invariant mass formed by adding the four-vectors of all the tracks forming the sec-  
 2006 ondary vertex  $< 6.5$  GeV
- 2007 • The invariant mass falls outside a window near 50 MeV, corresponding to the  $K_S^0$  resonance

2008 Secondary vertices are decomposed into three categories. If a secondary vertex is found meeting  
 2009 the above criteria, it is a "reco vertex". If no secondary vertex is found meeting all the above  
 2010 criteria, the event can be classified as a "pseudo vertex" if more than two tracks have a signed  
 2011 transverse impact parameter significance, relative to the primary vertex, greater than 2. "No  
 2012 vertex" is found if neither of the prior two classification criteria can be met.

2013 For each of the vertex categories, a set of variables is used to create a single discriminating  
 2014 variable, using a likelihood ratio technique. The following input variables are used:

- The invariant mass of the charged particles associated with the secondary vertex
- The multiplicity of charged tracks associated with the primary vertex
- The distance between the primary and secondary vertex in the transverse plane, divided by its error (only used in reco vertex category)
- The pseudorapidities of the charged particle tracks associated with the secondary vertices
- The track impact parameter significance of the highest  $p_T$  track with invariant mass larger than the charm quark threshold, 1.5 GeV.

The likelihood function is split to separate between the charm and light-flavor backgrounds and is defined as:

$$\mathcal{L}^{b,c,q} = f^{b,c,q}(\alpha) \times \prod_i f_\alpha^{b,c,q}(x_i) \quad (6.2)$$

where  $\alpha = 1,2,3$ , denotes the different vertex categories,  $x_i$  are the individual variables,  $q$  stands for the light flavor quarks, while  $b$  and  $c$  stand for the bottom and charm quarks respectively.  $f^{b,c,q}(\alpha)$  is the probability for a quark flavor  $b$ ,  $c$ , or  $q$ , to fall into category  $\alpha$ .  $f_\alpha^{b,c,q}(x_i)$  is the probability density function of the variable  $x_i$  in category  $\alpha$  for quark flavor  $b$ ,  $c$ , or  $q$ . The combined discriminant is defined as

$$d = f_{BG}(c) \times \frac{\mathcal{L}^b}{\mathcal{L}^c + \mathcal{L}^b} + f_{BG}(q) \times \frac{\mathcal{L}^b}{\mathcal{L}^q + \mathcal{L}^b} \quad (6.3)$$

where  $f_{BG}(c)$ , and  $f_{BG}(q)$  are the a-priori probabilities for the content of charm and light flavor quarks in non- $b$  jets.

A jet is considered  $b$ -tagged if the CSV discriminant is greater than 0.679, which is the medium working point defined by the BTAG Physics Object Group (POG) [132], defined in order to produce a light-flavor mistag rate at  $\sim 1\%$ , with the reconstruction efficiency for real  $b$ -jets at  $\sim 70\%$ .

Additionally, it is necessary to account for differences in the measured efficiency for  $b$ -tagging jets between data and simulation [133]. An event weight scale factor is used to correct the MC  $b$ -tagging efficiency ( $SF_{tag} = \epsilon_{tag}^{data} / \epsilon_{tag}^{MC}$ ). The scale factor is measured for three different cuts, or working points, on the CSV discriminant value, and it is binned in terms of the  $p_T$  and  $\eta$  and flavor of the jet.

In addition to providing jet flavor identification for event classification, the discriminant value of the algorithm will be used to separate between  $t\bar{t}H$  signal and  $t\bar{t}+jets$  background. Therefore, a correction value for the efficiency difference between data and MC over the whole range of

2043 discriminator values is needed, not just for three working points. This procedure was developed  
 2044 in the context of the search for the standard model Higgs boson produced in association with a  
 2045 W or Z boson, with the Higgs decaying to bottom quarks [134].

2046 For each of the three operating points and for each of the data/MC SFs, an equivalent cut  
 2047 on the CSV value is determined,  $CSV_{\text{equiv}}$ , such that

$$\epsilon_{CSV>CSV_{\text{orig}}}^{\text{data}} = SF_{CSV>CSV_{\text{orig}}} \cdot \epsilon_{CSV>CSV_{\text{orig}}}^{MC} = \epsilon_{CSV>CSV_{\text{equiv}}}^{MC} \quad (6.4)$$

2048 where the SFs are measured in data and the MC efficiency measurements are calculated for each  
 2049 sample.

2050 In order to correct or "reshape" the CSV discriminator output values, a function is applied to  
 2051 the MC to produce a corrected CSV value:  $CSV_{\text{corr}} = f(CSV_{\text{orig}})$ . Given that there are three  $b$ -  
 2052 tag efficiency measurements, there are three pairs of  $(CSV_{\text{orig}}, CSV_{\text{equiv}})$ . The reshaping function  
 2053 must satisfy  $f(CSV_{\text{equiv}}) = CSV_{\text{orig}}$  for each of the operating points and for the upper and lower  
 2054 values of the CSV discriminant to make sure those values do not change (e.g.,  $CSV = 0.0$  and  
 2055  $CSV = 1.0$ ). The whole range of CSV discriminant values is found by linearly interpolating  
 2056 between these five points (the three working points, and upper and lower limit of the discriminate  
 2057 range).

### 2058 6.2.8 Lepton + Jets Selection

2059 The final Lepton+Jets (LJ) selection is finally carried out by requiring that events have exactly  
 2060 one tight lepton ( $e$  or  $\mu$ ), and at least four jets. Events with any additional loose or tight leptons  
 2061 are vetoed so this analysis can later be combined with a diLepton final state, without double  
 2062 counting events. Additionally, each event must have at least three jets with  $p_T > 40$  GeV/c.

2063 Events are further categorized by the reconstructed jet, and  $b$ -tagged jet multiplicities as  
 2064 follows:

- 2065 •  $\geq 6$  jets,  $=2$   $b$ -tags: At least 6 jets, 2 of which are  $b$ -tagged
- 2066 •  $=4$  jets,  $=3$   $b$ -tags: Exactly 4 jets, 3 of which are  $b$ -tagged
- 2067 •  $=5$  jets,  $=3$   $b$ -tags: Exactly 5 jets, 3 of which are  $b$ -tagged
- 2068 •  $\geq 6$  jets,  $=3$   $b$ -tags: At least 6 jets, 3 of which are  $b$ -tagged
- 2069 •  $=4$  jets,  $=4$   $b$ -tags: Exactly 4 jets, 4 of which are  $b$ -tagged
- 2070 •  $=5$  jets,  $=4$   $b$ -tags: Exactly 5 jets, 4 of which are  $b$ -tagged
- 2071 •  $\geq 6$  jets,  $\geq 4$   $b$ -tags: At least 6 jets, with at least 4 of which are  $b$ -tagged

Events with either 4 or 5 jets, where 2 of those jets are  $b$ -tagged, make up two categories, which are used only as a control region to validate comparisons between collected data and simulations. The number of  $t\bar{t}H$  events increases with the number of jets and tags because the largest branching fraction is  $H$  to  $b\bar{b}$ . Data to monte carlo comparisons of the jet and  $b$ -tag multiplicities are shown in figure 6.6. The event yields for the  $\mu+jets$  and  $e+jets$  channels are shown in tables 6.11 and 6.10 respectively.

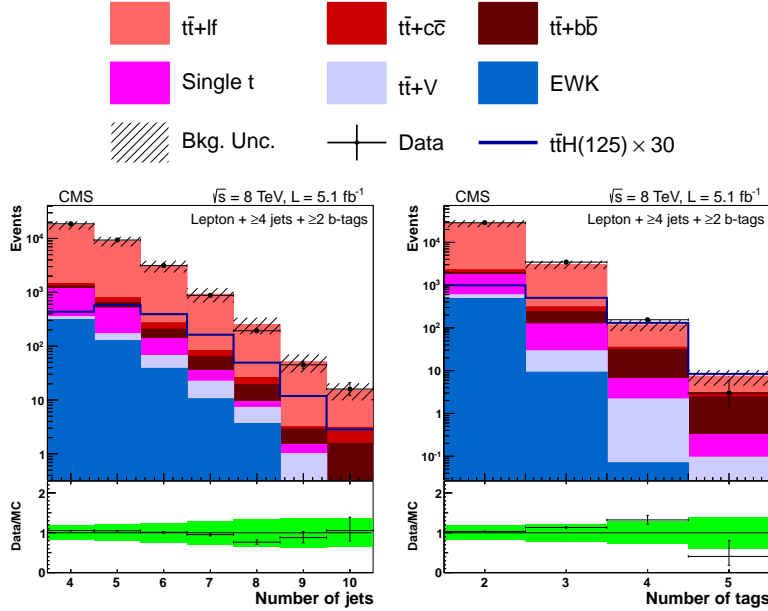


Figure 6.6: Number of jets (left) and number of  $b$ -tagged jets (right) in data and simulation for events with  $\geq 4$  jets +  $\geq 2$   $b$ -tags in the lepton+jets channel at 8 TeV. The background is normalized to the SM expectation; the uncertainty band (shown as a hatched band in the stack plot and a green band in the ratio plot) includes statistical and systematic uncertainties that affect both the rate and shape of the background distributions. The  $t\bar{t}H$  signal ( $m_H = 125\text{ GeV}/c^2$ ) is normalized to  $30 \times$  SM expectation.

### 2078 6.3 Multivariate Analysis

As discussed in the chapter introduction, no single variable offers sufficient discriminating power, to separate the  $t\bar{t}H$  signal from the  $t\bar{t} + jets$  background. Instead, the combined power of several input variables is utilized through a multivariate analysis (MVA) technique. For this analysis, the MVA algorithm chosen from the sub-class of artificial neural network (ANN) algorithms, known as multi-layer perceptrons (MLPs). The specific algorithm is the Clermont-Ferrand Multi-Layer Perceptron Artificial Neural Network (CFMlpANN). It was first developed at the University Blaise Pascal in Clermont-Ferrand, for the ALEPH experiment at the LEP collider to search for the Standard Model Higgs and has also been utilized by the BABAR experiment to search for rare  $B$  meson decays [135]. It has been implemented in the ROOT TMVA framework, available

Table 6.9: Expected event yields in  $5 \text{ fb}^{-1}$  for signal and backgrounds in the  $\mu+\text{jets}$  channel.

	$\geq 6$ jets 2 tags	4 jets 3 tags	5 jets 3 tags	$\geq 6$ jets 3 tags	$\geq 6$ jets 4 tags	4 jets 4 tags	5 jets $\geq 4$ tags	$\geq 6$ jets $\geq 4$ tags
$t\bar{t}H(125)$	$6.1 \pm 1.1$	$2.1 \pm 1.9$	$3.2 \pm 2.7$	$3.6 \pm 3.3$	$0.3 \pm 0.3$	$0.8 \pm 0.9$	$1.3 \pm 1.4$	
$t\bar{t}+\text{lf}$	$1750 \pm 480$	$680 \pm 150$	$460 \pm 110$	$270 \pm 84$	$9.5 \pm 3.2$	$13.0 \pm 4.2$	$20.6 \pm 7.8$	
$t\bar{t}+b\bar{b}$	$34 \pm 19$	$21 \pm 12$	$24 \pm 14$	$17.3 \pm 10.0$	$1.5 \pm 1.1$	$5.1 \pm 3.2$	$8.6 \pm 5.6$	
$t\bar{t}+c\bar{c}$	$29.5 \pm 8.7$	$10.0 \pm 2.9$	$13.2 \pm 3.9$	$11.1 \pm 3.5$	$0.2 \pm 0.2$	$0.2 \pm 0.1$	$1.1 \pm 0.8$	
$t\bar{t}V$	$18.7 \pm 3.9$	$2.3 \pm 0.6$	$3.3 \pm 0.8$	$4.1 \pm 1.1$	$0.1 \pm 0.0$	$0.4 \pm 0.2$	$0.8 \pm 0.2$	
Single $t$	$42.6 \pm 9.8$	$25.8 \pm 6.0$	$14.3 \pm 3.8$	$4.3 \pm 1.3$	$0.2 \pm 0.3$	$1.6 \pm 1.8$	$0.7 \pm 0.5$	
V+jets	$39 \pm 32$	$1.0 \pm 0.9$	$0.0 \pm 0.0$	$0.0 \pm 0.0$	$0.0 \pm 0.0$	$0.0 \pm 0.0$	$0.0 \pm 0.0$	
Diboson	$0.6 \pm 0.2$	$0.9 \pm 0.4$	$0.3 \pm 0.1$	$0.1 \pm 0.1$	$0.0 \pm 0.0$	$0.0 \pm 0.0$	$0.0 \pm 0.0$	
Total bkg	$1910 \pm 500$	$740 \pm 160$	$520 \pm 120$	$307 \pm 90$	$11.4 \pm 3.8$	$20.3 \pm 6.1$	$32 \pm 11$	
Data	1780	861	585	362	15	32	37	

Table 6.10: Expected event yields in  $5 \text{ fb}^{-1}$  for signal and backgrounds in the  $e+\text{jets}$  channel.

	$\geq 6$ jets 2 tags	4 jets 3 tags	5 jets 3 tags	$\geq 6$ jets 3 tags	$\geq 6$ jets 4 tags	4 jets 4 tags	5 jets $\geq 4$ tags	$\geq 6$ jets $\geq 4$ tags
$t\bar{t}H(125)$	$5.6 \pm 1.0$	$1.8 \pm 1.2$	$2.9 \pm 1.8$	$3.2 \pm 2.1$	$0.3 \pm 0.2$	$0.7 \pm 0.6$	$1.2 \pm 1.0$	
$t\bar{t}+\text{lf}$	$1720 \pm 470$	$640 \pm 140$	$410 \pm 94$	$293 \pm 85$	$8.6 \pm 2.9$	$14.5 \pm 5.2$	$20.7 \pm 7.8$	
$t\bar{t}+b\bar{b}$	$27 \pm 15$	$14.3 \pm 7.9$	$19 \pm 11$	$18 \pm 10$	$1.0 \pm 1.0$	$3.3 \pm 2.6$	$6.7 \pm 4.3$	
$t\bar{t}+c\bar{c}$	$32.8 \pm 9.4$	$9.6 \pm 2.9$	$11.8 \pm 3.5$	$14.8 \pm 4.8$	$0.4 \pm 0.3$	$0.6 \pm 0.6$	$2.6 \pm 1.4$	
$t\bar{t}V$	$17.0 \pm 3.6$	$2.1 \pm 0.6$	$2.8 \pm 0.7$	$4.5 \pm 1.1$	$0.0 \pm 0.0$	$0.3 \pm 0.1$	$0.6 \pm 0.2$	
Single $t$	$35.9 \pm 8.9$	$30.5 \pm 6.4$	$11.3 \pm 3.4$	$6.0 \pm 2.0$	$0.1 \pm 0.3$	$1.4 \pm 1.2$	$0.4 \pm 0.4$	
V+jets	$14 \pm 14$	$4.8 \pm 5.8$	$0.8 \pm 0.9$	$0.0 \pm 0.0$	$0.0 \pm 0.0$	$0.0 \pm 0.0$	$0.0 \pm 0.0$	
Diboson	$0.7 \pm 0.3$	$1.0 \pm 0.3$	$0.2 \pm 0.1$	$0.1 \pm 0.0$	$0.0 \pm 0.0$	$0.0 \pm 0.0$	$0.0 \pm 0.0$	
Total bkg	$1850 \pm 490$	$700 \pm 150$	$460 \pm 110$	$336 \pm 93$	$10.1 \pm 3.2$	$20.2 \pm 6.6$	$31 \pm 11$	
Data	1723	785	531	324	13	24	37	

Table 6.11: Expected event yields in  $5 \text{ fb}^{-1}$  for signal and backgrounds in the  $\mu+\text{jets}$  channel.

	$\geq 6$ jets 2 tags	4 jets 3 tags	5 jets 3 tags	$\geq 6$ jets 3 tags	4 jets $\geq 4$ tags	5 jets $\geq 4$ tags	$\geq 6$ jets $\geq 4$ tags
$t\bar{t}H(125)$	$11.7 \pm 1.9$	$3.9 \pm 1.9$	$6.1 \pm 3.1$	$6.9 \pm 3.5$	$0.6 \pm 0.3$	$1.5 \pm 0.8$	$2.5 \pm 1.3$
$t\bar{t}\ell\bar{\nu}$	$3460 \pm 940$	$1320 \pm 280$	$870 \pm 210$	$570 \pm 170$	$18.0 \pm 5.1$	$27.6 \pm 8.6$	$41 \pm 15$
$t\bar{t} + b\bar{b}$	$61 \pm 34$	$35 \pm 19$	$43 \pm 24$	$35 \pm 20$	$2.5 \pm 1.7$	$8.4 \pm 5.4$	$15.4 \pm 9.4$
$t\bar{t} + c\bar{c}$	$62 \pm 17$	$19.6 \pm 5.2$	$25.0 \pm 6.9$	$25.9 \pm 7.7$	$0.6 \pm 0.4$	$0.8 \pm 0.9$	$3.7 \pm 1.8$
$t\bar{t}V$	$35.7 \pm 7.5$	$4.5 \pm 1.1$	$6.1 \pm 1.4$	$8.6 \pm 2.1$	$0.1 \pm 0.1$	$0.7 \pm 0.2$	$1.5 \pm 0.4$
Single $t$	$79 \pm 18$	$56 \pm 11$	$25.6 \pm 6.3$	$10.3 \pm 2.9$	$0.3 \pm 0.6$	$3.1 \pm 2.2$	$1.0 \pm 0.6$
$V+\text{jets}$	$53 \pm 40$	$5.9 \pm 5.9$	$0.8 \pm 0.9$	$0.0 \pm 0.0$	$0.0 \pm 0.0$	$0.0 \pm 0.0$	$0.0 \pm 0.0$
Diboson	$1.2 \pm 0.4$	$1.8 \pm 0.6$	$0.5 \pm 0.2$	$0.2 \pm 0.1$	$0.0 \pm 0.0$	$0.0 \pm 0.0$	$0.0 \pm 0.0$
Total bkg	$3760 \pm 980$	$1440 \pm 300$	$970 \pm 230$	$650 \pm 190$	$21.5 \pm 6.1$	$41 \pm 12$	$63 \pm 21$
Data	$3503$	$1646$	$1116$	$686$	$28$	$56$	$74$

2088 in all CMSSW releases. A CFMlpANN is trained for each jet-tag category listed in section 6.2.8.  
 2089 A total of 10 input variables is used in each category, with the exception of the  $\geq 6$  jets,  $\geq 4$   
 2090  $b$ tags category, where the full reconstruction of the  $t\bar{t}H$  system is possible, features an additional  
 2091 variable that is the invariant mass of the di-jet system of  $b$ -jets selected by a  $\chi^2$  minimization  
 2092 algorithm.

### 2093 6.3.1 Artificial Neural Network Overview

2094 An artificial neural network (ANN), most generally speaking, is any collection of interconnected,  
 2095 simulated "neurons" which produce a certain response to a set of input variables [135]. A  
 2096 simulated neuron, is some independent function, which takes several input variables, performs  
 2097 a mathematical operation, and passes the result to one or more other neurons. In the most  
 2098 general case, a set of  $n$  input variables, connected to a single output, will produce on the order  
 2099  $n^2$  connections. For case of using the network to discriminate between signal from background  
 2100 (a yes or no answer on whether an event is signal-like), the ANN is mapping an  $n$ -dimensional  
 2101 space onto a one-dimensional space.

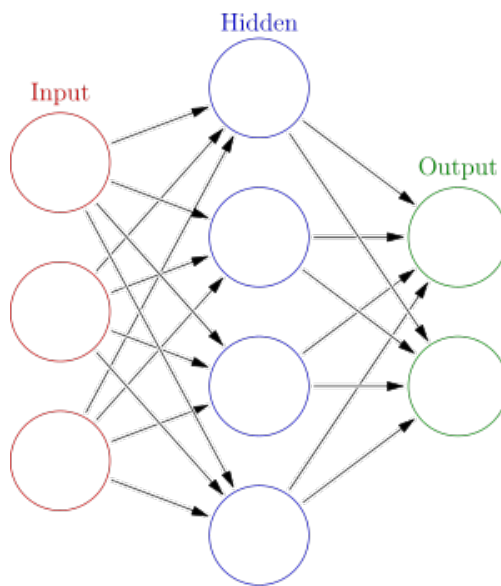


Figure 6.7: A simple example of a MLP type ANN, with one layer of input neurons that make connections to a hidden layer, which is connected to the output layer

2102 The multi-layer perceptron (MLP) is a specific type of arrangement of neurons. Any number  
 2103 of neurons are arranged into a single layer, and connections to other neurons are only made  
 2104 if they are arranged in a successive layer [135]. This is known as feed-forward network, and a  
 2105 simple example with one input layer, one hidden layer, and one output layer is shown in figure  
 2106 6.7. This limits the complexity of the connections formed by the neurons and allows for simplified

2107 calculations.

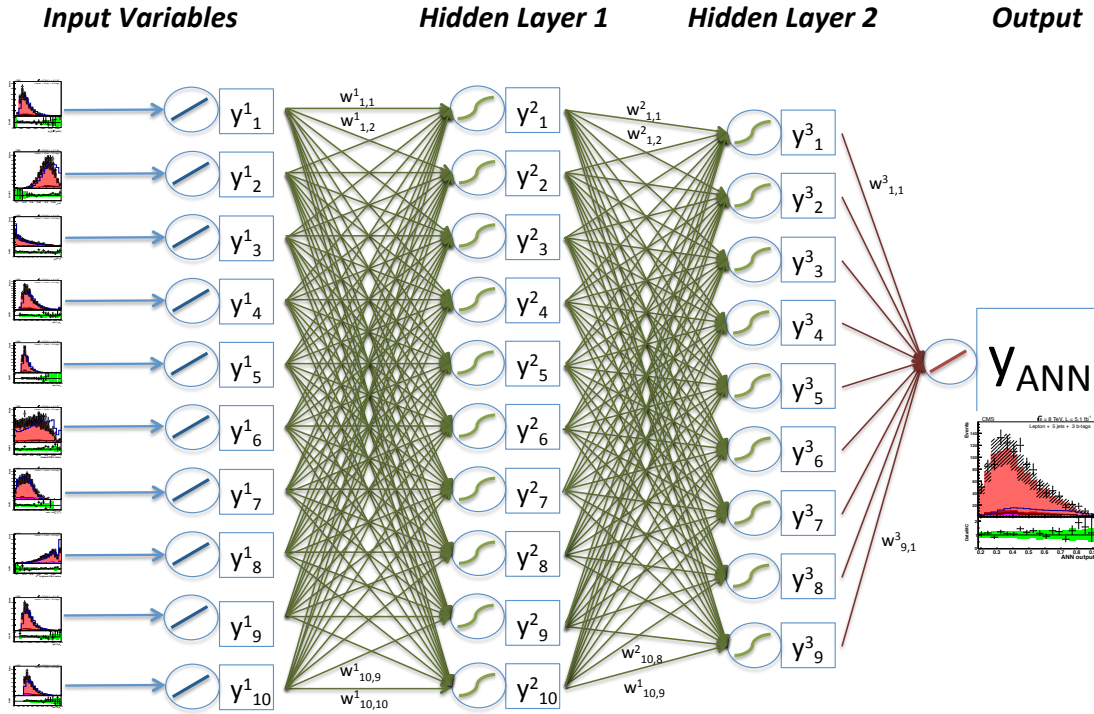


Figure 6.8: The CFMlpANN architecture used in this analysis features two hidden layers, and 10 input variables for each jet/tag category (11 variables for the  $\geq 6$ jets,  $\geq 4b$ -tags category)

2108 This analysis uses an architecture that consists of two hidden layers, with  $N$  and  $N - 1$   
2109 variables respectively, where  $N$  is the number of input variables for the given jet/tag category.  
2110 An example diagram is shown in figure 6.8. The output of the CFMlpANN algorithm is one-  
2111 dimensional discriminant with range from 0 to 1, for background-like and signal-like events.  
2112 Each neuron response is based on an activation function  $A(\alpha)$ , and a synapse response,  $\alpha$ .  
2113 In this case, a sigmoid function is used as the activation function:

$$A(\alpha) = \frac{1}{1 + e^{-x}} \quad (6.5)$$

2114 and the synapse response is a simple weighted sum:

$$\alpha = w_{0j}^{(l)} + \sum_{i=1}^n y_i^{(l)} w_{ij}^{(l)} \quad (6.6)$$

2115 The entire CFMlpANN response is then

$$y_{ANN} = \sum_{k=1}^{n-1} y_k^{(3)} w_{k1}^{(3)} = \sum_{k=1}^{n-1} A \left( \sum_{j=1}^n y_j^{(2)} w_{jk}^{(2)} \right) w_{k1}^{(3)} = \sum_{k=1}^{n-1} A \left( \sum_{j=1}^n A \left( \sum_{i=1}^n x_i w_{ij}^{(1)} \right) w_{jk}^{(2)} \right) w_{k1}^{(3)} \quad (6.7)$$

where  $n$  is the number of input variables for that jet tag category and  $A$  is the sigmoid function described in equation 6.5.

The CFMlpANN is trained with  $t\bar{t}H$  signal events and inclusive  $t\bar{t} + jets$  background events in order to optimize the weights  $w_{ij}^{(l)}$  that are used for each neuron connection such that the output,  $y_{ANN}$  is closest to 1 for signal-like events, and closest to 0 for background-like events. This process involves sending the CFMlpANN an event from a known source (either signal or background), calculating the response,  $y_{ANN}$ , and computing an error function associated with the answer, given by:

$$E(x_1, \dots, x_N | w) = \sum_{a=1}^N E_a(x_a | w) = \sum_{a=1}^N \frac{1}{2} (y_{ANN} - \hat{y}_a) \quad (6.8)$$

where  $\hat{y}_a$  is the correct response (either 0 or 1), knowing that the event was either signal or background, and  $N$  is the number of events used to train the CFMlpANN. The optimized set of weights is the set that minimizes this error function. This is done by the method of steepest descent, where a random set of weights is moved a small distance in the direction that gives the largest change in minimizing the error function.

$$w^{t+1} = w^t - \eta \nabla_w E \quad (6.9)$$

where  $\nabla_w$  is the direction that reduces the error function the most, and  $\eta$  is a parameter that determines how large of an adjustment is made. After the weights are adjusted, the CFMlpANN makes another iteration over the training events, re-calculating the CFMlpANN output for each event and the error function. For this analysis a total of 2000 iterations were used to train the CFMlpANN.

It is possible to bias the CFMlpANN response, by overtraining it. This is the case where the weights are over-adjusted to correctly classify events in the training sample. If overtrained, small fluctuations in the input variable distributions of authentic signal events can lead to incorrect classification of the signal events when the CFMlpANN attempts to classify the data. To avoid this, half of the simulated events for  $t\bar{t}H$  signal and  $t\bar{t} + jets$  background are used during training. After training, the other half are used to test the response of the algorithm. If properly trained, the testing and training samples should have identical CFMlpANN responses. The figure of merit used to assess this is the Kolmogorov-Smirnov test, which computes the probability that

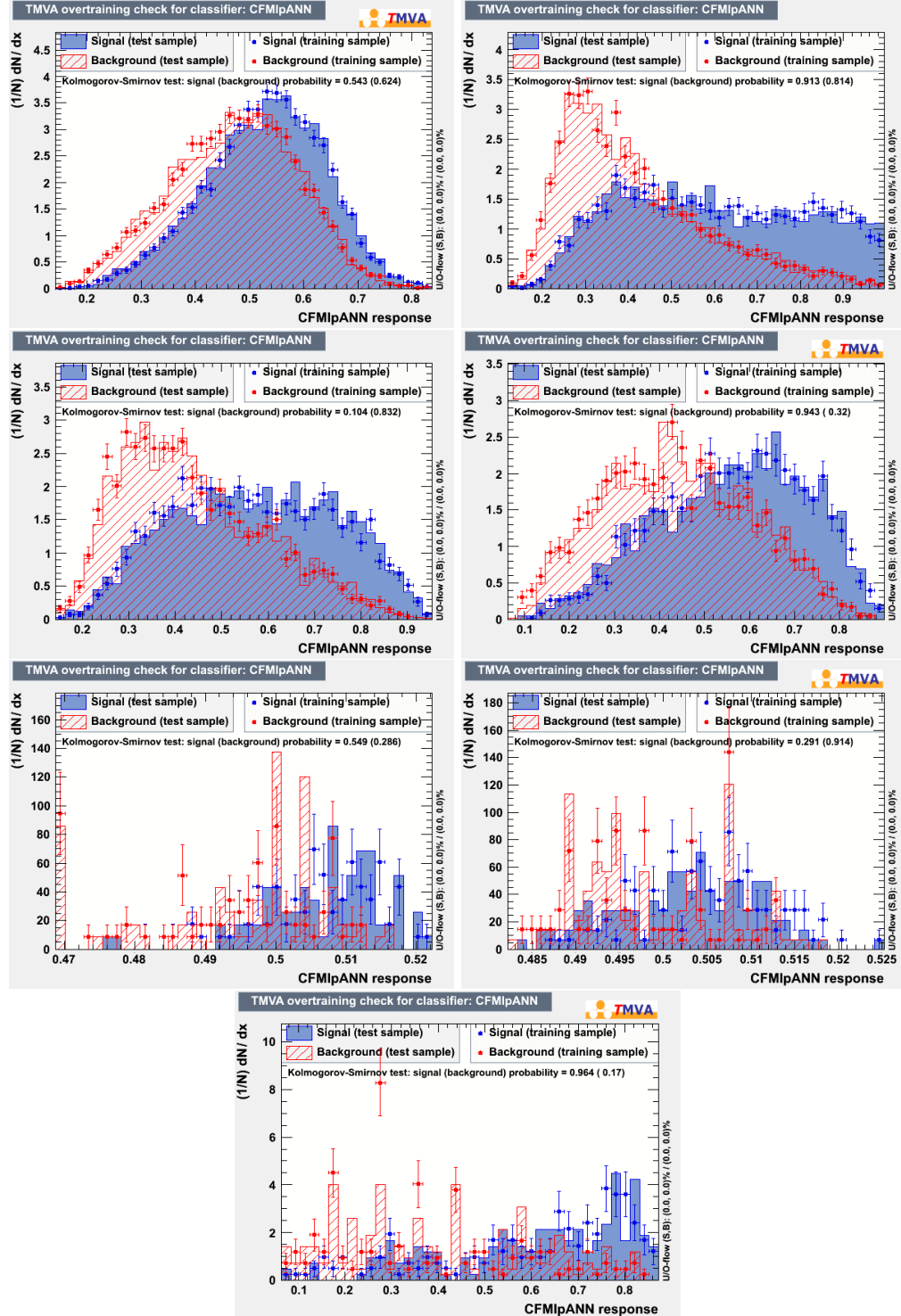


Figure 6.9: Comparisons of the testing and training samples used to optimize the CFMlpANN weights for each jet/tag category

2142 two distributions have been sampled from the same underlying probability distribution. The  
2143 results of the training and testing for each of the jet/tag categories is shown in figure 6.9. No  
2144 signs of overtraining are observed.

### 2145 6.3.2 MVA Input Variables, Data to Monte Carlo Comparisons

2146 As mentioned in the previous section, each jet/tag category has been trained with its own  
2147 CFMlpANN. Each category uses ten input variables, except for the  $\geq 6j$ ,  $\geq 4t$  category, which  
2148 uses eleven. A total of 24 unique input variables are used in the 7 different jet/tag categories  
2149 and are listed in table 6.12. The most discriminating variable for each category is denoted by  
2150 a  $\star$ . The inputs are selected from a ranked list based on initial separation between signal  
2151 and background. The separation of the individual variables is evaluated using a separation  
2152 benchmark  $\langle S^2 \rangle$  [135] defined as follows:

$$\langle S^2 \rangle = \frac{1}{2} \int \frac{(\hat{y}_S(y) - \hat{y}_B(y))^2}{\hat{y}_S(y) + \hat{y}_B(y)} dy, \quad (6.10)$$

2153 where  $y$  is the input variable, and  $\hat{y}_S$  and  $\hat{y}_B$  are the signal and background probability density  
2154 functions for that input variable in the signal and background samples, respectively. The maxi-  
2155 mum number of input variables used in each category is limited by the statistics in the simulated  
2156 samples used for the CFMlpANN training. The number of variables per category is determined  
2157 by reducing the number of variables until the minimum number of variables needed to maintain  
2158 roughly the same ANN performance is reached. In this case, 10 input variables yields stable and  
2159 approximately identical performance to using 15, while using 5 variables degraded discrimination  
2160 power significantly.

2161 The input variables used in the CFMlpANN can be broken down into several classes. The  
2162 first is related to jet, and multi-object kinematics. The  $b$ -jets produced by the Higgs boson tend  
2163 to have a harder  $p_T$  spectrum compared to  $b$ -jets produced from gluon radiation. Additionally,  
2164 the recoil of the Higgs off of the top-system produces small differences in the  $p_T$  and invariant  
2165 mass of the reconstructed  $t\bar{t} + jets$  system.

- 2166 • Jet 1  $p_T$  - the highest value of transverse jet momentum in the event
- 2167 • Jet 2  $p_T$  - the second highest value of transverse jet momentum in the event
- 2168 • Jet 3  $p_T$  - the third highest value of transverse jet momentum in the event
- 2169 • Jet 4  $p_T$  - the fourth highest value of transverse jet momentum in the event
- 2170 •  $p_T(\ell, E_T^{\text{miss}}, \text{jets})$  - the transverse momentum of the four-vector formed by summing the  
2171 four-vectors of the lepton, MET, and all selected jets in the event

Table 6.12: The ANN inputs for the nine jet-tag categories in the 8 TeV  $t\bar{t}H$  analysis in the lepton+jets and dilepton channels. The choice of inputs is optimized for each category. Definitions of the variables are given in the text. The best input variable for each jet-tag category is denoted by  $\star$ .

Jets Tags	Lepton+Jets						
	$\geq 6$ 2	4 3	5 3	$\geq 6$ 3	4 4	5 $\geq 4$	$\geq 6$ $\geq 4$
Jet 1 $p_T$		✓	✓		✓		
Jet 2 $p_T$		✓	✓				
Jet 3 $p_T$	✓	✓	✓			✓	
Jet 4 $p_T$	✓	✓	✓			✓	
$p_T(\ell, E_T^{\text{miss}}, \text{jets})$		★	✓		✓	✓	
$M(\ell, E_T^{\text{miss}}, \text{jets})$	✓	✓		✓	✓		✓
Average $M((j_m^{\text{untag}}, j_n^{\text{untag}}))$	✓			✓			
$M((j_m^{\text{tag}}, j_n^{\text{tag}})_{\text{closest}})$							✓
$M((j_m^{\text{tag}}, j_n^{\text{tag}})_{\text{best}})$							✓
Average $\Delta R(j_m^{\text{tag}}, j_n^{\text{tag}})$				✓	✓	✓	✓
Minimum $\Delta R(j_m^{\text{tag}}, j_n^{\text{tag}})$			✓				
$\Delta R(\ell, j_{\text{closest}})$						✓	✓
Sphericity	✓			✓			✓
Aplanarity	✓				✓		
$H_0$	✓						
$H_1$	✓				✓		
$H_2$				✓			✓
$H_3$	★			✓			✓
$\mu^{\text{CSV}}$	✓	✓	★	★	★	★	★
$(\sigma_n^{\text{CSV}})^2$	✓	✓	✓	✓	✓	✓	
Highest CSV value							✓
2 <sup>nd</sup> -highest CSV value	✓	✓	✓	✓	✓	✓	✓
Lowest CSV value	✓	✓	✓	✓	✓	✓	✓

- $M(\ell, E_T^{\text{miss}}, \text{jets})$  - the invariant mass of the four-vector formed by summing the four-vectors of the lepton, MET $\vec{j}$  and all selected jets in the event
- Average  $M((j_m^{\text{untag}}, j_n^{\text{untag}}))$  - the average di-Jet mass formed by all combinations of jets that have not been  $b$ -tagged in the event
- $M((j_m^{\text{tag}}, j_n^{\text{tag}})_{\text{closest}})$  - the invariant di-Jet mass of the two  $b$ -tagged jets that are closest to one another in the detector
- $M((j_m^{\text{tag}}, j_n^{\text{tag}})_{\text{best}})$  - the invariant mass constructed from the two tagged jets least likely to be a part of the  $t\bar{t}$  system as determined by a minimum  $\chi^2$  search among all the jet, lepton, and  $E_T^{\text{miss}}$  combinations in the event, using the  $W$  boson and top masses as kinematic constraints.

The next class of input variables describe the angular relationship between reconstructed objects in the event. These are event shape variables. Production of a relatively massive object, in addition to top quarks, such as the Higgs, tends to make  $t\bar{t}H$  events more spherically distributed in the detected, while the background events are more collimated. Variables in this class include angular correlations, like the opening angle between the tagged jets

- 2187 • Average  $\Delta R(j_m^{\text{tag}}, j_n^{\text{tag}})$  - the average  $\Delta R$  spatial separation between all combinations of  
2188  $b$ -tagged jets in the event
- 2189 • Minimum  $\Delta R(j_m^{\text{tag}}, j_n^{\text{tag}})$  - the smallest value of  $\Delta R$  measured between a pair of  $b$ -tagged  
2190 jets
- 2191 •  $\Delta R(\ell, j_{\text{closest}})$  - the  $\Delta R$  spatial separation of the lepton and the closest reconstructed jet
- 2192 • Sphericity - Event shape variable equal to  $\frac{3}{2}(\lambda_2 + \lambda_3)$ , where  $\lambda_2$  and  $\lambda_3$  are the second and  
2193 third eigenvalues of the sphericity tensor as described in[136]
- 2194 • Aplanarity - Event shape variable equal to  $\frac{3}{2}(\lambda_3)$ , where  $\lambda_3$  is the third eigenvalue of the  
2195 sphericity tensor as described in
- 2196 •  $H_0$  - the zeroth Fox-Wolfram moment [137]
- 2197 •  $H_1$  - the first Fox-Wolfram moment
- 2198 •  $H_2$  - the second Fox-Wolfram moment
- 2199 •  $H_3$  - the third Fox-Wolfram moment

2200 where  $\Delta R = \sqrt{\Delta\eta^2 + \Delta\phi^2}$ . The sphericity tensor is given by the equation:

$$S^{a,b} = \frac{\sum_i p_i^a p_i^b}{\sum_i |\hat{p}_i|^2} \quad (6.11)$$

2201 where  $a, b = x, y, z$  coordinates. This tensor is diagonalized, and solved for its eigenvalues,  
2202 which are used to compute the sphericity and aplanarity variables. The Fox-Wolfram moments  
2203 are defined are momentum weighted spherical harmonics, defined as:

$$H_\ell = \sum_{i,j=1}^{N_{\text{jets}}} \frac{|\hat{p}_i||\hat{p}_j|}{|\hat{p}|_{\text{tot}}^2} P_\ell(\cos \Omega_{ij}) \quad (6.12)$$

2204 where  $P_\ell(\cos \Omega_{ij})$  is the  $\ell^{\text{th}}$  spherical harmonic, with polar angle calculated between jets i and j.  
2205 The final class of variables is based on the discriminant output from the b-tagging algorithm.  
2206 For many of the categories, the average  $b$ -tag discriminant of all of the jets in the event tends to  
2207 be the most powerful single variable. This is due to the high multiplicity of authentic  $b$ -jets in  
2208 a  $t\bar{t}H$  event.

- 2209 •  $\mu^{\text{CSV}}$  - the average value of the output of the CSV algorithm for all selected jets in the  
2210 event.
- 2211 •  $(\sigma_n^{\text{CSV}})^2$  - the variance of the average value of the output of the CSV algorithm for all  
2212 selected jets in the event.

- 2213 • Highest CSV value - the highest value of the CSV discriminant for any selected jet in the  
2214 event

- 2215 •  $2^{nd}$ -highest CSV value - the second highest value of the CSV discriminant for any selected  
2216 jet in the event

- 2217 • Lowest CSV value - the lowest value of the CSV discriminant for any selected jet in the  
2218 event

2219 The modeling of the input variables is compared against data for each of the jet/tag diagrams  
2220 in the the following figures:

- 2221 •  $\geq 6$  jets, ==2 b-tags: Figure 6.10, and Figure 6.11

- 2222 • ==4 jets, ==3 b-tags: Figure 6.12, and Figure 6.13

- 2223 • ==5 jets, ==3 b-tags: Figure 6.14, and Figure 6.15

- 2224 •  $\geq 6$  jets, ==3 b-tags: Figure 6.16, and Figure 6.17

- 2225 • ==4 jets, ==4 b-tags: Figure 6.18, and Figure 6.19

- 2226 • ==5 jets, ==4 b-tags: Figure 6.20, and Figure 6.21

- 2227 •  $\geq 6$  jets,  $\geq 4$  b-tags: Figure 6.22, and Figure 6.23

2228 Below each histogram is a ratio of the yields for data over the simulated sample prediction. The  
2229 green band is the total uncertainty estimated for the simulation, and the error bars on the points  
2230 are determined by the statistical error on the data collected.

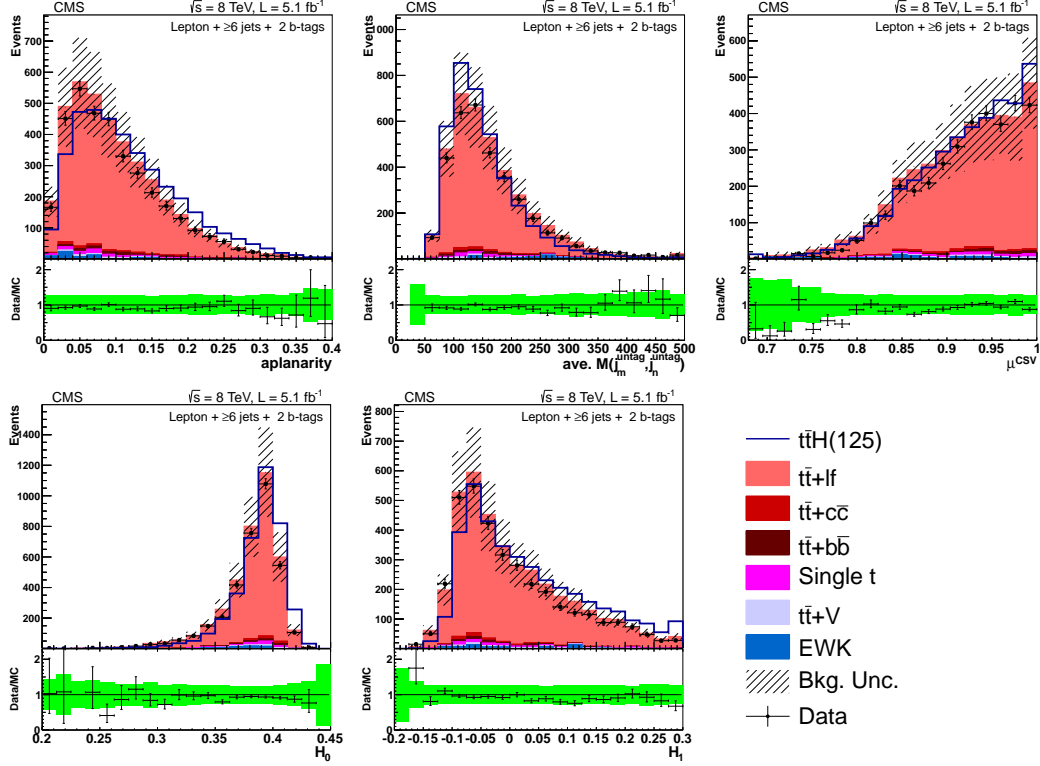


Figure 6.10: Lepton + jets data/MC comparison for the  $\geq 6$  jets + 2 tag category. The uncertainty band includes statistical and systematic uncertainties that affect both the rate and shape of the background distributions.

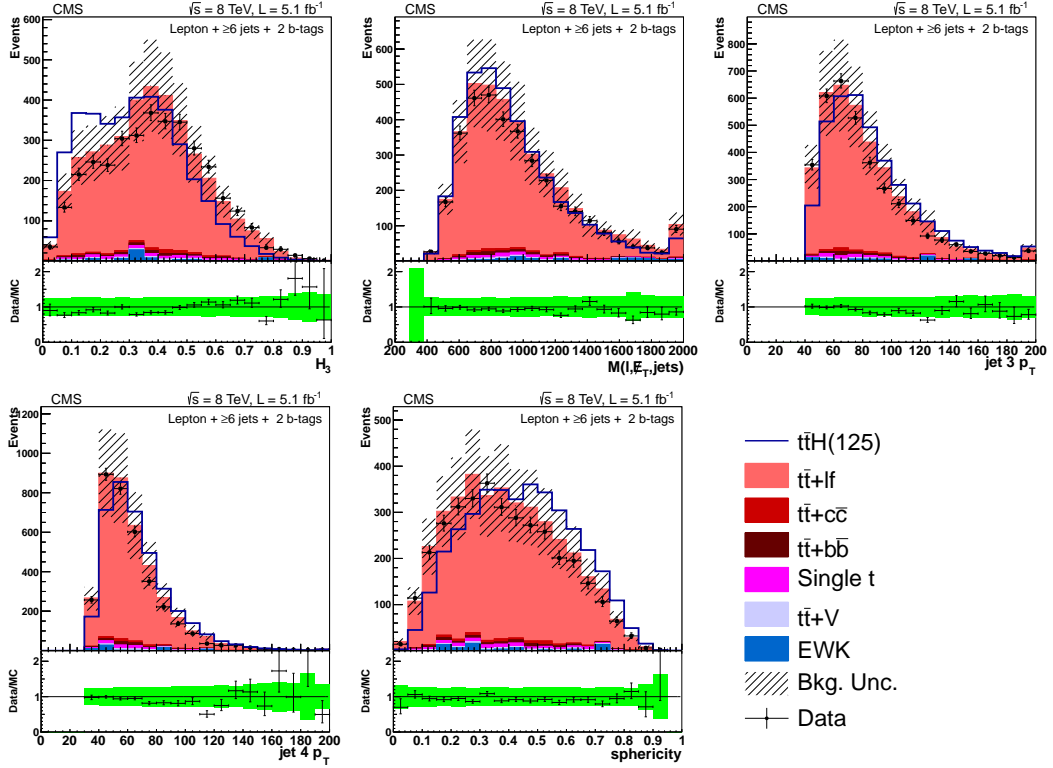


Figure 6.11: Lepton + jets data/MC comparison for the  $\geq 6$  jets + 2 tag category. The uncertainty band includes statistical and systematic uncertainties that affect both the rate and shape of the background distributions.

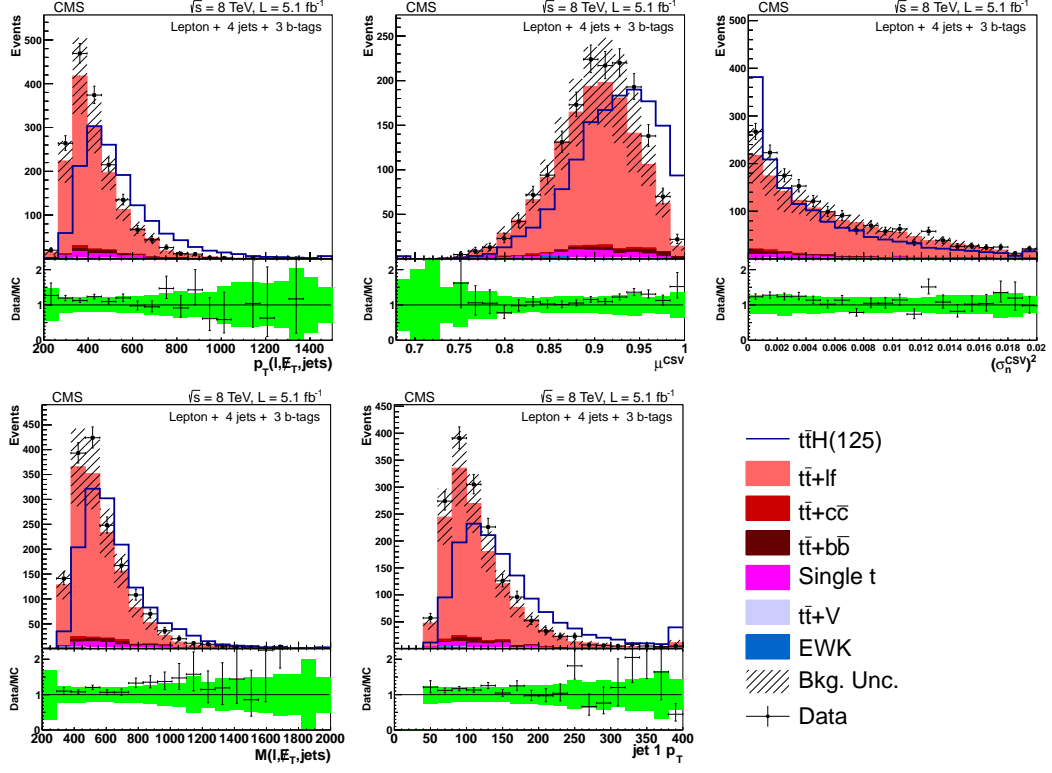


Figure 6.12: Lepton + jets data/MC comparison for the 4 jets + 3 tag category. The uncertainty band includes statistical and systematic uncertainties that affect both the rate and shape of the background distributions.

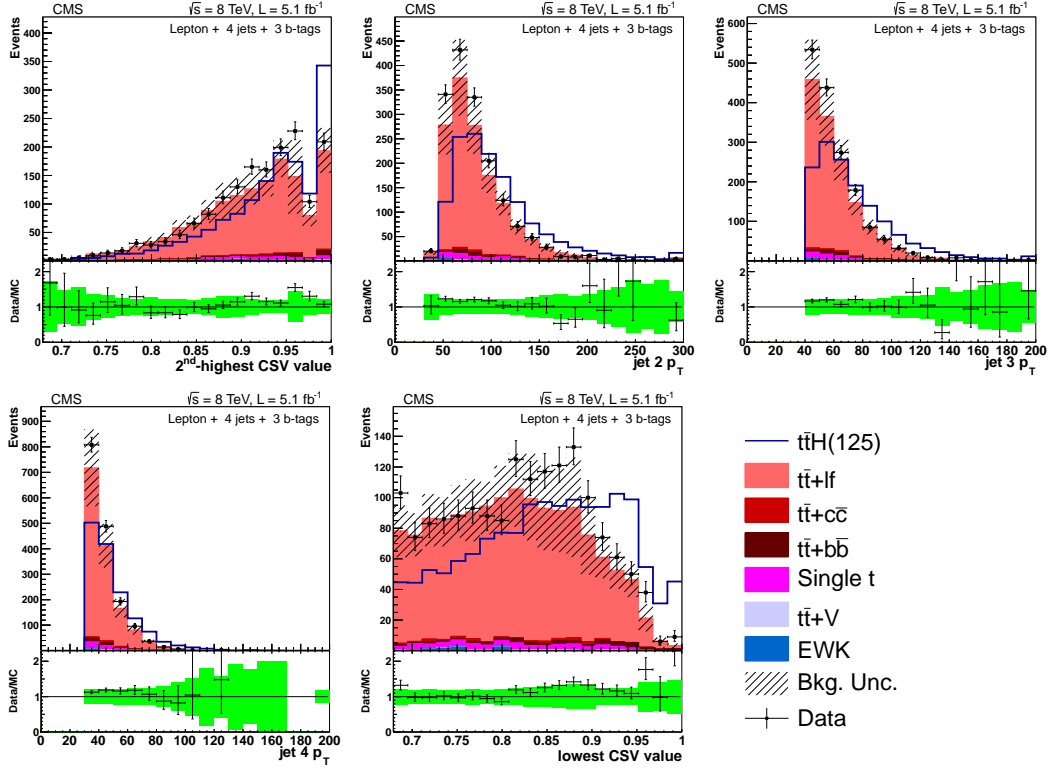


Figure 6.13: Lepton + jets data/MC comparison for the 4 jets + 3 tag category. The uncertainty band includes statistical and systematic uncertainties that affect both the rate and shape of the background distributions.

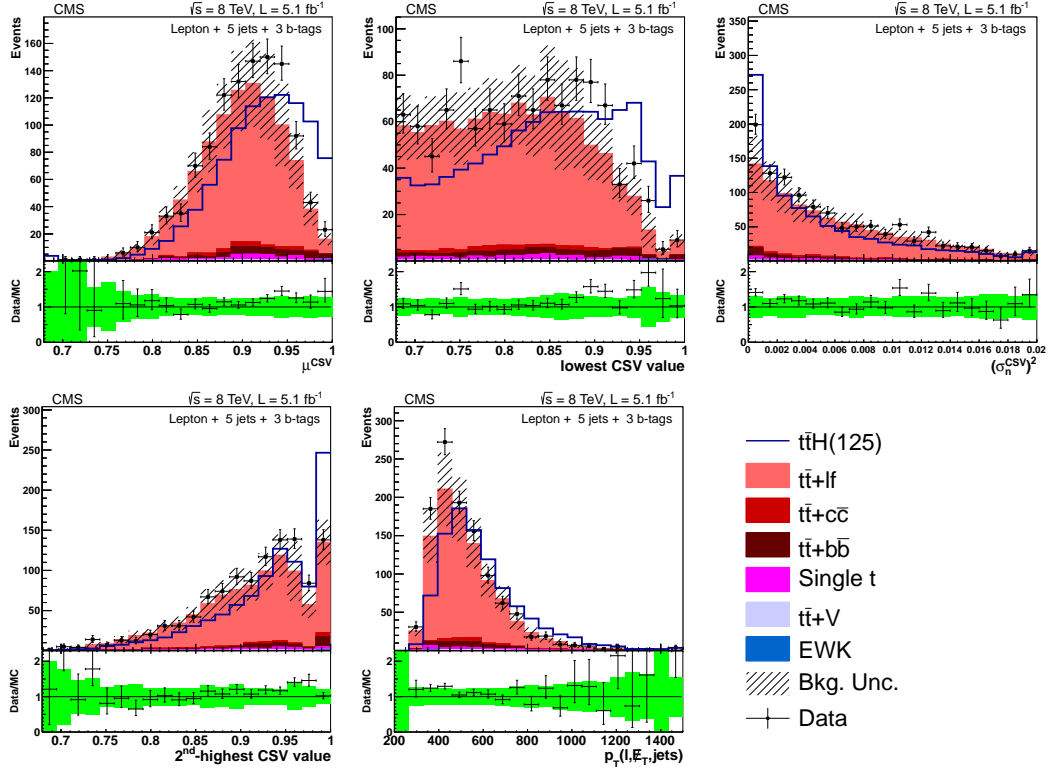


Figure 6.14: Distributions of the five ANN input variables with rankings 1 through 5, in terms of separation, for the 5 jets + 3 b-tags category of the lepton+jets channel at 8 TeV. Definitions of the variables are given in the text. The background is normalized to the SM expectation; the uncertainty band (shown as a hatched band in the stack plot and a green band in the ratio plot) includes statistical and systematic uncertainties that affect both the rate and shape of the background distributions. The  $t\bar{t}H$  signal ( $m_H = 125 \text{ GeV}/c^2$ ) is normalized to the total background yield, for easier comparison of the shapes.

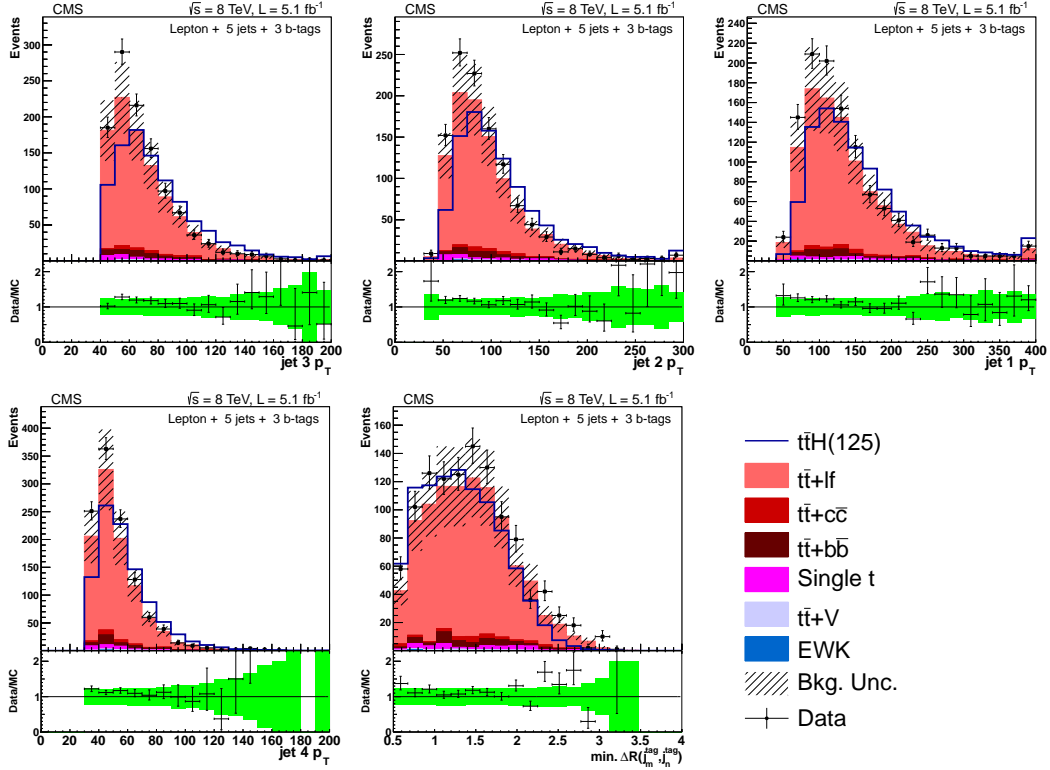


Figure 6.15: Distributions of the five ANN input variables with rankings 6 through 10, in terms of separation, for the 5 jets + 3 b-tags category of the lepton+jets channel at 8 TeV. Definitions of the variables are given in the text. The background is normalized to the SM expectation; the uncertainty band (shown as a hatched band in the stack plot and a green band in the ratio plot) includes statistical and systematic uncertainties that affect both the rate and shape of the background distributions. The  $t\bar{t}H$  signal ( $m_H = 125 \text{ GeV}/c^2$ ) is normalized to the total background yield, for easier comparison of the shapes.

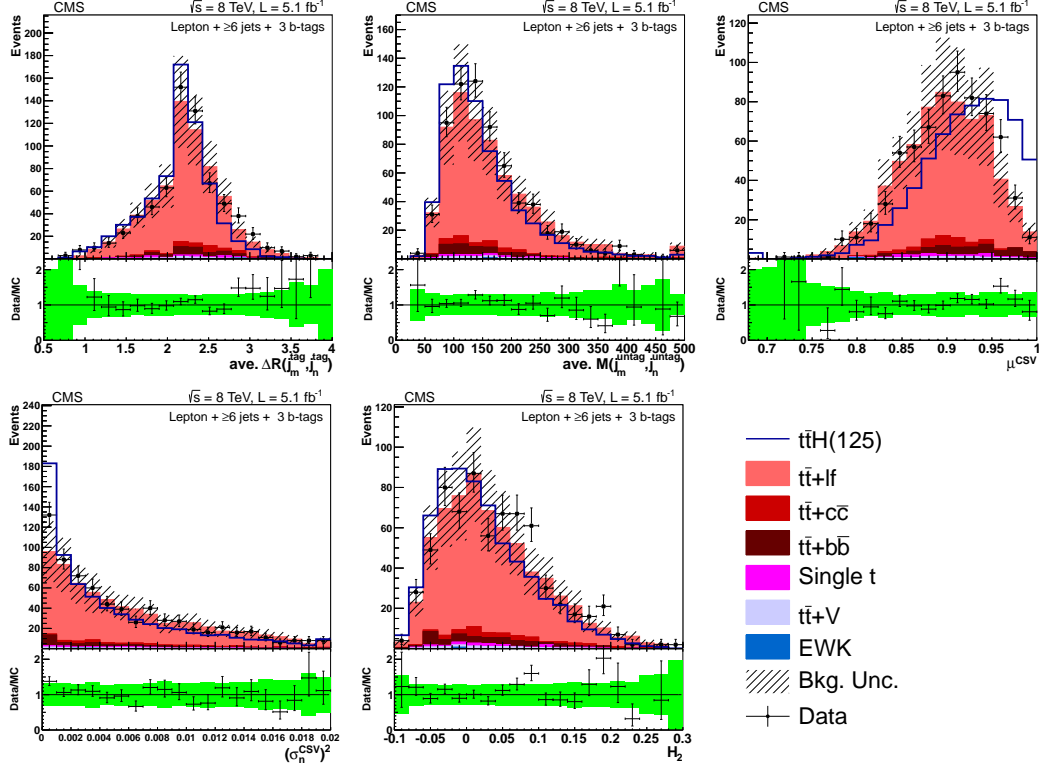


Figure 6.16: Lepton + jets data/MC comparison for the  $\geq 6$  jets + 3 tag category. The uncertainty band includes statistical and systematic uncertainties that affect both the rate and shape of the background distributions.

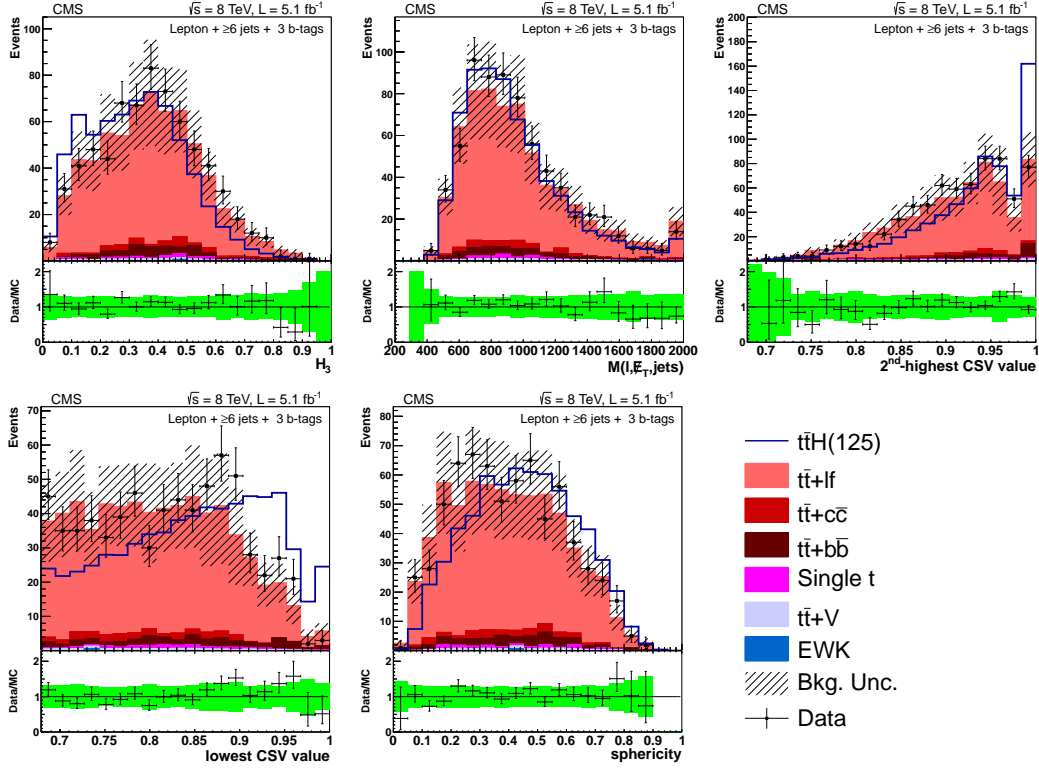


Figure 6.17: Lepton + jets data/MC comparison for the  $\geq 6$  jets + 3 tag category. The uncertainty band includes statistical and systematic uncertainties that affect both the rate and shape of the background distributions.

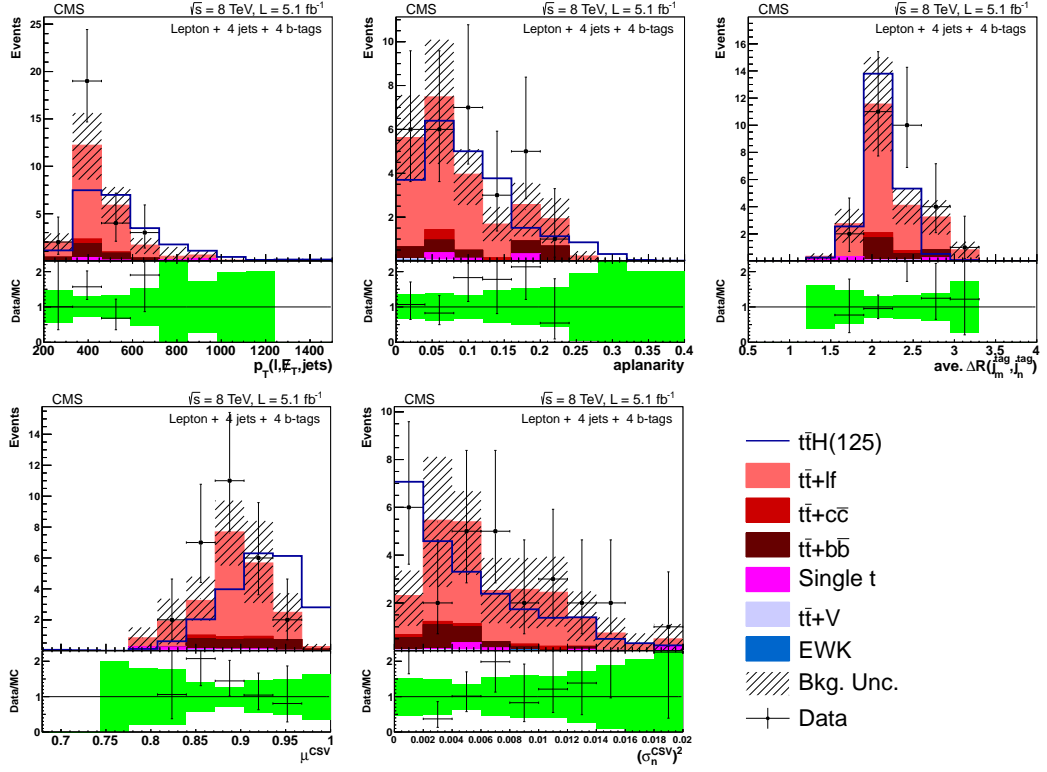


Figure 6.18: Lepton + jets data/MC comparison for the 4 jets + 4 tag category. The uncertainty band includes statistical and systematic uncertainties that affect both the rate and shape of the background distributions.

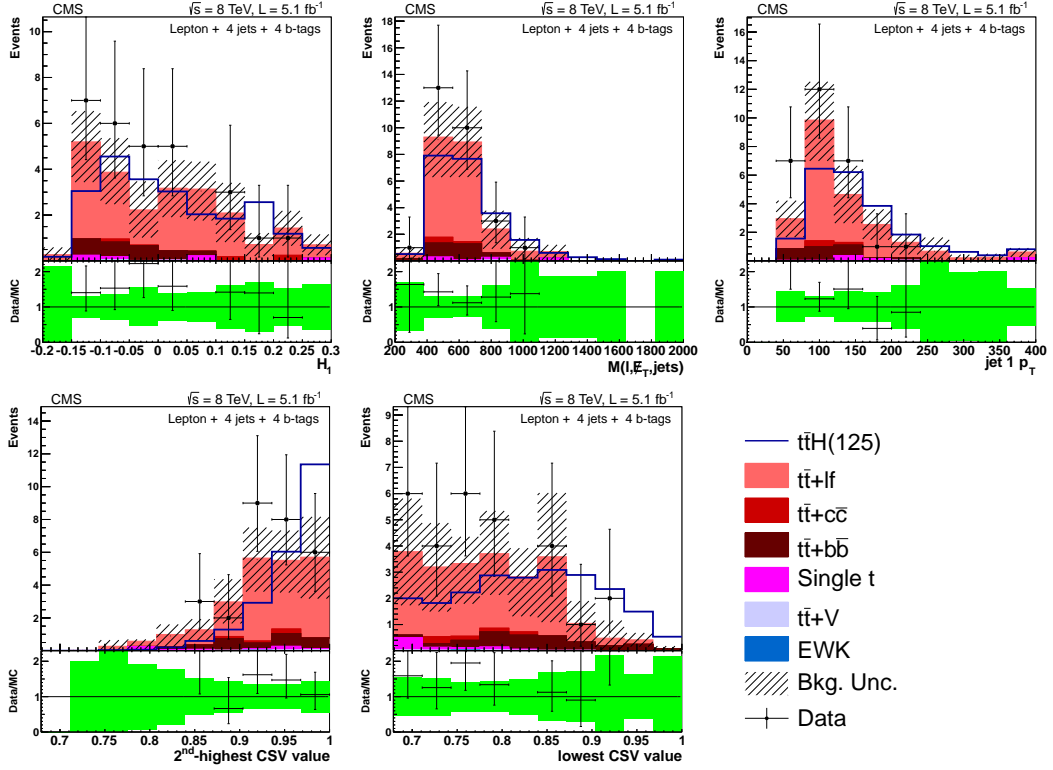


Figure 6.19: Lepton + jets data/MC comparison for the 4 jets + 4 tag category. The uncertainty band includes statistical and systematic uncertainties that affect both the rate and shape of the background distributions.

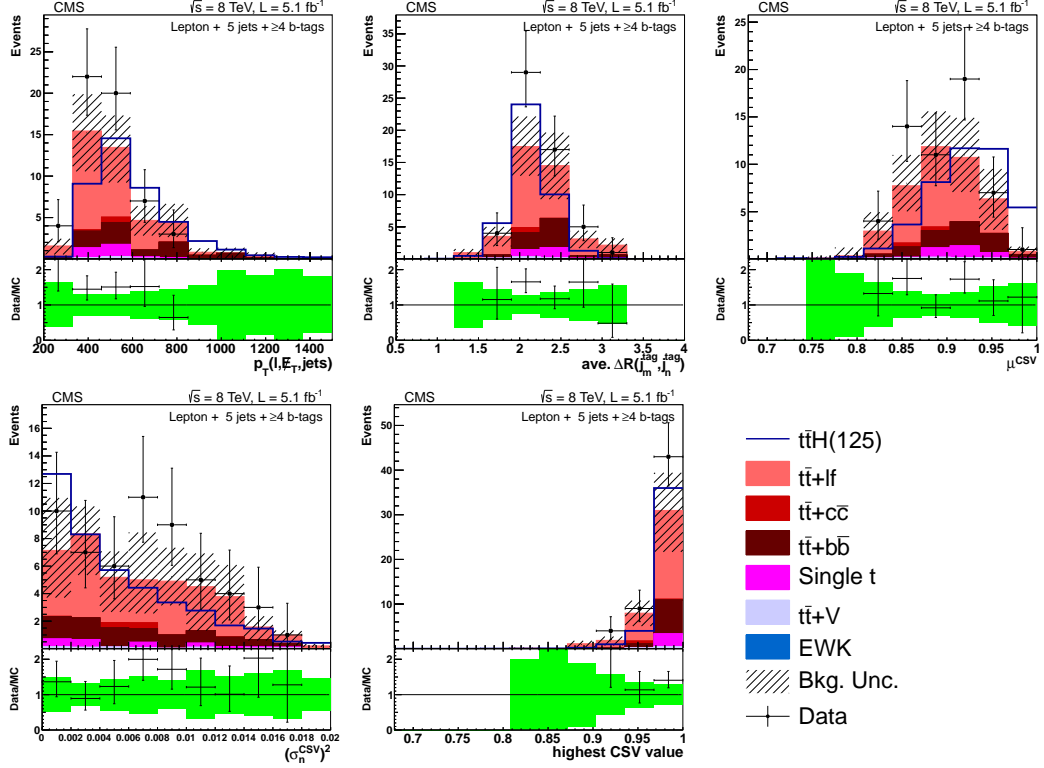


Figure 6.20: Lepton + jets data/MC comparison for the 5 jets + 4 tag category. The uncertainty band includes statistical and systematic uncertainties that affect both the rate and shape of the background distributions.

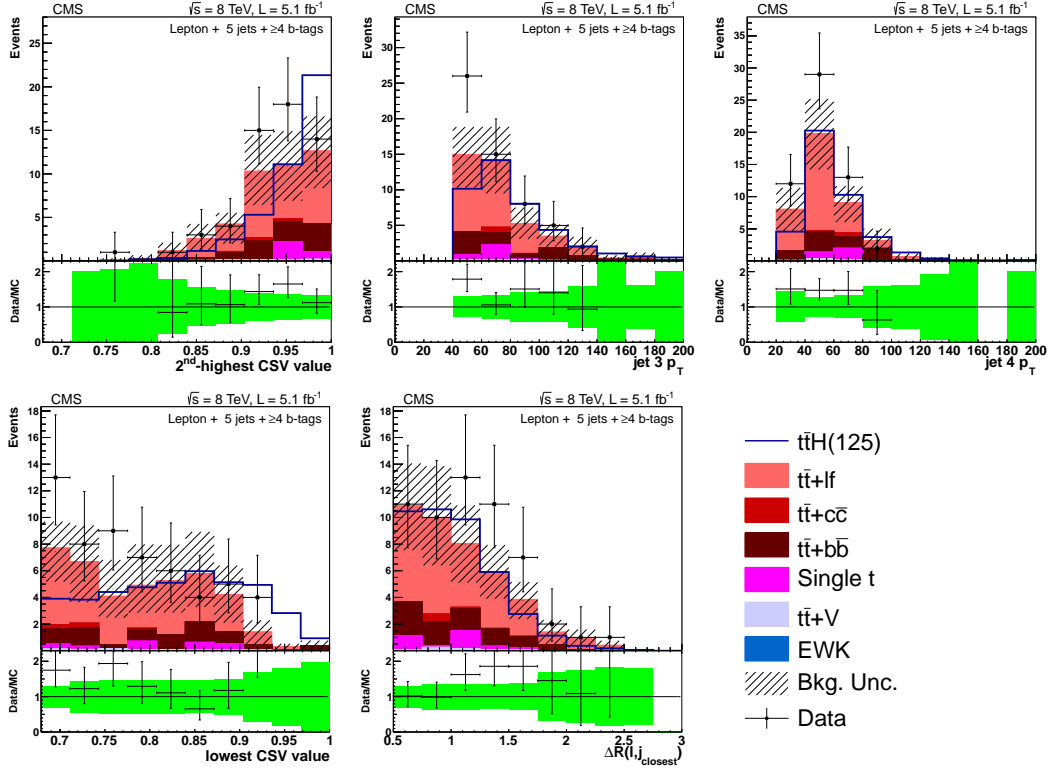


Figure 6.21: Lepton + jets data/MC comparison for the 5 jets + 4 tag category. The uncertainty band includes statistical and systematic uncertainties that affect both the rate and shape of the background distributions.

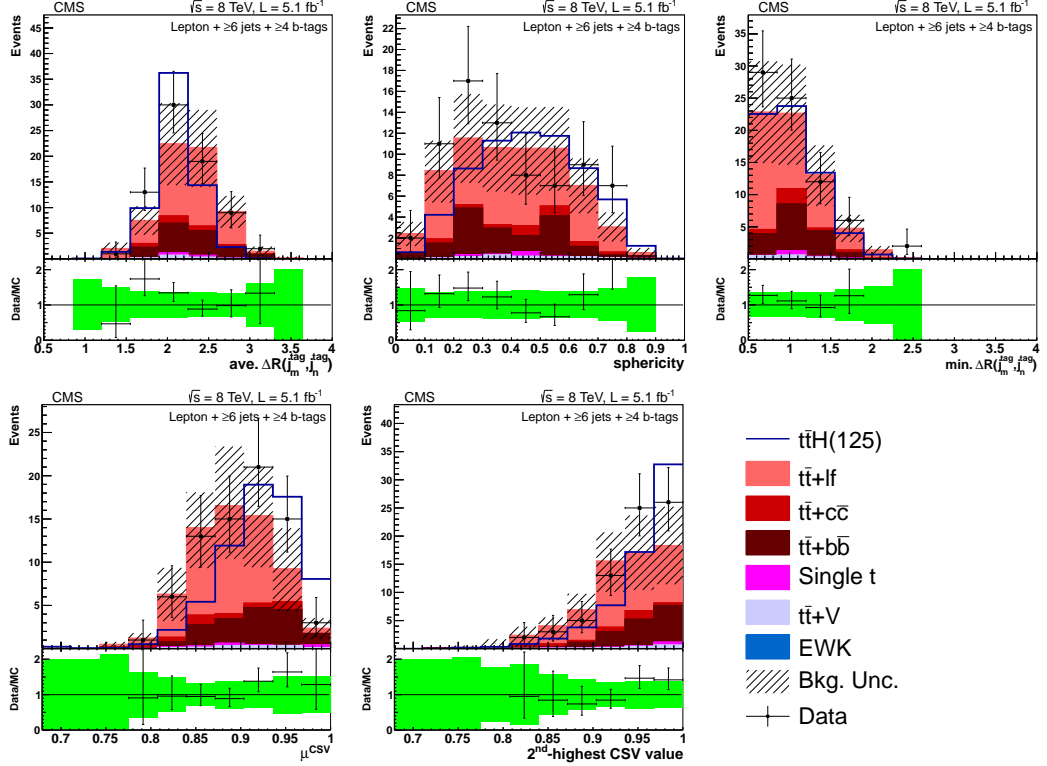


Figure 6.22: Lepton + jets data/MC comparison for the  $\geq 6$  jets + 4 tag category. The uncertainty band includes statistical and systematic uncertainties that affect both the rate and shape of the background distributions.

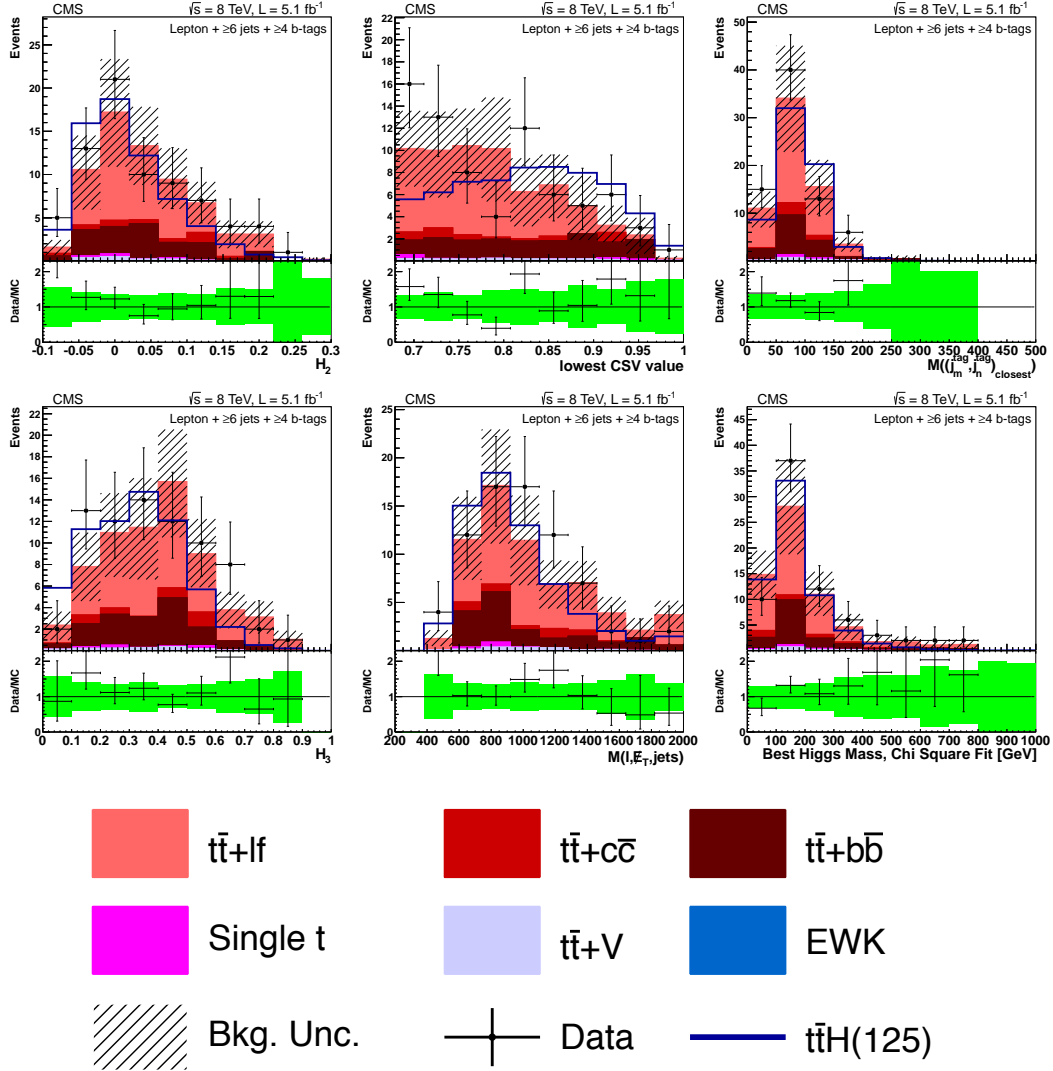


Figure 6.23: Lepton + jets data/MC comparison for the  $\geq 6$  jets + 4 tag category. The uncertainty band includes statistical and systematic uncertainties that affect both the rate and shape of the background distributions.

### <sup>2231</sup> 6.3.3 MVA Output, Data to Monte Carlo Comparisons

<sup>2232</sup> Data to Monte Carlo comparisons for the CFMlpANN output can be seen on figure 6.24. In  
<sup>2233</sup> the plots, the signal shape has been multiplied by a factor of 30 in order to make its shape  
<sup>2234</sup> visible, and in order to gauge a scale of the expected size of signal to background in each jet/tag  
<sup>2235</sup> category.

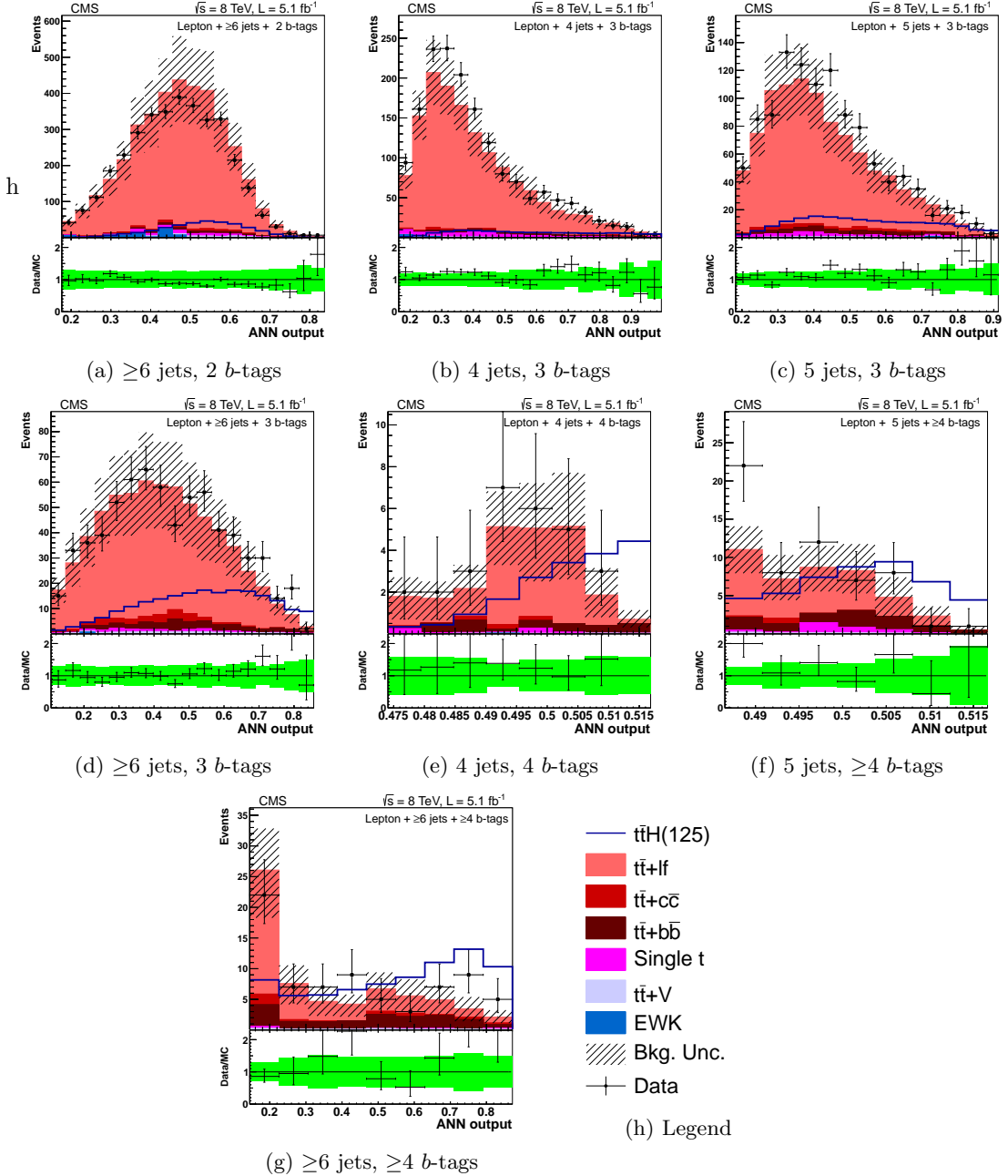


Figure 6.24: The distributions of the CFMlpANN output for lepton+jets events at 8 TeV in the various analysis categories. Background-like events have a low CFMlpANN output value. Signal-like events have a high CFMlpANN output value. The background is normalized to the SM expectation; the uncertainty (shown as a hatched band in the stack plot and a green band in the ratio plot) includes statistical and systematic uncertainties that affect both the rate and shape of the background distributions. The  $t\bar{t}H$  signal ( $m_H = 125 \text{ GeV}/c^2$ ) is normalized to  $30 \times$  SM expectation.

## 2236 6.4 Systematic Uncertainties

2237 There are three types of systematic effects considered in this analysis: those that affect only the  
 2238 rates of signal or background processes, those that affect only the shapes of the CFMlpANN  
 2239 discriminants for signal or background processes, and those that affect both the rate and the  
 2240 shape. In the last case, the rate and shape effects are treated simultaneously so that they are  
 2241 considered completely correlated. Unless otherwise noted, all of the uncertainties listed here  
 2242 apply equally to signal and background and are treated as 100% correlated between the two.  
 2243 Below is a list of systematic effects considered for this analysis:

Table 6.13: Summary of the systematic uncertainties considered on the inputs to the limit calculation. Except where noted, each row in this table will be treated as a single, independent nuisance parameter.

Source	Rate Uncertainty	Shape	Remarks
Luminosity (8 TeV)	2.2%	No	All signal and backgrounds
Lepton ID/Trig	4%	No	All signal and backgrounds
Pileup	1%	No	All signal and backgrounds
Additional Pileup Corr.	–	Yes	All signal and backgrounds
Jet Energy Resolution	1.5%	No	All signal and backgrounds
Jet Energy Scale	0-60%	Yes	All signal and backgrounds
b-Tag SF ( $b/c$ )	0-33.6%	Yes	All signal and backgrounds
b-Tag SF (mistag)	0-23.5%	Yes	All signal and backgrounds
MC Statistics	–	Yes	All backgrounds
PDF ( $gg$ )	9%	No	For $gg$ initiated processes ( $t\bar{t}$ , $t\bar{t}Z$ , $t\bar{t}H$ )
PDF ( $q\bar{q}$ )	4.2-7%	No	For $q\bar{q}$ initiated processes ( $t\bar{t}W$ , $W$ , $Z$ ).
PDF ( $qg$ )	4.6%	No	For $qg$ initiated processes (single top)
QCD Scale ( $t\bar{t}H$ )	15%	No	For NLO $t\bar{t}H$ prediction
QCD Scale ( $t\bar{t}$ )	2-12%	No	For NLO $t\bar{t}$ and single top predictions
QCD Scale (V)	1.2-1.3%	No	For NNLO $W$ and $Z$ prediction
QCD Scale (VV)	3.5%	No	For NLO diboson prediction
Madgraph Scale ( $t\bar{t}$ )	0-20%	Yes	$t\bar{t}$ + jets/ $bb$ / $c\bar{c}$ uncorrelated. Varies by jet bin.
Madgraph Scale (V)	20-60%	No	Varies by jet bin.
$t\bar{t} + bb$	50%	No	Only $t\bar{t} + bb$ .

2244 **Jet Energy Scale (JES):** The Jet Energy Scale systematic is based on the uncertainty on the  
 2245 L1, L2, L3, and L2L3 residual corrections to the reconstructed jet energy, as described  
 2246 in section 6.2.6. To evaluate the effect on the CFMlpANN output, the jet energy scale is  
 2247 shifted by one standard deviation up and down using the standard JetMET procedure [138].  
 2248 For each variation, the jet energies are recalculated, allowing for new jets to pass the  
 2249 selection where once they failed, or fail the selection where once they passed, resulting  
 2250 in a migration of events across jet/tag categories. Finally, the CFMlpANN response is  
 2251 recalculated, and the effect for signal and the  $t\bar{t} + jets$  background is shown in figure 6.25.

**Jet Energy Resolution (JER):** The jet  $p_T$  resolution in MC differs from that observed in  
 data by approximately 10% in a  $\eta$  dependent way, as described in table ??, as per the  
 recommendations of the JetMET group [139]. The value of the jet  $p_T$  is adjusted according

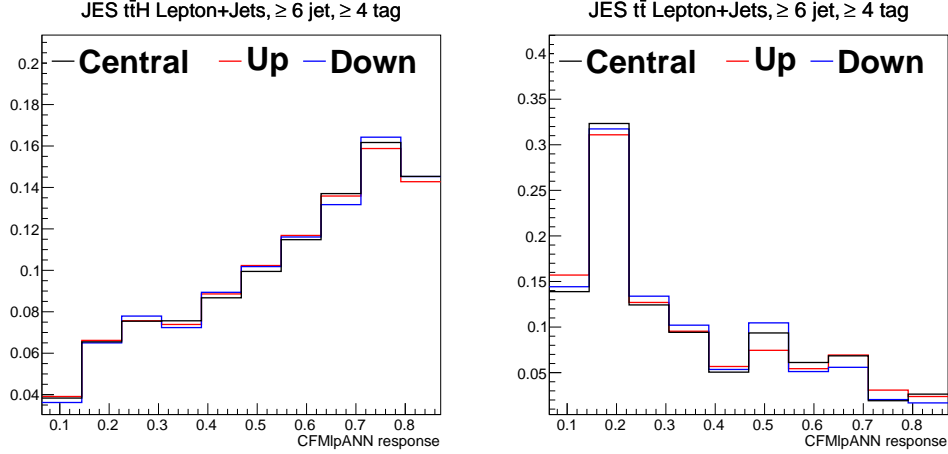


Figure 6.25: Comparison of the MVA discriminator for JES shift upwards (red) and downwards (blue) relative to the nominal (black) shape for the  $t\bar{t}H(120)$  signal (left) and the main background sample  $t\bar{t}$ + light flavor (right). The plots shown are from the  $\geq 6$  jet  $\geq 4$  tag category in the lepton+jets channel. All plots are normalized to unit area.

JES systematic yield change			
sys	shift	lepton+jets	
		$t\bar{t}H(120)$	$t\bar{t}$
JES	up	+8.6%	+12.1%
	down	-8.4%	-7.3%

Table 6.14: Relative yield change due to JES shift up/down for the  $\geq 6$  jets +  $\geq 4$  tags category in the lepton+jets channel.

to the formula:

$$p'_T = \max [0, p_T^{gen} + c(p_T^{reco} - p_T^{gen})] \quad (6.13)$$

2252     The correction factor  $c$  is taken from table ???. To assess the effect of the systematic  
 2253     uncertainty on the JER, the value of  $c$  is shifted up and down by standard deviation, the  
 2254     JER correction is applied to the jets using this new  $c$  value, and the event rates and ANN  
 2255     shapes are recalculated. The effect of the JER on the shape variation is negligible, so it is  
 2256     treated as a rate-only effect in limit setting.

2257     **b-tag Scale Factor:** The uncertainty in the  $b$ -tagging scale factor is assessed according to the  
 2258     prescriptions developed by the BTag POG [140]. Each per-jet  $b$ -tag scale factor is shifted  
 2259     up or down by its uncertainty, and the new CSV output value corresponding to that  
 2260     uncertainty is recalculated. This new CSV value is used to determine both the number of  
 2261     tags associated with that systematic and the new shape of variables that use the CSV  
 2262     output, such as the average CSV value for  $b$ -tagged jets. This uncertainty effects both rate  
 2263     and shape estimates. The effects of the  $b$ -tag scale factors on the ANN shape and event  
 2264     yields are summarized in Fig. 6.26 and Table 6.15 respectively.

2265     **Lepton ID and Trigger Scale Factors:** As discussed previously, an uncertainty of 4% covers

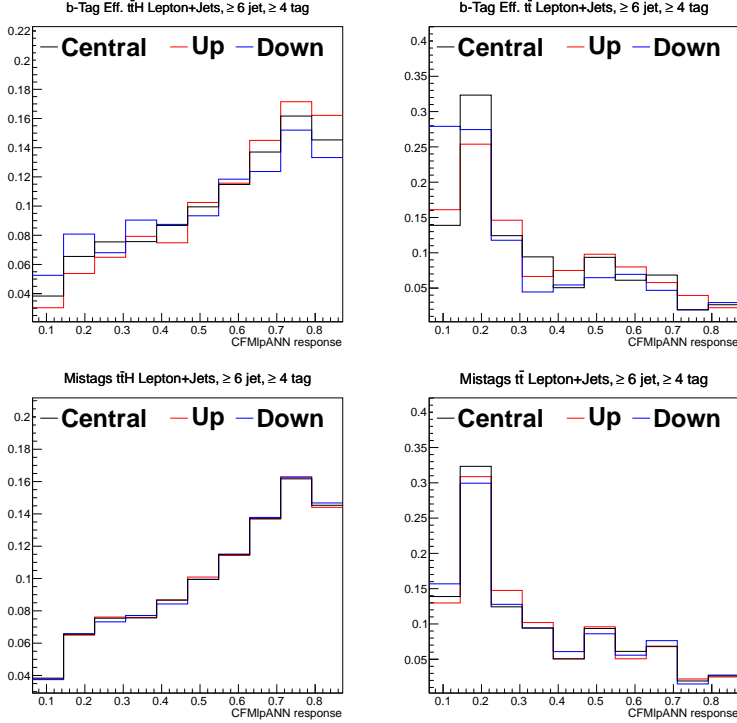


Figure 6.26: Comparison of the MVA discriminator for  $b$ -tag scale factor shift upwards (red) and downwards (blue) relative to the nominal (black) shape for the  $t\bar{t}H(120)$  signal (left) and the main background sample  $t\bar{t} + \text{light flavor}$  (right). The plots are from the  $\geq 6$  jets +  $\geq 4$  tags category in the lepton+jets channel. All plots are normalized to unit area.

$b$ -tag systematic yield change			
		lepton+jets	
sys	shift	$t\bar{t}H(120)$	$t\bar{t}$
heavy flavor SF	up	+14.9%	+23.7%
	down	-15.3%	-16.0%
light flavor SF	up	+0.7%	+5.7%
	down	-1.1%	-4.2%

Table 6.15: Relative yield change due to  $b$ -tag scale factor shift up/down for the  $\geq 6$  jets +  $\geq 4$  tags category in the lepton+jets channel.

variations of the combined trigger, ID, and isolation scale factor.

**Pileup Reweighting:** The uncertainty on the pileup reweighting comes from changing the minimum bias cross section used to calculate the pileup reweighting by  $\pm 7\%$  from the default value of 69.4 mb. The pileup reweighting is calculated using the shifted cross sections and the new weights are applied to determine the uncertainty on both the rate and shapes. Since the effect of the pileup on the shape variation is negligible, the effects of pileup are accounted through a rate-only uncertainty for the limit calculations.

**Additional Pileup Correction** The uncertainty associated with the additional pileup correction, described in section 6.1.5, is applied as a pure shape uncertainty to all processes. Fig. 6.27 shows the effects of the additional pileup correct uncertainty on the CFMlpANN shape.

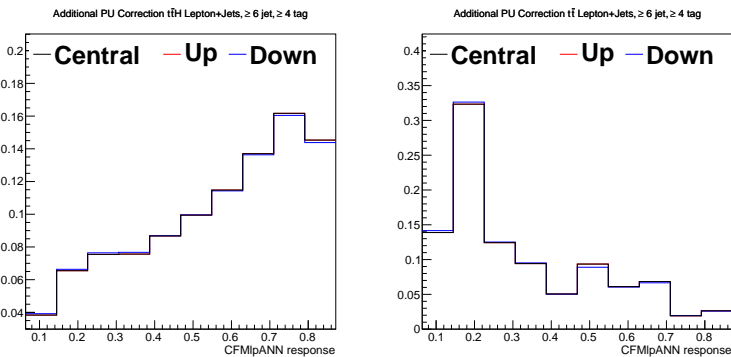


Figure 6.27: Comparison of the MVA discriminator for additional PU correction systematic upwards (red) and downwards (blue) relative to the nominal (black) shape for the  $t\bar{t}H(120)$  signal (left) and the main background sample  $t\bar{t} + \text{light flavor}$  (right). The plots are from the  $\geq 6$  jets +  $\geq 4$  tags category in the lepton+jets channel. All plots are normalized to unit area.

**Cross Sections:** The expectation for signal and background yields are derived from theoretical predictions of at least NLO accuracy. Uncertainties affecting these normalizations are summarized in table 6.16. Where appropriate, factors contributing to these uncertainties that are common to multiple processes are treated as 100% correlated. Note that for the  $t\bar{t}+\text{jets}$  (including  $t\bar{t} + b\bar{b}$  and  $t\bar{t} + c\bar{c}$  processes, as well as the  $V+\text{jets}$  processes, there is an additional uncertainty coming from the scale choice in Madgraph that effects these channels in a jet-bin specific way. This uncertainty is not included in the table 6.16, but is detailed in the next point.

**Luminosity:** The uncertainty on the luminosity estimate is 2.2%. This affects all rates.

**Madgraph  $Q^2$  Uncertainty:** Although that backgrounds are normalized using NLO accurate theoretical calculations, these are only applicable to inclusive distributions. To extrapolate

Process	pdf			QCD Scale			
	$gg$	$qb$	$qg$	$t\bar{t}$	$V$	$VV$	$t\bar{t}H$
$t\bar{t}H$	9%						12.5%
$t\bar{t}+\text{jets}$	9%			12%			
$t\bar{t} + W$		7%		15%			
$t\bar{t} + Z$	9%			15%			
Single top			4.6%	2%			
$W+\text{jets}$		4.8%			1.3%		
$Z+\text{jets}$		4.2%			1.2%		
Dibosons						3.5%	

Table 6.16: Cross section uncertainties used for the limit settings. Each column in the table is an independent source of uncertainty, except for the last column which represents uncertainties uncorrelated with any others. Uncertainties in the same column for two different processes (different rows) are completely correlated.

2288 olate these inclusive predictions to exclusive rates in particular jet bins requires the use  
 2289 of a Monte Carlo sample. The MADGRAPH generator is used at the matrix element level  
 2290 and includes tree-level calculations for processes with multiple additional jets, matched  
 2291 to the PYTHIA parton shower to model additional soft and collinear radiation. Since the  
 2292 MADGRAPH + PYTHIA is tree-level, the choice of the renormalization and factorizations  
 2293 scales in this calculation has a significant impact. To include the effects of this uncertainty,  
 2294 the factorization and renormalization scales are varied by a factor of two. The ideal way  
 2295 to study this effect would be to generate dedicated samples with the varied scale choice,  
 2296 however the required statistics to get a precise determination of the systematic effect is  
 2297 computationally prohibitive. Therefore, as an alternative, we reweight the samples, divid-  
 2298 ing by the appropriate power of  $\alpha_s$  and the *pdf* values at the original scale, and multiplying  
 2299 by the values at the new scale choice. This reweighting procedure is supported by the CMS  
 2300 Monte Carlo Generators group, and has been validated against dedicated scale-varied sam-  
 2301 ples and has been shown to produce consistent results [141]. This reweighting procedure  
 2302 provides both a rate and a shape uncertainty, separately for  $t\bar{t}$ +light flavor,  $t\bar{t} + c\bar{c}$ , and  
 2303  $t\bar{t} + b\bar{b}$  components of the  $t\bar{t}$  sample. Figure 6.28 shows the shape and rate variations for  
 2304 selected event categories. To prevent the strength of the  $t\bar{t}$ +jets constraint from over-  
 2305 constraining the  $t\bar{t} + b\bar{b}$  and  $t\bar{t} + c\bar{c}$  components, we allow the Madgraph scale to vary  
 2306 independently for these three components.

2307 **MC Statistics Uncertainty:** To account for the effect of limited MC statistics in the analysis,  
 2308 a method described by Barlow and Beeston, is used to select regions of the CFMlpANN  
 2309 output that should have additional nuisance parameters applied [?, ?]. For the CFMlpANN  
 2310 shapes of every MC process in all different categories, each bin is allowed to float within  
 2311 statistic uncertainty and a corresponding nuisance parameter is added. To make the limit

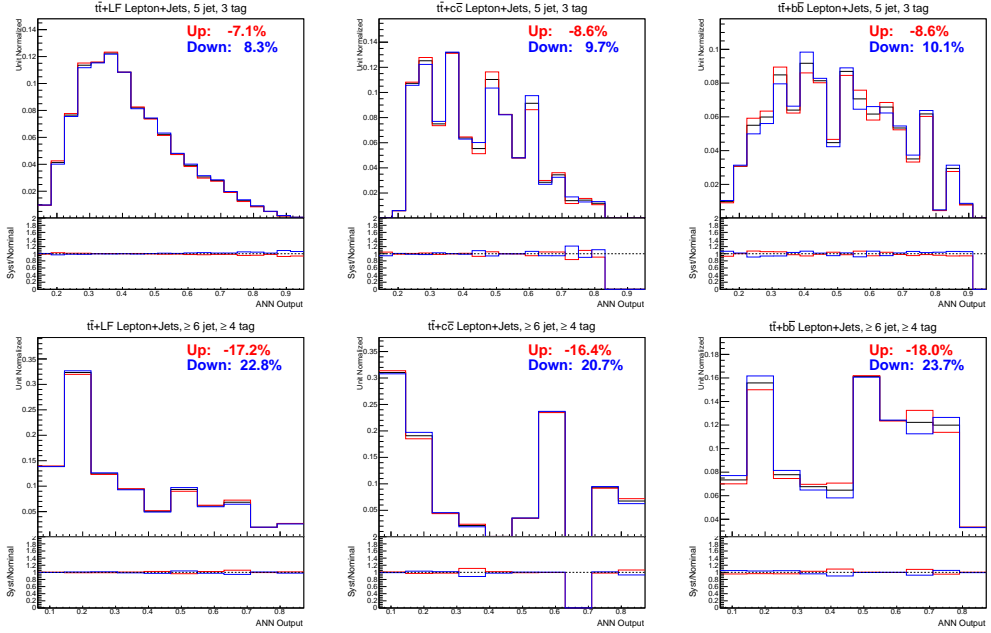


Figure 6.28: The rate and shape variations for selected categories due to the  $Q^2$  uncertainty.

computation more efficient and stable, bins are removed as nuisance parameters if the MC statistics uncertainty is negligible compared to the data statistics uncertainty or where there is no appreciable contribution from signal. In total, there are 60 nuisance parameters used to describe the MC statistics for this analysis. Tests show that the effect of neglecting bins as described above is smaller than 5%.

**Additional  $t\bar{t} + b\bar{b}$  Rate Uncertainty:**  $t\bar{t} + b\bar{b}$  background is very similar to our signal, the uncertainty on its rate and shape will have a big impact on our search. Due to the lack of more accurate next leading order(NLO) theoretical predication for this process, we obtained this background and assessed its uncertainty based on the inclusive 8 TeV  $t\bar{t}$  sample. Since the inclusive  $t\bar{t}$  sample is generated with Madgraph + Pythia, we need to apply a K-factor to the Madgraph cross section. According to calculations done in [142], the K-factor from leading order(LO) to NLO ranges between 1.2 and 1.8, depending on the scale choice. To be conservative, an extra 50% rate uncertainty is assigned to  $t\bar{t} + b\bar{b}$  which corresponds to a K-factor of 1.7 for  $\sigma_{NLO}/\sigma_{Madgraph}$ . Studies also showed consistently that  $t\bar{t} + b\bar{b}$  rate is correct to within factor of 2 in control regions dominated by  $t\bar{t}$ +light flavor statistics. The extra 50% rate uncertainty should possibly include additional uncertainty beyond the 20% from  $Q^2$  scale to account for the differences between NLO and Madgraph.

In order to validate this assessment further, a dedicated CFMlpANN was trained to separate  $t\bar{t} + b\bar{b}$  from the  $t\bar{t} + jets$  background. In order to have sufficient statistics, two jet/tag categories are used: 5jets,  $\geq 3b$ -tags, and  $\geq 6$ jets,  $\geq 3b$ -tags. The nominal  $t\bar{t} + b\bar{b}$  cross section

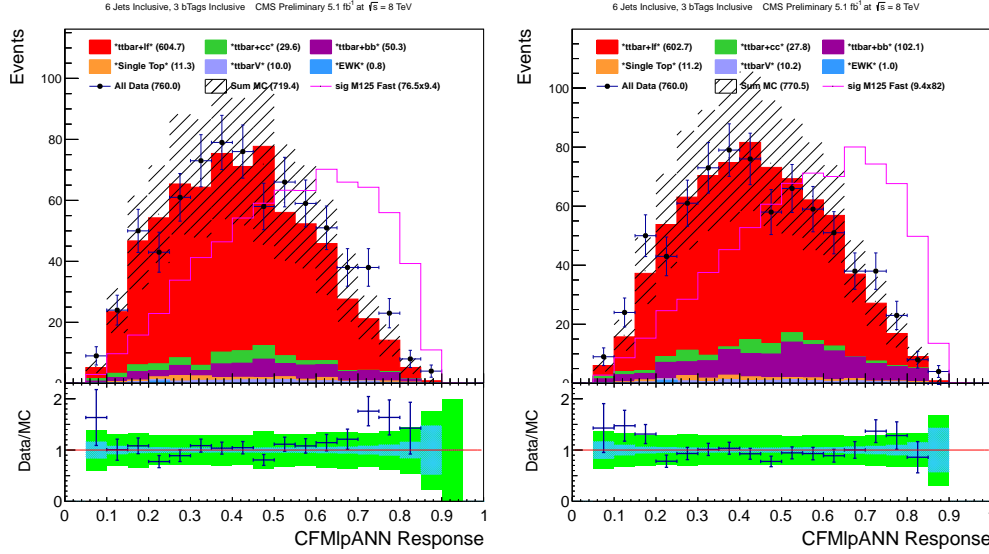


Figure 6.29: A dedicated CFMlpANN trained to isolate  $t\bar{t} + b\bar{b}$  from  $t\bar{t} + \text{jets}$ . The left plot shows is for the case of nominal  $t\bar{t} + b\bar{b}$  cross-section, the right plot shows the case for  $x2 t\bar{t} + b\bar{b}$  cross-section. The left-most region of both plots is the most sensitive to the  $t\bar{t} + b\bar{b}$  normalization, and shows no significant improvement in data to MC agreement, justifying the reasoning that an uncertainty larger than 50% is needed.

2332 was doubled, in an attempt to observe an improvement in the range of the discriminant  
 2333 that was enriched in  $t\bar{t} + b\bar{b}$ . However, as figure 6.29 shows, no significant improvement  
 2334 was seen, justifying the reasoning that an uncertainty much larger than 50% is needed.

## 2335 6.5 Statistical Methods

2336 In the lack of an observation of any deviation from SM predictions, upper limits are set on the  
 2337 Higgs boson production cross section, with respect to the SM expectation,  $\sigma^{95\%}/\sigma^{SM}$ . Although  
 2338 the analysis has been optimized for Higgs decays to  $b$ -quarks, there is still acceptance from  $WW$   
 2339 and  $ZZ$  decays. As such, limits on the inclusive decay of the Higgs boson are set. The statistical  
 2340 method used to report results is the modified frequentist approach, also known as  $CL_s$ .

2341 For the  $CL_s$  method, the likelihood function  $\mathcal{L}(\text{data}|\mu, \theta)$  is defined as

$$\mathcal{L}(\text{data}|\mu, \theta) = \text{Poisson}(\text{data}|\mu \cdot s(\theta) + b(\theta)) \cdot p(\tilde{\theta}|\theta) \quad (6.14)$$

$$= \prod_i \frac{(\mu s_i + b_i)^{n_i}}{n_i!} e^{-(\mu s_i + b_i)} \cdot p(\tilde{\theta}|\theta) \quad (6.15)$$

2342 where  $\mu$  is the signal strength modifier which is often reported in the upper limit results as the  
 2343 ratio of the cross-section upper limit over the standard model cross-section and  $\theta$  represents a  
 2344 full set of nuisance parameters that are used to incorporate systematic uncertainties [143]. The

2345 Probability Distribution Function (*pdf*) of the nuisance parameter  $p(\tilde{\theta}|\theta)$ , where  $\tilde{\theta}$  is the default  
 2346 value, reflects the degree of confidence in what the true value of  $\theta$  is. For rate uncertainties, this  
 2347 is parameterized by a log-normal distribution given by:

$$\rho(\theta) = \frac{1}{\sqrt{2\pi} \ln \kappa} \exp \left( -\frac{(\ln(\theta/\tilde{\theta}))^2}{2\ln(\kappa)^2} \right) \frac{1}{\theta} \quad (6.16)$$

2348 where  $\kappa$  is the parameter used to determine the width of the uncertainty, and  $\tilde{\theta}$  is the nominal  
 2349 value of the distribution. Shape uncertainties can be taken into account by "vertical morphing"  
 2350 [144]. For each shape uncertainty, two additional histograms of the CFMlpANN output  
 2351 are needed, with  $\pm 1\sigma$  variations of the systematic uncertainty in question. When building the  
 2352 likelihood, the systematic is associated to a nuisance parameter taken from a unit gaussian dis-  
 2353 tribution, which is used to parameterize a quadratic interpolation for shifts below the  $1\sigma$  value  
 2354 of a given bin, and linear interpolation for values beyond.

2355 To compare the compatibility of the data with the *background – only* ( $\mu = 0$ ) and *signal +*  
 2356 *background* hypotheses, where the signal is allowed to be scaled by some factor  $\mu$ , the test  
 2357 statistic  $\tilde{q}_\mu$  is constructed based on the profile likelihood ratio:

$$\tilde{q}_\mu = -2 \ln \frac{\mathcal{L}(\text{data}|\mu, \hat{\theta}_\mu)}{\mathcal{L}(\text{data}|\hat{\mu}, \hat{\theta})} \quad , 0 \leq \hat{\mu} \leq \mu \quad (6.17)$$

2358 where  $\hat{\theta}_\mu$  refers to the conditional maximum likelihood estimator of  $\theta$ , given the signal strength  
 2359 parameter  $\mu$  and data. The pair of parameter estimators  $\hat{\mu}$  and  $\hat{\theta}$  correspond to the global  
 2360 maximum of the likelihood.

2361 To perform the full  $CL_S$  technique, *pdf's* of the results of the *background – only*,  $f(\tilde{q}_\mu|\mu, \hat{\theta}_\mu^{obs})$ ,  
 2362 and *signal + background*,  $f(\tilde{q}_\mu|0, \hat{\theta}_\mu^{obs})$  test statistics are formed by creating *psuedo – datasets*  
 2363 of the signal and background CFMlpANN distributions, with the values of  $\hat{\theta}_0^{obs}$  and  $\hat{\theta}_\mu^{obs}$  fixed,  
 2364 but allowing the shapes and normalizations of the CFMlpANN distributions to vary within  
 2365 the constraints of the nuisance parameter shapes. Once the *pdfs* for each of the test statistics  
 2366 are constructed, the *p*-value associated with each hypothesis,  $p_\mu$  and  $p_0$ , are evaluated by the  
 2367 following integrals:

$$p_\mu = P(\tilde{q}_\mu \geq \tilde{q}_\mu^{obs} | \text{signal + background}) = \int_{\tilde{q}_\mu^{obs}}^{\inf} f(\tilde{q}_\mu|\mu, \hat{\theta}_\mu^{obs}) d\tilde{q}_\mu \quad (6.18)$$

2368 for the *signal + background* hypothesis, and

$$1 - p_0 = P(\tilde{q}_\mu \geq \tilde{q}_\mu^{obs} | \text{background – only}) = \int_{\tilde{q}_0^{obs}}^{\inf} f(\tilde{q}_\mu|0, \hat{\theta}_0^{obs}) d\tilde{q}_\mu \quad (6.19)$$

2369 for the *background – only* hypothesis.  $CL_s(\mu)$  is calculated as a ratio of these  $p$ -values:

$$CL_s(\mu) = \frac{p_\mu}{1 - p_0} \quad (6.20)$$

2370 To quote the 95% upper limit on  $\mu$ ,  $\mu^{95\% CL}$ , the value of  $\mu$  is adjusted until  $CL_s = 0.05$ .

2371 The frequentist  $CL_s$  approach uses a large number of pseudo-experiments to extract the  
2372 limit results. The "asymptotic" approach makes an analytic approximation of the full  $CL_s$   
2373 technique and therefore avoids throwing pseudo-experiments [145]. The *pdfs*,  $f(\tilde{q}_\mu|\mu, \hat{\theta}_\mu^{obs})$ , and  
2374  $f(\tilde{q}_\mu|0, \hat{\theta}_\mu^{obs})$  are approximated as a falling exponential below  $q_{\mu,A}$ , and a Gaussian above, where  
2375  $q_{\mu,A}$  is the test statistic of the Asimov dataset, the background only hypothesis with nominal  
2376 nuisance value parameters. The asymptotic approach is used for optimization and the results of  
2377 this analysis. For the limits set from the combined Lepton+Jets and di-Lepton channels, using  
2378 both 7 and 8 TeV data, the results are calculated using the full  $CL_s$  treatment. Comparisons  
2379 have shown that limits obtained with the two techniques agree at the 10% level.

2380 In the limit calculation, the backgrounds are decomposed into the following distinct cate-  
2381 gories:  $t\bar{t}$ +jets,  $t\bar{t} + b\bar{b}$ ,  $t\bar{t} + c\bar{c}$ , single top (*s*-channel, *t*-channel, and *tW*-channel combined),  
2382  $W$ +jets,  $Z$ +jets,  $t\bar{t} + W$ ,  $t\bar{t} + Z$ , and dibosons ( $WW$ ,  $WZ$ , and  $ZZ$  combined). The rates and  
2383 shapes of these background processes, as well as the signal are allowed to vary according to a set  
2384 of nuisance parameters, and the values of these nuisance parameters are constrained according  
2385 to the uncertainties summarized in Table 7.13. Except where noted below, each row in that table  
2386 represents a single nuisance parameter, completely correlated across all categories and processes  
2387 to which it applies. The exceptions to this approach are as follows:

- 2388 • In the case of the Madgraph  $Q^2$  uncertainty, there are separate nuisance parameters for  
2389 each of the three components of the  $t\bar{t}$  background (+jets, + $b\bar{b}$ , and + $c\bar{c}$ ). Furthermore, for  
2390 the  $t\bar{t}$ +jets component, the uncertainty is actually broken into three nuisance parameters  
2391 for the contributions coming from diagrams with zero extra partons, one extra parton, or  
2392 at least two extra partons.
- 2393 • For the *b*-tagging efficiency and mistag rate uncertainties, the rate and shape components  
2394 are described by separate, independent nuisance parameters. Furthermore, each event  
2395 selection category has its own, independent nuisance parameter. This is to prevent the  
2396 high statistics background rich regions from over-constraining the shape uncertainties in  
2397 the lower statistics, more signal rich regions.

2398 For systematic effects such as the jet energy scale or the rate component of the *b*-tagging  
2399 scale factor that may cause migration between event categories, care has been taken to correlate  
2400 properly the different categories so that, for example, increasing the jet energy scale will cause

the appropriate increases and decreases in the yields in various categories. The binning of the CFMlpANN output is chosen to minimize the impact of MC statistics and, as described in section 6.4 the MC statistics for bins where the MC statistical uncertainty causes a significant impact are accounted for.

## 6.6 Results and Conclusions

The variable used for signal extraction is the shape of the MVA output discriminator distribution. The fit of the simulated samples to the measured data will test for the presence of signal and, in its absence, it will set upper limits on the Higgs boson cross section. Besides the MVA discriminator shapes for data, background and signal, inputs to the "Higgs Combination" package also include the number of events passing our selection for each of the above processes. Various systematic uncertainties described in section 6.4 have all been taken into account in our limit calculation. The Higgs mass points we set limits for are: 110, 115, 120, 125, 130, 135 and 140  $\text{GeV}/c^2$ . The upper limits are shown in Tab. 6.17 and Fig. 6.30.

Higgs Mass	Observed	Median	Expected 68% C.L. Range	95% C.L. Range
110 $\text{GeV}/c^2$	5.9	3.1	[2.1,4.6]	[1.6,6.8]
115 $\text{GeV}/c^2$	7.2	3.9	[2.7,5.7]	[2.0,8.1]
120 $\text{GeV}/c^2$	8.8	4.8	[3.4,6.9]	[2.5,9.7]
125 $\text{GeV}/c^2$	9.5	5.4	[3.8,7.9]	[2.8,11.1]
130 $\text{GeV}/c^2$	11.4	6.6	[4.6,9.6]	[3.4,13.7]
135 $\text{GeV}/c^2$	15.0	8.9	[6.3,12.8]	[4.7,18.1]
140 $\text{GeV}/c^2$	17.0	11.0	[7.7,15.9]	[5.7,22.5]

Table 6.17: Expected and observed upper limits for SM Higgs for lepton + jets channel using the first 5.1  $\text{fb}^{-1}$  of the 2012 dataset. These limits were extracted using the asymptotic method.

For this first 5.1  $\text{fb}^{-1}$  of data collected by the CMS detector, the first search for the Standard Model Higgs boson produced in association with top-quark pairs. Although there have been no observed sign of Higgs production in association with top quarks, upper limits are set on the production cross-section, using the statistical methods described above. If this data set was repeatedly collected, allowing for statistical fluctuations, it should be expected that, for a Standard Model Higgs boson, with mass,  $m_H = 125 \text{ GeV}$ , that 95% of the results would fail to observe the  $t\bar{t}H$  signal unless its cross-section was modified by a factor of 9.5. From simulations alone, this expected factor is 5.4, a difference of less than  $2\sigma$  from the observed data.

The results of this analysis were combined with previous results in this channel from 7 TeV data and with a di-lepton final state channel and published in the Journal of High Energy Physics (JHEP) in May of 2013 [146]. The combined analytical power of all of the channels allowed for an upper limit of 5.8 times the predicted Standard Model cross section. This is less than  $1\sigma$

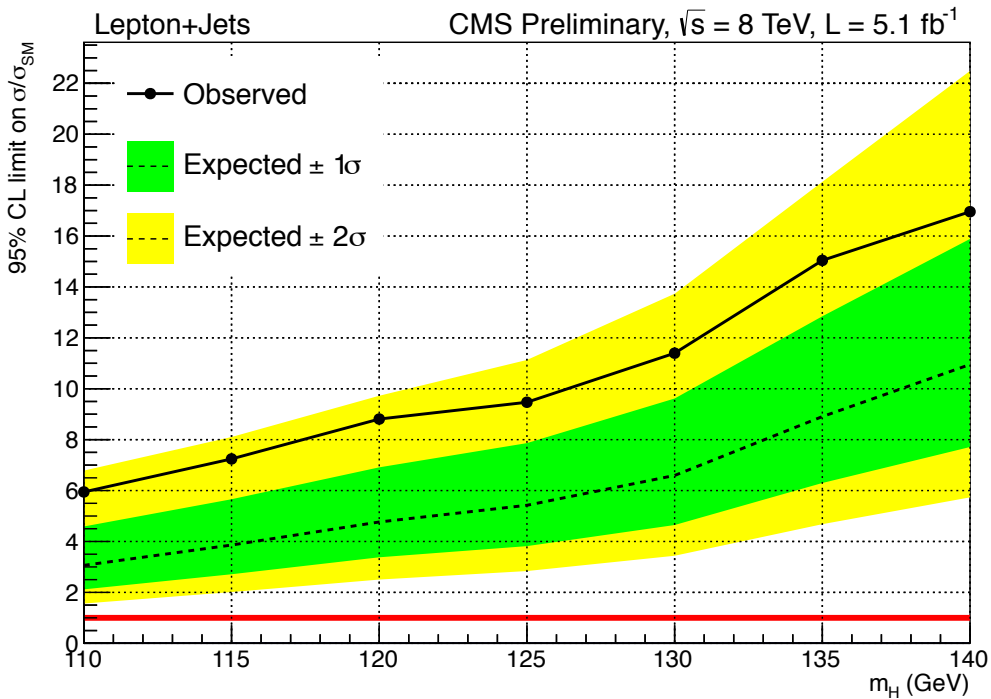


Figure 6.30: The expected and observed 95% CL upper limits on the signal strength parameter  $\mu = \sigma/\sigma_{SM}$  for the lepton+jets channel using the 2012 dataset. These limits were extracted using the asymptotic method.

<sup>2426</sup> away from the expected factor of 5.2 from simulations alone.

2427 **Chapter 7**

2428 **Analysis II: The Complete 19.5**  
2429  **$\text{fb}^{-1}$  of 8 TeV data**

2430 The CMS experiment recorded  $19.5 \text{ fb}^{-1}$  of data in the complete 8 TeV run during 2012.  
2431 The previous analysis was updated with the full dataset. A similar lepton and jet selection  
2432 is used, with the same classification scheme for events, based on the reconstructed jet and  $b$ -  
2433 tag multiplicity. New signal and background simulations were generated to account for the  
2434 increased dataset, requiring new calibration factors for the pileup, lepton and jet reconstruction,  
2435 and  $b$ -tagging efficiency. Additionally, a new type of multivariate analysis (MVA) technique was  
2436 employed, in place of the Clermont-Ferrand Multi-Layer Perceptron Artificial Neural Network  
2437 (CFMlpANN), a Boosted Decision Tree (BDT) is used for signal extraction and limit setting. The  
2438 number of input variables that were investigated for use in each jet/tag category, was expanded,  
2439 and some new variables were found to offer slightly more discriminating power. The discriminant  
2440 of a specialized BDT, trained to separate  $t\bar{t} + b\bar{b}$  from  $t\bar{t}H$ , was added as an input variable to  
2441 the BDT trained in the 5 jet,  $\geq 4$   $b$ -tag;  $\geq 6$  jet, 3  $b$ -tag; and  $\geq 6$  jet,  $\geq 4$   $b$ -tag categories.

2442 **7.1 Data and Simulated Samples**

2443 As described in the earlier chapters, data is collected through an HLT trigger path and stored  
2444 offline for analysis later. Simulated samples are generated with the latest theoretical and empir-  
2445 ical inputs for the proton PDF, standard model cross sections, and hadronic showering. These  
2446 events are processed with a simulation of the detector environment, and the subsequent elec-  
2447 tronic response of each of its elements. Finally, physics objects, such as electrons, and muons  
2448 are reconstructed with the particle-flow algorithm described in a previous chapter.

<sup>2449</sup> **7.1.1 Data Samples**

<sup>2450</sup> The results presented here are based on the full  $\sim 19.5 \text{ fb}^{-1}$  of the 2012 CMS dataset. Table 7.1  
<sup>2451</sup> lists the datasets used for this analysis, based on single muon and single electron triggers used to  
<sup>2452</sup> collect the data. Luminosities are quoted from the HF luminosity calculation and have a 2.2%  
<sup>2453</sup> uncertainty.

Dataset	Run Range	Integrated Luminosity
/SingleMu/Run2012A-13Jul2012-v1/AOD	190456–193621	$0.81 \text{ fb}^{-1}$
/SingleMu/Run2012A-recover-06Aug2012-v1/AOD	190782–190949	$0.08 \text{ fb}^{-1}$
/SingleMu/Run2012B-13Jul2012-v1/AOD	193834–196531	$4.40 \text{ fb}^{-1}$
/SingleMu/Run2012C-24Aug2012-v1/AOD	198022–198523	$0.50 \text{ fb}^{-1}$
/SingleMu/Run2012C-PromptReco-v2/AOD	198941–203746	$6.39 \text{ fb}^{-1}$
/SingleMu/Run2012D-PromptReco-v1/AOD	203768–208686	$7.27 \text{ fb}^{-1}$
<b>Total SingleMu</b>	<b>190645–208686</b>	<b><math>19.5 \text{ fb}^{-1}</math></b>
/SingleElectron/Run2012A-13Jul2012-v1/AOD	190456–193621	$0.81 \text{ fb}^{-1}$
/SingleElectron/Run2012A-recover-06Aug2012-v1/AOD	190782–190949	$0.08 \text{ fb}^{-1}$
/SingleElectron/Run2012B-13Jul2012-v1/AOD	193834–196531	$4.40 \text{ fb}^{-1}$
/SingleElectron/Run2012C-24Aug2012-v1/AOD	198022–198523	$0.50 \text{ fb}^{-1}$
/SingleElectron/Run2012C-PromptReco-v2/AOD	198941–203746	$6.40 \text{ fb}^{-1}$
/SingleElectron/Run2012D-PromptReco-v1/AOD	203768–208686	$7.27 \text{ fb}^{-1}$
<b>Total SingleElectron</b>	<b>190645–208686</b>	<b><math>19.5 \text{ fb}^{-1}</math></b>

Table 7.1: The datasets analyzed for this analysis.

<sup>2454</sup> **7.1.2 Signal Samples**

<sup>2455</sup> The  $t\bar{t}H$  signal is modeled using the PYTHIA Monte Carlo generator. The samples and associated  
<sup>2456</sup> cross sections used are listed in Table 7.2.

<sup>2457</sup> **7.1.3 Background Samples**

<sup>2458</sup> To model the backgrounds, this analysis primarily uses Monte Carlo (MC) samples from the  
<sup>2459</sup> "Summer12" MC campaign, discussed in the previous chapter. Most of the samples are generated  
<sup>2460</sup> either with the MADGRAPH tree-level matrix element generator matched to PYTHIA for the  
<sup>2461</sup> parton shower, or with the NLO generator POWHEG combined with PYTHIA. These samples are  
<sup>2462</sup> reconstructed with the same CMSSW version as the data samples listed above. Similarly to the  
<sup>2463</sup> previous analysis, the pileup distribution in all MC samples is reweighted, using the procedure  
<sup>2464</sup> listed below so that the MC pileup distribution matches the one expected for data. Table 7.3  
<sup>2465</sup> lists the background MC samples and associated cross sections.

<sup>2466</sup> For this analysis, the  $t\bar{t} + jets$  background, is decomposed into four components. The  $t\bar{t} + b\bar{b}$ ,  
<sup>2467</sup> background is separated into two classes:  $t\bar{t} + b\bar{b}$  events in which both b-quarks are well separated  
<sup>2468</sup> and energetic enough to be reconstructed, and events in which either the two b-quarks are so  
<sup>2469</sup> close together they merge into the same jet or one of the b-quarks is too soft or forward to be  
<sup>2470</sup> reconstructed as a jet. The latter contribution is referred to as  $t\bar{t} + b$ .

Mass	Higgs Decay	Dataset	Cross Sect.
110 $\text{GeV}/c^2$	$H \rightarrow \text{all}$	/TTH_Inclusive_M110_8TeV_pythia6/Summer12_DR53X-PU_S10_START53_V7Av1/AODSIM	0.1887 pb
115 $\text{GeV}/c^2$	$H \rightarrow \text{all}$	/TTH_Inclusive_M115_8TeV_pythia6/Summer12_DR53X-PU_S10_START53_V7Av1/AODSIM	0.1663 pb
120 $\text{GeV}/c^2$	$H \rightarrow \text{all}$	/TTH_Inclusive_M120_8TeV_pythia6/Summer12_DR53X-PU_S10_START53_V7Av1/AODSIM	0.1470 pb
122.5 $\text{GeV}/c^2$	$H \rightarrow \text{all}$	/TTH_Inclusive_M122_5.8TeV_pythia6/Summer12_DR53X-PU_S10_START53_V7Av1/AODSIM	0.1383 pb
125 $\text{GeV}/c^2$	$H \rightarrow \text{all}$	/TTH_Inclusive_M125_8TeV_pythia6/Summer12_DR53X-PU_S10_START53_V7Av1/AODSIM	0.1302 pb
127.5 $\text{GeV}/c^2$	$H \rightarrow \text{all}$	/TTH_Inclusive_M127_5.8TeV_pythia6/Summer12_DR53X-PU_S10_START53_V7Av1/AODSIM	0.1227 pb
130 $\text{GeV}/c^2$	$H \rightarrow \text{all}$	/TTH_Inclusive_M130_8TeV_pythia6/Summer12_DR53X-PU_S10_START53_V7Av1/AODSIM	0.1157 pb
135 $\text{GeV}/c^2$	$H \rightarrow \text{all}$	/TTH_Inclusive_M135_8TeV_pythia6/Summer12_DR53X-PU_S10_START53_V7Av1/AODSIM	0.1031 pb
140 $\text{GeV}/c^2$	$H \rightarrow \text{all}$	/TTH_Inclusive_M140_8TeV_pythia6/Summer12_DR53X-PU_S10_START53_V7Av1/AODSIM	0.09207 pb
110 $\text{GeV}/c^2$	$H \rightarrow \tau\tau$	/TTH_HToTauTau_M-110_8TeV_pythia6/Summer12_DR53X-PU_S10_START53_V7A-v1/AODSIM	0.0150 pb
115 $\text{GeV}/c^2$	$H \rightarrow \tau\tau$	/TTH_HToTauTau_M-115_8TeV_pythia6/Summer12_DR53X-PU_S10_START53_V7A-v1/AODSIM	0.0150 pb
120 $\text{GeV}/c^2$	$H \rightarrow \tau\tau$	/TTH_HToTauTau_M-120_8TeV_pythia6/Summer12_DR53X-PU_S10_START53_V7A-v1/AODSIM	0.0103 pb
122.5 $\text{GeV}/c^2$	$H \rightarrow \tau\tau$	/TTH_HToTauTau_M-122_5.8TeV_pythia6/Summer12_DR53X-PU_S10_START53_V7A-v1/AODSIM	0.0093 pb
125 $\text{GeV}/c^2$	$H \rightarrow \tau\tau$	/TTH_HToTauTau_M-125_8TeV_pythia6/Summer12_DR53X-PU_S10_START53_V7A-v1/AODSIM	0.0082 pb
127.5 $\text{GeV}/c^2$	$H \rightarrow \tau\tau$	/TTH_HToTauTau_M-127_5.8TeV_pythia6/Summer12_DR53X-PU_S10_START53_V7A-v1/AODSIM	0.0072 pb
130 $\text{GeV}/c^2$	$H \rightarrow \tau\tau$	/TTH_HToTauTau_M-130_8TeV_pythia6/Summer12_DR53X-PU_S10_START53_V7A-v1/AODSIM	0.0063 pb
135 $\text{GeV}/c^2$	$H \rightarrow \tau\tau$	/TTH_HToTauTau_M-135_8TeV_pythia6/Summer12_DR53X-PU_S10_START53_V7A-v1/AODSIM	0.0046 pb
140 $\text{GeV}/c^2$	$H \rightarrow \tau\tau$	/TTH_HToTauTau_M-140_8TeV_pythia6/Summer12_DR53X-PU_S10_START53_V7A-v1/AODSIM	0.0032 pb

Table 7.2: List of signal MC datasets and cross sections used to determine the SM expectation.

Sample	Dataset	Cross Sect.
$t\bar{t}$ + jets	/TTJets_MassiveBinDECAY_TuneZ2star_8TeVmadgraph-tauola/Summer12_DR53XPU_S10_START53_V7Av1/AODSIM	245.8 pb
$t\bar{t} \rightarrow \text{all}$	/TTJets_MassiveBinDECAY_TuneZ2star_8TeVmadgraph-tauola/Summer12_DR53XPU_S10_START53_V7Av2/AODSIM	
$t\bar{t} \rightarrow \text{jets}$	/TTJets_HadronicMGDecays_8TeVmadgraph/Summer12_DR53XPU_S10_START53_V7A_extv1/AODSIM	112.33 pb
$t\bar{t} \rightarrow \ell\nu + 4 \text{ jets}$	/TTJets_SemiLeptMGDecays_8TeVmadgraph/Summer12_DR53XPU_S10_START53_V7A_extv1/AODSIM	107.66 pb
$t\bar{t} \rightarrow \ell\nu\nu + 2 \text{ jets}$	/TTJets_FullLeptMGDecays_8TeVmadgraph/Summer12_DR53XPU_S10_START53_V7Av2/AODSIM	25.81 pb
$t\bar{t} + W$	/TTWJets_8TeVmadgraph/Summer12_DR53XPU_S10_START53_V7Av1/AODSIM	0.249 pb
$t\bar{t} + Z$	/TTZJets_8TeVmadgraph_v2/Summer12_DR53XPU_S10_START53_V7Av1/AODSIM	0.208 pb
$W + \text{jets}$	/WJetsToLNu_TuneZ2Star_8TeVmadgraphtarball/Summer12_PU_S7_START52_V9v1/AODSIM	36257.2 pb
$W + 1 \text{ jet}$	/W1JetsToLNu_TuneZ2Star_8TeVmadgraph/Summer12_DR53XPU_S10_START53_V7Av1/AODSIM	6440.4 pb
$W + 2 \text{ jets}$	/W2JetsToLNu_TuneZ2Star_8TeVmadgraph/Summer12_DR53XPU_S10_START53_V7Av1/AODSIM	2087.2 pb
$W + 3 \text{ jets}$	/W3JetsToLNu_TuneZ2Star_8TeVmadgraph/Summer12_DR53XPU_S10_START53_V7Av1/AODSIM	619.0 pb
$W + 4 \text{ jets}$	/W4JetsToLNu_TuneZ2Star_8TeVmadgraph/Summer12_DR53XPU_S10_START53_V7Av1/AODSIM	255.2 pb
$Z/\gamma^* + \text{jets}$ $10 \text{ GeV}/c^2 < M_{\ell\ell} < 50 \text{ GeV}/c^2$ $M_{\ell\ell} > 50 \text{ GeV}/c^2$	/DYJetsToLL_M-10To50_TuneZ2Star_8TeV-madgraph/Summer12_DR53X-PU_S10_START53_V7A-v1/AODSIM /DYJetsToLL_M-50_TuneZ2Star_8TeV-madgraph-tarball/Summer12_DR53X-PU_S10_START53_V7A-v1/AODSIM	14702 pb 3505.7 pb
$Z/\gamma^* + 1 \text{ jet}$	/DY1JetsToLL_M-50_TuneZ2Star_8TeV-madgraph/Summer12_DR53X-PU_S10_START53_V7A-v1/AODSIM	666.7 pb
$Z/\gamma^* + 2 \text{ jets}$	/DY2JetsToLL_M-50_TuneZ2Star_8TeV-madgraph/Summer12_DR53X-PU_S10_START53_V7A-v1/AODSIM	215.1 pb
$Z/\gamma^* + 3 \text{ jets}$	/DY3JetsToLL_M-50_TuneZ2Star_8TeV-madgraph/Summer12_DR53X-PU_S10_START53_V7A-v1/AODSIM	66.07 pb
$Z/\gamma^* + 4 \text{ jets}$	/DY4JetsToLL_M-50_TuneZ2Star_8TeV-madgraph/Summer12_DR53X-PU_S10_START53_V7A-v1/AODSIM	27.38 pb
Single $t$ $s\text{-channel}$	/T_s-channel_TuneZ2star_8TeV-powheg-tauola/Summer12_DR53X-PU_S10_START53_V7A-v1/AODSIM	3.79 pb
$t\text{-channel}$	/T_t-channel_TuneZ2star_8TeV-powheg-tauola/Summer12_DR53X-PU_S10_START53_V7A-v1/AODSIM	56.4 pb
$tW$	/T_tW-channel-DR_TuneZ2star_8TeV-powheg-tauola/Summer12_DR53X-PU_S10_START53_V7A-v1/AODSIM	11.1 pb
Single $\bar{t}$ $s\text{-channel}$	/Tbar_s-channel_TuneZ2star_8TeV-powheg-tauola/Summer12_DR53X-PU_S10_START53_V7A-v1/AODSIM	1.76 pb
$t\text{-channel}$	/Tbar_t-channel_TuneZ2star_8TeV-powheg-tauola/Summer12_DR53X-PU_S10_START53_V7A-v1/AODSIM	30.7 pb
$tW$	/Tbar_tW-channel-DR_TuneZ2star_8TeV-powheg-tauola/Summer12_DR53X-PU_S10_START53_V7A-v1/AODSIM	11.1 pb
$WW$	/WW_TuneZ2star_8TeV_pythia6_tauola/Summer12_DR53X-PU_S10_START53_V7A-v1/AODSIM	54.8 pb
$WZ$	/WZ_TuneZ2star_8TeV_pythia6_tauola/Summer12_DR53X-PU_S10_START53_V7A-v1/AODSIM	32.3 pb
$ZZ$	/ZZ_TuneZ2star_8TeV_pythia6_tauola/Summer12_DR53X-PU_S10_START53_V7A-v1/AODSIM	7.7 pb

Table 7.3: List of background MC datasets and cross sections used for normalization.

### 2471 7.1.4 MC pileup reweighting

2472 As discussed in section 6.1.4, the large instantaneous luminosities provided by the LHC result in  
 2473 the overlap of multiple proton-proton collisions during a single read-out window. These "pileup  
 2474 events" affect many aspects of the reconstruction, including lepton isolation and jet energy  
 2475 resolution, thus the simulated samples must accurately reproduce these effects.

2476 As with the last analysis, for the simulation, it is known how many additional interactions  
 2477 were added to every generated event. For the data, the number of pileup interactions for each unit  
 2478 of time depends on the instantaneous luminosity for each bunch pair and the total inelastic cross  
 2479 section,  $\sigma_{inelastic}$ . Empirically, it was found that  $\sigma_{inelastic} = 69.4$  mb described the data well.  
 2480 Changing of this value by  $\pm 7\%$  are used for the  $\pm 1\sigma$  variations for the associated systematic  
 2481 uncertainty. Figure 7.1 shows the number of reconstructed vertices for data and for the  $t\bar{t}$   
 2482 MC sample, both before and after pileup reweighting. After reweighting, the data and MC  
 2483 distributions agree very well, indicating that the pileup reweighting is working as expected.

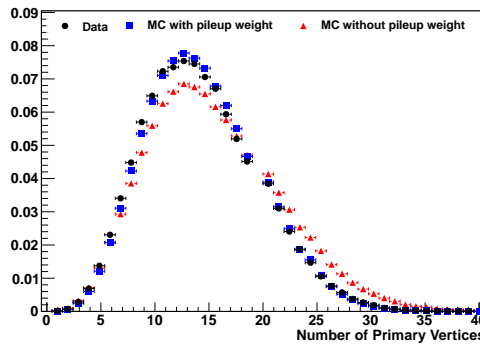


Figure 7.1: Comparison of number of reconstructed vertices for data (black) and the sum of all background MC samples before (red) and after (blue) pileup reweighting. After pileup reweighting, the MC matches the data well.

### 2484 7.1.5 Top $p_T$ Reweighting

2485 It has been observed that the spectra of leptons and jets produced from top quark decays have  
 2486 softer  $p_T$  distribution than are predicted by the Monte Carlo. Investigations have shown that the  
 2487  $p_T$  spectra of leptons and jets is softer than data and have traced this expected to the top quark  
 2488  $p_T$  distribution [147, 148]. Measurements of the differential cross section for top pair production  
 2489 as a function of the top quark  $p_T$ , have allowed for the creation of correction factors for this effect.  
 2490 These predictions of the  $t\bar{t}$  + jets Monte Carlo are also more consistent with calculations done at  
 2491 approximate NNLO accuracy. This correction factor replaces the additional pileup reweighting  
 2492 factor based on the  $H_T$  distribution, binned by number of reconstructed vertices.

2493 The scale factor used to correct the Madgraph top quark  $p_T$  distributions are shown in figure

<sup>2494</sup> 7.2. The associated uncertainty is a band shown in green, and corresponds to no correction  
<sup>2495</sup> factor for the down variation, and a doubling of the correction factor for the up variation. The  
<sup>2496</sup> scale factors are taken from a polynomial of the form:

$$SF = 1.18246 + 2.10061 \times 10^{-6} p_T (p_T - 2 \times 463.312)$$

<sup>2497</sup> For  $p_T > 463.312 \text{ GeV}/c$ , a constant scale factor of 0.732 is used.

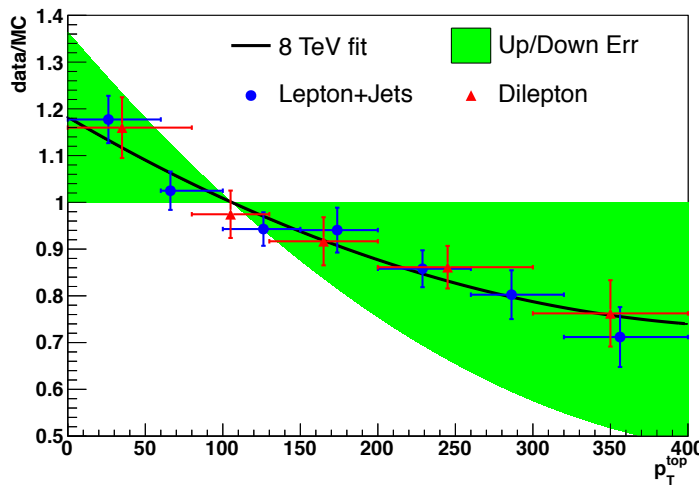


Figure 7.2: The scale factors from top differential cross section group, the fitting as well as the  $\pm 1\sigma$  variations.

<sup>2498</sup> The top  $p_T$  scale factor improves the agreement between data and Monte Carlo. Figure 7.3  
<sup>2499</sup> compares the leading jet  $p_T$  distributions before and after reweighting. Before the correction,  
<sup>2500</sup> the leading jet  $p_T$  ratio plot forms a line with a slope, which is removed after the correction.

## <sup>2501</sup> 7.2 Event Selection

<sup>2502</sup> This section defines the common physics objects and event selection requirements. Events are  
<sup>2503</sup> required to pass quality filters, ensuring optimal operation of electronics and reconstruction, as  
<sup>2504</sup> described in section 6.2.1. The same lepton selection is used that was employed in the previous  
<sup>2505</sup> analysis, with events being selected by triggers described in section ???. Leptons are classified  
<sup>2506</sup> into two categories, tight and loose, defined for muons in section 6.2.3 and for electrons in 6.2.4.  
<sup>2507</sup> For this analysis, exactly one tight muon or exactly one tight electron is required and events  
<sup>2508</sup> with any additional loose leptons are rejected. Lepton reconstruction efficiency scale factors are  
<sup>2509</sup> discussed in 6.2.5. The selection for jets is also the same, with the same procedure for correcting  
<sup>2510</sup> the energy as in section 6.2.6. The only significant change to the event selection comes from the

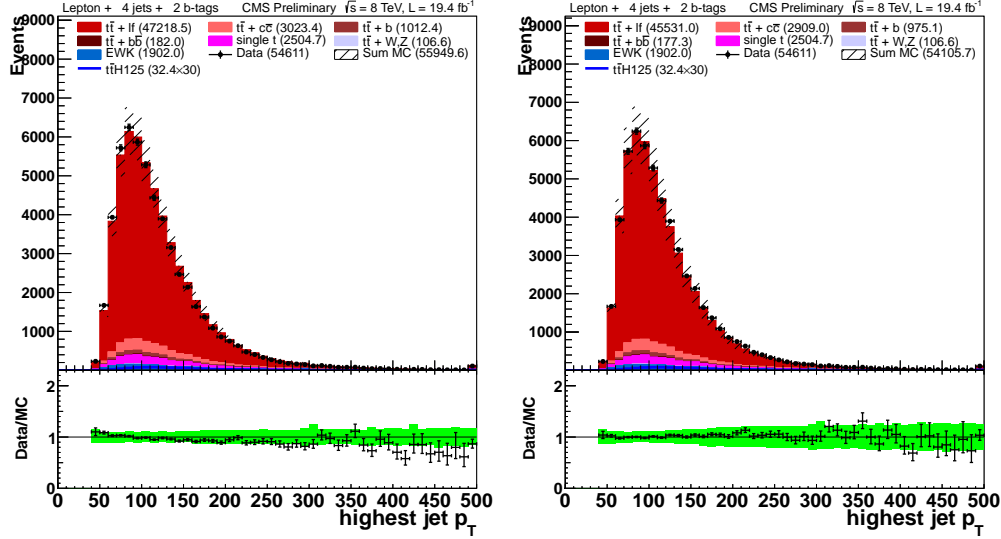


Figure 7.3: Leading jet  $p_T$  distribution for 8 TeV lepton plus jet events with  $\geq 4$  jets and  $\geq 2$  tags. The left-hand plot shows the distribution before top  $p_T$  reweighting. The right-hand plot shows the distribution after top  $p_T$  reweighting. Note that the ratio in the right-hand plot is flatter than the left-hand plot.

2511  $b$ -tag scale factors used to calibrate the differences between efficiency in data and simulation for  
2512 the CSV algorithm.

### 2513 7.2.1 $b$ -tag discriminant reweighting

2514 As described in section 6.2.7, the algorithm used to tag jets as coming from a  $b$ -quark, is the  
2515 Combined Secondary Vertex (CSV) algorithm. Differences have been observed in the measured  
2516 efficiency for  $b$ -tagging jets between data and simulation [133]. To account for these efficiency  
2517 differences, a scale factor to correct the MC  $b$ -tagging efficiency. Moreover, we found that the  
2518 CSV distribution of MC doesn't match that of data, there making it necessary to correct the  
2519 shape of the discriminant distribution as well.

2520 A  $b$ -tag CSV reweighting method has been developed to address not only the difference in  
2521 efficiency, but the difference in the shape of the discriminant distribution as well [149]. The  
2522 method is based on a "tag and probe" approach. Events with two leptons, and exactly two jets  
2523 are initially selected. One jet is required to pass a "tight" working point, characterized by a  
2524 CSV value with  $\sim 90\%$  efficiency and  $\leq 1\%$  mistag rate. Then, the other jet is required to pass  
2525 the analysis working point to assess the efficiency there. The results are binned by  $p_T$ ,  $\eta$ , jet  
2526 flavor and CSV value.

2527 For MC the truth is available to assess the efficiency. For data, the full 8 TeV DoubleMu,  
2528 DoubleElectron and MuEG datasets taken in 2012 are used. The scale factors for heavy flavor  
2529 jets were derived in the dilepton channel, using a  $t\bar{t}$  enriched control sample dominated by events

which have two  $b$  flavor jets from the top pair decay. The scale factors for light flavor jets in the dilepton channel, using a control sample dominated by  $Z + \text{jets}$  events where there are two light flavor jets. The scale factors for light flavor jets will account for the mis-tag efficiency discrepancy between data and MC. For events with one jet passing the tag requirements, the CSV distribution for the probe jet in given  $p_t$  and  $\eta$  bins. The total MC yields are normalized to the data yields. In order to account for heavy or light flavor contamination, the MC is divided into samples of heavy flavor and light flavor components and then non-relevant part from data is subtracted. The scale factor is then given by the ratio of subtracted data CSV distribution and the relevant MC CSV distribution, as shown below:

$$SF(CSV, p_t, \eta) = \frac{\text{Data} - MC_A}{MC_B} \quad (7.1)$$

where A, B = heavy flavor component or light flavor component.

Unlike the last analysis, where scale factors were applied to adjust the value of the CSV distribution, correction factor for this analysis is an event-by-event weight. If the jet is a  $b$  flavor jet, a heavy flavor scale factor is assigned to it; if it is a  $c$  flavor jet, a flat scale factor of 1.0 is applied, with the same uncertainty as a  $b$  flavor jet would receive; otherwise, if it is a light flavor jet, a light flavor scale factor is assigned. The total scale factor for the event is the product of all the scale factors of the jets:

$$SF_{\text{total}} = \prod_i^{N_{\text{jets}}} SF_{jet_i} = SF_{jet_1} \cdot SF_{jet_2} \cdot \dots \quad (7.2)$$

### 7.2.2 Lepton + Jets Selection

As with the previous analysis, the final selection requires events have exactly one tight lepton ( $e$  or  $\mu$ ), and at least four jets. Events with any additional loose or tight leptons are vetoed so this analysis can later be combined with a diLepton final state, without double counting events.

Additionally, each event must have at least three jets with  $p_T > 40 \text{ GeV}/c$ .

As before, events are further categorized by the reconstructed jet, and  $b$ -tagged jet multiplicities:

- $\geq 6$  jets,  $\geq 2$   $b$ -tags: At least 6 jets, 2 of which are  $b$ -tagged
- $\geq 4$  jets,  $\geq 3$   $b$ -tags: Exactly 4 jets, 3 of which are  $b$ -tagged
- $\geq 5$  jets,  $\geq 3$   $b$ -tags: Exactly 5 jets, 3 of which are  $b$ -tagged
- $\geq 6$  jets,  $\geq 3$   $b$ -tags: At least 6 jets, 3 of which are  $b$ -tagged
- $\geq 4$  jets,  $\geq 4$   $b$ -tags: Exactly 4 jets, 4 of which are  $b$ -tagged

2558 •  $\geq 5$  jets,  $\geq 4$   $b$ -tags: Exactly 5 jets, 4 of which are  $b$ -tagged

2559 •  $\geq 6$  jets,  $\geq 4$   $b$ -tags: At least 6 jets, with at least 4 of which are  $b$ -tagged

2560 Table 7.4 gives the event yield for MC backgrounds, both the total and each contribution,  
 2561 the expected event yield for signal  $t\bar{t}H$  ( $m_H = 125$  GeV/c $^2$ ), and the data observed in each  
 2562 category. Figure 7.4 shows the data/MC comparison for the number of jets and the number of  
 2563 tagged jets distributions for events with one lepton ( $e$  or  $\mu$ ),  $\geq 4$  jets and  $\geq 2$   $b$ -tags, it also  
 2564 includes a plot showing the event yields for data and each MC background in each category.

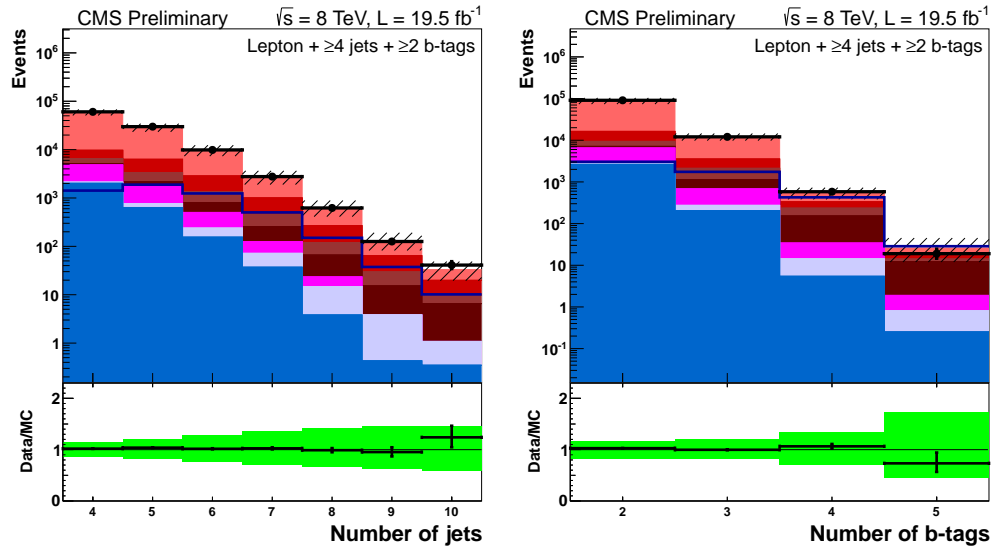


Figure 7.4: Comparison of yields for the different categories (top), number of jets (bottom left), and number of tagged jets (bottom right) in data and Monte Carlo for events with one lepton  $\mu$  or  $e$ ,  $\geq 4$  jets and  $\geq 2$  tags.

	$\geq 6$ jets 2 tags	4 jets 3 tags	5 jets 3 tags	$\geq 6$ jets 3 tags	4 jets 4 tags	5 jets $\geq 4$ tags	$\geq 6$ jets $\geq 4$ tags
$t\bar{t}H(125)$	$33.4 \pm 8.1$	$14.0 \pm 3.0$	$21.1 \pm 4.5$	$23.1 \pm 5.5$	$1.8 \pm 0.5$	$5.2 \pm 1.4$	$8.3 \pm 2.3$
$t\bar{t}+lf$	$7650 \pm 2000$	$4710 \pm 820$	$2610 \pm 530$	$1260 \pm 340$	$74 \pm 30$	$79 \pm 34$	$71 \pm 36$
$t\bar{t}+b$	$530 \pm 300$	$350 \pm 190$	$360 \pm 200$	$280 \pm 160$	$21 \pm 12$	$29 \pm 17$	$33 \pm 20$
$t\bar{t}+b\bar{b}$	$220 \pm 120$	$99 \pm 52$	$158 \pm 85$	$200 \pm 110$	$13.1 \pm 7.3$	$38 \pm 21$	$78 \pm 47$
$t\bar{t}+c\bar{c}$	$1710 \pm 1110$	$440 \pm 230$	$520 \pm 290$	$470 \pm 280$	$19 \pm 11$	$32 \pm 18$	$52 \pm 31$
$t\bar{t}V$	$99 \pm 27$	$16.2 \pm 3.8$	$23.9 \pm 5.7$	$28.8 \pm 7.4$	$1.1 \pm 0.4$	$2.5 \pm 0.7$	$5.8 \pm 1.8$
Single $t$	$264 \pm 54$	$235 \pm 41$	$116 \pm 22$	$55 \pm 14$	$3.4 \pm 1.6$	$10.3 \pm 5.3$	$7.3 \pm 3.1$
$V+jets$	$160 \pm 110$	$122 \pm 95$	$44 \pm 38$	$29 \pm 27$	$2.1 \pm 2.4$	$1.9 \pm 1.7$	$1.2 \pm 1.3$
Diboson	$5.9 \pm 1.6$	$6.3 \pm 1.4$	$2.4 \pm 0.7$	$1.0 \pm 0.4$	$0.3 \pm 0.2$	$0.1 \pm 0.1$	$0.2 \pm 0.1$
Total bkg	$10630 \pm 2790$	$5970 \pm 1060$	$3830 \pm 790$	$2310 \pm 620$	$133 \pm 44$	$193 \pm 62$	$249 \pm 90$
Data	10724	5667	3983	2426	122	219	260

Table 7.4: Observed data event yields, expected event yields in  $19.5$  fb $^{-1}$  for signal and backgrounds in the lepton+jets channel.

## 2565 7.3 Multivariate Analysis

2566 The MVA technique used to analyze the full 8 TeV dataset is a Boosted Decision Tree (BDT).  
 2567 Each jet/tag category is trained with half of the simulated  $t\bar{t}H$  events for signal, and half of  
 2568 the simulated  $t\bar{t} + jets$  events as background. The top 10 variables, ranked with the separation  
 2569 figure of merit given in equation 6.10, are used as input variables. The BDT distribution of the  
 2570 discriminant is then used for signal extraction and limit setting.

### 2571 7.3.1 Boosted Decision Tree Overview

2572 A Boosted Decision Tree (BDT) is a code structure that makes a sequence of binary decisions  
 2573 to classify events as either signal-like or background-like [135]. For this analysis, the BDT uses  
 2574 10 input variables for each jet/tag category. The BDT looks at the distribution of events for  
 2575 signal and background, with 40 bins with a maximum and minimum value determined by the  
 2576 the largest and smallest values respectively for either the signal or the background. Out of these  
 2577 10 variables, the BDT selects the variable which maximizes the Ginni Index, which is given by  
 2578 the equation:

$$GiniIndex = p \times (1 - p) \quad (7.3)$$

2579 where the purity,  $p = s/b$ , is the ratio of the integral number of signal,  $s$ , events and background,  
 2580  $b$ , events above or below the cut value chosen by the BDT. This effectively tries to find a cut on a  
 2581 variable that maximizes the amount signal in sample afterwards, creating a background-like set  
 2582 of events, and a signal-like set of events. After the first cut is chosen, the distributions for each  
 2583 of the variables above and below the cut value are re-examined. A second cut on a variable,  
 2584 at a point that maximizes the Ginni Index is found, for each of the signal and background-like  
 2585 regions formed by the first cut. This process continues for a user-defined number of cuts. Since  
 2586 the input events are known to be singal-like or background-like, the purity of the final region  
 2587 that an event is classified as is used as the output for this set of decisions, known as a decision  
 2588 tree. Figure 7.5 shows a diagram of the general process.

2589 The BDT in this analysis uses 5 cuts for a single tree. The reason for using a small number, is  
 2590 that the BDT employs a process known as "boosting" to enhance its discriminating power.

2591 Boosting is the process of using multiple, or a forest, of individual decision trees to cast  
 2592 a majority vote for the decision to classify the event as signal-like or background-like [135].  
 2593 Events from the training sample, which were misclassified, are given a larger weight, making  
 2594 their contribution to the distributions of the input variable more prominent, making it more  
 2595 likely for the next decision tree to classify the event correctly. The final discriminant,  $F(\hat{x}, P)$ ,

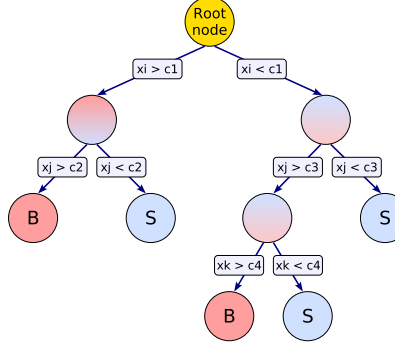


Figure 7.5: Example of a decision tree, which chooses a set of variables to cut on, in order to produce a region of events with high signal purity

2596 of the forest of decision trees is given by:

$$F(\hat{x}, P) = \sum_{m=0}^M \beta_m f(x; a_m); \quad P \in (\beta_m; a_m)_0^M \quad (7.4)$$

2597 where  $P$  is the set of parameter, whose values are optimized to create an optimized classification  
2598 decision. For  $M$  trees in the forest,  $\beta_m$  is the weight for the output of a single decision tree,  
2599  $f(x; a_m)$ , which is the purity,  $s/b$  of the final region of the tree an individual event is classified  
2600 into. The set of input variables for a single decision tree,  $m$ , is denoted by  $a_m$ .

2601 This analysis uses the "Gradient" method of boosting [135]. After the first tree is has been  
2602 built, the "loss function",  $L(F, y)$ , is calculated with the function:

$$L(F, y) = \ln \left( 1 + e^{-2F(\hat{x})y} \right) \quad (7.5)$$

2603 where  $y$  is the true value of the classification of the event (1 for signal, 0 for background).  
2604 This function has a minimum value when all of the events have been classified correctly. The  
2605 loss function is then minimized by varying the set of parameters,  $P \in (\beta_m; a_m)_0^M$ , using the  
2606 steepest-descent method. A random selection of events are reweighted, and the loss-function is  
2607 re-calculated. The error rate of classifying events for the previous tree is used to calculate the  
2608 new weight,  $\alpha$ , of events for the next tree:

$$\alpha = \frac{1 - err}{err} \quad (7.6)$$

2609 where  $err$  is the error rate. After events are re-weighted, a new decision tree is created and the  
2610 process is repeated, iteratively minimizing the loss function until a desired set of decision trees  
2611 are created. This analysis uses a forest of 100 decision trees to separate the  $t\bar{t}H$  signal from the  
2612  $t\bar{t} + jets$  background.

Overtraining was checked in a similar procedure that was used in the last analysis. Half the events for the signal and background samples are used to train the BDT, the other half are used to test it. The response to the BDT is calculated for both the testing and training sample, and the Kolomogrov-Smirnoff statistic is used as a figure of merit to judge the compatibility of the two samples. As seen in figure 7.6, there are no significant deviations between the testing and training samples, implying that no overtraining has occurred.

### 7.3.2 MVA Input Variables, Data to Monte Carlo Comparisons

The set of 10 input variables for each jet/tag category were chosen through their ranking using the separation figure of merit given in equation 6.10. The categories most sensitive to signal, 5 jets,  $\geq 4$  b-tags;  $\geq 6$  jets,  $\geq 3$  b-tags; and  $\geq 6$  jets,  $\geq 4$  b-tags all include a variable, which is the output discriminant of a dedicated BDT trained to separate  $t\bar{t}H$  signal from  $t\bar{t} + b\bar{b}$  background. Table 7.5 gives a description of each of the input variables used. Table 7.6 describes which variables are used in each jet/tag category, and table 7.7 lists the variables used in the dedicated  $t\bar{t}H$ ,  $t\bar{t} + b\bar{b}$  BDT.

The modeling of the input variables is compared against data for each of the jet/tag diagrams in the the following figures:

- $\geq 6$  jets,  $\geq 2$  b-tags: Figure 7.7
- $\geq 4$  jets,  $\geq 3$  b-tags: Figure 7.8
- $\geq 5$  jets,  $\geq 3$  b-tags: Figure 7.9
- $\geq 6$  jets,  $\geq 3$  b-tags: Figure 7.10, and Figure 7.11
- $\geq 4$  jets,  $\geq 4$  b-tags: Figure 7.12
- $\geq 5$  jets,  $\geq 4$  b-tags: Figure 7.13, and Figure 7.14
- $\geq 6$  jets,  $\geq 4$  b-tags: Figure 7.15, and Figure 7.16

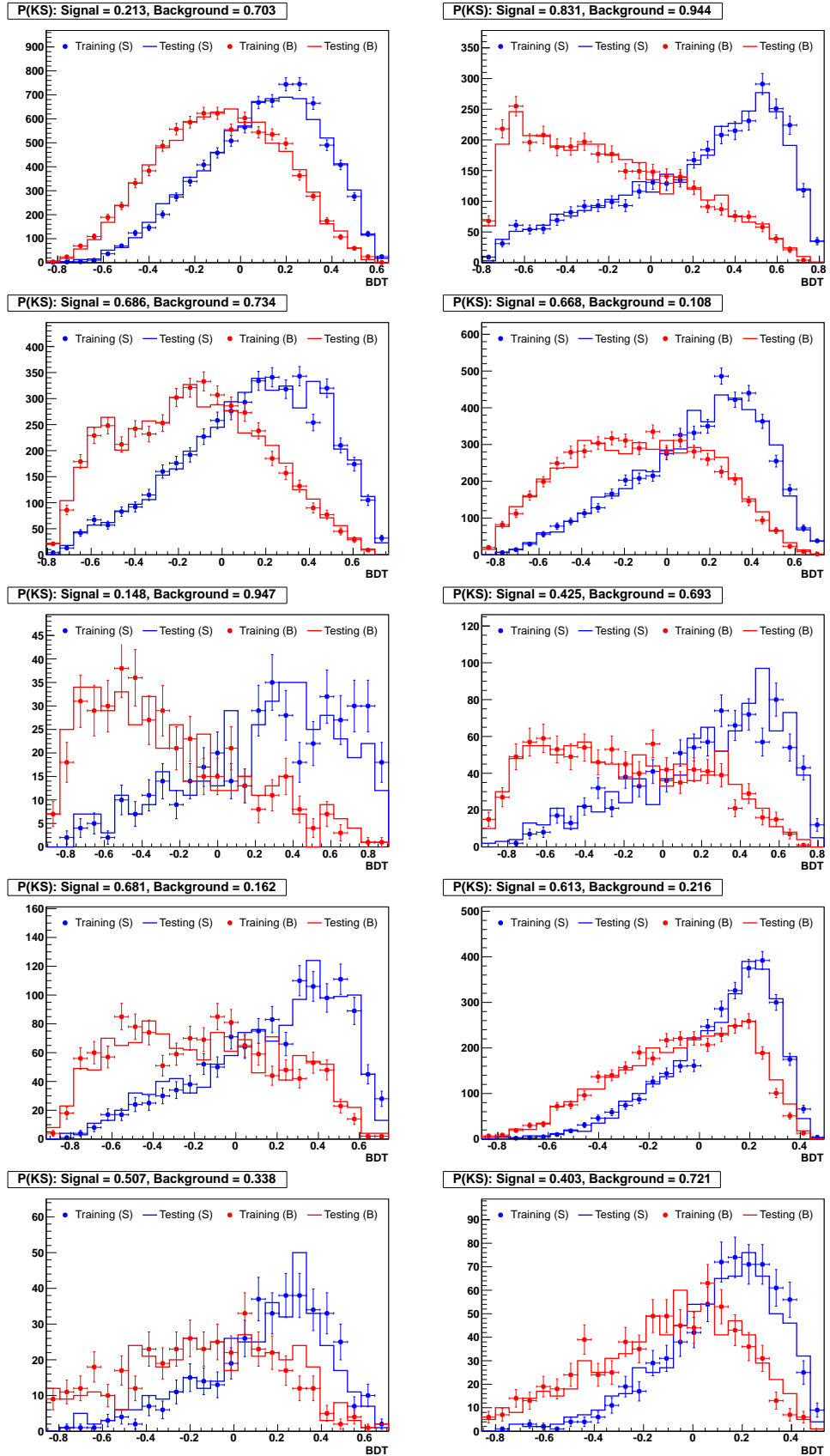


Figure 7.6: Comparisons of the testing and training samples used to optimize the BDT weights for each jet/tag category

Table 7.5: Event variables used in dilepton and lepton+jets BDT training and their descriptions.

abs $\Delta\eta$ (leptonic top, bb)	Delta-R between the leptonic top reconstructed by the best Higgs mass algorithm and the $b$ -jet pair chosen by the algorithm
abs $\Delta\eta$ (hadronic top, bb)	Delta-R between the hadronic top reconstructed by the best Higgs mass algorithm and the $b$ -jet pair chosen by the algorithm
aplanarity	Event shape variable equal to $\frac{3}{2}(\lambda_3)$ , where $\lambda_3$ is the third eigenvalue of the sphericity tensor as described in [?].
ave CSV (tags/non-tags)	Average $b$ -tag discriminant value for $b$ -tagged/non- $b$ -tagged jets
ave $\Delta R$ (tag,tag)	Average $\Delta R$ between $b$ -tagged jets
best Higgs mass	A minimum-chi-squared fit to event kinematics is used to select two $b$ -tagged jets as top-decay products. Of the remaining $b$ -tags, the invariant mass of the two with highest $E_t$ is saved.
best $\Delta R(b,b)$	The $\Delta R$ between the two $b$ -jets chosen by the best Higgs mass algorithm
closest tagged dijet mass	The invariant mass of the two $b$ -tagged jets that are closest in $\Delta R$
dev from ave CSV (tags)	The square of the difference between the $b$ -tag discriminant value of a given $b$ -tagged jet and the average $b$ -tag discriminant value among $b$ -tagged jets, summed over all $b$ -tagged jets
highest CSV (tags)	Highest $b$ -tag discriminant value among $b$ -tagged jets
$H_0, H_1, H_2, H_3$	The first few Fox-Wolfram moments [?] (event shape variables)
HT	Scalar sum of transverse momentum for all jets with $p_T > 30 \text{ GeV}/c$
$\sum p_T(\text{jets, leptons, MET})$	The sum of the $p_T$ of all jets, leptons, and MET
$\sum p_T(\text{jets, leptons})$	The sum of the $p_T$ of all jets, leptons
jet 1, 2, 3, 4 $p_T$	The transverse momentum of a given jet, where the jet numbers correspond to rank by $p_T$
lowest CSV (tags)	Lowest $b$ -tag discriminant value among $b$ -tagged jets
mass(lepton,jet,MET)	The invariant mass of the 4-vector sum of all jets, leptons, and MET
mass(lepton,closest tag)	The invariant mass of the lepton and the closest $b$ -tagged jet in $\Delta R$
max $\Delta\eta$ (jet, ave jet $\eta$ )	max difference between jet eta and avg delta eta between jets
max $\Delta\eta$ (tag, ave jet $\eta$ )	max difference between tag eta and avg delta eta between jets
max $\Delta\eta$ (tag, ave tag $\eta$ )	max difference between tag eta and avg delta eta between tags
median inv. mass (tag pairs)	median invariant mass of all combinations of $b$ -tag pairs
M3	The invariant mass of the 3-jet system with the largest transverse momentum.
MHT	Vector sum of transverse momentum for all jets with $p_T > 30 \text{ GeV}/c$
MET	Missing transverse energy
min $\Delta R$ (lepton,jet)	The $\Delta R$ between the lepton and the closest jet (LJ channel)
min $\Delta R$ (tag,tag)	The $\Delta R$ between the two closest $b$ -tagged jets
min $\Delta R$ (jet,jet)	The $\Delta R$ between the two closest jets
$\sqrt{\Delta\eta(t^{lep},bb) \times \Delta\eta(t^{had},bb)}$	square root of the product of abs $\Delta\eta$ (leptonic top, bb) and abs $\Delta\eta$ (hadronic top, bb)
second-highest CSV (tags)	Second-highest $b$ -tag discriminant value among $b$ -tagged jets
sphericity	Event shape variable equal to $\frac{3}{2}(\lambda_2 + \lambda_3)$ , where $\lambda_2$ and $\lambda_3$ are the second and third eigenvalues of the sphericity tensor as described in [?].
$(\Sigma \text{ jet } p_T)/(\Sigma \text{ jet E})$	The ratio of the sum of the transverse momentum of all jets and the sum of the energy of all jets
tagged dijet mass closest to 125 $t\bar{t}b\bar{b}/t\bar{t}H$ BDT	The invariant mass of the $b$ -tagged pair closest to $125 \text{ GeV}/c^2$ BDT used to discriminate between $t\bar{t}b\bar{b}$ and $t\bar{t}H$ in the LJ $\geq 6$ jets, $\geq 4$ tags, $\geq 6$ jets + 3 tags, and 5 jets + $\geq 4$ tags categories. See text for description and table 7.7 for list of variables.

4 jets, 3 tags	4 jets, 4 tags	
jet 1 $p_T$ jet 2 $p_T$ jet 3 $p_T$ jet 4 $p_T$ M3 $\sum p_T(\text{jets,lepton,MET})$ HT lowest CSV (tags) MHT MET	jet 1 $p_T$ jet 2 $p_T$ jet 4 $p_T$ HT $\sum p_T(\text{jets,lepton,MET})$ M3 ave CSV (tags) second-highest CSV (tags) third-highest CSV (tags) lowest CSV (tags)	
5 jets, 3 tags	5 jets, $\geq 4$ tags	
jet 1 $p_T$ jet 2 $p_T$ jet 3 $p_T$ jet 4 $p_T$ $\sum p_T(\text{jets,lepton,MET})$ $(\Sigma \text{jet } p_T)/(\Sigma \text{jet E})$ HT ave CSV (tags) third-highest CSV (tags) fourth-highest CSV (jets)	max $\Delta\eta$ (tag, ave jet $\eta$ ) $\sum p_T(\text{jets,lepton,MET})$ $(\Sigma \text{jet } p_T)/(\Sigma \text{jet E})$ ave $\Delta R(\text{tag,tag})$ ave CSV (tags) dev from ave CSV (tags) second-highest CSV (tags) third-highest CSV (tags) lowest CSV (tags) ttbb/ttH BDT	
$\geq 6$ jets, 2 tags	$\geq 6$ jets, 3 tags	
$\sum p_T(\text{jets,lepton,MET})$ HT mass(lepton,closest tag) max $\Delta\eta$ (jet, ave jet $\eta$ ) min $\Delta R$ (lepton,jet) $H_2$ sphericity $(\Sigma \text{jet } p_T)/(\Sigma \text{jet E})$ third-highest CSV (jets) fourth-highest CSV (jets)	$H_0$ sphericity $(\Sigma \text{jet } p_T)/(\Sigma \text{jet E})$ max $\Delta\eta$ (jet, ave jet $\eta$ ) $\sum p_T(\text{jets,lepton,MET})$ ave CSV (tags) second-highest CSV (tags) third-highest CSV (tags) fourth-highest CSV (jets) ttbb/ttH BDT	$(\Sigma \text{jet } p_T)/(\Sigma \text{jet E})$ ave $\Delta R(\text{tag,tag})$ product( $\Delta\eta$ (leptonic top, bb), $\Delta\eta$ (hadronic top, bb)) closest tag mass max $\Delta\eta$ (tag, ave tag $\eta$ ) ave CSV (tags) third-highest CSV (tags) fourth-highest CSV (tags) best Higgs mass ttbb/ttH BDT

Table 7.6: BDT input variable assignments for the lepton+jets categories.

5 jets, $\geq 4$ tags	$\geq 6$ jets, 3 tags	$\geq 6$ jets, $\geq 4$ tags
ave $\Delta R(\text{tag,tag})$ max $\Delta\eta$ (tag, ave tag $\eta$ ) $(\Sigma \text{jet } p_T)/(\Sigma \text{jet E})$ tagged dijet mass closest to 125 $H_1$ $H_3$ $\sum p_T(\text{jets,lepton,MET})$ fourth-highest CSV (tags) aplanarity MET	tagged dijet mass closest to 125 $(\Sigma \text{jet } p_T)/(\Sigma \text{jet E})$ $\sqrt{\Delta\eta(t^{lep}, bb) \times \Delta\eta(t^{had}, bb)}$ $H_1$ $H_3$ M3 max $\Delta\eta$ (tag, ave tag $\eta$ ) max $\Delta\eta$ (tag, ave jet $\eta$ ) max $\Delta\eta$ (jet, ave jet $\eta$ ) abs $\Delta\eta$ (hadronic top, bb) abs $\Delta\eta$ (leptonic top, bb) sphericity aplanarity min $\Delta R(\text{tag,tag})$ jet 3 $p_T$	$H_3$ ave $\Delta R(\text{tag,tag})$ closest tagged dijet mass sphericity max $\Delta\eta$ (tag, ave jet $\eta$ ) max $\Delta\eta$ (tag, ave tag $\eta$ ) mass(lepton,jet,MET) $(\Sigma \text{jet } p_T)/(\Sigma \text{jet E})$ abs $\Delta\eta$ (leptonic top, bb) abs $\Delta\eta$ (hadronic top, bb) $\sqrt{\Delta\eta(t^{lep}, bb) \times \Delta\eta(t^{had}, bb)}$ ave CSV (tags) best $\Delta R(b,b)$ best Higgs mass median inv. mass (tag pairs)

Table 7.7: List of variables used as inputs in each of the ttbb/ttH BDTs. See table 7.5 for definitions.

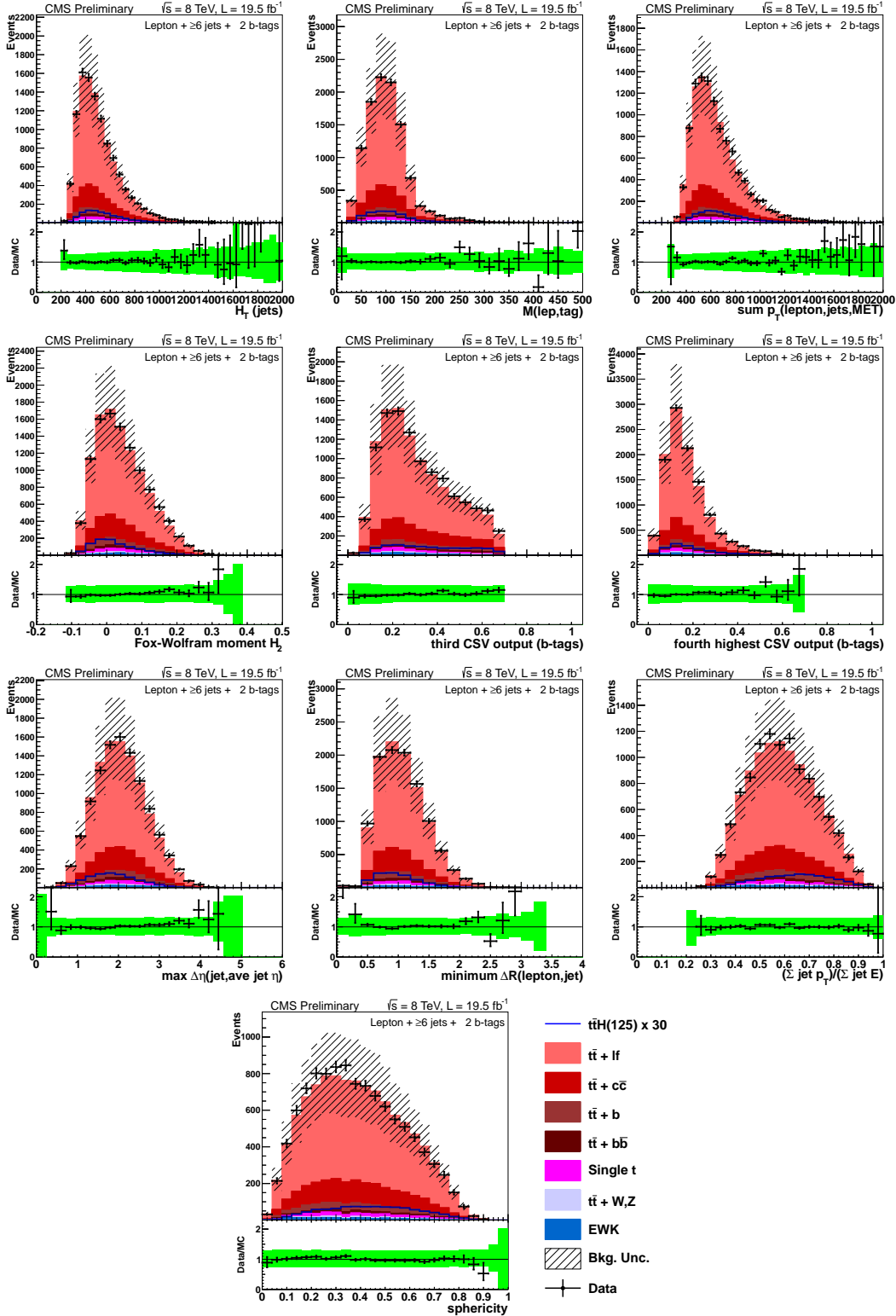


Figure 7.7: Data/MC comparisons for events with one lepton and  $\geq 6$  jets + 2 b-tags. The uncertainty band includes statistical and systematic uncertainties that affect both the rate and shape of the background distributions.

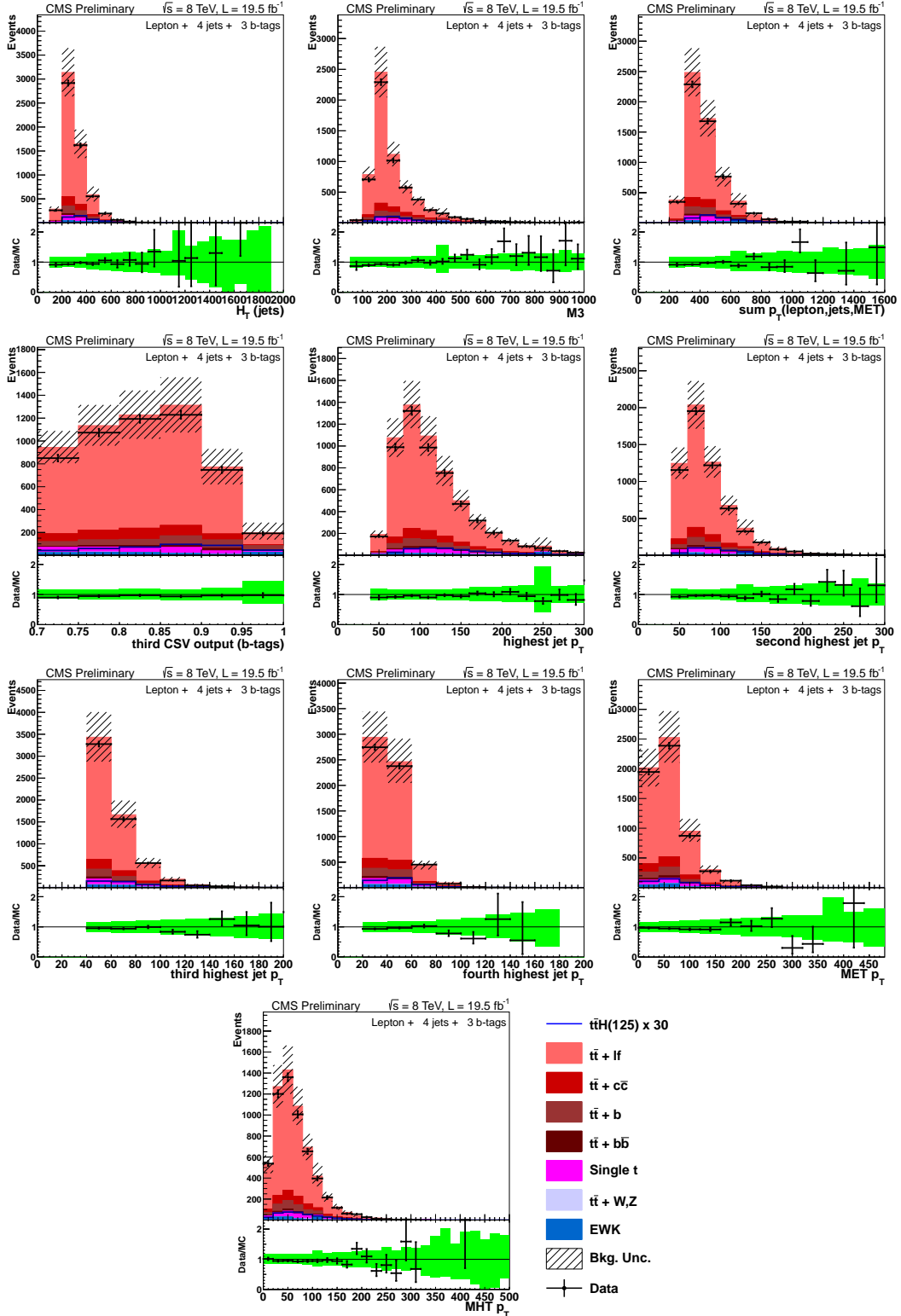


Figure 7.8: Data/MC comparisons for events with one lepton and 4 jets + 3 b-tags. The uncertainty band includes statistical and systematic uncertainties that affect both the rate and shape of the background distributions.

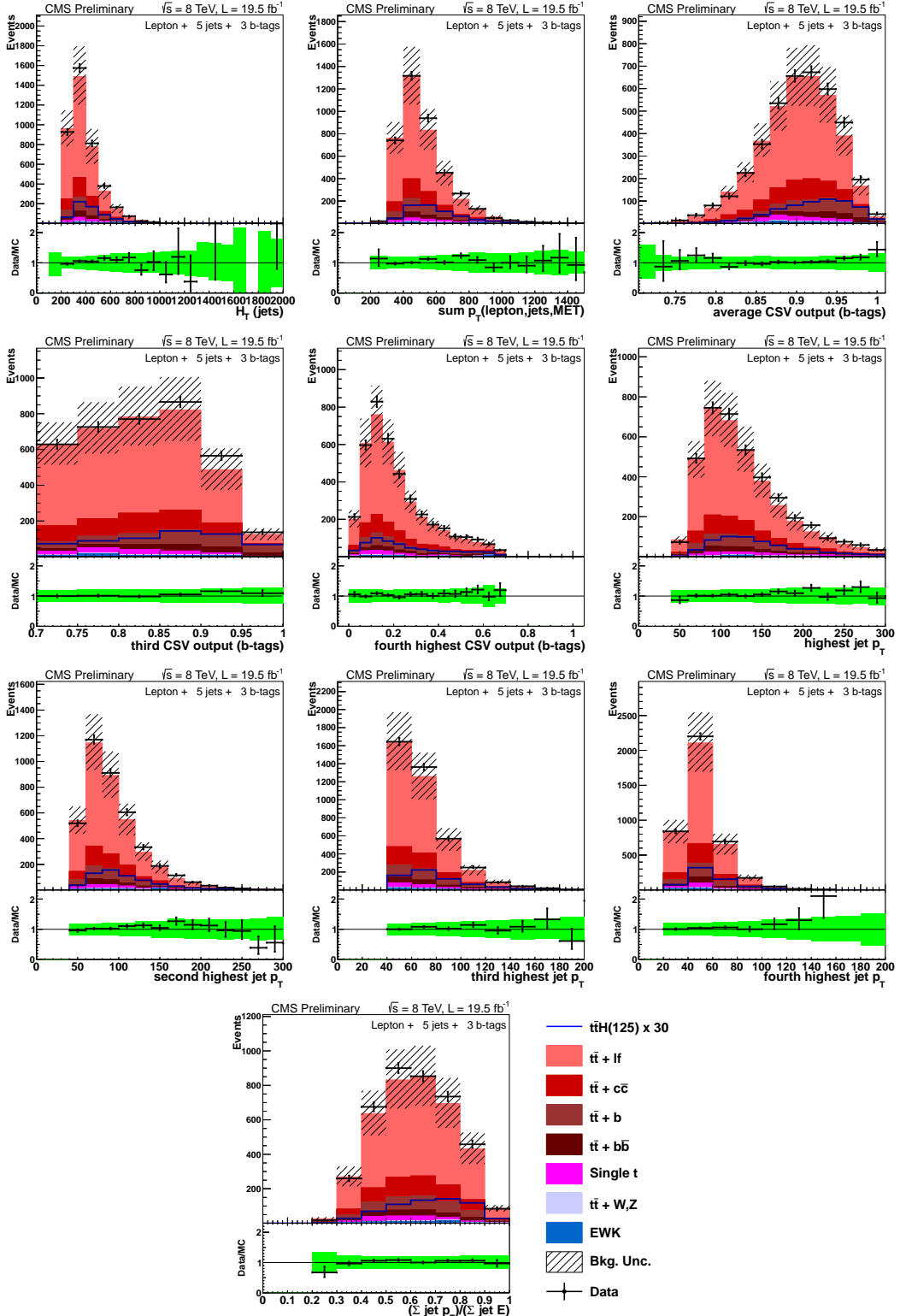


Figure 7.9: Data/MC comparisons for events with one lepton and 5 jets + 3 b-tags. The uncertainty band includes statistical and systematic uncertainties that affect both the rate and shape of the background distributions.

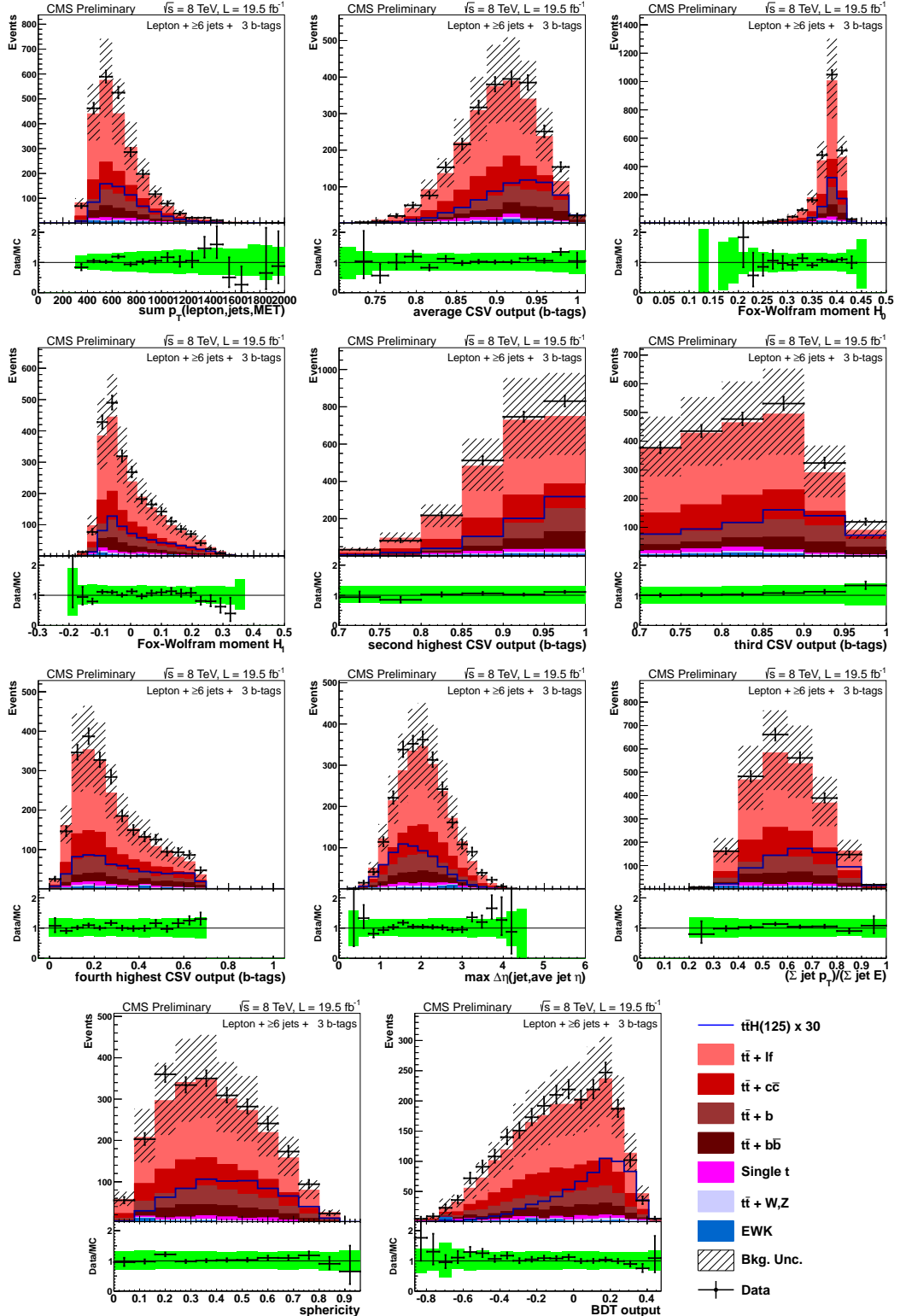


Figure 7.10: Data/MC comparisons for events with one lepton and  $\geq 6$  jets + 3 b-tags. The uncertainty band includes statistical and systematic uncertainties that affect both the rate and shape of the background distributions.

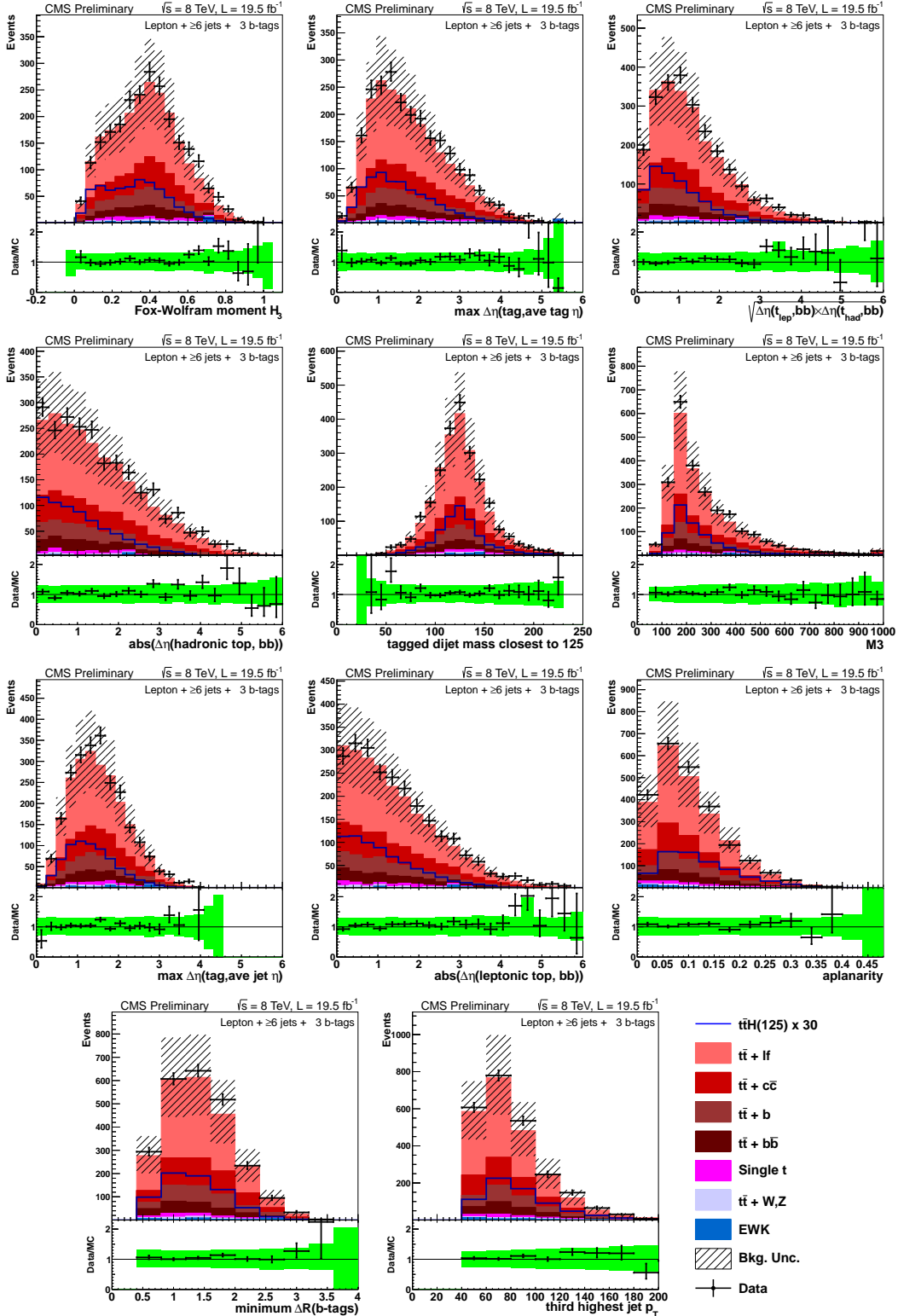


Figure 7.11: Data/MC comparisons for events with one lepton and  $\geq 6$  jets + 3 b-tags. The uncertainty band includes statistical and systematic uncertainties that affect both the rate and shape of the background distributions.

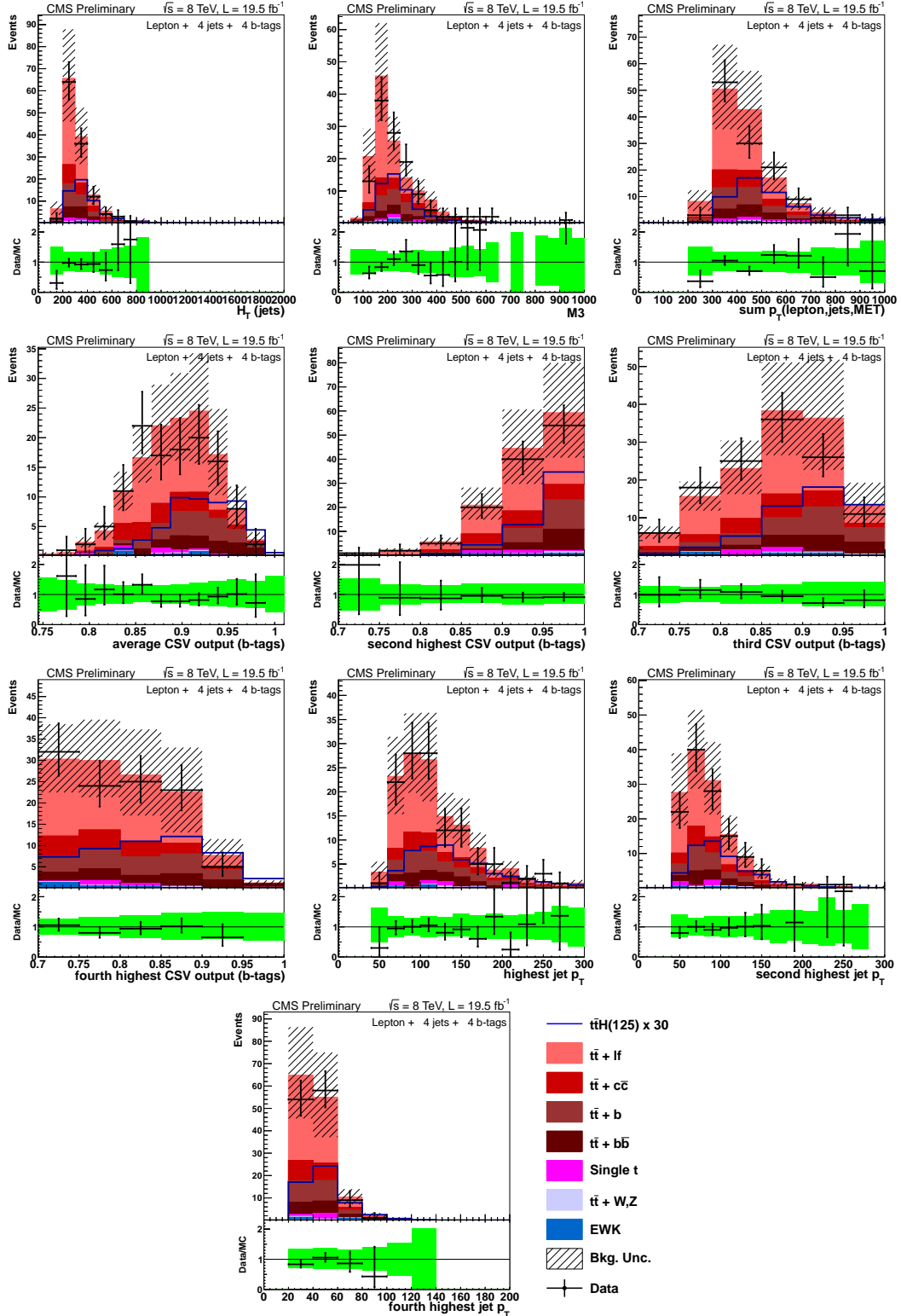


Figure 7.12: Data/MC comparisons for events with one lepton and 4 jets + 4 b-tags. The uncertainty band includes statistical and systematic uncertainties that affect both the rate and shape of the background distributions.

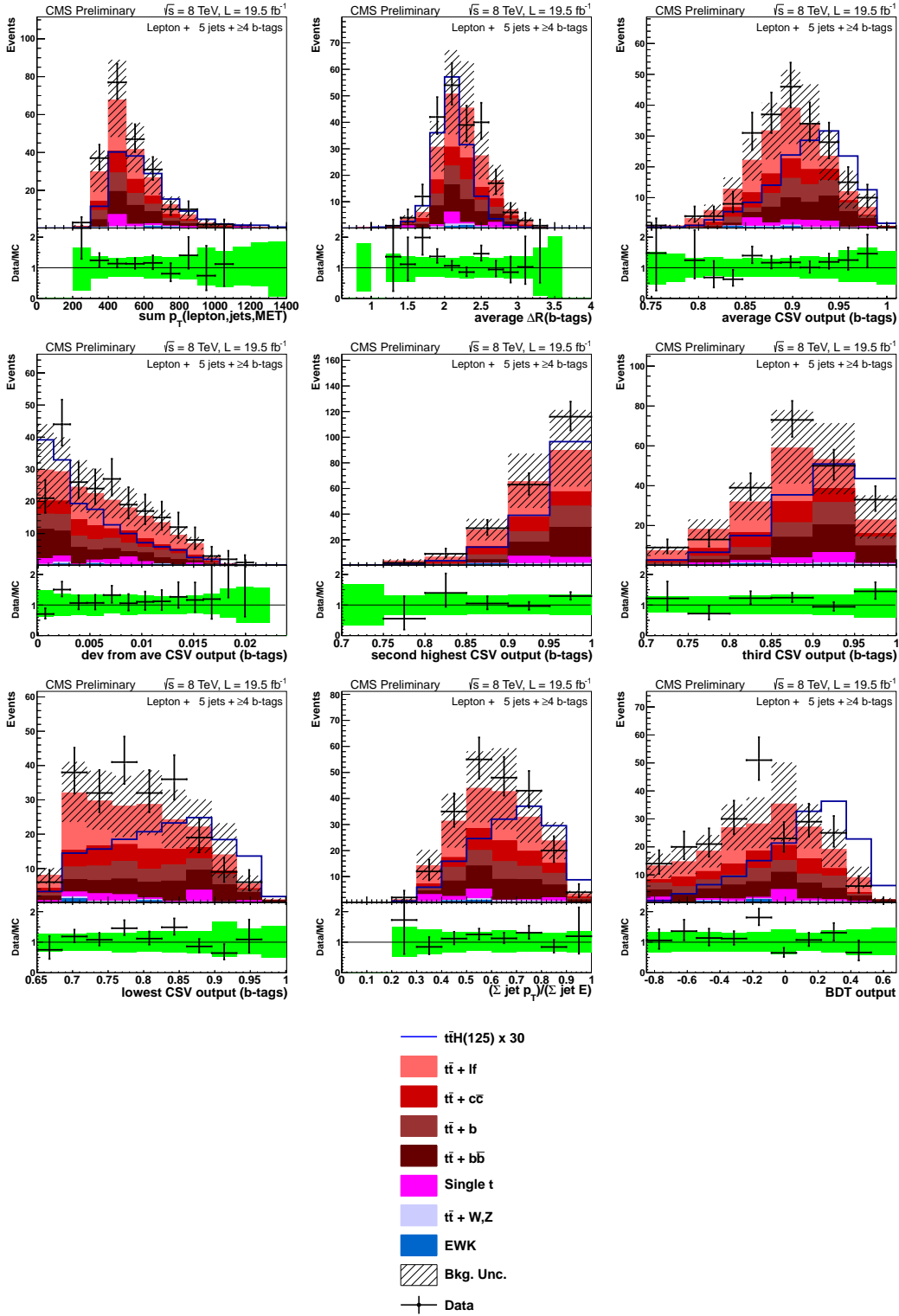


Figure 7.13: Data/MC comparisons for events with one lepton and 5 jets  $+ \geq 4$  b-tags. The uncertainty band includes statistical and systematic uncertainties that affect both the rate and shape of the background distributions.

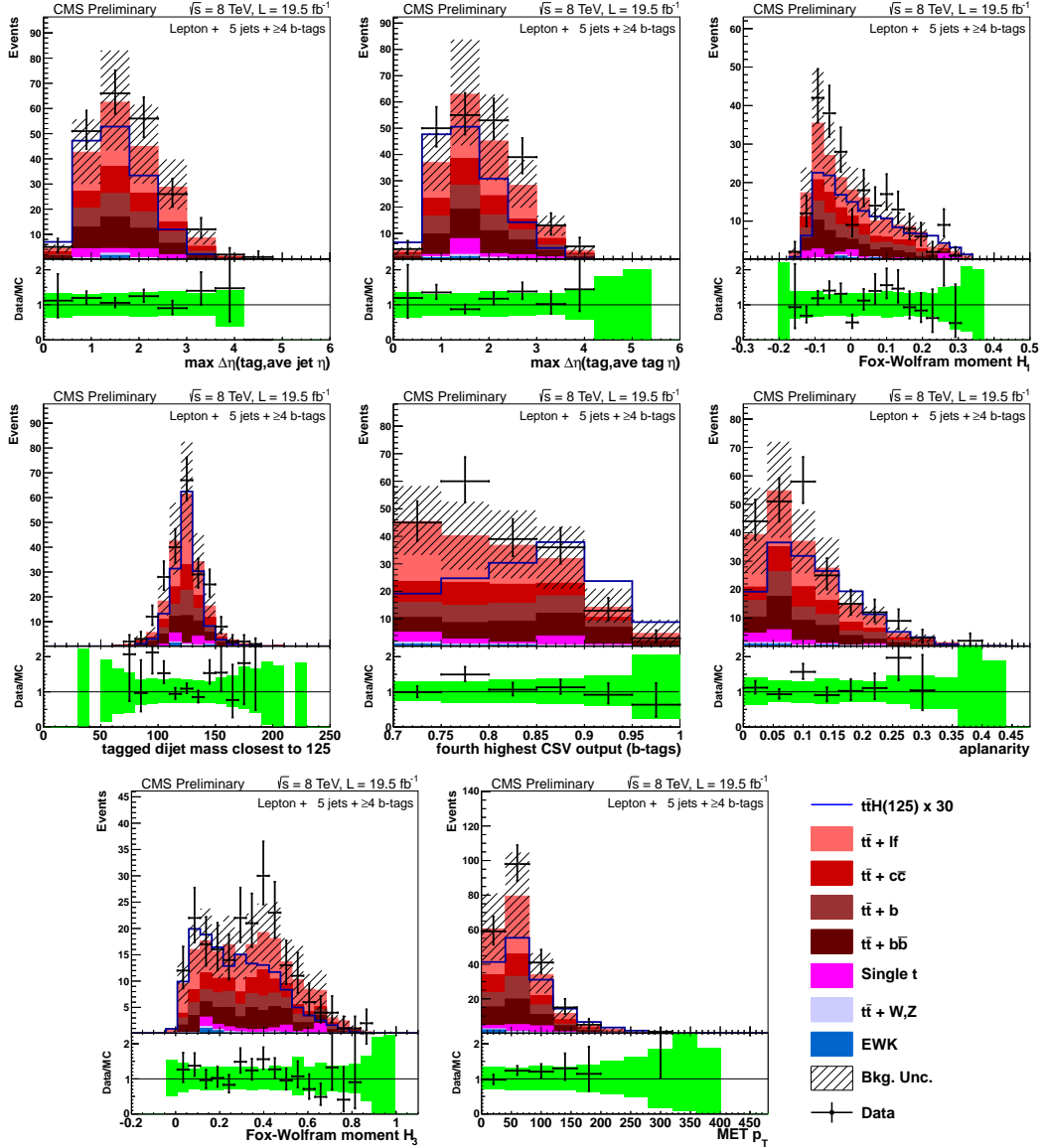


Figure 7.14: Data/MC comparisons for events with one lepton and 5 jets  $+ \geq 4$  b-tags. The uncertainty band includes statistical and systematic uncertainties that affect both the rate and shape of the background distributions.

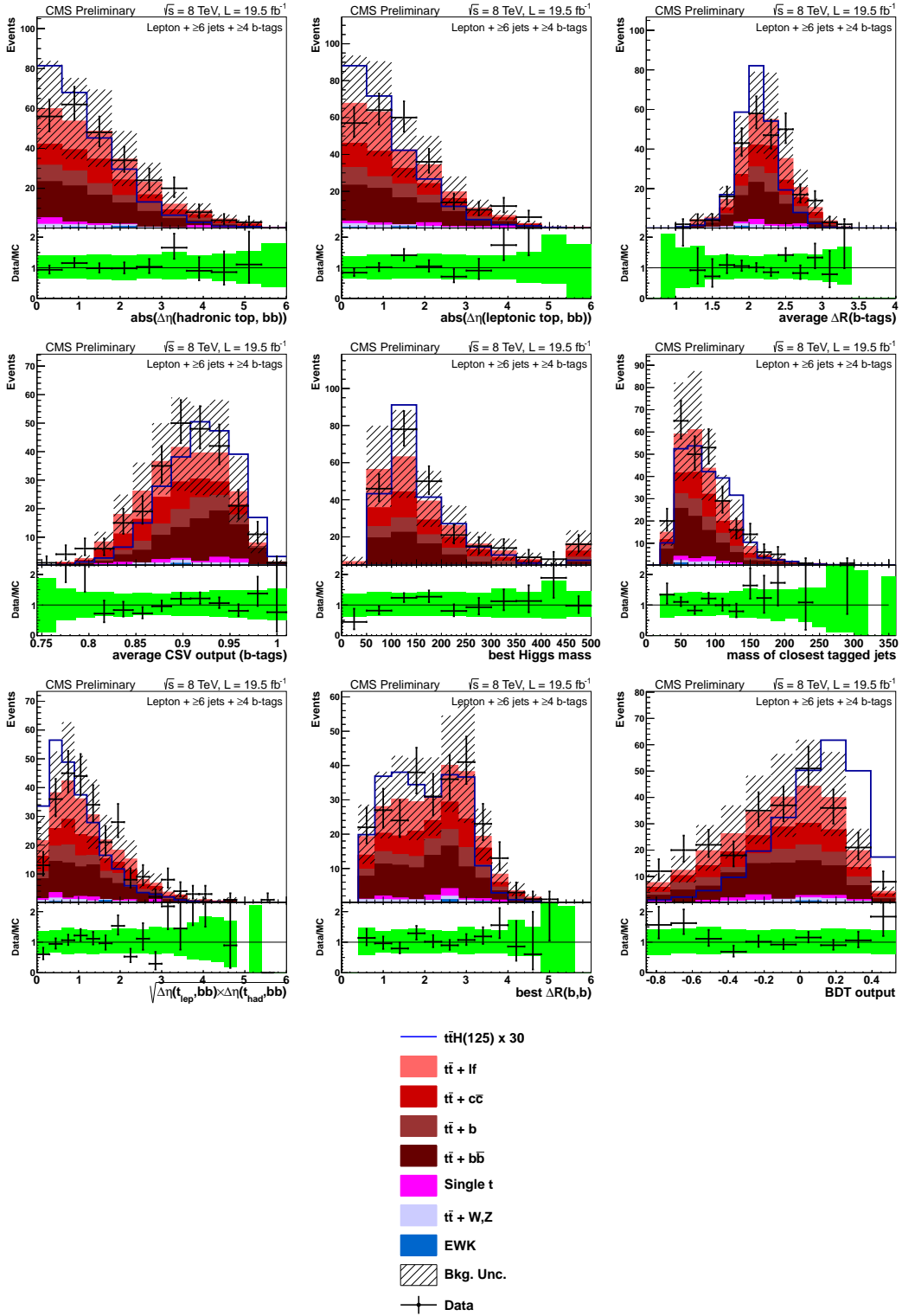


Figure 7.15: Data/MC comparisons for events with one lepton and  $\geq 6$  jets +  $\geq 4$  b-tags. The uncertainty band includes statistical and systematic uncertainties that affect both the rate and shape of the background distributions.

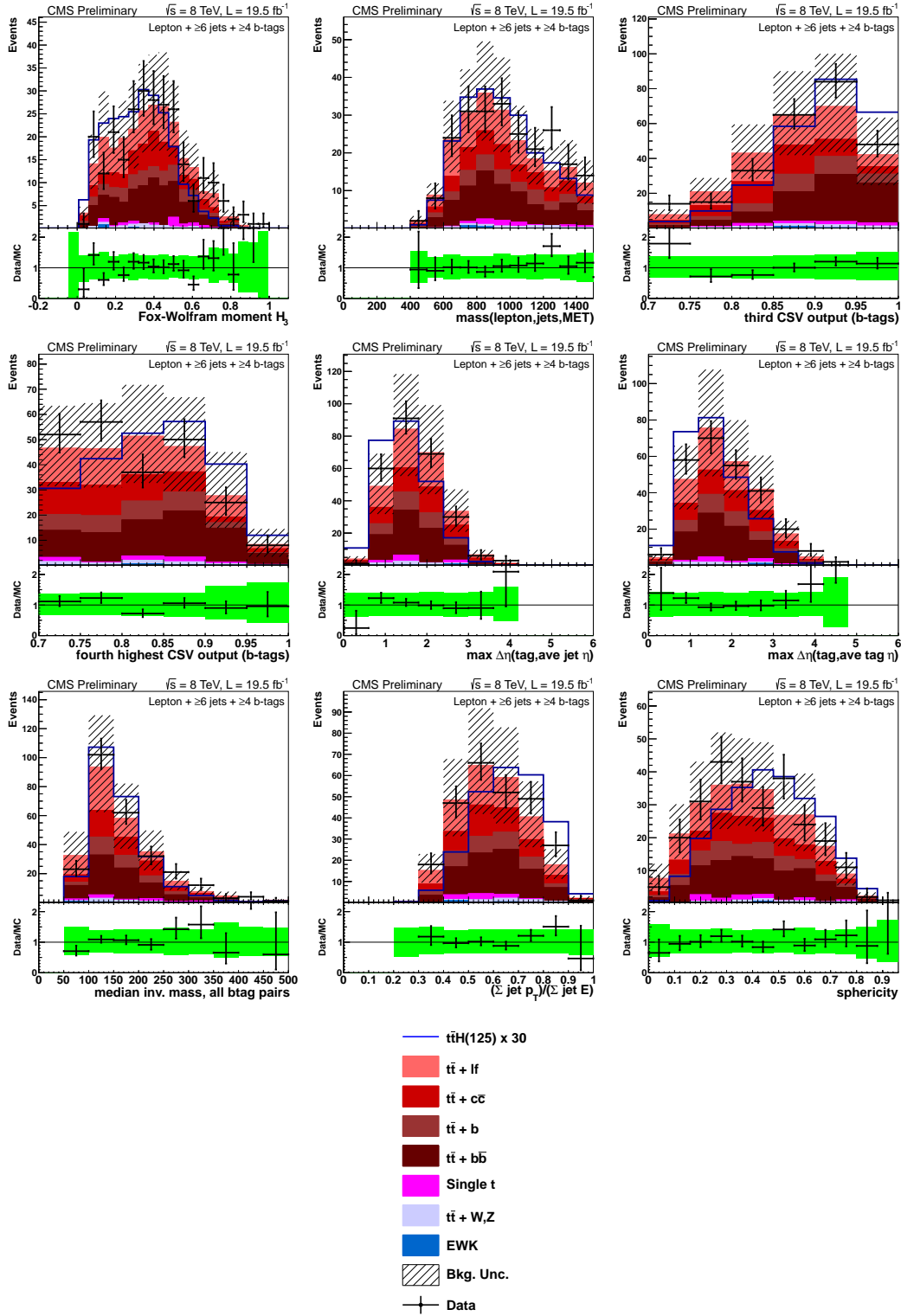


Figure 7.16: Data/MC comparisons for events with one lepton and  $\geq 6$  jets +  $\geq 4$  b-tags. The uncertainty band includes statistical and systematic uncertainties that affect both the rate and shape of the background distributions.

### 2636 7.3.3 MVA Output, Data to Monte Carlo Comparisons

2637 The distributions of the BDT output discriminators in each category are shown in Fig. 7.17. For  
 2638 these figures, the uncertainty band includes statistical and systematic uncertainties, e.g. JES  
 2639 and  $b$ -tag SF uncertainties, that are described in section 7.4.

## 2640 7.4 Systematic Uncertainties

2641 The evaluation of several of the systematic uncertainties follows the same procedure as described  
 2642 in the previous chapter. For these cases, the reader is directed to previous description of the  
 2643 uncertainty. Systematic uncertainties that are new to this analysis include those associated with  
 2644 the new  $b$ -tag calibration method and the top- $p_T$  reweighting. Where appropriate, comparisons  
 2645 between the shapes of the nominal and  $\pm 1\sigma$  variations are made.

2646 **Jet Energy Scale (JES):** See section 6.4 for a description of the evaluation of this systematic.

2647 Shape comparisons between the nominal and the  $\pm 1\sigma$  variations are shown in figure 7.18.

2648 Table 7.8 shows the effect on the rate for the  $\geq 6$  jets +  $\geq 4$  tags category.

JES systematic yield change			
		lepton+jets	
sys	shift	$t\bar{t}H(125)$	$t\bar{t} + b\bar{b}$
JES	up down	+9.1% -7.7%	+8.3% -10.6%

Table 7.8: Relative yield change due to JES shift up/down for the  $\geq 3$  tag category in the dilepton channel and the  $\geq 6$  jets +  $\geq 4$  tags category in the lepton+jets channel.

2649 **Jet Energy Resolution (JER):** See section 6.4 for a description of the evaluation of this  
 2650 systematic.

2651  **$b$ -tag Scale Factors:** New scale factors to account for the differences in efficiency between  
 2652 data and simulation for the CSV  $b$ -tagging algorithm is described in section 7.2.1. There  
 2653 are three sources of systematic uncertainty on both the heavy flavor and light flavor scale  
 2654 factors: JES, purity, and statistics, and each source of variation is considered separately.  
 2655 The  $b$ -tag uncertainty associated with the JES is evaluated at the same time the overall  
 2656 JES uncertainty is considered. When the JES is shifted for the jet kinematics up or down  
 2657 by  $1\sigma$ , the  $b$ -tag scale factor values, which depend on the  $p_T$  of the jet in question, shift as  
 2658 well. This correlates the  $b$ -tag uncertainty from JES with the overall JES uncertainty. The  
 2659 other two sources of  $b$ -tag uncertainty are each evaluated independently for light-flavor and  
 2660 heavy-flavor. The purity uncertainty is controlled by a separate nuisance parameter for  
 2661 light and heavy flavor. Variation of this parameter is associated with changing the pre-

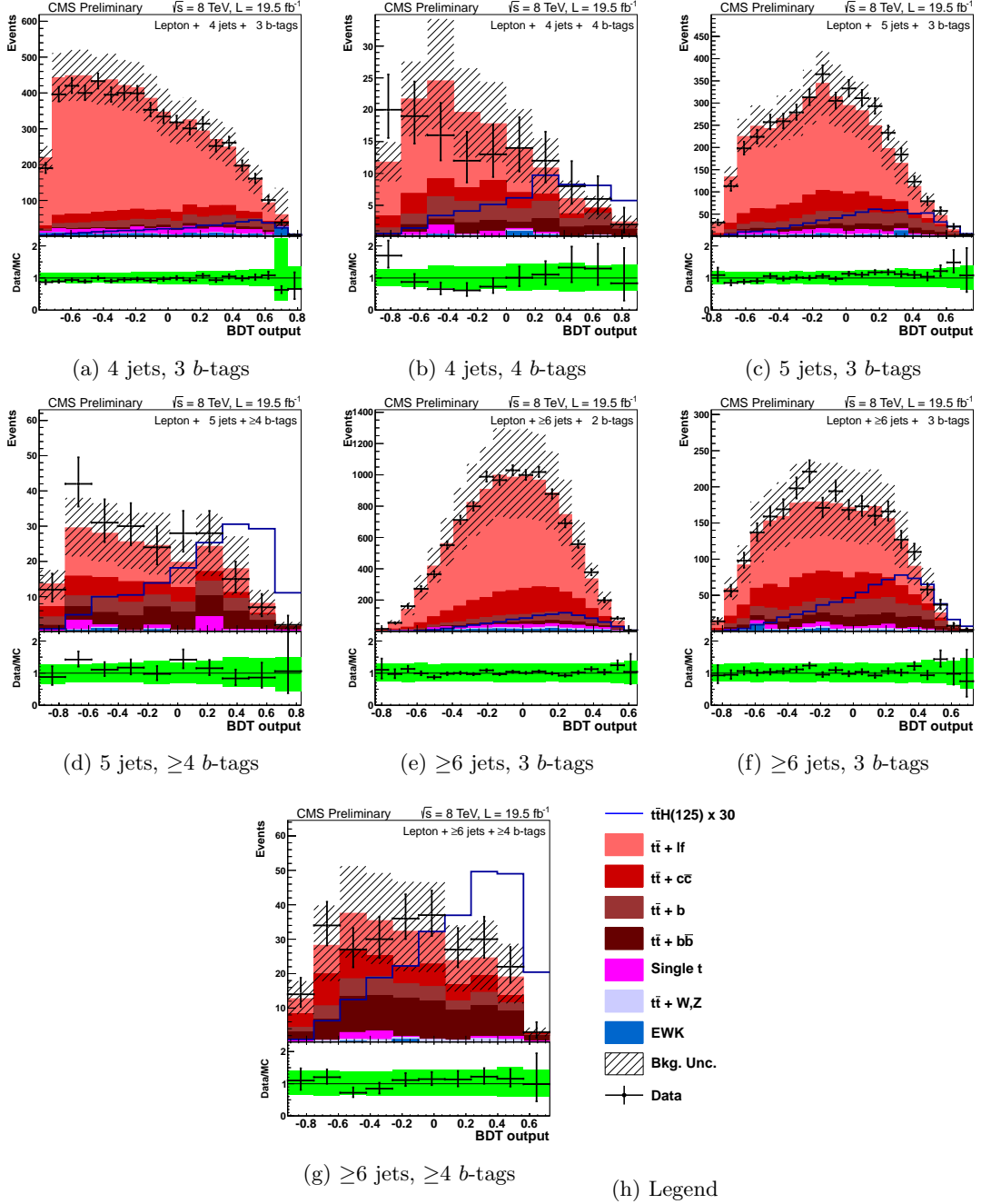


Figure 7.17: Final BDT output for lepton + jet events. Background-like events have a low BDT output value. Signal-like events have a high BDT output value. The uncertainty band includes statistical and systematic uncertainties that affect both the rate and shape of the background distributions. The top, middle and, bottom rows are events with 4, 5, and  $\geq 6$  jets, respectively, while the left, middle, and right-hand columns are events with 2, 3, and  $\geq 4$   $b$ -tags, respectively. The  $t\bar{t}H$  signal ( $m_H = 125$  GeV) is normalized to  $30 \times$  SM expectation.

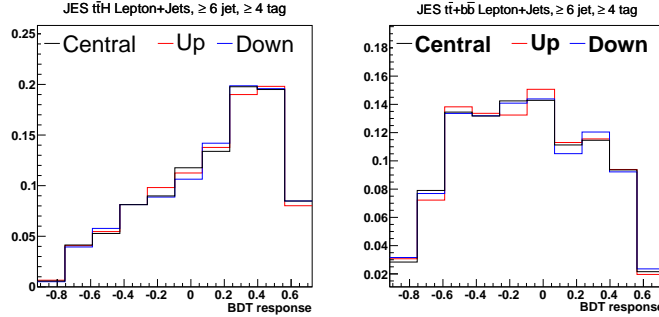


Figure 7.18: Comparison of the MVA discriminator for JES shift upwards (red) and downwards (blue) relative to the nominal (black) shape for the  $t\bar{t}H(125)$  signal (left) and the main background sample  $t\bar{t} + b\bar{b}$  (right). The plots are from the  $\geq 6$  jet  $\geq 4$  tag category in the lepton+jets channel. All plots are normalized to unit area.

diction of simulated heavy-flavor events in the light-flavor control region, and visa versa.

Figures 7.19 and 7.20 and Table 7.9 show the effect of this uncertainty on the final BDT shapes. The impact of statistical uncertainties associated with the scale factor determination are controlled by means of four total nuisance parameters, two for heavy-flavor and two for light-flavor. For each jet flavor, the first nuisance parameter controls distortions in the CSV distribution corresponding to an overall tilt. This is consistent with a migration of events from one end of the CSV range to the other. The second nuisance parameter controls distortions of a more complicated nature, where the upper and lower ends of the distribution change relative to the center. Figures 7.21 and 7.22, and Table 7.9 show the size of the shape and rate impact on the final BDT shape. For charm jets scale factors, the overall relative uncertainty is retained from the heavy flavor scale factors, doubled in size and used to construct two separate nuisance parameters to control the uncertainties. These two uncertainties associated with charm jets scale factors are not correlated with respect to all the uncertainties for the heavy flavor and light flavor scale factors. Figure 7.23 and Table 7.9 show the size of the shape and rate impact on the final BDT shape.

**Electron and Muon ID and Trigger Scale Factors:** A rate uncertainty of 1.4% is assigned for single-lepton events. A single nuisance parameter is used for all lepton-related and is correlated between muons and electrons. Uncertainties for electrons and muons are treated identically, and in the case where there is a difference, the larger uncertainty is used. Uncertainties from ID and isolation are fully uncorrelated and are combined in quadrature for the value of the nuisance parameter.

The total lepton efficiency uncertainty is composed of two parts. Both parts were measured using the method described in [150], which is a "tag and probe" method based on lepton events near the  $Z$  boson mass resonance. The first part is a 1% uncertainty on the lepton

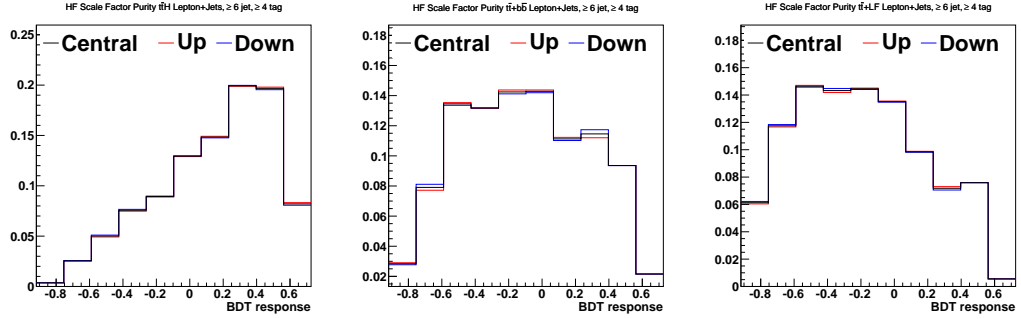


Figure 7.19: Comparison of the MVA discriminator when shifting the light flavor contamination in the heavy flavor scale factor determination shift upwards (red) and downwards (blue) relative to the nominal (black) shape for the  $t\bar{t}H(125)$  signal (top row) and  $t\bar{t} + b\bar{b}$  and  $t\bar{t} + LF$  background samples (middle row and bottom row respectively). The plots are from the  $LJ \geq 6$  jet  $\geq 4$  category. All plots are normalized to unit area.

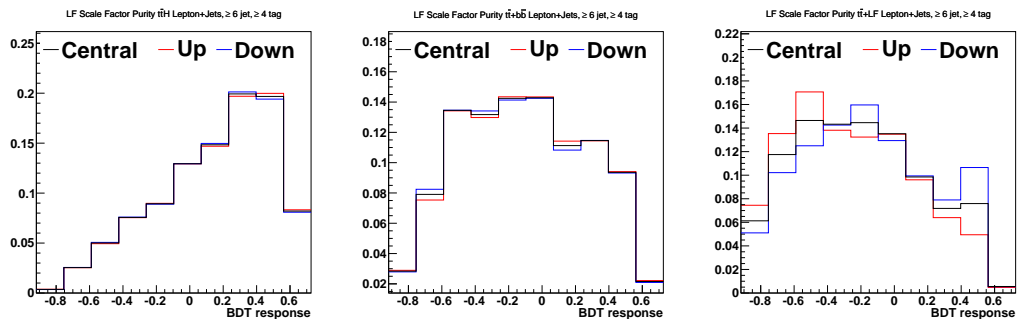


Figure 7.20: Comparison of the MVA discriminator when shifting the heavy flavor contamination in the light flavor scale factor determination shift upwards (red) and downwards (blue) relative to the nominal (black) shape for the  $t\bar{t}H(125)$  signal (top row) and  $t\bar{t} + b\bar{b}$  and  $t\bar{t} + LF$  background samples (middle row and bottom row respectively). The plots are from the  $LJ \geq 6$  jet  $\geq 4$  category. All plots are normalized to unit area.

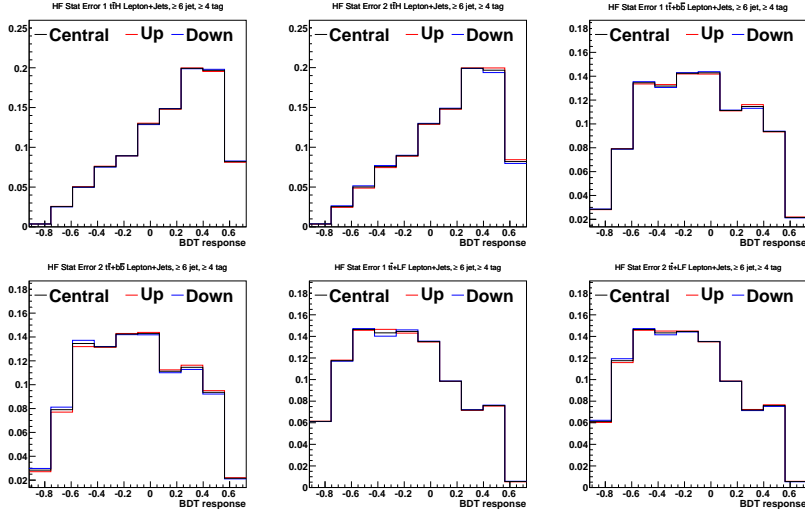


Figure 7.21: Comparison of the MVA discriminator when shifting to account for the statistical uncertainty on the heavy flavor scale factor extraction. Two classes of distortion in the scale factor are considered: linear distortions (labeled “Stat. Error 1”) and nonlinear distortions (labeled “Stat. Error 2”). Both shift upwards (red) and downwards (blue) relative to the nominal (black) shape for the  $t\bar{t}H(125)$  signal (top row) and  $t\bar{t} + b\bar{b}$  and  $t\bar{t} + \text{LF}$  background samples (middle row and bottom row respectively) are shown. The plots are from the  $\geq 6$  jet  $\geq 4$  category. All plots are normalized to unit area.

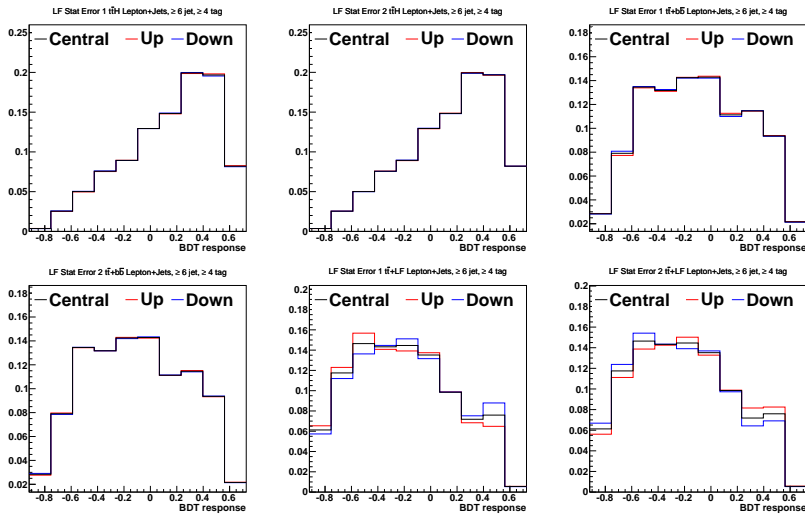


Figure 7.22: Comparison of the MVA discriminator when shifting to account for the statistical uncertainty on the light flavor scale factor extraction. Two classes of distortion in the scale factor are considered: linear distortions (labeled “Stat. Error 1”) and nonlinear distortions (labeled “Stat. Error 2”). Both shift upwards (red) and downwards (blue) relative to the nominal (black) shape for the  $t\bar{t}H(125)$  signal (top row) and  $t\bar{t} + b\bar{b}$  and  $t\bar{t} + \text{LF}$  background samples (middle row and bottom row respectively) are shown. The plots are from the  $\geq 6$  jet  $\geq 4$  category. All plots are normalized to unit area.

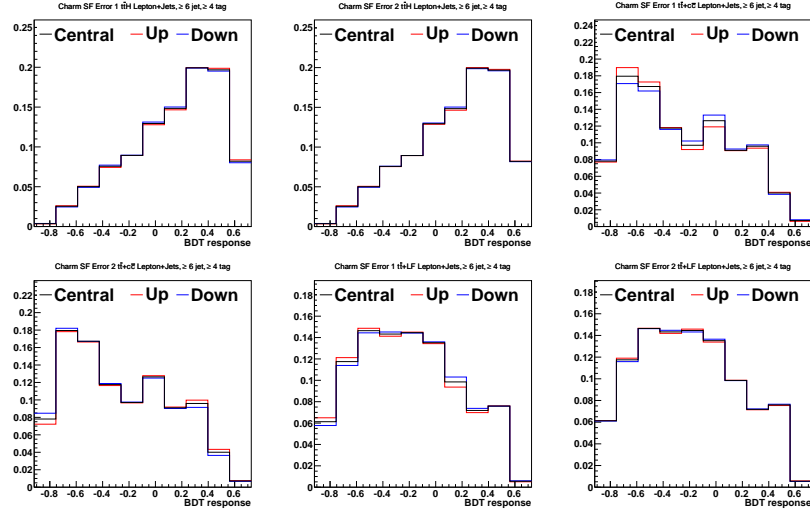


Figure 7.23: Comparison of the MVA discriminator when shifting to account for the uncertainty on the charm jets scale factor extraction. Two classes of distortion in the scale factor are considered: linear distortions (labeled “Error 1”) and nonlinear distortions (labeled “Error 2”). Both shift upwards (red) and downwards (blue) relative to the nominal (black) shape for the  $t\bar{t}H(125)$  signal (top row) and  $t\bar{t} + c\bar{c}$  and  $t\bar{t} + \text{LF}$  background samples (middle row and bottom row respectively) are shown. The plots are from the  $\geq 6$  jet  $\geq 4$  tag category. All plots are normalized to unit area.

b-tag systematic yield change					
		lepton+jets			
sys	shift	$t\bar{t} H(125)$	$t\bar{t} + \text{LF}$	$t\bar{t} + bb$	
Heavy Flavor SF Purity	up	+13.2%	+7.4%	+13.3%	
	down	-12.1%	-7.2%	-12.1%	
Light Flavor SF Purity	up	-3.4%	-32.2%	-4.4%	
	down	+3.4%	+43.9%	+4.4%	
Heavy Flavor SF Stat. Err. 1	up	-12.1%	-6.6%	-11.8%	
	down	+13.3%	+6.8%	+12.9%	
Heavy Flavor SF Stat. Err. 2	up	+8.9%	+5.0%	+9.1%	
	down	-8.3%	-4.9%	-8.5%	
Light Flavor SF Stat. Err. 1	up	+0.5%	-15.6%	+0.1%	
	down	-0.5%	+17.7%	-0.1%	
Light Flavor SF Stat. Err. 2	up	+1.8%	+10.1%	+2.1%	
	down	-1.7%	-8.9%	-2.0%	
sys	shift	$t\bar{t} H(125)$	$t\bar{t} + \text{LF}$	$t\bar{t} + cc$	
Charm jets SF Err. 1	up	+5.1%	-3.4%	-5.6%	
	down	-5.1%	+3.3%	+5.0%	
Charm jets SF Err. 2	up	+6.0%	+4.2%	+12.7%	
	down	-5.9%	-4.2%	-11.7%	

Table 7.9: This table summarizes the rate effect of the six independent nuisance parameters that characterize the  $b$ -tag uncertainties. (Note: The  $b$ -tag rate uncertainties associated with JES variations are already included with the JES rate uncertainties in Table 6.14. The impact of statistical uncertainties is in the heavy-flavor and light-flavor scale factor extraction is incorporated using two separate nuisance parameters, as described above. The uncertainty labeled “Stat. Err. 1” represents statistical uncertainties resulting a linear distortion of the CSV scale factor, while the one labeled “Stat. Err. 2” corresponds to nonlinear distortions.

identification and isolation scale factor. The second part of the total lepton efficiency uncertainty is a 1% trigger scale factor uncertainty.

**Pileup Reweighting:** See section 6.4 for a description of the evaluation of this systematic.

**Top Quark  $p_T$  Reweighting:** The systematic uncertainty on the top  $p_T$  reweighting is assessed as follows: the uncorrected Monte Carlo shapes are used as  $-1\sigma$  systematic uncertainty, and doubling the correction factor gives the  $+1\sigma$  variation. This creates a deviation that is the same size as the original observed difference between data and Monte Carlo. This uncertainty is shown in Fig. 7.2. Fig. 7.24 shows the effects of the uncertainty on the top quark  $p_T$  on the BDT shape and Table 7.10 shows the effect on the rates.

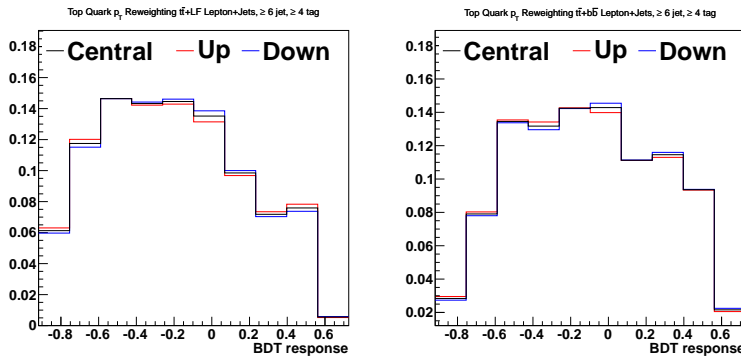


Figure 7.24: Comparison of the MVA discriminator for shifts in top quark  $p_T$  reweighting upwards (red) and downwards (blue) relative to the nominal (black) shape for the  $t\bar{t}$  + LF background (left) and the  $t\bar{t}$  +  $b\bar{b}$  (right). The plots are from the  $\geq 6$  jets +  $\geq 4$  tags category in the lepton+jets channel. All plots are normalized to unit area.

Top quark $p_T$ reweighing systematic yield change			
sys	shift	lepton+jets	
		$t\bar{t}$	$t\bar{t} + b\bar{b}$
Top quark $p_T$ Reweighting	up	-5.2%	-7.0%
	down	+5.2%	+7.0%

Table 7.10: Relative yield change due to varying the top quark  $p_T$  reweighting. The “up” variation corresponds to apply twice as much correction to the top quark  $p_T$  distribution as the nominal, while the “down” correction corresponds to applying no correction to the default MC top quark  $p_T$  distribution.

**Cross Sections:** See section 6.4 for a description of the evaluation of this systematic. Uncertainties affecting these normalizations are summarized in Table 7.11.

**Luminosity:** The uncertainty on the luminosity estimate is 2.2%. This affects all rates.

**Madgraph  $Q^2$  Uncertainty:** See section 6.4 for a description of the evaluation of this systematic.

Process	pdf			QCD Scale			
	gg	qb	qg	t̄t	V	VV	t̄tH
t̄tH	9%						12.5%
t̄t+jets	2.6%			3%			
t̄t + W		7%		15%			
t̄t + Z	9%			15%			
Single top			4.6%	2%			
W+jets		4.8%			1.3%		
Z+jets		4.2%			1.2%		
Dibosons						3.5%	

Table 7.11: Cross section uncertainties used for the limit settings. Each column in the table is an independent source of uncertainty, except for the last column which represents uncertainties uncorrelated with any others. Uncertainties in the same column for two different processes (different rows) are completely correlated.

2700      Figure 7.25 shows the shape and Table 7.12 shows the rate variations for selected event  
 2701      categories.

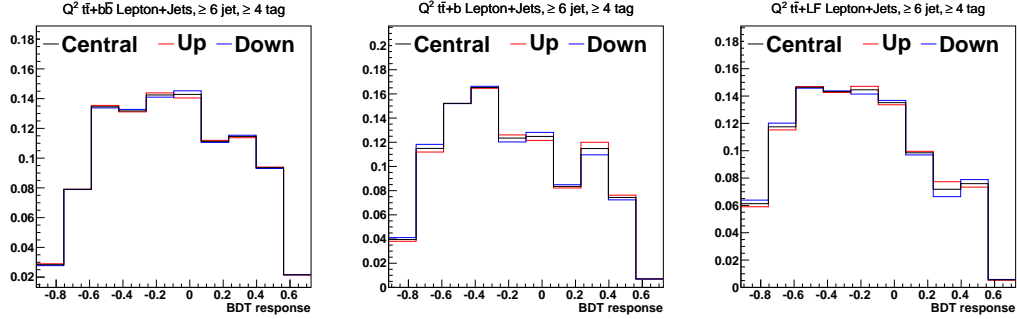


Figure 7.25: Comparison of the MVA discriminator when shifting the  $Q^2$  scale up and down by its uncertainties. Shown are the shift upwards (red) and downwards (blue) relative to the nominal (black) shape for the  $t\bar{t} + b\bar{b}$  (top row)  $t\bar{t} + b$  (middle row) and  $t\bar{t} + \text{LF}$  (bottom) background samples. The plots are from the  $LJ \geq 6$  jet  $\geq 4$  tag category. All plots are normalized to unit area.

$Q^2$ systematic yield change					
sys	shift	lepton+jets			
		$t\bar{t} + \text{LF}$	$t\bar{t} + b$	$t\bar{t} + b\bar{b}$	
$Q^2$ Uncertainty		-13.8%	-16.1%	-17.6%	
	up	+17.6%	+20.8%	+23.3%	
	down				

Table 7.12: This table summarizes the rate effect of shifting  $Q^2$  scale uncertainty for Madgraph. Note that the shifts are made independently for the following topologies:  $t\bar{t} + 0p$ ,  $t\bar{t} + 1p$ ,  $t\bar{t} + 2p$ ,  $t\bar{t} + c\bar{c}$ ,  $t\bar{t} + b$ , and  $t\bar{t} + b\bar{b}$ .

2702      **MC Statistics Uncertainty:** See section 6.4 for a description of the evaluation of this sys-  
 2703      tematic.

2704      **Extra  $t\bar{t}+\text{HF}$  Rate Uncertainty:** See section 6.4 for a description of the evaluation of this  
 2705      systematic.

2706 Table 7.13 summarizes the systematic uncertainties assessed on the signal and backgrounds  
2707 for this analysis. It describes how each systematic is treated in the fit used for signal extraction.

Source	Shape?	Notes
Luminosity	No	Signal and all backgrounds
Lepton ID/Trig	No	Signal and all backgrounds
Pileup	No	Signal and all backgrounds
Jet Energy Resolution	No	Signal and all backgrounds
Jet Energy Scale	Yes	Signal and all backgrounds
$b$ -Tag HF fraction	Yes	Signal and all backgrounds
$b$ -Tag HF stats (linear)	Yes	Signal and all backgrounds
$b$ -Tag HF stats (quadratic)	Yes	Signal and all backgrounds
$b$ -Tag LF fraction	Yes	Signal and all backgrounds
$b$ -Tag LF stats (linear)	Yes	Signal and all backgrounds
$b$ -Tag LF stats (quadratic)	Yes	Signal and all backgrounds
$b$ -Tag Charm (linear)	Yes	Signal and all backgrounds
$b$ -Tag Charm (quadratic)	Yes	Signal and all backgrounds
QCD Scale ( $t\bar{t}H$ )	No	Scale uncertainty for NLO $t\bar{t}H$ prediction
QCD Scale ( $t\bar{t}$ )	No	Scale uncertainty for NLO $t\bar{t}$ and single top predictions
QCD Scale ( $V$ )	No	Scale uncertainty for NNLO $W$ and $Z$ prediction
QCD Scale ( $VV$ )	No	Scale uncertainty for NLO diboson prediction
pdf ( $gg$ )	No	Pdf uncertainty for $gg$ initiated processes ( $t\bar{t}$ , $t\bar{t}Z$ , $t\bar{t}H$ )
pdf ( $q\bar{q}$ )	No	Pdf uncertainty for $q\bar{q}$ initiated processes ( $t\bar{t}W$ , $W$ , $Z$ ).
pdf ( $qg$ )	No	Pdf uncertainty for $qg$ initiated processes (single top)
Madgraph $Q^2$ Scale ( $t\bar{t} + 0p, 1p, 2p$ )	Yes	Madgraph $Q^2$ scale uncertainty for $t\bar{t} + jets$ split by parton number. There is one nuisance parameter per parton multiplicity and they are uncorrelated.
Madgraph $Q^2$ Scale ( $t\bar{t} + b\bar{b}/c\bar{c}$ )	Yes	Madgraph $Q^2$ scale uncertainty for $t\bar{t} + jets/b\bar{b}/c\bar{c}$ .
Madgraph $Q^2$ Scale ( $V$ )	No	Varies by jet bin.
$\tau$ Energy Scale	Yes	Tau signal and background
$\tau$ ID efficiency	Yes	Tau signal and background
$\tau$ Jet Fake Rate	Yes	Tau signal and background
$\tau$ Electron Fake Rate	Yes	Tau signal and background

Table 7.13: Summary for the of the systematic uncertainties considered on the inputs to the limit calculation. Except where noted, each row in this table will be treated as a single, independent nuisance parameter.

2708 Table 7.14 shows the results of the comparing the variation in rate for the sum of  $t\bar{t} + lf + b\bar{b} + c\bar{c}$   
2709 backgrounds. The systematic that produces the largest variation of the backgrounds is the QCD  
2710 scale uncertainty on the  $t\bar{t} + b\bar{b}$  background. The next largest variation comes from: the amount  
2711 of  $t\bar{t} + b\bar{b}$ , the  $b$ -tagging efficiency and fake rate, and the jet energy scale. The next most important  
2712 effect is the top quark  $p_T$  correction, and it is more than three times smaller than the QCD scale  
2713 uncertainty on  $t\bar{t} + b\bar{b}$ .

## 2714 7.5 Statistical Methods

2715 The same procedure that was used in the previous analysis, and desrcied in section 6.5.

Uncertainties on the sum of $t\bar{t} + lf$ , $t\bar{t} + b$ , $t\bar{t} + b\bar{b}$ , and $t\bar{t} + c\bar{c}$ events with $\geq 6$ jets and $\geq 4$ b-tags		
Source	Rate	Shape?
QCD Scale ( $t\bar{t} + b\bar{b}$ )	17%	No
$b$ -Tag HF contamination	17%	Yes
QCD Scale ( $t\bar{t} + c\bar{c}$ )	11%	No
Jet Energy Scale	11%	Yes
$b$ -Tag LF contamination	9.6%	Yes
$b$ -Tag HF stats (linear)	9.1%	Yes
QCD Scale ( $t\bar{t} + b$ )	7.1%	No
Madgraph $Q^2$ Scale ( $t\bar{t} + b\bar{b}$ )	6.8%	Yes
$b$ -Tag Charm Uncertainty (quadratic)	6.7%	Yes
Top Pt Correction	6.7%	Yes
$b$ -Tag HF stats (quadratic)	6.4%	Yes
$b$ -Tag LF stats (linear)	6.4%	Yes
Madgraph $Q^2$ Scale ( $t\bar{t} + 2$ partons)	4.8%	Yes
$b$ -Tag LF stats (quadratic)	4.8%	Yes
Luminosity	4.4%	No
Madgraph $Q^2$ Scale ( $t\bar{t} + c\bar{c}$ )	4.3%	Yes
Madgraph $Q^2$ Scale ( $t\bar{t} + b$ )	2.6%	Yes
Lepton ID/Trig	1.4 (2.8)%	No
QCD Scale ( $t\bar{t}$ )	3%	No
pdf ( $gg$ )	2.6%	No
Jet Energy Resolution	1.5%	No
Pileup	1%	No
$b$ -Tag Charm Uncertainty (linear)	0.6%	Yes

Table 7.14: Specific effect of systematics on predicted background yields for events with  $\geq 6$  jets and  $\geq 4$  b-tags. Here we only consider the sum of the largest backgrounds,  $t\bar{t} + lf$ ,  $t\bar{t} + b$ ,  $t\bar{t} + b\bar{b}$ , and  $t\bar{t} + c\bar{c}$ . These three backgrounds account for 94% of all background events. The signal is 3.5% of the yield of the three main backgrounds. The signal fraction is directly comparable to the variations of the background in the table. The table shows that the signal is much smaller than many of the background variations.

## 2716 7.6 Results and Conclusions

2717 In the lack of a significant excess of events in data, upper limits are once again set on the  
 2718  $t\bar{t}H$  production rate. The shape of the BDT discriminator distribution is used to fit the simulated  
 2719 signal and backgrounds samples to the data. Besides the BDT discriminator shapes for data,  
 2720 background and signal, inputs to the limit setting include the number of events passing the  
 2721 selection for each process. Systematics that are used are nuisance parameters are described in  
 2722 the previous section. The Higgs mass points we set limits for are: 110, 115, 120, 125, 130, 135  
 2723 and  $140 \text{ GeV}/c^2$ . For the lepton+jets channel, the limits are shown in Tab. 7.15 and Fig. 7.26.

Higgs Mass	Observed	Median	Expected 68% C.L. Range	Expected 95% C.L. Range
110 $\text{GeV}/c^2$	3.6	3.3	[2.4,4.7]	[1.8,6.6]
115 $\text{GeV}/c^2$	4.1	3.5	[2.4,4.9]	[1.8,6.9]
120 $\text{GeV}/c^2$	4.3	4.0	[2.9,5.8]	[2.1,8.1]
125 $\text{GeV}/c^2$	4.9	4.7	[3.3,6.7]	[2.5,9.4]
130 $\text{GeV}/c^2$	6.8	6.0	[4.3,8.6]	[3.2,12.0]
135 $\text{GeV}/c^2$	7.4	7.1	[5.0,10.2]	[3.7,14.2]
140 $\text{GeV}/c^2$	9.0	9.6	[6.9,13.7]	[5.2,18.9]

Table 7.15: Expected and observed upper limits for SM Higgs for lepton + jets channel using the 2012 dataset. These limits were extracted using the asymptotic method.

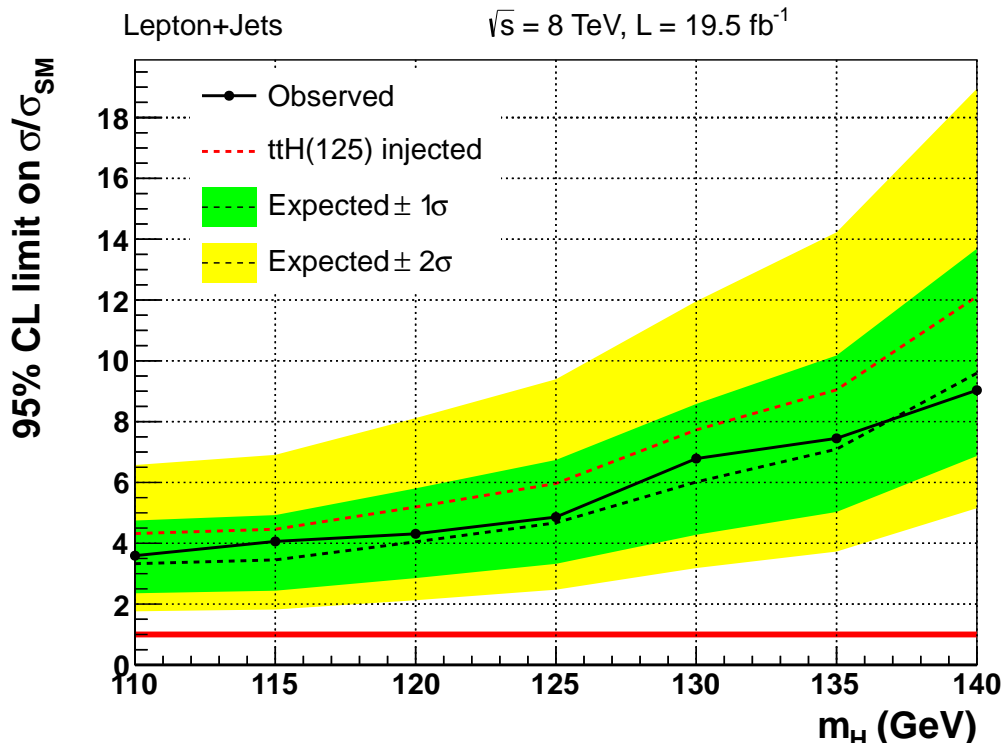


Figure 7.26: The expected and observed 95% CL upper limits on the signal strength parameter  $\mu = \sigma/\sigma_{SM}$  for the lepton+jets channel using the 2012 dataset. These limits were extracted using the asymptotic method.

2724 For the full  $19.4 \text{ fb}^{-1}$  of 8 TeV data collected by the CMS detector, an updated search

for the Standard Model Higgs boson produced in association with top-quark pairs has been performed. The increase in expected sensitivity did not increase by a factor of  $\sim 2$  that one would naively expect from increasing the statistics by a factor of  $\sim 4$ . This is because, largely due to the different set of systematic uncertainties used, the analysis entered a regime where statistical uncertainty was no longer the dominant factor that degraded sensitivity. If this data set was repeatedly collected, allowing for statistical fluctuations, it should be expected that, for a Standard Model Higgs boson, with mass,  $m_H = 125$  GeV, that 95% of the results would fail to observe the  $t\bar{t}H$  signal unless its cross-section was modified by a factor of 4.9. From simulations alone, this expected factor is 4.7, an difference of less than  $1\sigma$  from the observed data.

The results of this analysis were combined with previous results in this channel from 7 TeV data and with di-lepton, same-sign di-lepton, hadronic tau, di-photon, and multi-lepton final state channels and published in the Journal of High Energy Physics (JHEP) in September of 2014 [151]. The combined analytical power of all of the channels allowed for an upper limit of 4.5 times the predicted Standard Model cross section. This is slightly more than  $2\sigma$  away from the expected factor of 2.7 from simulations alone.

2740 **Chapter 8**

2741 **Analysis Improvements**

2742 The analyses described in the previous two chapters use sophisticated multivariate analysis  
2743 (MVA) techniques to perform signal extraction and limit setting. However, there are several  
2744 improvements that can still be made to optimize signal extraction and increase sensitivity. The  
2745 following section will describe the implementation of the latest simulation techniques in order  
2746 to improve the modeling the signal and background processes. The final section will discuss  
2747 variables from these new simulations that can be used to enhance the identification of final state  
2748 jets with their roles in the  $t\bar{t}$  system.

2749 **8.1 aMC@NLO, MadSpin, and Pythia8 Monte Carlo**

2750 One of the largest sources of uncertainty in each analysis comes from the theoretical uncertainty  
2751 of the Leading Order (LO) monte carlo sample used to estimate background rates and shapes.  
2752 In order to accurately model the high jet-multiplicity environment of the  $t\bar{t}H$  final state, higher-  
2753 order calculations in perturbation theory are necessary. Recently, the aMC@NLO framework  
2754 has been released, and is an automated tool for event generation that utilizes Next-to-Leading  
2755 Order (NLO) QCD predictions [152]. This framework takes advantage of recent theoretical  
2756 developments in the automation of calculating spin-entangled decays from heavy resonances,  
2757 which is packaged in the program MadSpin [153]. The event generator, aMC@NLO, using  
2758 MadSpin to calculate the decays of the top quark,  $W$  and  $Z$  bosons, is then interfaced to Pythia  
2759 8 to framework perform the parton shower and hadronization [154]. Each stage of this event  
2760 generation process uses the latest technological developments in monte carlo simulation, which  
2761 were unavailable at the time of the previous analyses.

2762 For process where additional jets are simulated in the final state, there will be an additional  
2763 complication since the parton shower and hadronization are performed separately and the con-

tributions for NLO processes will be double counted in several cases. This occurs when a process with an additional jet in the final state is created in the matrix element level by aMC@NLO and later, another event is created with no additional jets in the final state at the matrix element level, but when the parton shower occurs in Pythia 8, an additional jet can be generated, creating two events from a single underlying theoretical contribution. The removal of these overlapping events is carried out by a method known as FXFX merging [155]. This algorithm tracks the heritage of final state jets, in order to determine whether it was created as part of the matrix element or later during the parton shower. Due to the higher accuracy of modeling the kinematics of partons calculated in the matrix element stage, the algorithm removes events where additional jets are created in the parton shower, ensuring that the underlying process with an additional final state jets are created at the matrix element level, utilizing the NLO QCD calculations in aMC@NLO.

The utilization of these event generation techniques to simulate  $t\bar{t}H$  and  $t\bar{t} + jets$  backgrounds will improve the kinematic modeling of these high-jet multiplicity processes. A dedicated  $t\bar{t} + b\bar{b}$  sample with a large number of events generated with this framework would improve the modeling of the irreducible background. Unfortunately, these event generation tools were only recently released and the computational time required to generate samples with the equivalent statistical power of those used in the previous analyses is prohibitive on the time scale of this dissertation. However, each of the following samples were created using the process described above with 500,000 events each:

- $t\bar{t} + 0, 1, \text{ and } 2$  additional jets
- $t\bar{t} + b\bar{b}$
- $t\bar{t}H + 0, \text{ and } 1$  additional jets

The number of events generated is not sufficient to create a control region to assess calibrations of jet energy,  $b$ -tag efficiency, or lepton identification and reconstruction efficiency. However, since all of these processes are generated in an identical framework, it is reasonable to assume that calibrations applied will be similar for each, and as such comparisons amongst the samples can still provide insight into how they can be used to improve the analysis. Figure 8.1 shows a comparison between the number of reconstructed jets and  $b$ -tagged jets that pass the selection used in the previous analysis, with a lowered  $p_T$  threshold of 25 GeV. As before, the jet multiplicity of  $t\bar{t}H$  has a much longer distribution than the  $t\bar{t} + jets$  backgrounds, making it very important that these high-multiplicity events are modeled with the highest precision available.

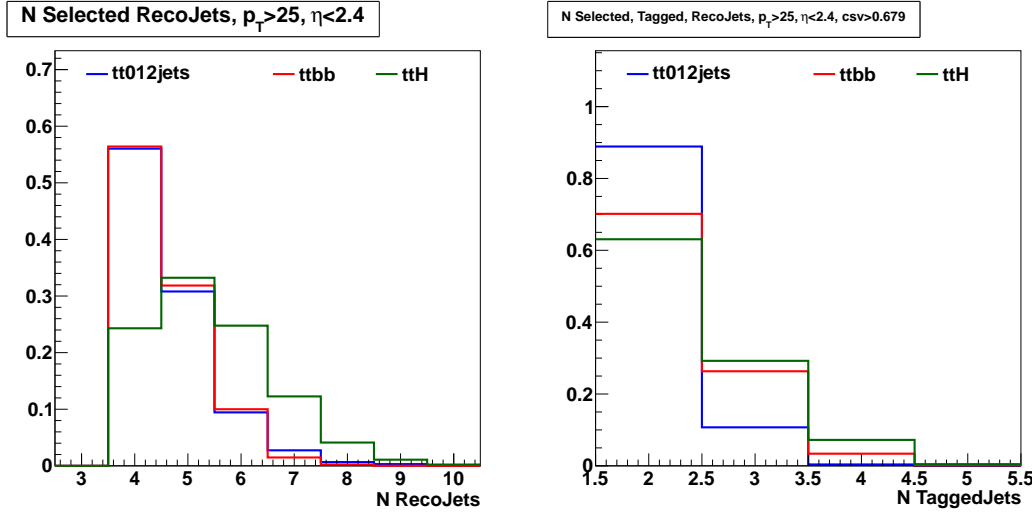


Figure 8.1: The number of reconstructed jets passing selection (left) and that have additionally been  $b$ -tagged (right) for  $t\bar{t}H$ ,  $t\bar{t} + jets$ , and  $t\bar{t} + b\bar{b}$  samples generated with the aMC@NLO and Pythia 8 framework

## 2796 8.2 Analysis Techniques Under Development

2797 One of the most difficult challenges of the  $t\bar{t}H$  final state is the combinatorics of possible  $b$ -jet  
2798 candidates coming from the Higgs decay. The correct associate of jets to their roles in the decay  
2799 of the top quarks would greatly reduce the number of jets as candidates for Higgs daughters.  
2800 This is done, in some degree, in the analyses described in previous chapters via the "best Higgs  
2801 mass" variable. This is a  $\chi^2$  minimization that relies only on the masses of the top quark,  $W$  and  
2802 Higgs bosons in the event, to decide which jets are associated to the decays of which particles.  
2803 These mass variable will be useful in identifying jets from the  $t\bar{t}$  system. Figure X shows the  
2804 case for the  $W$  boson mass evaluated for jets which have been correctly associated to the MC  
2805 truth generated partons in blue, and for the incorrect associations in green.

2806 The implementation of Madspin in the aMC@NLO framework allows for the highest precision  
2807 on the spin correlations of the decay products from the  $t\bar{t}H$  and  $t\bar{t}$  systems. The angular  
2808 relationships among the decay products provide additional discrimination power for the correct  
2809 association of jets to their roles in the  $t\bar{t}H$  and  $t\bar{t}$  systems. The spin correlations of the decay  
2810 products are enhanced by boosting to a reference frame that is more sensitive to differences in  
2811 the angles between the correctly and incorrectly associated objects in the event. The reference  
2812 frame of choice is formed by first identifying all of the potential candidates of the semi-leptonic  
2813  $t\bar{t}$  decay:

- 2814 •  $\bar{b}$ -quark coming from the  $t$ -quark
- 2815 •  $b$ -quark coming from  $\bar{t}$ -quark
- 2816 • up-type quark from hadronic  $W$  boson decay

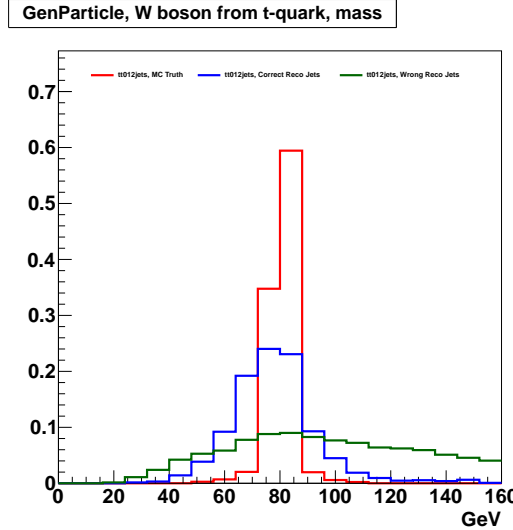


Figure 8.2: The invariant mass of the  $W$  boson in the  $t\bar{t}$  decay for the case of the MC truth (red), correctly associated reconstructed jets (blue), and incorrectly associated reconstructed jets (green)

2817     • down-type quark from the hadronic  $W$  boson decay  
 2818     The four-vector of the entire  $t\bar{t}$  system can be formed, and the hadronic candidates are  
 2819     boosted to a frame where the  $t\bar{t}$  system itself is at rest. Then, the  $t$ -quark, and its daughters  
 2820     are boosted to a frame such that the  $t$ -quark is at rest. Finally, the  $\bar{t}$ -quark, and its daughters  
 2821     are boosted to a frame such that the  $\bar{t}$ -quark is at rest. Then the angles between their decay  
 2822     products is evaluated. Typically, these studies are performed in the di-lepton channel since the  
 2823     angular resolution is much better in leptons than in jets. Figure 8.3 shows the cosine of the  
 2824     momentum 3-vector between the  $b$ -quarks from  $t$  and  $\bar{t}$ , the lepton and the up-type  $W$ -boson  
 2825     daughter, and the lepton and the down-type  $W$ -boson daughter.

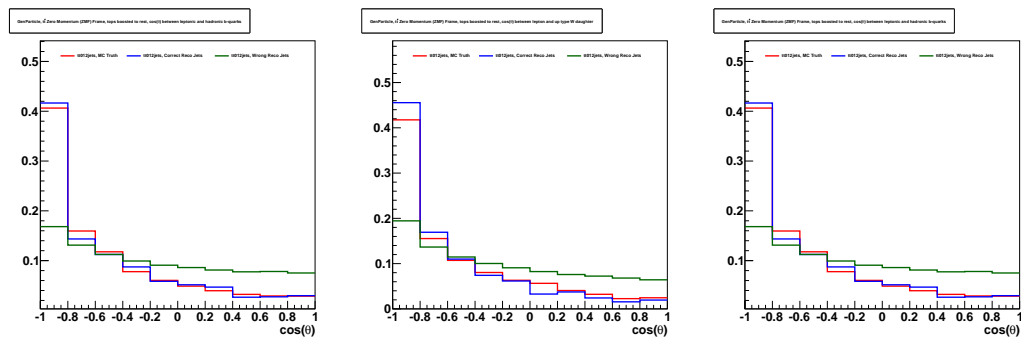


Figure 8.3: The cosine of the angle between the momentum three-vectors for the  $b$ -quarks from the top decays (left), the lepton and the up-type  $W$  boson daughter (center), and the lepton and the down-type  $W$  boson daughter (right)

2826     All three distributions have peaking values that provide discrimination between the jets correctly  
 2827     associated to the MC truth generator-level partons of the  $t\bar{t}$  decay, and the jets which are  
 2828     incorrectly associated. In each plot, the green represents the incorrect associations, while the

blue represents the correct associations, and the red represents the MC truth from the generated parton. An additional angle of interest is the difference in the  $\phi$  coordinate between daughters of the  $t\bar{t}$  decay. Figure 8.4 shows the distributions for the  $\Delta\phi$  between the  $b$ -quarks from the top decays, the lepton and up-type  $W$ -boson daughter, and the lepton and the down-type  $W$ -boson daughter. The case of the correctly associated jets has two sharp peaks near  $\phi = \pm 2$ , where the distribution is more uniform for incorrectly associated jets.

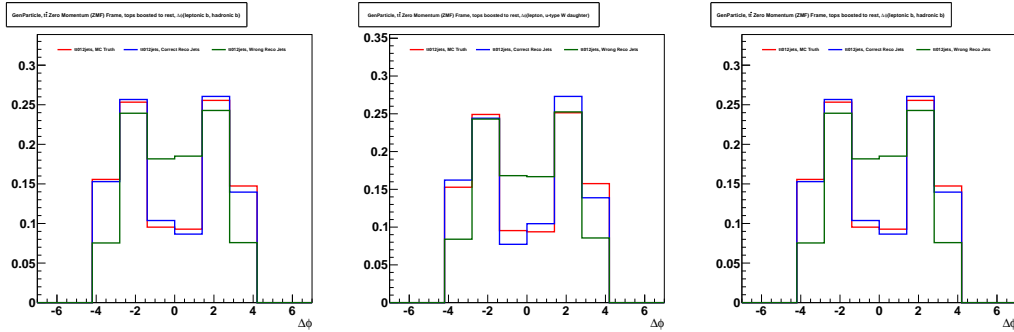


Figure 8.4: The difference in the  $\phi$  coordinate between the momentum three-vectors for the  $b$ -quarks from the top decays (left), the lepton and the up-type  $W$  boson daughter (center), and the lepton and the down-type  $W$  boson daughter (right)

A final variable of interest for jet association would be the charge of lepton multiplied against the charge of the  $b$ -quark that is associated with the same top-quark. These two values, due to charge conservation, will always be negative when multiplied. The charge of the jet is calculated from a  $p_T$  weighted sum of the tracks contained in the cluster, where the curvature of each track tells the charge of the hadron creating the signature. Since there are many hadrons clustered together to form a jet, there is a large degradation on resolution of the charge of the jet, however for the peak of this distribution is negative for correctly associated jets, and positive for incorrect jets, as shown in figure 8.5.

A jet association algorithm can be formed by using an MVA technique to provide a discriminant for how likely a certain combination of jets from an event are correctly associated to their roles in the decay of the  $t\bar{t}$  system. A training sample of correctly and incorrectly associated jets can be trained using the following variables:

- Invariant Mass of the Hadronic  $W$  boson
- Invariant Mass of the Leptonic  $W$  boson
- Invariant Mass of the Hadronic top-quark
- Invariant Mass of the Leptonic top-quark
- $\cos\theta_{b,\bar{b}}$  in the frame where  $t\bar{t}$  system and  $t$ -quarks are at rest respectively

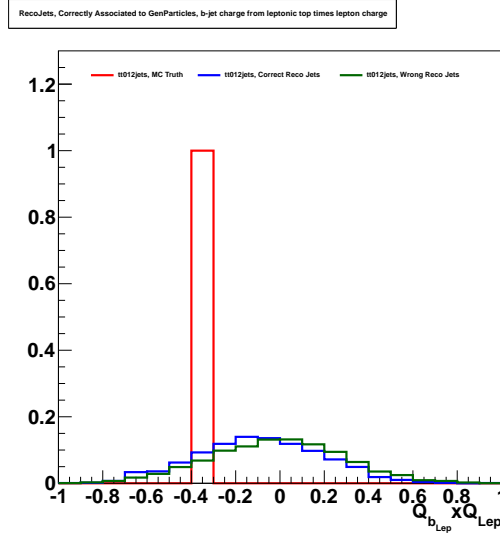


Figure 8.5: Jet times lepton charge, for the  $b$ -jet associated with the same top as the lepton. Green shows incorrectly associated reconstructed jets, blue shows correctly associated jets, and red is the MC truth

- 2852     •  $\cos \theta_{lep, up-typeWdaughter}$  in the frame where  $t\bar{t}$  system and  $t$ -quarks are at rest respectively
  - 2853     •  $\cos \theta_{lep, down-typeWdaughter}$  in the frame where  $t\bar{t}$  system and  $t$ -quarks are at rest respec-
  - 2854       tively
  - 2855     •  $\Delta\phi(\theta_{b,\bar{b}})$  in the frame where  $t\bar{t}$  system and  $t$ -quarks are at rest respectively
  - 2856     •  $\Delta\phi(\theta_{lep, up-typeWdaughter})$  in the frame where  $t\bar{t}$  system and  $t$ -quarks are at rest respec-
  - 2857       tively
  - 2858     •  $\Delta\phi(\theta_{lep, down-typeWdaughter})$  in the frame where  $t\bar{t}$  system and  $t$ -quarks are at rest respec-
  - 2859       tively
  - 2860     • The product of the lepton and  $b$ -quark associated with the same  $t$ -quark
- 2861       An additional improvement to the analysis will rely on a dedicated MVA for each of the  
 2862        $t\bar{t} + X$  backgrounds, where  $X$  is light flavor, single  $c$ ,  $c\bar{c}$ , single  $b$ , and  $b\bar{b}$ . A dedicated  $t\bar{t} + b\bar{b}$  and  
 2863       even a  $t\bar{t} + c\bar{c}$  sample with sufficiently large enough events to train an MVA would be ideal. The  
 2864       discriminants from each of the backgrounds would be combined as input variables to a second  
 2865       MVA, in order to produce a discriminant for how likely the event is from a  $t\bar{t}H$  decay.

2866 **Chapter 9**

2867 **Conclusions and Summary**

2868 In 2012, the Large Hadron Collider (LHC) produced the highest energy proton-proton collisions,  
2869 with center of mass energies of 8 TeV. Protons, with humble beginnings in a bottle of Hydrogen,  
2870 travel through a multi-stage accelerator complex, before being injected into the 27.6 km LHC  
2871 ring as two counter-rotating beams. Superconducting radio-frequency cavities accelerate the  
2872 beams during each revolution, constrained to the circular path by more than a thousand 8 T  
2873 superconducting dipole magnets, as each beam is brought to an energy of 4 TeV.

2874 At one of the four points on the LHC ring where the proton beams are squeezed together  
2875 to produce collisions, sits the Compact Muon Solenoid (CMS) experiment, a general purpose  
2876 particle detector designed to elucidate the mechanism of electroweak symmetry breaking, and  
2877 explore physics interactions at the TeV energy scale. This 14,000 ton, 15 m tall device, provides  
2878 hermetic,  $4\pi$ , coverage of the interaction region, and is composed of a system of sub-detectors,  
2879 with a cylindrical symmetry about the beam-line and interaction region, which work in paral-  
2880 lel to identify and measure the kinematic properties of particles produced during  $pp$  collisions.  
2881 The inner tracking system is composed of more than 70 million silicon pixel and strip detec-  
2882 tors that provide  $\mu\text{m}$  spatial resolution on the trajectory of charged particles. An electromag-  
2883 netic calorimeter (ECAL) surrounds the inner tracker, and is composed of more than 75,000  
2884 lead-tungstate crystals, which absorb energy from electromagnetically interacting particles, with  
2885 electrons and photons depositing almost all of their energy in this sub-detector. The hadronic  
2886 calorimeter (HCAL) surrounds the ECAL, absorbing the energy of charged and neutral hadrons  
2887 with stacks of brass absorber material with layers of plastic scintillator to sample the energy  
2888 in between. The outermost system are the muon chambers, which utilize three different types  
2889 of detector technologies to provide fast timing to trigger measurements and excellent spatial  
2890 resolution on muons, an important signature for many TeV energy scale processes. Hardware  
2891 and firmware installed on the detector provide an instant, but basic reconstruction of a collision,

allowing for the amount of collisions recorded to be reduced from a rate of 40 MHz down to 10 kHz. Events are additionally filtered through the use of software to a manageable rate of 100 Hz.

Once the first  $5.1 \text{ fb}^{-1}$  of 8 TeV data was collected by the CMS detector, a search for the Standard Model Higgs boson, produced in association with top-quark pairs ( $t\bar{t}H$ ) was performed in the final state with a single lepton, at least 4 jets and at least 2  $b$ -tags. The search region was divided into categories based on the jet and  $b$ -tag multiplicity of the final state, and a Clermont-Ferrand Multi-Layer Perceptron Artificial Neural Network (CFMlpANN) was trained to provide a one-dimensional discriminant for how likely the event is to be from the  $t\bar{t}H$  signal, or one of the  $t\bar{t} + \text{jets}$  backgrounds. No significant excess of events in the data was observed, and an observed (expected) upper limit on the production rate of  $t\bar{t}H$  at 9.5 (5.4) times the rate predicted by the Standard Model. This final state was combined with a di-lepton final state, and the previous results from the 7 TeV dataset collected in 2011, to produce an observed (expected) upper limit on the  $t\bar{t}H$  process as 5.8 (5.2) times the Standard Model rate and published in the Journal of High Energy Physics (JHEP) in May of 2013.

A second analysis was performed on the full  $19.5 \text{ fb}^{-1}$  dataset of 8 TeV data collected by CMS. This also used a final state with a single lepton, at least 4 jets, and at least 2  $b$ -tags, and a search region divided into categories based on the jet and  $b$ -tag multiplicity of the final state. A different multivariate analysis (MVA) technique was employed: a Boosted Decision Tree (BDT) was trained to separate the  $t\bar{t}H$  signal from the  $t\bar{t} + \text{jets}$  background for each of the jet/tag categorizations. Once again, no significant excess of events is observed, and an observed (expected) upper limit on the  $t\bar{t}H$  production rate is set at 4.9 (4.7) times the Standard Model prediction. This analysis was combined with same and opposite sign di-lepton, multi-lepton, and hadronic tau final states to produce an observed (expected) upper limit of 4.5 (2.5) time the predicted rate of  $t\bar{t}H$  production.

In preparation to perform this search in the next dataset collected by CMS, several investigations have been performed on ways to improve the sensitivity of the analysis to the  $t\bar{t}H$  signal. One of the most important improvements will be the incorporation of next-to-leading order (NLO) QCD effects into the simulation of  $t\bar{t}H$  signal and  $t\bar{t} + \text{jets}$  background. This will improve the modeling of high jet-multiplicity events, which characterize both the signal and background in this analysis. These improved simulations will also incorporate the latest techniques to calculate the spin-correlations of the decay products from heavy resonances in top-quark and  $W$  boson decays, via the MadSpin framework. This will allow the angular correlations of the daughters of the  $t\bar{t}$  system to be used to correctly associate jets in an event to their roles in the  $t\bar{t}$  decay, thereby reducing the combinatorics of jets that can possibly be associated with jets from the

<sup>2927</sup> Higgs decay.

<sup>2928</sup> With the experience gained in previous analyses, and improvements already underway, the  
<sup>2929</sup> observation of a  $t\bar{t}H$  signal will be increasingly likely in the larger statistics, higher-energy  
<sup>2930</sup> datasets collected in the future by  $t\bar{t}H$ . In the lack of an observation, now or in the future, these  
<sup>2931</sup> upper limits can be used to constrain future models involving physics beyond the Standard Model  
<sup>2932</sup> (BSM) that would predict enhancements to final states explored in these first two  $t\bar{t}H$  analyses.

# 2933 Bibliography

- 2934 [1] S. Bethke, “The 2009 World Average of alpha(s)”, *Eur.Phys.J.* **C64** (2009) 689–703,  
2935 doi:10.1140/epjc/s10052-009-1173-1, arXiv:0908.1135.
- 2936 [2] “Image, Higgs Potential”.  
2937 URL <http://inspirehep.net/record/1086544/files/higgspotential.png>.
- 2938 [3] “Image, CMS Standard Model Processes”.  
2939 URL <https://twiki.cern.ch/twiki/bin/view/CMSPublic/PhysicsResultsSMP>.
- 2940 [4] “Image, Hierarchy Problem”. URL <http://upload.wikimedia.org/wikipedia/commons/thumb/6/68/Hqmc-vector.svg/300px-Hqmc-vector.svg.png>.
- 2941
- 2942 [5] “LHC Aerial View”.  
2943 URL <http://www.coepp.org.au/files/coepp/images/cern-aerial2.jpg>.
- 2944 [6] “LHC, Delivered Luminosity”. URL [http://cms-service-lumi.web.cern.ch/cms-service-lumi/publicplots/int\\_lumi\\_cumulative\\_pp\\_2.png](http://cms-service-lumi.web.cern.ch/cms-service-lumi/publicplots/int_lumi_cumulative_pp_2.png).
- 2945
- 2946 [7] J.-L. Caron, “The LHC injection complex.. L’ensemble d’injection du LHC.”, (May,  
2947 1993). AC Collection. Legacy of AC. Pictures from 1992 to 2002.
- 2948 [8] L. Evans and P. Bryant, “LHC Machine”, *JINST* **3** (2008) S08001,  
2949 doi:10.1088/1748-0221/3/08/S08001.
- 2950 [9] M. Barnes et al., “Injection and extraction magnets: Kicker magnets”,  
2951 arXiv:1103.1583.
- 2952 [10] “Image, Klystron operations”.  
2953 URL <http://upload.wikimedia.org/wikipedia/commons/a/aa/Klystron.enp.gif>.
- 2954 [11] “Image, Klystron operations”. URL <http://cds.cern.ch/record/43017?ln=en>.
- 2955 [12] “Image, CERN LHC, Layout of the 5 cryogenic islands”. URL <http://d29qn7q9z0j1p6.cloudfront.net/content/roypta/370/1973/3887/F12.medium.gif>.
- 2956

- [2957] [13] P. Lebrun, “Large Cryogenic Helium Refrigeration System for the LHC”, Technical  
 Report LHC-Project-Report-629. CERN-LHC-Project-Report-629, CERN, Geneva, Feb,  
 2003. revised version number 1 submitted on 2003-02-19 11:44:11.
- [2960] [14] “Image, CERN LHC, Beam Screen”. URL [http://home.web.cern.ch/sites/home.web.cern.ch/files/engineering\\_page/2013/01/beam-screen\\_0.jpg](http://home.web.cern.ch/sites/home.web.cern.ch/files/engineering_page/2013/01/beam-screen_0.jpg).
- [2962] [15] CMS Collaboration, “The CMS experiment at the CERN LHC”, *JINST* **3** (2008)  
 S08004, doi:10.1088/1748-0221/3/08/S08004.
- [2964] [16] “Image, CMS Higgs Physics Results, H- $\nu$ ZZ- $\nu$ l Inv. Mass”. URL [https://twiki.cern.ch/twiki/pub/CMSPublic/Hig13002PubTWiki/ZZMass\\_7Plus8TeV\\_70-1000\\_3GeV.pdf](https://twiki.cern.ch/twiki/pub/CMSPublic/Hig13002PubTWiki/ZZMass_7Plus8TeV_70-1000_3GeV.pdf).
- [2966] [17] “Image, CMS Higgs Physics Results, H- $\nu$ GammaGamma Inv. Mass”. URL [https://twiki.cern.ch/twiki/pub/CMSPublic/Hig13001PubTWiki/Fig\\_19.pdf](https://twiki.cern.ch/twiki/pub/CMSPublic/Hig13001PubTWiki/Fig_19.pdf).
- [2968] [18] CMS Collaboration, “Observation of a new boson at a mass of 125 GeV with the CMS  
 experiment at the LHC”, *Phys.Lett.B* (2012) arXiv:1207.7235.
- [2970] [19] ATLAS Collaboration, “Observation of a new particle in the search for the Standard  
 Model Higgs boson with the ATLAS detector at the LHC”, *Phys.Lett.B* (2012)  
 arXiv:1207.7214.
- [2973] [20] M. E. Peskin and D. V. Schroeder, “An Introduction to Quantum Field Theory”.  
 Westview Press, URL <http://www.westviewpress.com>, 1995.
- [2975] [21] K. G. Wilson, “Renormalization Group and Critical Phenomena. I. Renormalization  
 Group and the Kadanoff Scaling Picture”, *Phys. Rev. B* **4** (Nov, 1971) 3174–3183,  
 doi:10.1103/PhysRevB.4.3174.
- [2978] [22] K. G. Wilson, “Renormalization Group and Critical Phenomena. II. Phase-Space Cell  
 Analysis of Critical Behavior”, *Phys. Rev. B* **4** (Nov, 1971) 3184–3205,  
 doi:10.1103/PhysRevB.4.3184.
- [2981] [23] H. Weyl, “The theory of groups and quantum mechanics”. Dover Press,  
 URL <https://ia700807.us.archive.org/20/items/ost-chemistry-quantumtheoryofa029235mbp/quantumtheoryofa029235mbp.pdf>,  
 1930.
- [2985] [24] C. N. Yang and R. L. Mills, “Conservation of Isotopic Spin and Isotopic Gauge  
 Invariance”, *Phys. Rev.* **96** (Oct, 1954) 191–195, doi:10.1103/PhysRev.96.191.

- 2987 [25] M. Gell-Mann, “A Schematic Model of Baryons and Mesons”, *Phys.Lett.* **8** (1964)  
 2988 214–215, doi:10.1016/S0031-9163(64)92001-3.
- 2989 [26] G. Zweig, “An SU<sub>3</sub> model for strong interaction symmetry and its breaking; Version 1”,  
 2990 Technical Report CERN-TH-401, CERN, Geneva, Jan, 1964.
- 2991 [27] G. Zweig, “An SU<sub>3</sub> model for strong interaction symmetry and its breaking; Version 2”,.
- 2992 [28] O. W. Greenberg, “Spin and Unitary-Spin Independence in a Paraquark Model of  
 2993 Baryons and Mesons”, *Phys. Rev. Lett.* **13** (Nov, 1964) 598–602,  
 2994 doi:10.1103/PhysRevLett.13.598.
- 2995 [29] P. Higgs, “Broken symmetries, massless particles and gauge fields”, *Physics Letters* **12**  
 2996 (1964), no. 2, 132 – 133, doi:[http://dx.doi.org/10.1016/0031-9163\(64\)91136-9](http://dx.doi.org/10.1016/0031-9163(64)91136-9).
- 2997 [30] S. Weinberg, “A Model of Leptons”, *Phys. Rev. Lett.* **19** (Nov, 1967) 1264–1266,  
 2998 doi:10.1103/PhysRevLett.19.1264.
- 2999 [31] S. L. Glashow, “Partial-symmetries of weak interactions”, *Nuclear Physics* **22** (1961),  
 3000 no. 4, 579 – 588, doi:[http://dx.doi.org/10.1016/0029-5582\(61\)90469-2](http://dx.doi.org/10.1016/0029-5582(61)90469-2).
- 3001 [32] A. Salam and J. Ward, “Electromagnetic and weak interactions”, *Physics Letters* **13**  
 3002 (1964), no. 2, 168 – 171, doi:[http://dx.doi.org/10.1016/0031-9163\(64\)90711-5](http://dx.doi.org/10.1016/0031-9163(64)90711-5).
- 3003 [33] Nobelprize.org, “The Nobel Prize in Physics 1957”.  
 3004 URL [http://www.nobelprize.org/nobel\\_prizes/physics/laureates/1957/](http://www.nobelprize.org/nobel_prizes/physics/laureates/1957/).
- 3005 [34] N. Cabibbo, “Unitary Symmetry and Leptonic Decays”, *Phys. Rev. Lett.* **10** (Jun,  
 3006 1963) 531–533, doi:10.1103/PhysRevLett.10.531.
- 3007 [35] M. Kobayashi and T. Maskawa, “CP Violation in the Renormalizable Theory of Weak  
 3008 Interaction”, *Prog.Theor.Phys.* **49** (1973) 652–657, doi:10.1143/PTP.49.652.
- 3009 [36] G. Arnison et al., “Experimental observation of isolated large transverse energy electrons  
 3010 with associated missing energy at s=540 GeV”, *Physics Letters B* **122** (1983), no. 1,  
 3011 103 – 116, doi:[http://dx.doi.org/10.1016/0370-2693\(83\)91177-2](http://dx.doi.org/10.1016/0370-2693(83)91177-2).
- 3012 [37] G. Arnison et al., “Experimental observation of lepton pairs of invariant mass around 95  
 3013 GeV/c<sup>2</sup> at the {CERN} {SPS} collider”, *Physics Letters B* **126** (1983), no. 5, 398 –  
 3014 410, doi:[http://dx.doi.org/10.1016/0370-2693\(83\)90188-0](http://dx.doi.org/10.1016/0370-2693(83)90188-0).
- 3015 [38] M. Banner et al., “Observation of single isolated electrons of high transverse momentum  
 3016 in events with missing transverse energy at the {CERN} pp collider”, *Physics Letters B*

- <sup>3017</sup> **122** (1983), no. 56, 476 – 485,  
<sup>3018</sup> doi:[http://dx.doi.org/10.1016/0370-2693\(83\)91605-2](http://dx.doi.org/10.1016/0370-2693(83)91605-2).
- <sup>3019</sup> [39] P. Bagnaia et al., “Evidence for Z $0e^+e^-$  at the {CERN} pp collider”, *Physics Letters B*  
<sup>3020</sup> **129** (1983), no. 12, 130 – 140,  
<sup>3021</sup> doi:[http://dx.doi.org/10.1016/0370-2693\(83\)90744-X](http://dx.doi.org/10.1016/0370-2693(83)90744-X).
- <sup>3022</sup> [40] The ALEPH, DELPHI, L3, OPAL, SLD Collaborations, the LEP Electroweak Working  
<sup>3023</sup> Group, the SLD Electroweak and Heavy Flavour Groups, “Precision Electroweak  
<sup>3024</sup> Measurements on the Z Resonance”, *Phys. Rept.* **427** (2006) 257,  
<sup>3025</sup> arXiv:[hep-ex/0509008](https://arxiv.org/abs/hep-ex/0509008).
- <sup>3026</sup> [41] The ALEPH, DELPHI, L3, OPAL Collaborations, the LEP Electroweak Working Group,  
<sup>3027</sup> “Electroweak Measurements in Electron-Positron Collisions at W-Boson-Pair Energies at  
<sup>3028</sup> LEP”, *Phys. Rept.* **532** (2013) 119, arXiv:[1302.3415](https://arxiv.org/abs/1302.3415).
- <sup>3029</sup> [42] “Image, LEP ZPole”. URL <http://lepewwg.web.cern.ch/LEPEWWG/1/Nnu.eps>.
- <sup>3030</sup> [43] “Image, CDF Top Quark Mass”.  
<sup>3031</sup> URL [http://www-cdf.fnal.gov/physics/new/top/public\\_mass.html](http://www-cdf.fnal.gov/physics/new/top/public_mass.html).
- <sup>3032</sup> [44] “Image, CMS Higgs Mass”. URL [http://cms-higgs-results.web.cern.ch/cms-higgs-results/Comb/HIG-14-009-Paper/sqr\\_mass\\_all.pdf](http://cms-higgs-results.web.cern.ch/cms-higgs-results/Comb/HIG-14-009-Paper/sqr_mass_all.pdf).
- <sup>3034</sup> [45] F. Abe et al., “Observation of Top Quark Production in  $\bar{p}p$  Collisions with the Collider  
<sup>3035</sup> Detector at Fermilab”, *Phys. Rev. Lett.* **74** (Apr, 1995) 2626–2631,  
<sup>3036</sup> doi:[10.1103/PhysRevLett.74.2626](https://doi.org/10.1103/PhysRevLett.74.2626).
- <sup>3037</sup> [46] S. Abachi et al., “Search for High Mass Top Quark Production in  $p\bar{p}$  Collisions at  $\sqrt{s} =$   
<sup>3038</sup> 1.8 TeV”, *Phys. Rev. Lett.* **74** (Mar, 1995) 2422–2426,  
<sup>3039</sup> doi:[10.1103/PhysRevLett.74.2422](https://doi.org/10.1103/PhysRevLett.74.2422).
- <sup>3040</sup> [47] LHC Higgs Cross Section Working Group Collaboration, “Handbook of LHC Higgs Cross  
<sup>3041</sup> Sections: 3. Higgs Properties”, doi:[10.5170/CERN-2013-004](https://doi.org/10.5170/CERN-2013-004), arXiv:[1307.1347](https://arxiv.org/abs/1307.1347).
- <sup>3042</sup> [48] W. Beenakker et al., “Higgs radiation off top quarks at the Tevatron and the LHC”,  
<sup>3043</sup> *Phys.Rev.Lett.* **87** (2001) 201805, doi:[10.1103/PhysRevLett.87.201805](https://doi.org/10.1103/PhysRevLett.87.201805),  
<sup>3044</sup> arXiv:[hep-ph/0107081](https://arxiv.org/abs/hep-ph/0107081).
- <sup>3045</sup> [49] W. Beenakker et al., “NLO QCD corrections to t anti-t H production in hadron  
<sup>3046</sup> collisions”, *Nucl.Phys.* **B653** (2003) 151–203, doi:[10.1016/S0550-3213\(03\)00044-0](https://doi.org/10.1016/S0550-3213(03)00044-0),  
<sup>3047</sup> arXiv:[hep-ph/0211352](https://arxiv.org/abs/hep-ph/0211352).

- 3048 [50] R. Frederix et al., “Scalar and pseudoscalar Higgs production in association with a  
 3049 top-antitop pair”, *Phys.Lett.* **B701** (2011) 427–433,  
 3050 doi:10.1016/j.physletb.2011.06.012, arXiv:1104.5613.
- 3051 [51] M. Garzelli, A. Kardos, C. Papadopoulos, and Z. Trocsanyi, “Standard Model Higgs  
 3052 boson production in association with a top anti-top pair at NLO with parton showering”,  
 3053 *Europhys.Lett.* **96** (2011) 11001, doi:10.1209/0295-5075/96/11001,  
 3054 arXiv:1108.0387.
- 3055 [52] S. Dawson, L. Orr, L. Reina, and D. Wackerlo, “Associated top quark Higgs boson  
 3056 production at the LHC”, *Phys.Rev.* **D67** (2003) 071503,  
 3057 doi:10.1103/PhysRevD.67.071503, arXiv:hep-ph/0211438.
- 3058 [53] T. Gleisberg et al., “Event generation with SHERPA 1.1”, *JHEP* **0902** (2009) 007,  
 3059 doi:10.1088/1126-6708/2009/02/007, arXiv:0811.4622.
- 3060 [54] P. Artoisenet, R. Frederix, O. Mattelaer, and R. Rietkerk, “Automatic spin-entangled  
 3061 decays of heavy resonances in Monte Carlo simulations”, *JHEP* **1303** (2013) 015,  
 3062 doi:10.1007/JHEP03(2013)015, arXiv:1212.3460.
- 3063 [55] F. Cascioli, P. Maierhofer, and S. Pozzorini, “Scattering Amplitudes with Open Loops”,  
 3064 *Phys.Rev.Lett.* **108** (2012) 111601, doi:10.1103/PhysRevLett.108.111601,  
 3065 arXiv:1111.5206.
- 3066 [56] F. Krauss, R. Kuhn, and G. Soff, “AMEGIC++ 1.0: A Matrix element generator in  
 3067 C++”, *JHEP* **0202** (2002) 044, doi:10.1088/1126-6708/2002/02/044,  
 3068 arXiv:hep-ph/0109036.
- 3069 [57] T. Gleisberg and F. Krauss, “Automating dipole subtraction for QCD NLO  
 3070 calculations”, *Eur.Phys.J.* **C53** (2008) 501–523,  
 3071 doi:10.1140/epjc/s10052-007-0495-0, arXiv:0709.2881.
- 3072 [58] Planck Collaboration, “Planck 2013 results. I. Overview of products and scientific  
 3073 results”, *Astron.Astrophys.* **571** (2014) A1, doi:10.1051/0004-6361/201321529,  
 3074 arXiv:1303.5062.
- 3075 [59] V. Rubin, N. Thonnard, and J. Ford, W.K., “Rotational properties of 21 SC galaxies  
 3076 with a large range of luminosities and radii, from NGC 4605 /R = 4kpc/ to UGC 2885  
 3077 /R = 122 kpc/”, *Astrophys.J.* **238** (1980) 471, doi:10.1086/158003.

- [60] Super-Kamiokande Collaboration Collaboration, “Measurements of the solar neutrino flux from Super-Kamiokande’s first 300 days”, *Phys.Rev.Lett.* **81** (1998) 1158–1162, doi:10.1103/PhysRevLett.81.1158, arXiv:hep-ex/9805021.
- [61] KamLAND Collaboration Collaboration, “Measurement of neutrino oscillation with KamLAND: Evidence of spectral distortion”, *Phys.Rev.Lett.* **94** (2005) 081801, doi:10.1103/PhysRevLett.94.081801, arXiv:hep-ex/0406035.
- [62] MINOS Collaboration Collaboration, “Observation of muon neutrino disappearance with the MINOS detectors and the NuMI neutrino beam”, *Phys.Rev.Lett.* **97** (2006) 191801, doi:10.1103/PhysRevLett.97.191801, arXiv:hep-ex/0607088.
- [63] S. P. Martin, “A Supersymmetry primer”, *Adv.Ser.Direct.High Energy Phys.* **21** (2010) 1–153, doi:10.1142/9789814307505\_0001, arXiv:hep-ph/9709356.
- [64] J. Aguilar-Saavedra, R. Benbrik, S. Heinemeyer, and M. Prez-Victoria, “Handbook of vectorlike quarks: Mixing and single production”, *Phys.Rev.* **D88** (2013), no. 9, 094010, doi:10.1103/PhysRevD.88.094010, arXiv:1306.0572.
- [65] G. Burdman, M. Perelstein, and A. Pierce, “Large Hadron Collider tests of a little Higgs model”, *Phys.Rev.Lett.* **90** (2003) 241802, doi:10.1103/PhysRevLett.90.241802, arXiv:hep-ph/0212228.
- [66] M. Perelstein, M. E. Peskin, and A. Pierce, “Top quarks and electroweak symmetry breaking in little Higgs models”, *Phys.Rev.* **D69** (2004) 075002, doi:10.1103/PhysRevD.69.075002, arXiv:hep-ph/0310039.
- [67] H.-C. Cheng, I. Low, and L.-T. Wang, “Top partners in little Higgs theories with  $T$  parity”, *Phys. Rev. D* **74** (Sep, 2006) 055001, doi:10.1103/PhysRevD.74.055001.
- [68] H.-C. Cheng, B. A. Dobrescu, and C. T. Hill, “Electroweak symmetry breaking and extra dimensions”, *Nucl.Phys.* **B589** (2000) 249–268, doi:10.1016/S0550-3213(00)00401-6, arXiv:hep-ph/9912343.
- [69] M. S. Carena, E. Ponton, J. Santiago, and C. E. Wagner, “Light Kaluza Klein States in Randall-Sundrum Models with Custodial SU(2)”, *Nucl.Phys.* **B759** (2006) 202–227, doi:10.1016/j.nuclphysb.2006.10.012, arXiv:hep-ph/0607106.
- [70] C. T. Hill, “Topcolor: Top quark condensation in a gauge extension of the standard model”, *Phys.Lett.* **B266** (1991) 419–424, doi:10.1016/0370-2693(91)91061-Y.

- 3108 [71] R. Contino, L. Da Rold, and A. Pomarol, “Light custodians in natural composite Higgs  
 3109 models”, *Phys.Rev.* **D75** (2007) 055014, doi:10.1103/PhysRevD.75.055014,  
 3110 arXiv:hep-ph/0612048.
- 3111 [72] “CERN Linac2 Duoplasmatron Schematic”.  
 3112 URL <http://linac2.home.cern.ch/linac2/sources/source.htm>.
- 3113 [73] “CERN Linac2 Duoplasmatron Image”. URL <http://linac2.web.cern.ch/linac2/>  
 3114 CF002521-ProtonSourceDuoplasmatronRichardChristianss.jpg.
- 3115 [74] “RFQ Schematic”. URL [http://www.lnl.infn.it/images/acc\\_fig14.jpg](http://www.lnl.infn.it/images/acc_fig14.jpg).
- 3116 [75] “Example RFQ Image”. URL [http://www.toyama-en.com/accelerator/images/rfq\\_downstream\\_webLarge.jpg](http://www.toyama-en.com/accelerator/images/rfq_downstream_webLarge.jpg).
- 3117 [76] “Inside an Alvarez Tube”. URL [https://cds.cern.ch/record/1281668/files/DTL\\_proto\\_assembled\\_image.jpg?subformat=icon](https://cds.cern.ch/record/1281668/files/DTL_proto_assembled_image.jpg?subformat=icon).
- 3118 [77] “CERN Linac2 Alvarez Tubes”. URL [http://www.toyama-en.com/accelerator/images/rfq\\_downstream\\_webLarge.jpg](http://www.toyama-en.com/accelerator/images/rfq_downstream_webLarge.jpg).
- 3119 [78] M. Benedikt et al., “LHC Design Report Vol3 - The Injection Chain”. CERN, Geneva,  
 3120 2004.
- 3121 [79] C. Hill et al., “Tests of the CERN proton linac performance for LHC - type beams”,  
 3122 *eConf* **C000821** (2000) TUD17, arXiv:physics/0008102.
- 3123 [80] “Image, CERN PSbooster injection from Linac2”.  
 3124 URL [http://www.lhc-facts.ch/img/psb/psb\\_injektion.jpg](http://www.lhc-facts.ch/img/psb/psb_injektion.jpg).
- 3125 [81] “Image, CERN PSbooster is 4 vertically stacked synchotrons”.  
 3126 URL <http://www.lhc-facts.ch/img/psb/psb.jpg>.
- 3127 [82] “Image, CERN PSbooster Layout”.  
 3128 URL <http://psb-machine.web.cern.ch/psb-machine/layout.gif>.
- 3129 [83] “Image, CERN PSbooster Section 10 Layout”.  
 3130 URL <http://psb-machine.web.cern.ch/psb-machine/sectors/sect10.gif>.
- 3131 [84] “Image, CERN PSbooster CO2 RF Cavity”. URL [http://cern-accelerators-optics.web.cern.ch/cern-accelerators-optics/PS\\_BOOSTER/Pictures/P10L1.JPG](http://cern-accelerators-optics.web.cern.ch/cern-accelerators-optics/PS_BOOSTER/Pictures/P10L1.JPG).
- 3132 [85] “Image, CERN PSbooster 2 batch filling scheme of the PS”.  
 3133 URL <http://ps-div.web.cern.ch/ps-div/LHC-PS/schindlrf.gif>.

- <sup>3138</sup> [86] K. S. Klaus Hanke, and Michel Chanel.
- <sup>3139</sup> [87] “Image, CERN PSbooster Layout”.
- <sup>3140</sup> URL <http://psb-machine.web.cern.ch/psb-machine/>.
- <sup>3141</sup> [88] S. Baird, “Accelerators for pedestrians; rev. version”, Technical Report AB-Note-2007-014. CERN-AB-Note-2007-014. PS-OP-Note-95-17-Rev-2.
- <sup>3142</sup> CERN-PS-OP-Note-95-17-Rev-2, CERN, Geneva, Feb, 2007.
- <sup>3143</sup>
- <sup>3144</sup> [89] “Image, CERN PS Layout”.
- <sup>3145</sup> URL <http://psring.web.cern.ch/psring/psring/pscomplex.gif>.
- <sup>3146</sup> [90] “Image, CERN PS Dipoles”.
- <sup>3147</sup> URL <http://home.web.cern.ch/sites/home.web.cern.ch/files/styles/medium/public/image/accelerator/2013/01/accelerators-ps.jpg?itok=5E3Tp4Q0>.
- <sup>3148</sup>
- <sup>3149</sup> [91] “Image, CERN SPS, Layout”.
- <sup>3150</sup> URL <https://espace.cern.ch/be-dep/OP/sps/pictures/sps2.PNG>.
- <sup>3151</sup> [92] “Image, CERN SPS Beamline”.
- <sup>3152</sup> URL <http://home.web.cern.ch/sites/home.web.cern.ch/files/styles/medium/public/image/accelerator/2013/01/sps.jpg?itok=iLnNGjdI>.
- <sup>3153</sup>
- <sup>3154</sup> [93] “Image, CERN SPS, Inside 200 MHz RF Cavity”.
- <sup>3155</sup> URL <http://rsta.royalsocietypublishing.org/content/roypta/370/1973/3887/F24.large.jpg?width=800&height=600&carousel=1>.
- <sup>3156</sup>
- <sup>3157</sup> [94] “Image, CERN SPS 200 MHz RF Cavity”. URL <https://cds.cern.ch/record/969086/files/7505156X.jpg?subformat=icon-1440>.
- <sup>3158</sup>
- <sup>3159</sup> [95] “CERN Website, Super Proton Synchrotron”.
- <sup>3160</sup> URL <http://home.web.cern.ch/about/accelerators/super-proton-synchrotron>.
- <sup>3161</sup> [96] G. Dme, “The SPS acceleration system travelling wave drift-tube structure for the
- <sup>3162</sup> CERN SPS”,.
- <sup>3163</sup> [97] O. S. Brning et al., “LHC Design Report Vol1 - The Main Ring”. CERN, Geneva, 2004.
- <sup>3164</sup> [98] “CERN, List of All LHC Magnets”. URL [http://lhc-machine-outreach.web.cern.ch/lhc-machine-outreach/components/magnets/types\\_of\\_magnets.htm](http://lhc-machine-outreach.web.cern.ch/lhc-machine-outreach/components/magnets/types_of_magnets.htm).
- <sup>3165</sup>
- <sup>3166</sup> [99] M. Barnes, J. Borburgh, B. Goddard, and M. Hourican, “Injection and extraction
- <sup>3167</sup> magnets: septa”, [arXiv:1103.1062](https://arxiv.org/abs/1103.1062).

- 3168 [100] “Image, CERN LHC, Dipole Magnet, Dual Bore”.  
3169 URL <http://lhc-machine-outreach.web.cern.ch/lhc-machine-outreach/>  
3170 components/magnets\_files/image002.jpg.
- 3171 [101] “Image, CERN LHC, Dipole Magnet, field”. URL <http://lhc-machine-outreach.web.cern.ch/lhc-machine-outreach/images/dipole-field.gif>.
- 3173 [102] J. Beauquis, “LHC Dipole Geometry Parameters, Comparisons between Producers”,  
3174 *eConf* **C04100411** (2004) 046.
- 3175 [103] “Image, CERN LHC, Dipole Magnet, Staging Area”. URL [https://cds.cern.ch/record/994212/files/transp-2001-001\\_05.jpg?subformat=icon-1440](https://cds.cern.ch/record/994212/files/transp-2001-001_05.jpg?subformat=icon-1440).
- 3177 [104] “Image, CERN LHC, Quadrupole Magnet, Cross Section Schematic”.  
3178 URL <https://cds.cern.ch/record/841485>.
- 3179 [105] “Image, CERN LHC, Quadrupole Magnet, Staging Area”. URL <http://www.triumf.ca/sites/default/files/images/twinquadrupolemagnets.preview.jpg>.
- 3181 [106] “Image, CERN LHC, Quadrupole Magnet, Focusing Schematic”.  
3182 URL [http://www.lhc-closer.es/img/subidas/4\\_6\\_3\\_3.png](http://www.lhc-closer.es/img/subidas/4_6_3_3.png).
- 3183 [107] “Image, CERN LHC, Multipole Magnet, Focusing Schematic”.  
3184 URL <http://www.lhc-closer.es/img/subidas/Multipoles.jpg>.
- 3185 [108] “Image, CERN LHC, Magnetic Cell Layout”.  
3186 URL [http://www.lhc-closer.es/img/subidas/4\\_6\\_3\\_4.png](http://www.lhc-closer.es/img/subidas/4_6_3_4.png).
- 3187 [109] “Image, CERN LHC, Interaction Region Schematic”.  
3188 URL [http://www.lhc-closer.es/img/subidas/4\\_6\\_3\\_6.jpg](http://www.lhc-closer.es/img/subidas/4_6_3_6.jpg).
- 3189 [110] J.-L. Caron, “Superconducting cavity with its cryostat. Cavit supraconductrice dans son  
3190 cryostat.”, May, 1994. AC Collection. Legacy of AC. Pictures from 1992 to 2002.
- 3191 [111] “Image, CERN LHC, Superconducting RF Cavities, Staged”.  
3192 URL [http://www.lhc-closer.es/img/subidas/4\\_7\\_2\\_2.jpg](http://www.lhc-closer.es/img/subidas/4_7_2_2.jpg).
- 3193 [112] “Image, CERN LHC, Superconducting RF Cavities, Installed”.  
3194 URL [http://home.web.cern.ch/sites/home.web.cern.ch/files/image/engineering\\_page/2013/01/rf-cavity.jpg](http://home.web.cern.ch/sites/home.web.cern.ch/files/image/engineering_page/2013/01/rf-cavity.jpg).
- 3196 [113] “Outreach, CERN LHC, Cryogenic System”. URL <http://home.web.cern.ch/about/engineering/cryogenics-low-temperatures-high-performance>.

- <sup>3198</sup> [114] “The challenge of keeping cool”,,
- <sup>3199</sup> [115] “Outreach, CERN LHC, Vacuum System”. URL <http://home.web.cern.ch/about/engineering/vacuum-empty-interplanetary-space>.
- <sup>3200</sup>
- <sup>3201</sup> [116] CMS Collaboration Collaboration, “Particle-Flow Event Reconstruction in CMS and Performance for Jets, Taus, and MET”, Technical Report CMS-PAS-PFT-09-001, <sup>3202</sup> CERN, 2009. Geneva, Apr, 2009.
- <sup>3203</sup>
- <sup>3204</sup> [117] CMS Collaboration, “Description and performance of track and primary-vertex <sup>3205</sup> reconstruction with the CMS tracker”, *JINST* **9** (2014), no. 10, P10009, <sup>3206</sup> doi:10.1088/1748-0221/9/10/P10009, arXiv:1405.6569.
- <sup>3207</sup> [118] R. Frhwirth, “Application of Kalman filtering to track and vertex fitting”, <sup>3208</sup> *Nucl.Instrum.Meth.* **A262** (1987) 444–450, doi:10.1016/0168-9002(87)90887-4.
- <sup>3209</sup> [119] CMS Electromagnetic Calorimeter Group Collaboration, “Intercalibration of the barrel <sup>3210</sup> electromagnetic calorimeter of the CMS experiment at start-up”, *JINST* **3** (2008) <sup>3211</sup> P10007, doi:10.1088/1748-0221/3/10/P10007.
- <sup>3212</sup> [120] K. Cankocak, Y. Onel, P. de Barbaro, and D. Vishnevskiy, “CMS HCAL Installation and <sup>3213</sup> Commissioning”, Technical Report CMS-CR-2008-047, CERN, Geneva, Jul, 2008.
- <sup>3214</sup> [121] CMS Collaboration Collaboration, “Commissioning of the CMS ECAL calibration with <sup>3215</sup> muons from cosmic rays and beam dumps”, Technical Report CMS-CR-2009-339, CERN, <sup>3216</sup> Geneva, Nov, 2009.
- <sup>3217</sup> [122] CMS Collaboration Collaboration, “Performance of the CMS Hadron Calorimeter with <sup>3218</sup> Cosmic Ray Muons and LHC Beam Data”, *J. Instrum.* **5** (Nov, 2009) T03012 . 35 p.
- <sup>3219</sup> [123] CMS Collaboration Collaboration, “HCAL performance from first collisions data”,,
- <sup>3220</sup> [124] CMS Collaboration Collaboration, “Particle-flow commissioning with muons and <sup>3221</sup> electrons from J/Psi and W events at 7 TeV”, Technical Report CMS-PAS-PFT-10-003, <sup>3222</sup> CERN, 2010. Geneva, 2010.
- <sup>3223</sup> [125] W. Adam, R. Frhwirth, A. Strandlie, and T. Todor, “Reconstruction of Electrons with <sup>3224</sup> the Gaussian-Sum Filter in the CMS Tracker at the LHC”,,
- <sup>3225</sup> [126] M. Cacciari, G. P. Salam, and G. Soyez, “The Anti-k(t) jet clustering algorithm”, *JHEP* <sup>3226</sup> **0804** (2008) 063, doi:10.1088/1126-6708/2008/04/063, arXiv:0802.1189.

- 3227 [127] CMS Collaboration Collaboration, “Commissioning of the Particle-Flow reconstruction  
 3228 in Minimum-Bias and Jet Events from pp Collisions at 7 TeV”, Technical Report  
 3229 CMS-PAS-PFT-10-002, CERN, Geneva, 2010.
- 3230 [128] Particle Data Group Collaboration, “Review of Particle Physics”, *Chin.Phys. C***38**  
 3231 (2014) 090001, doi:10.1088/1674-1137/38/9/090001.
- 3232 [129] “MET Optional Filters”.  
 3233 <https://twiki.cern.ch/twiki/bin/view/CMS/MissingETOptionalFilters>.
- 3234 [130] CMS Collaboration, “Jet Energy Resolution in CMS at  $\sqrt{s}=7$  TeV”,.
- 3235 [131] C. Weiser, “A Combined Secondary Vertex Based B-Tagging Algorithm in CMS”,  
 3236 Technical Report CMS-NOTE-2006-014, CERN, Geneva, Jan, 2006.
- 3237 [132] “Operating Points for  $b$ -Tag Algorithms”.  
 3238 <https://twiki.cern.ch/twiki/bin/viewauth/CMS/BTagPerformanceOP>.
- 3239 [133] “ $b$ -Jet Identification in the CMS Experiment”,.
- 3240 [134] VHbb Team, “Search for the SM Higgs Boson Produced in Association with W or Z and  
 3241 Decaying to Bottom Quarks (ICHEP 2012)”, CMS Note 2012/181, 2012.
- 3242 [135] A. Hocker et al., “TMVA - Toolkit for Multivariate Data Analysis”, *PoS ACAT* (2007)  
 3243 040, arXiv:physics/0703039.
- 3244 [136] J. D. Bjorken and S. J. Brodsky, “Statistical Model for Electron-Positron Annihilation  
 3245 into Hadrons”, *Phys. Rev. D* **1** (1970) 1416, doi:10.1103/PhysRevD.1.1416.
- 3246 [137] G. C. Fox and S. Wolfram, “Event Shapes in  $e^+e^-$  Annihilation”, *Nucl. Phys. B* **149**  
 3247 (1979) 413, doi:10.1016/0550-3213(79)90003-8.
- 3248 [138] “Jet Energy Scale Uncertainties”. <https://twiki.cern.ch/twiki/bin/view/CMS/WorkBookJetEnergyCorrections>.
- 3250 [139] “Jet Energy Resolution Uncertainties”.  
 3251 <https://twiki.cern.ch/twiki/bin/view/CMS/JetResolution>.
- 3252 [140] “ $b$ -Tag Scale Factor Uncertainties”.  
 3253 <https://twiki.cern.ch/twiki/bin/viewauth/CMS/BtagPOG>.
- 3254 [141] T. Peiffer., “ $Q^2$  Systematic MC Samples re-weighting”. <https://indico.cern.ch/getFile.py/access?contribId=5&resId=0&materialId=slides&confId=177717>, 2012.

- 3256 [142] A. Bredenstein, A. Denner, S. Dittmaier, and S. Pozzorini, “NLO QCD corrections to  
 3257 top anti-top bottom anti-bottom production at the LHC: 2. full hadronic results”,  
 3258 (2010). [arXiv:1001.4006](https://arxiv.org/abs/1001.4006).
- 3259 [143] The ATLAS Collaboration, The CMS Collaboration, The LHC Higgs Combination  
 3260 Group Collaboration, “Procedure for the LHC Higgs boson search combination in  
 3261 Summer 2011”, Technical Report CMS-NOTE-2011-005. ATL-PHYS-PUB-2011-11,  
 3262 CERN, Geneva, Aug, 2011.
- 3263 [144] J. Conway, “Incorporating Nuisance Parameters in Likelihoods for Multisource Spectra”,  
 3264 [arXiv:1103.0354](https://arxiv.org/abs/1103.0354).
- 3265 [145] G. Cowan, K. Cranmer, E. Gross, and O. Vitells, “Asymptotic formulae for  
 3266 likelihood-based tests of new physics”, *Eur.Phys.J. C***71** (2011) 1554,  
 3267 doi:[10.1140/epjc/s10052-011-1554-0](https://doi.org/10.1140/epjc/s10052-011-1554-0), doi:[10.1140/epjc/s10052-013-2501-z](https://doi.org/10.1140/epjc/s10052-013-2501-z),  
 3268 [arXiv:1007.1727](https://arxiv.org/abs/1007.1727).
- 3269 [146] CMS Collaboration, “Search for the standard model Higgs boson produced in association  
 3270 with a top-quark pair in pp collisions at the LHC”, *JHEP* **1305** (2013) 145,  
 3271 doi:[10.1007/JHEP05\(2013\)145](https://doi.org/10.1007/JHEP05(2013)145), [arXiv:1303.0763](https://arxiv.org/abs/1303.0763).
- 3272 [147] CMS Collaboration, “Measurement of the differential top-quark pair production cross  
 3273 section in the dilepton channel in pp collisions at  $\sqrt{s} = 8$  TeV.”, CMS PAS TOP-12-028,  
 3274 2012.
- 3275 [148] CMS Collaboration, “Measurement of the differential top-quark pair production cross  
 3276 section in the lepton+jets channel in pp collisions at  $\sqrt{s} = 8$  TeV.”, CMS PAS  
 3277 TOP-12-027, 2012.
- 3278 [149] CMS Collaboration, “Calibration of the Combined Secondary Vertex b-Tagging  
 3279 discriminant using dileptonic ttbar and Drell-Yan events”, CMS Note 2013/130, 2013.
- 3280 [150] CMS Collaboration, “Dilepton trigger and lepton identification efficiencies for the top  
 3281 quark pair production cross section measurement at 8 TeV in the dilepton decay  
 3282 channel.”, CMS AN AN-12-389, 2012.
- 3283 [151] CMS Collaboration, “Search for the associated production of the Higgs boson with a  
 3284 top-quark pair”, *JHEP* **1409** (2014) 087,  
 3285 doi:[10.1007/JHEP09\(2014\)087](https://doi.org/10.1007/JHEP09(2014)087), doi:[10.1007/JHEP10\(2014\)106](https://doi.org/10.1007/JHEP10(2014)106), [arXiv:1408.1682](https://arxiv.org/abs/1408.1682).

- 3286 [152] J. Alwall et al., “The automated computation of tree-level and next-to-leading order  
3287 differential cross sections, and their matching to parton shower simulations”, *JHEP*  
3288 **1407** (2014) 079, doi:10.1007/JHEP07(2014)079, arXiv:1405.0301.
- 3289 [153] P. Artoisenet, R. Frederix, O. Mattelaer, and R. Rietkerk, “Automatic spin-entangled  
3290 decays of heavy resonances in Monte Carlo simulations”, *JHEP* **1303** (2013) 015,  
3291 doi:10.1007/JHEP03(2013)015, arXiv:1212.3460.
- 3292 [154] T. Sjostrand, S. Mrenna, and P. Z. Skands, “A Brief Introduction to PYTHIA 8.1”,  
3293 *Comput.Phys.Commun.* **178** (2008) 852–867, doi:10.1016/j.cpc.2008.01.036,  
3294 arXiv:0710.3820.
- 3295 [155] R. Frederix and S. Frixione, “Merging meets matching in MC@NLO”, *JHEP* **1212**  
3296 (2012) 061, doi:10.1007/JHEP12(2012)061, arXiv:1209.6215.

# <sup>3297</sup> List of Acronyms

<sup>3298</sup> **ATLAS** A Toroidal LHC Apparatus

<sup>3299</sup> **BSM** Beyond the Standard Model

<sup>3300</sup> **CERN** European Center for Nuclear Research

<sup>3301</sup> **CMS** Compact Muon Solenoid

<sup>3302</sup> **ECAL** Electromagnetic Calorimeter

<sup>3303</sup> **FSR** Final State Radiation

<sup>3304</sup> **HCAL** Hadronic Calorimeter

<sup>3305</sup> **ISR** Initial State Radiation

<sup>3306</sup> **JHEP** Journal of High Energy Physics

<sup>3307</sup> **LHC** Large Hadron Collider

<sup>3308</sup> **LO** Leading Order

<sup>3309</sup> **MVA** Multi-Variate Analysis

<sup>3310</sup> **NLO** Next to Leading Order

<sup>3311</sup> **QCD** Quantum Chromodynamics

<sup>3312</sup> **QED** Quantum Electrodynamics

<sup>3313</sup> **QFT** Quantum Field Theory

<sup>3314</sup> **SM** Standard Model